INVESTIGATION OF THE HERSCHEL-QUINCKE TUBE CONCEPT IN A RECTANGULAR LINED DUCT

By

Jeonghoon Kim

Dissertation submitted to the Faculty of the
Virginia Polytechnic Institute and State University
in partial fulfillment of the requirements for the degree of

Master of Science
in
Mechanical Engineering

Ricardo A. Burdisso, Chair
Marty E. Johnson
Wing F. Ng

September 20, 2001
Blacksburg, Virginia

Keywords: aeroacoustics, liner, Herschel-Quincke tube, higher-order modes

INVESTIGATION OF THE HERSCHEL-QUINCKE TUBE CONCEPT IN A RECTANGULAR LINED DUCT

By

Jeonghoon Kim

Committee chairman: Ricardo A. Burdisso, Mechanical Engineering

(ABSTRACT)

In this research an innovative combination of the Herschel-Quincke tubes and traditional liners is proposed for application in noise reduction of aircraft engines. The approach consists of installing Herschel-Quincke (HQ) tubes on lined rectangular ducts. An analytical model was developed to predict the effects of HQ tubes applied to rectangular lined ducts. The technique involves assuming the tube-duct interfaces as finite piston sources. These sources couple the acoustic field inside the duct with the acoustic field within the HQ tubes. The accuracy of the analytical model was validated with experimental data. Three different types of experimental configurations were tested: liner only, HQ tube with a hard wall duct, and HQ tubes with liners. Analytical predictions were shown to correlate well with the experimental data. Two typical types of liners, perforate and linear, were tested in these investigations. The perforate and linear liners with HQ systems showed better sound attenuations than the HQ tubes with hard walled ducts and liners only systems. The performance of the perforate and linear liners with HQ tubes were investigated in various configurations. The results indicated possible combinations which show great potential for reducing the noise within the ducts

Acknowledgments

I would like to thank my research advisor, Prof. Ricardo Burdisso, who provided the opportunity to join an exciting research project, for his kind and insightful guidance in my research. I would like to acknowledge Prof. Wing. F. Ng and Prof. Marty Johnson for serving on my advisory committee.

I would like to express my sincere gratitude toward all my friends in the Vibration and Acoustics Laboratories who helped me during the course of this research. Especially, I would like to thank Dr. Jinwei Feng and Raphael Hallez, who graduated recently, and my office mate, José Alonso. I am indebted to the Aerostructures group of the Goodrich Corporation, San Diego CA, for their financial and technical support. I would particularly recognize the technical mentor of this research group, Dr. Hwa-Wan Kwan.

Finally, I would like to thank my family, especially my wife, Misun Jeong, who encouraged and prayed for me ever since I began this research. I thank God with all my heart who provided the strength and wisdom to finish this research.

Contents

List of figures

List of tables

Chapter 1. Introduction

Ever since aircraft have become a major mode of transportation, the problem of aircraft noise has grown increasingly significant, particularly at airports and surrounding communities. Furthermore, the regulations on aircraft noise requirements have become more stringent as residents around airports have become more concerned about noise problems. In the last few decades, various attempts have been made to reduce the noise from aircraft engines. A common way to reduce the fan noise of engines has been to directly change the design of the fan. For example, the geometry of the fan blades and the rotor vanes can be modified to reduce the generated noise due to rotor-stator interactions [1-3]. Systems with increased spacings between rotor and stator, as well as fans with leaned blades were investigated. Although these systems achieve significant noise reduction, these innovative systems also triggered vortex shedding and stress concentration in the structure of the blades.

Passive treatments also have been extensively used to reduce fan noise [4]. These porous material systems are typically placed on the inlet walls of the engine, and their efficiency was proportional to the length of the applied treatment. These liner systems can be classified as the absorber type, the resonator type, and a type which has a combination of both of these characteristics. Absorber liners consist of a thick layer of porous material, and will attenuate broadband noise. However, these are not particularly suitable for attenuating large amplitude components of discrete frequencies. Resonant liners consist of a thin sheet of perforated facing material separated from an impervious surface by a cavity divided into compartments by a honeycomb spacer structure; this forms an array of resonators which effectively attenuate a predominantly narrow frequency band of noise. However, this system is not very effective over a broader band frequency range. Lastly, a liner combining the essential features of both types, consisting of a thin porous absorptive facing material backed by resonant cavities, has good attenuation characteristics over a wide range of frequencies.

Although the applications of liners were effective, the shorter inlet ducts of modern ultra high bypass turbofan engines and the lower blade passage frequencies (BPFs) for these engines made the traditional passive liner technology less efficient in attenuating the fan noise. Because of these difficulties, active noise control techniques integrated with a passive system provided the potential of producing an effective noise control solution for fans. [5-9]

However, despite the recent advances in active noise control methods for controlling the BPF tone and harmonics, the complexity of these systems imply that the implementation of a practical system for production may be still many years away. Furthermore, it has been reported that simply reducing the BPF tone and harmonics, i.e., without any reduction in the broadband levels, may result in little or no reduction in the EPNL, which is the metric used to quantify aircraft flyover noise [10,11]. Thus, it is likely that a noise control system in combination with broadband noise control will have to be implemented to produce an effective noise control solution for turbofan engines.

In this research, a new noise reduction approach has been investigated. This approach combines a traditional liner with Herschel-Quincke (HQ) tubes. An HQ tube is a hollow side-duct that travels along the engine axis and attaches to the inlet at each of the two ends of the tube. This thesis presents the experimental and analytical results of the work that was performed on the application of the HQ tube concept for the reduction broadband noise in lined rectangular ducts. The concept of the HQ tube for noise attenuation is well known for plane-wave duct acoustics. In general, HQ tubes can provide attenuation of sound traveling down a duct at a number of discrete frequencies, which are dictated by the tube parameters such as length, area, and so forth. The tubes can be designed so that the cancellation of frequencies correspond to frequencies at which reduction is desired, e.g., undesirable tones. This research is focused on investigating the effectiveness of combining the HQ tubes system with the traditional passive liner system. With the strategic design of the combined system, the HQ tubes are expected to reduce the low frequency and tonal noise, and the passive liner to reduce the higher broadband frequency noise. For simplicity, this investigation was performed on sound attenuation in a lined rectangular duct with the HQ tubes on one of the duct walls.

The duct has a uniform steady flow. The effectiveness of the passive liners on sound attenuation for a given duct geometry was evaluated when combined with the HQ tubes.

1.1 Review of The Herschel-Quincke Technique

Previous research on the HQ concept has been limited to the control of simple one-dimensional plane waves in ducts as shown in figure 1.1. A brief explanation of the noise cancellation observed with the HQ tube in the case of the plane wave is that some part of the sound energy that flows in the main duct goes into the HQ tube at its entrance. It travels through the tube and recombines with the rest of energy flowing through the main duct at the exit of the tube. Because the sound in the tube has traveled a longer distance, there are frequencies where the sound at the tube exit is out-of-phase with the sound in the main duct; sound cancellation happens at those frequencies. These frequencies are controlled by the geometrical parameters of the HQ tubes, including length, diameter, opening area of the tube, and so forth.

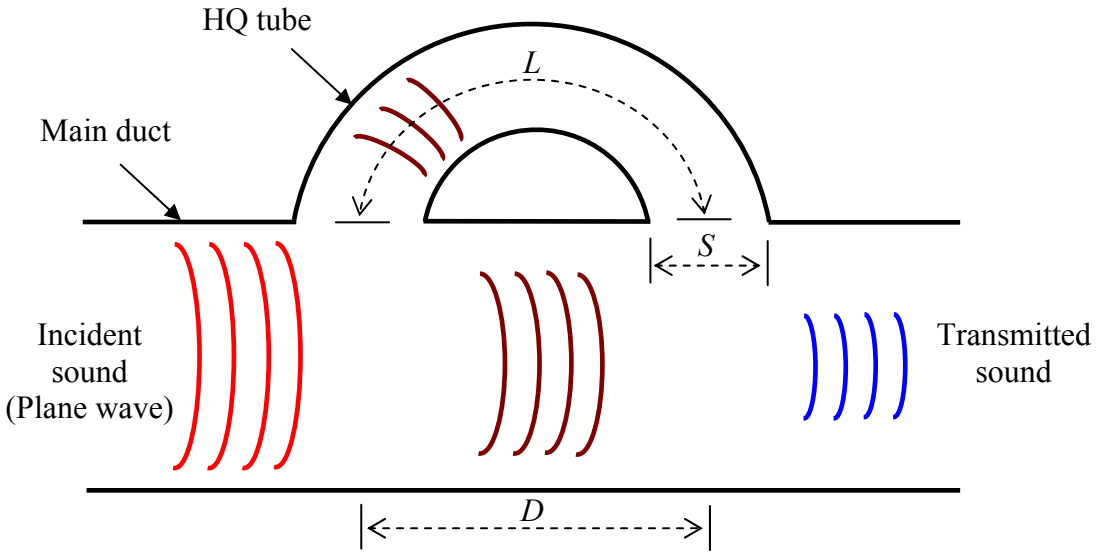

Figure 1.1: Schematic of the Herschel-Quincke tube for the control of plane waves.

Herschel [12] first discussed the idea of the acoustic interference of musical tones with such a system in 1833, and in 1866 Quincke [13] experimentally validated that Herschel's system did effectively cancel sound. Stewart [14] verified that cancellation does occur when the path length difference is $(2m+1)(\lambda/2)$ as Hersche predicted, but also when the path length difference is $m\lambda$, with limited attenuation at other transitional frequencies. However, Stewart's model assumed that the cross-sectional areas of the parallel duct sections were equal. Selamet, et. al. [15], extended Stewart's work by deriving an analytical model without the limitations on duct cross-sectional geometry. The effect of multiple HQ tubes and reflection at the duct opening was more recently addressed, again for plane-waves only [16].

Recently, higher order modes attenuation in two-dimensional hard walled ducts has been analytically investigated using HQ waveguides [17]. This investigation included a model to predict the effect of an HQ tube in the presence of higher order modes, and discussed the potential of the combination of the HQ tube with a passive liner to increase the attenuation of the sound pressure level more effectively.

The potential of HQ tubes to reduce noise from turbofan engines was recently investigated by Burdisso and J. Smith, on a running Pratt & Whitney JT15D turbofan engine [18]. The optimization approach to find most effective geometry of the HQ tubes was also investigated [1]. The results showed a very good reduction of tonal noise at discrete frequencies, as well as broadband noise. The results demonstrated the remarkable potential of the Herschel-Quincke concept for reducing noise from turbofan engines.

The investigation presented in this thesis will extend these efforts to study the effect of combining liners with HQ tubes. The approach used in this study consists of installing Herschel-Quincke (HQ) tubes (waveguide) in a rectangular lined duct. The HQ concept applied to a lined rectangular duct is illustrated in figure 1.2, where two HQ tubes are positioned on the top of the rectangular duct. The top wall of the duct is also lined.

The theoretical analysis is based on a rectangular duct with one side lined in the presence of uniform flow. The analysis provides the sound attenuation spectrum for a given duct with specified acoustic lining parameters. Theoretically predicted attenuation

spectra are compared with experimental results in order to determine the accuracy and validity of the present modeling approach.

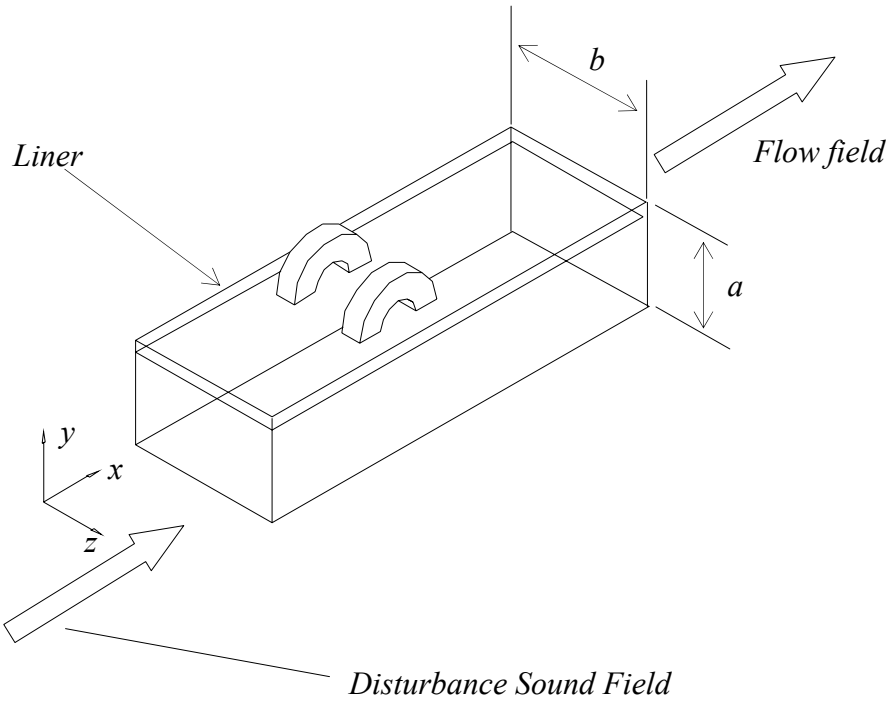

Figure 1.2: The HQ concept applied to a rectangular lined duct.

For this research, it is important to understand the structure of acoustic liners. There are two types of liners that are typically used in turbofan engines. Figure 1.3 (a) shows the typical structure of acoustic liner. Liners consist of a thin sheet of perforated facing material separated from an impervious surface by a cavity divided into compartments by a honeycomb spacer structure. The perforate face sheet has a flow resistance controlled by percentage open area (number of holes and hole size) and thickness and grazing flow speed. Figure 1.3 (b) shows a cross section of this perforate liner. The impedance properties of these types of liners are sensitive to the grazing flow. Thus, it is common practice to bond to the perforate face sheet a wire mesh as shown in figure 1.3 (c). The effect of this wire mesh is to make the acoustic impedance insensitive

to the grazing flow. These liners are referred as “linear” liners (DynaRohr is a trade mark of Goodrich).

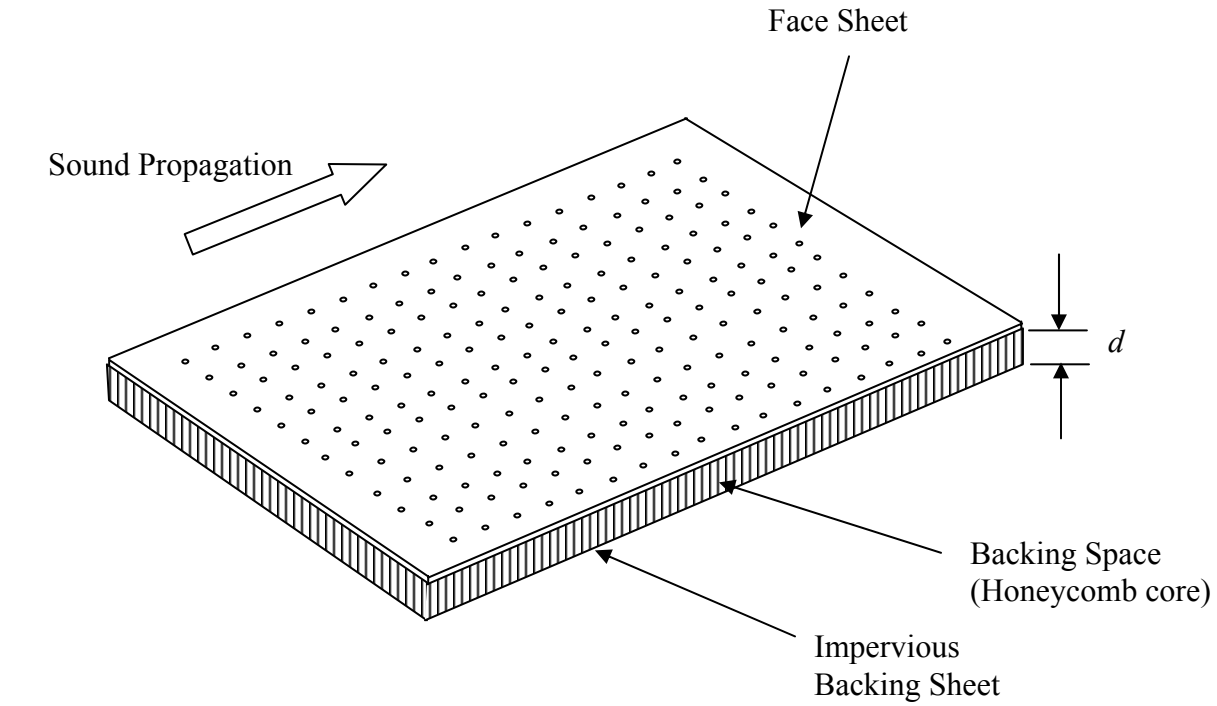

(a)

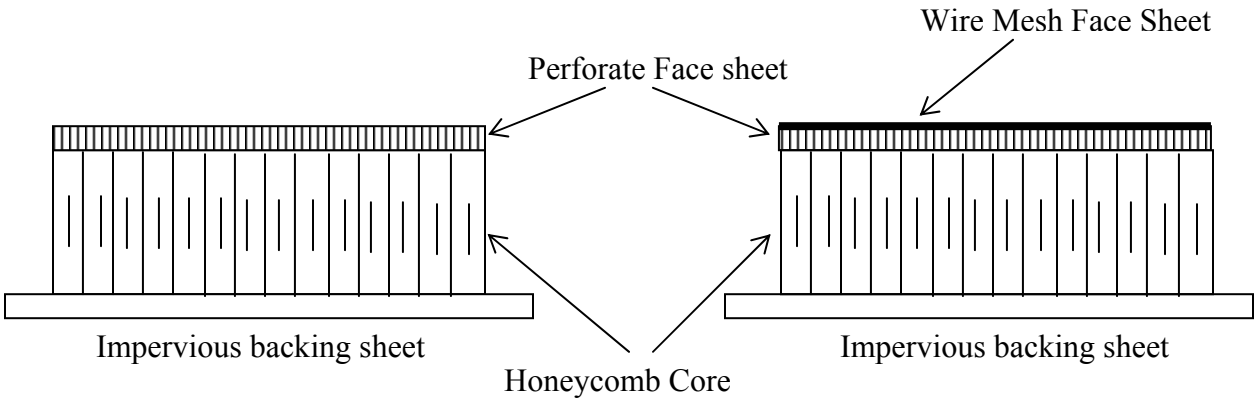

(b) (c)

Figure 1.3: (a) Typical lining configuration
(b) Structure of perforate liner
(c) Structure of a linear liner (DynaRohr liner)

1.2 Objectives

This thesis uses experimental and analytical approaches to investigate the HQ waveguide and passive liner applied to rectangular duct. The first objective of this study is to experimentally investigate the noise reduction potential of the liner with HQ tubes. To achieve this goal, various types of liner-HQ tube systems are tested and evaluated.

The second objective of this work is to develop a model of the HQ tube system mounted on a lined rectangular duct. The modeling technique is developed in order to take into account the propagation of higher-order modes in a rectangular lined duct. The expression to predict the transmission of acoustic energy in the duct mounted with a liner-HQ system is derived. The analytical modeling technique, which describes the sound field within the duct that is excited by a known higher-order mode disturbance and modified by the presence of the HQ tubes, is presented.

The last objective is to validate the model by comparing the predicted results to the experimentally measured data. The effectiveness of combining a passive liner with HQ tubes is verified. Finally, the study is concluded with some final remarks, including recommendations for further research.

1.3 Organization

The remainder of this thesis is organized into three chapters. The theoretical development of the study is presented in Chapter 2. In this chapter, the techniques used to create a model of the HQ system which is mounted on a lined rectangular duct are explained. In chapter 3, the modeling techniques are validated with experimental data. The descriptions of the experiments for different configurations and the test results are presented, and numerical predictions are compared to the experimental results. Two different liners for the HQ-tube systems are tested numerically and experimentally. Finally, conclusions drawn from this study, along with recommendations for further research, are presented in Chapter 4.

Chapter 2. Theoretical Development

In this section, the modeling technique of liner-HQ system for a rectangular duct is presented. The rectangular duct has dimensions "*a*" and "*b*" and it is of infinite length, as shown in figure 2.1(a). The top wall of the infinite duct is assumed lined. It is also assumed that there is a uniform flow field with Mach number M propagating in the positive *x*-direction. Because the effect of the tubes on the duct is modeled as piston sources, the sound field generated by a piston source is developed in Appendix A. Finally, the expressions for the modal amplitudes and transmitted sound power are presented in section 2.2.

2.1 Modeling Technique

In this section, the modeling of the HQ tube mounted on the lined rectangular duct is developed. The hard wall condition is considered as a special case of the liner; i.e. liner with zero admittance. The noise source disturbance sound field was modeled as a set of modes propagating with known amplitudes at $x = 0$. The HQ-tubes are then separated

from the infinite duct and models of the sound field were developed for the tubes and the duct independently, as indicated in figures 2.1(b) and (c). The effect of the tubes on the duct are modeled as finite piston sources at the tube-duct interfaces. Thus, the sound field generated by a piston source in the infinite duct is required. To this end, the acoustic eigenvalue problem was solved to find the duct acoustic eigenproperties that were then used to expand the pressure field inside the duct by a finite piston source on the wall. These derivations are presented in detail in Appendix A, while only the final results are used in this chapter.

The pressure due to the disturbance p_d, at any point in the duct, can be expressed as the sum of a set of modes as:

$$p_d(x,y,z,t) = \sum_{n=0}^{N_d} \sum_{m=0}^{M_d} A_{nm}^d \Phi_{nm}^{(+)}(y,z) e^{-ik_x^{(+)}x} e^{i\omega t} \tag{2.1}$$

where *n* and *m* represents the (*n,m*) mode, A_{nm}^d is the complex amplitude of the (*n,m*) mode, $\Phi_{nm}^{(+)}(y,z)$ is the mode shape in the positive *x*-direction propagation, $k_x^{(+)}$ is the axial wavenumber of a positive *x*-direction traveling or decaying mode, and N_d and M_d are the number of *n* and *m* modes included in the disturbance (see Appendix A).

The pressure variation on the cross-sectional plane of the duct is a function of the modes, $\Phi_{nm}^{(+)}(y,z)$. Figure 2.2 shows a few modal patterns defined by the indices *n* and *m* for a hard walled duct. The dark and light areas in this figure represent positive and negative acoustic pressure. For a hard walled duct, the propagation characteristics of the modes are dictated by the cut-off frequency. If the driving frequency is lower than the cut-off frequency, then the wave will decay exponentially as it propagates along the duct. However, if the driving frequency is higher than the cut-off frequency, then the mode will propagate down the duct with a fixed amplitude (if there is no acoustic treatment). Therefore, the cut-off frequency is a determinant criterion that dictates the propagation characteristics of the modes. This frequency is a function of the flow Mach number and

the mode order, i.e. the cut-off frequency increases as the mode order increases. In a lined duct, the mode cut-off frequency is not defined. The modes will attenuate as they propagate along the duct.

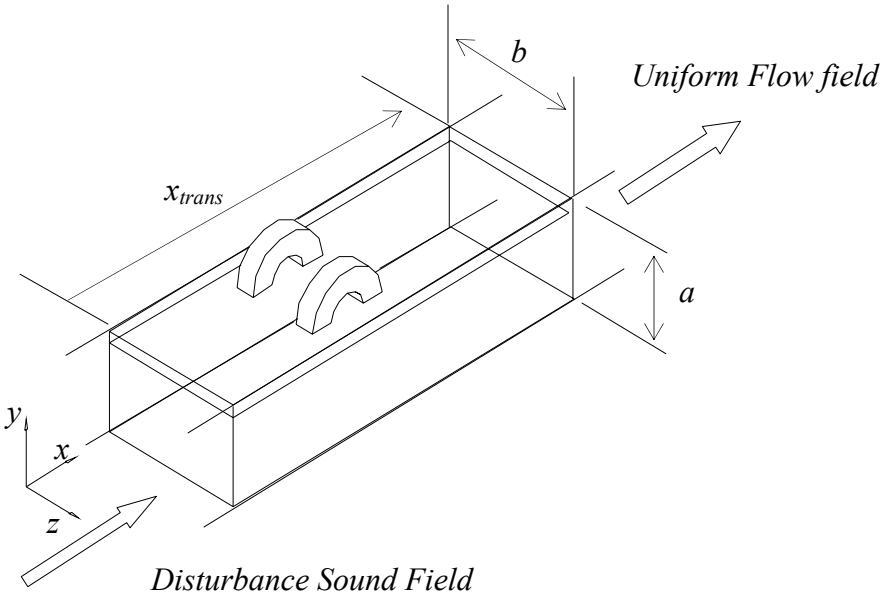

(a) Infinite lined rectangular duct with HQ system

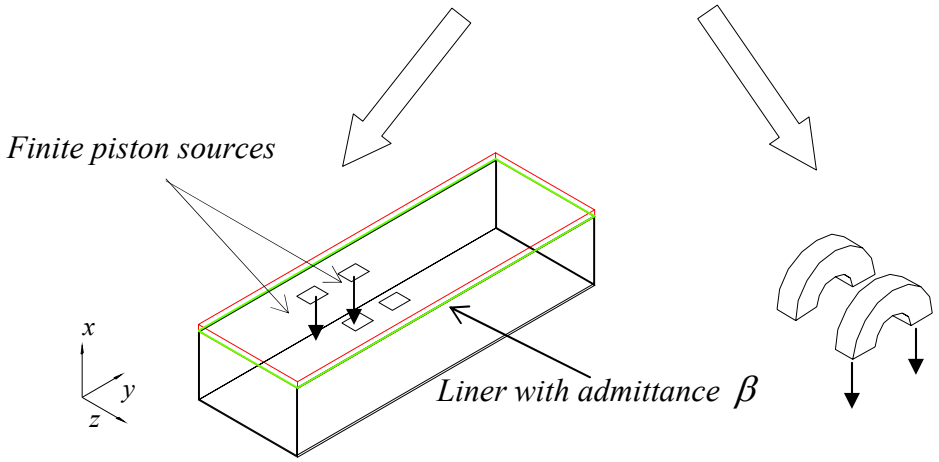

(b) Model of the duct with finite piston sources (c) Model of the HQ tubes

Figure 2.1: (a) Lined rectangular duct mounted with HQ tubes modeled as an infinite duct. Model of sound fields (b) inside the duct and (c) inside the HQ tubes are developed individually.

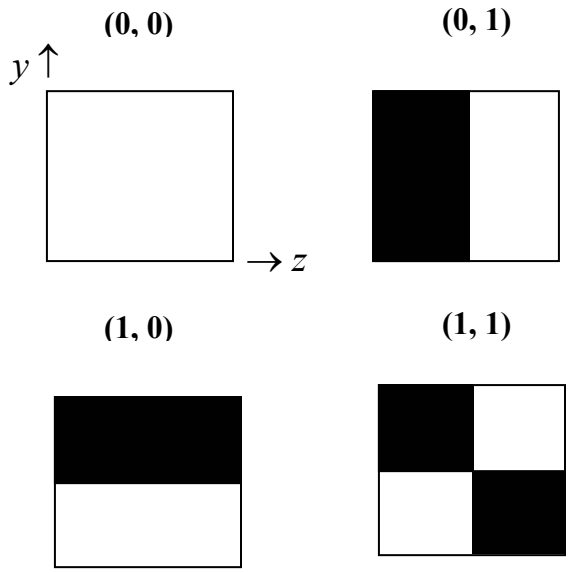

Figure 2.2: The (*n, m*) mode pattern in the cross-sectional plane of the rectangular duct. Indices *n* and *m* represent *y* and *z* pressure variation, respectively.

The acoustic field inside the duct, including the effect of the tubes, was obtained from the superposition of the sound pressure due to the disturbance and due to the finite piston sources that represent the effect of the tubes on the duct. The number of piston sources (N_s) is twice the number of tubes (N), i.e. $N_s=2N$. The two piston sources corresponding to the ℓ^{th} tube will be identified by the subscripts "*i*" (input) and "*o*"(output), as shown in figure 2.3. That is, $v_{\ell i}$ and $v_{\ell o}$ are the input and output velocities of the ℓ^{th} tube piston sources, respectively. Thus, the pressure in the duct is

$$P(x,y,z,t) = P_d(x,y,z) + \sum_{r=1}^{N_s} v_r\, p(x,y,z|x_r,y_r,z_r) \tag{2.2}$$

where $p(x,y,z|x_r,y_r,z_r)$ is the pressure at (x,y,z) due to a unit velocity of the r^{th} piston position at (x_r,y_r,z_r) and the pressure due to the disturbance $p_d(x,y,z)$ given in eq.(2.1). Note that y_r will take the value of either $y_r = 0$ or $y_r = a$ for tubes position on the bottom and top walls, respectively.

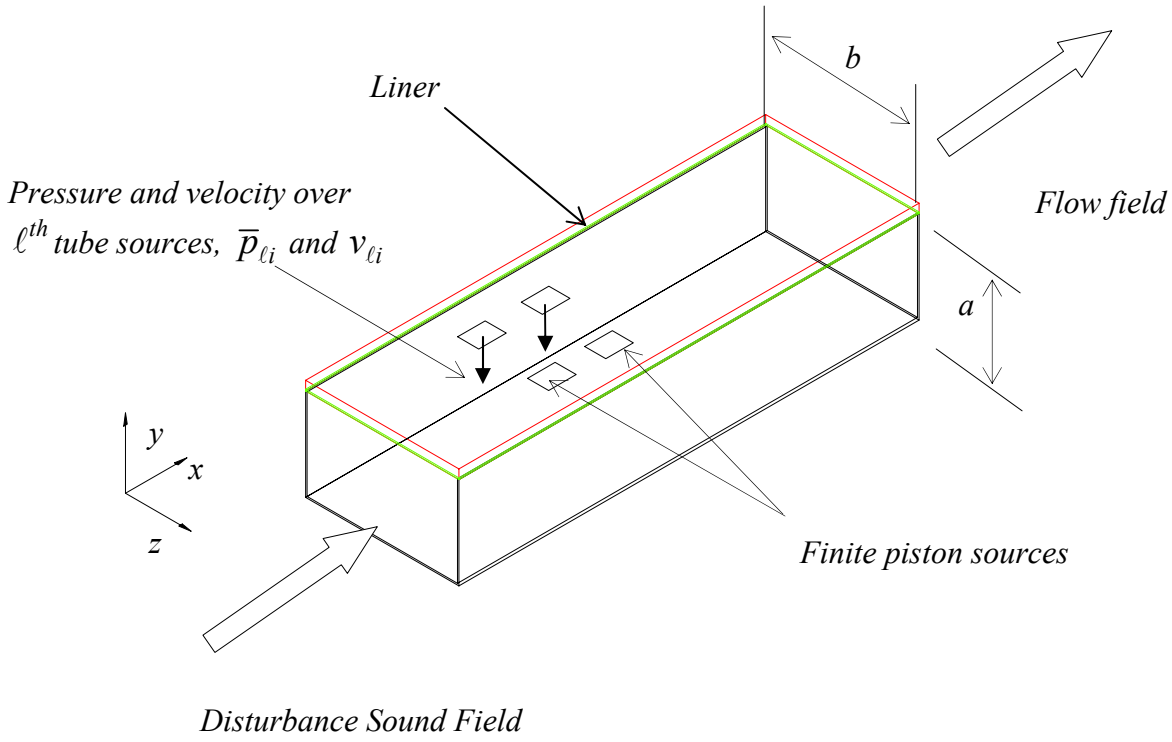

Figure 2.3: Rectangular duct with finite piston sources modeling the effect of HQ tubes on the duct.

To solve for these unknown piston velocities, the average pressure over each piston source is computed. The average pressure over the pistons can be expressed in the following matrix form as

$$\begin{Bmatrix} \overline{p}_{1i} \\ \overline{p}_{1o} \\ \vdots \\ \overline{p}_{\ell i} \\ \overline{p}_{\ell o} \\ \vdots \\ \overline{p}_{Ni} \\ \overline{p}_{No} \end{Bmatrix} = \begin{bmatrix} Z_{1i1i} & Z_{1i1o} & Z_{1i2i} & Z_{1i2o} & \cdots & & & \\ Z_{1o1i} & Z_{1o1o} & Z_{1o2i} & Z_{1o2o} & & & & \\ Z_{2i1i} & Z_{2i1o} & \ddots & & & & & \\ Z_{2o1i} & Z_{2o1o} & & & & & & \\ \vdots & & & & Z_{\ell i\ell i} & Z_{\ell i\ell o} & & \\ & & & & Z_{\ell o\ell i} & Z_{\ell o\ell o} & & \\ & & & & & \ddots & & \\ & & & & & & Z_{NiNi} & Z_{NiNo} \\ & & & & & & Z_{NoNi} & Z_{NoNo} \end{bmatrix} \begin{Bmatrix} v_{1i} \\ v_{1o} \\ \vdots \\ v_{\ell i} \\ v_{\ell o} \\ \vdots \\ v_{Ni} \\ v_{No} \end{Bmatrix} + \begin{Bmatrix} \overline{p}^{d}_{1i} \\ \overline{p}^{d}_{1o} \\ \vdots \\ \overline{p}^{d}_{\ell i} \\ \overline{p}^{d}_{\ell o} \\ \vdots \\ \overline{p}^{d}_{Ni} \\ \overline{p}^{d}_{No} \end{Bmatrix}$$

(2.3)

where $\overline{p}^{d}_{\ell i}$ and $\overline{p}^{d}_{\ell o}$ are the average pressures over the piston sources corresponding to the ℓ^{th} tube due to the disturbance. The average pressure over the piston sources of the ℓ^{th} tube due to the disturbance is described in Appendix A (see eq. A.4.4).

On the other hand, a general element Z_{rs} of the matrix in equation (2.3) represents the average pressure over the "*r*" piston source due to a unit velocity of the "*s*" piston source, i.e. impedance function. These impedance functions are derived in Appendix A and depend on the relative positions of the piston sources (see eqs.A.3.31, 33, and 35)

The next step is to model the sound field inside each tube. In practice, the HQ tubes are constructed as a semi-circle or other smooth shapes. However, for modeling purposes they are considered as straight tubes with uniform cross-sections, including the

perforated screen used in practice at the tube-duct interfaces. In addition, the sound field inside a tube is assumed to consist of plane waves only, a valid assumption below the first cut-off frequency of the tube. It is also assumed that there is no flow inside the tube. Thus, the tube dynamics can be described in terms of the acoustic variables at the tube ends, i.e. the velocity $v_{\ell i}^t$ and $v_{\ell o}^t$, and the pressure $p_{\ell i}^t$ and $p_{\ell o}^t$, as shown in figure 2.4.

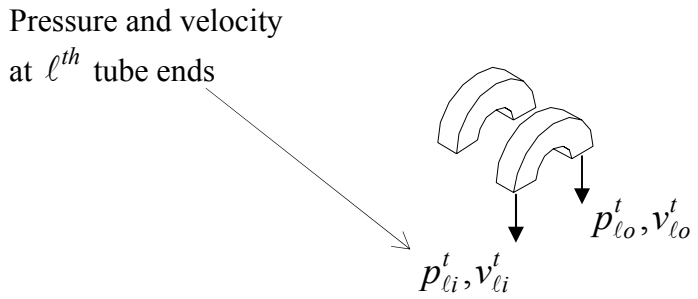

Figure 2.4: Model of the HQ tubes.

The relation between the pressure and particle velocity at the tube's ends is obtained in terms of the impedance matrix for the ℓ^{th} tube that can be expressed as

$$\begin{Bmatrix} p_{\ell i}^t \\ p_{\ell o}^t \end{Bmatrix} = \begin{bmatrix} Z_{ii}^{t\ell} & Z_{io}^{t\ell} \\ Z_{oi}^{t\ell} & Z_{oo}^{t\ell} \end{bmatrix} \begin{Bmatrix} v_{\ell i}^t \\ v_{\ell o}^t \end{Bmatrix} \tag{2.4}$$

The impedance matrix in (2.4) is derived in Appendix A, and includes the effect of the perforated screen used in practice at the tube-duct interfaces to prevent flow separation (see eq. A.5.9).

Equation (2.4) gives the impedance matrix for the ℓ^{th} tube alone. Once the tubes are put together in the duct in some particular configuration, the pressure at the end of the tubes can be written in matrix form as

$$\begin{Bmatrix} p_{1i}^t \\ p_{1o}^t \\ \hline \vdots \\ \hline p_{\ell i}^t \\ p_{\ell o}^t \\ \hline \vdots \\ \hline p_{Ni}^t \\ p_{No}^t \end{Bmatrix} = \begin{bmatrix} Z_{ii}^{t1} & Z_{io}^{t1} & 0 & 0 & \cdots & & \\ Z_{oi}^{t1} & Z_{oo}^{t1} & 0 & 0 & & & \\ 0 & 0 & \ddots & & & & \\ 0 & 0 & & & & & \\ & & & Z_{ii}^{t\ell} & Z_{io}^{t\ell} & & \\ \vdots & & & Z_{oi}^{t\ell} & Z_{oo}^{t\ell} & & \\ & & & & & \ddots & \\ & & & & & Z_{ii}^{tN} & Z_{io}^{tN} \\ & & & & & Z_{oi}^{tN} & Z_{oo}^{tN} \end{bmatrix} \begin{Bmatrix} v_{1i}^t \\ v_{1o}^t \\ \hline \vdots \\ \hline v_{\ell i}^t \\ v_{\ell o}^t \\ \hline \vdots \\ \hline v_{Ni}^t \\ v_{No}^t \end{Bmatrix} \qquad (2.5)$$

Since the tubes are not interconnected, the impedance matrix in eq. (2.5) consists of the impedance matrices of each HQ tube on its diagonal (eq. (2.4)), and zeros everywhere else.

The sound fields inside the duct and inside the HQ tubes that were developed independently are now assembled to find an expression for the particle velocity at the ends of each tube, i.e. piston velocities. The model for the coupled tubes-duct system is obtained by matching:

(i) the average pressure on the surface of the source to the pressure in the tube, i.e. $\overline{p}_{\ell i} = p_{\ell i}^t$ and $\overline{p}_{\ell o} = p_{\ell o}^t$, and

(ii) the source velocity to the particle velocity in the tube, $v_{\ell i} = v_{\ell i}^t$ and $v_{\ell o} = v_{\ell o}^t$.

Thus, replacing equation (2.5) into the left-hand side of equation (2.3) and after straight forward mathematical manipulations, the unknown source velocities can be obtained in terms of the impedance matrices and pressure due to the disturbance as

$$
\begin{Bmatrix} v_{1i} \\ v_{1o} \\ \hdashline \vdots \\ \hdashline v_{\ell i} \\ v_{\ell o} \\ \hdashline \vdots \\ \hdashline v_{Ni} \\ v_{No} \end{Bmatrix} = \left(\begin{bmatrix} Z_{ii}^{t1} & Z_{io}^{t1} & 0 & 0 & \cdots & & \\ Z_{oi}^{t1} & Z_{oo}^{t1} & 0 & 0 & & & \\ 0 & 0 & \ddots & & & & \\ 0 & 0 & & & & & \\ & & & Z_{ii}^{t\ell} & Z_{io}^{t\ell} & & \\ \vdots & & & Z_{oi}^{t\ell} & Z_{oo}^{t\ell} & & \\ & & & & \ddots & & \\ & & & & & Z_{ii}^{tN} & Z_{io}^{tN} \\ & & & & & Z_{oi}^{tN} & Z_{oo}^{tN} \end{bmatrix} - \right.
$$

$$
\left. \begin{bmatrix} Z_{1i1i} & Z_{1i1o} & Z_{1i2i} & Z_{1i2o} & \cdots & & \\ Z_{1o1i} & Z_{1o1o} & Z_{1o2i} & Z_{1o2o} & & & \\ Z_{2i1i} & Z_{2i1o} & \ddots & & & & \\ Z_{2o1i} & Z_{2o1o} & & & & & \\ & & & Z_{\ell i\ell i} & Z_{\ell i\ell o} & & \\ \vdots & & & Z_{\ell o\ell i} & Z_{\ell o\ell o} & & \\ & & & & \ddots & & \\ & & & & & Z_{NiNi} & Z_{NiNo} \\ & & & & & Z_{NoNi} & Z_{NoNo} \end{bmatrix}^{-1} \begin{Bmatrix} \overline{p}_{1i}^{d} \\ \overline{p}_{1o}^{d} \\ \hdashline \vdots \\ \hdashline \overline{p}_{\ell i}^{d} \\ \overline{p}_{\ell o}^{d} \\ \hdashline \vdots \\ \hdashline \overline{p}_{Ni}^{d} \\ \overline{p}_{No}^{d} \end{Bmatrix}
$$

(2.6)

Once the velocity of each piston source is found, the pressure at any point in the duct can easily be calculated as the superposition of the disturbance and piston sources sound fields as in equation 2.2. Expressions for the sound field and transmitted acoustic power upstream of the HQ-tube arrays are found to determine the performance of the HQ system.

2.2 Modal Amplitudes and Transmitted Sound Power

The performance of the liner-HQ system can be evaluated by computing the sound power reduction with respect to the liner only system at a position downstream of HQ tubes, x_{trans}, as shown in figure 2.1 (a). In order to compute the sound power reduction of the liner-HQ system, it is necessary to compute the pressure field downstream of the HQ tubes. To compute the sound pressure field at position x_{trans}, the modal amplitude at x_{trans} need to be calculated. Once the modal amplitudes of the liner-HQ system at x_{trans} are found, the modal amplitude without HQ tubes are easily calculated by setting to zero the piston source velocity.

The pressure field downstream of the HQ tubes, i.e. the transmitted field, is computed by adding the pressure due to each piston source and the incident disturbance as shown in eq. (2.2). The pressures due to a unit velocity of the r^{th} source can be written as

$$p\ (x,y,z\big|x_r,y_r,z_r) = \sum_{n}^{N_g}\sum_{m}^{M_g}(A_{nm}^{(+)})_r\,\Phi_{nm}^{(+)}(y,z)e^{-ik_x^{(+)}x} \qquad x > x_r \qquad (2.7)$$

where $\left(A_{nm}^{(+)}\right)_r$ is the complex modal amplitude due to the r^{th} piston velocity. The modal amplitudes are obtained in Appendix A. For the hard wall case, this amplitude is given as

$$(A_{nm}^{(+)})_r = \frac{k_o \rho c}{ab} \frac{\Phi_{nm}^{(+)}(y_r, z_r)}{\Lambda_{nm}(1-M^2)(k_x^{(+)} - k_x^{(-)})} \times 2d_r \frac{\sin(m\pi d_r / b)}{(m\pi d_r / b)} 2d_r \frac{\sin(k_x^{(+)} d_r)}{k_x^{(+)} d_r} e^{ik_x^{(+)} x_r} \tag{2.8}$$

while for the lined case is

$$\left(A_{nm}^{(+)}\right)_r = \frac{k_o \rho c}{ab} \sum_{r=0}^{N_g} \frac{T_{rn,m}^{(+)} \Phi_{rm}^{(+)}\left(y_r, z_r\right)}{\left(1-M^2\right)} \times 2d_r \frac{\sin(m\pi d_r / b)}{(m\pi d_r / b)} e^{ik_x^{(+)} x_r} \frac{\sin\left(k_{\mathrm{x}}^{(+)} d_r\right)}{k_{\mathrm{x}}^{(+)} d_r} 2d_r \tag{2.9}$$

The source velocity v_r in (2.2) is obtained from the solution of the system of the equation in (2.6). Replacing (2.1) and (2.7) into (2.2), the pressure downstream of the tubes at location x_{trans} can be written as

$$p_t(x, y, z) = \sum_{n=0}^{N_g} \sum_{m=0}^{M_g} (A_{nm})_{hq}^{(+)} \Phi_{nm}^{(+)}(y, z) e^{-ik_x^{(+)} x_{trans}} \tag{2.10}$$

where

$$(A_{nm})_{hq}^{(+)} = A_{nm}^{d} + \sum_{r=1}^{2N} (A_{nm}^{(+)})_r v_r \tag{2.11}$$

is the modal amplitude of the transmitted (*n,m*) mode.

The total acoustic power can now be computed from the modal amplitudes. To this end, the acoustic intensity in the *z*-direction is written as [21]

$$I_x = \frac{1}{2} real\left[p v_x^* + \rho c \left| v_x \right|^2 M + \frac{\left| p \right|^2}{\rho c} M + v_x p^* M^2 \right] \tag{2.12}$$

where v_x is the particle velocity in the *x*-direction, and the asterisk (*) denotes a complex conjugate. To compute the intensity, the particle velocity in the *x*-direction is obtained from Euler's equation as shown in Appendix A.

The acoustic power is then obtained by integrating the intensity over the cross sectional area of the duct as

$$W = \int_0^a \int_0^b I_x dy dx \tag{2.13}$$

For the case of hard wall, the total transmitted sound power is given as (see Appendix A in eq.A.6.12)

$$W_{hq}(x_{trans}) = \sum_{n=0}^{N_g} \sum_{m=0}^{M_g} \frac{\left| \left(A_{nm}^{(+)} \right)_{hq} \right|^2}{\rho c} ab \Lambda_{nm} \left\{ \left(1 + M^2 \right) Real\left[\frac{\left(k_x^{(+)} \right)^*}{\left(k_o - k_x^{(+)} M \right)^*} \right] + \frac{M \left| k_x^{(+)} \right|^2}{\left| k_o - k_x^{(+)} M \right|^2} + M \right\} \tag{2.14}$$

For the case of a lined duct, the computation of the acoustic power is more involved because the modes are not orthogonal (see eq. A.6.13). The acoustic power is then given as (see Appendix A).

$$W_{hq}\left(x_{trans}\right)=\frac{1}{2}real\left[\sum_{m=0}^{M_g}\sum_{n=0}^{N_g}\sum_{r=0}^{N_g}\frac{A_{nm}^{(+)}A_{rm}^{(+)^*}ab\hat{\Lambda}_{nr,m}^{(+)}}{\rho c}\frac{\left(k_x^{(+)}\right)_{rm}^*}{k_o-\left(k_x^{(+)}\right)_{rm}^* M}+\right.$$

$$\sum_{m=0}^{M_g}\sum_{n=0}^{N_g}\sum_{r=0}^{N_g}\frac{A_{nm}^{(+)^*}A_{rm}^{(+)}ab\hat{\Lambda}^{*(+)}_{nr,m}}{\rho c}M^2\frac{\left(k_x^{(+)}\right)_{rm}}{k_o-\left(k_x^{(+)}\right)_{rm}M}+$$

$$\sum_{m=0}^{M_g}\sum_{n=0}^{N_g}\sum_{r=0}^{N_g}\frac{A_{nm}^{(+)}A_{rm}^{(+)^*}ab\hat{\Lambda}_{nr,m}^{(+)}}{\rho c}M\frac{\left(k_x^{(+)}\right)_{nm}\left(k_x^{(+)}\right)_{rm}^*}{\left(k_o-\left(k_x^{(+)}\right)_{nm}M\right)\left(k_o-\left(k_x^{(+)}\right)_{rm}^*M\right)}+$$

$$\left.\sum_{m=0}^{M_g}\sum_{n=0}^{N}\sum_{r=0}^{N_g}\frac{A_{nm}^{(+)}A_{rm}^{(+)^*}ab\hat{\Lambda}_{nr,m}^{(+)}}{\rho c}M\right] \tag{2.15}$$

The acoustic power with liner only, $W_{liner}\left(x_{trans}\right)$, can be calculated by letting the piston source velocity v_r equal to zeros.

The sound power level reduction, referred here as insertion loss (*IL*), due to the HQ tube can be obtained as

$$IL(dB)=L_W^{hq}-L_W^{liner}=10\log_{10}\left(\frac{W_{hq}\left(x_{trans}\right)}{W_{liner}\left(x_{trans}\right)}\right) \tag{2.16}$$

where L_W^{hq} and L_W^{liner} are the acoustic sound power level for liner-HQ and liner configurations, respectively.

Chapter 3. Numerical and Experimental Studies

3.1 Introduction

In the previous chapter, a modeling technique was developed to predict the effect of the HQ tubes-liner system applied to the rectangular duct. In order to validate this numerical approach, the predicted results will be compared with experimental data. In section 3.2, the experimental facility, the tests performed, and measurement technique are presented. The descriptions of the experimental configurations are explained in section 3.2.3. In section 3.3, results are presented for representative experimental configurations. The results for the liners only are presented in section 3.3.1. The results for HQ tubes on a hard walled duct are presented in section 3.3.2. Finally, results for the HQ-tubes in conjunction with liners are presented in section 3.3.3. In section 3.4.1, the numerical predictions are presented while the numerical and experimental comparisons are presented in section 3.4.2.

3.2 Experimental Test Description

In this section, explanation of the experimental facility, measurement, and test configurations are presented.

3.2.1 Experimental Facility

All the experiments were performed in the rectangular flow duct facility at Goodrich Aerospace, Aerostructures group, San Diego, California. The rectangular flow duct was used to estimate the sound power level attenuations resulting from various combinations of liners and HQ waveguide systems.

The experimental facility consists of a source chamber, a receiving chamber, and a duct connecting the two chambers, as shown in figure 3.1(a). The duct changes from a circular to a rectangular cross-section from the chambers towards the center section. The test section, where test samples are implemented, is in the middle section of the duct.

A compressor supplies a continuous airflow into the duct through the source chamber. The maximum airflow velocity at the test section is of Mach 0.6.

The test section shown in figure 3.1(b) is a rectangular duct with a length of 0.61m (24 in), a height of 0.1m (3.9 in), and a width of 0.127m (5 in). One or both side plates (5 in wide) can be removed and replaced with testing samples, i.e. liners, liner-HQ panels, and so forth. The upper and bottom walls are fixed and are made of very stiff plates, i.e. hard wall condition. As an example, two HQ tubes mounted on one of the side walls are shown in figure 3.1 (c).

The source chamber shown in figure 3.1(a) has several speakers inside to generate high intensity broadband noise in the range of 250~7000 Hz. This sound field propagates through the duct and test section into the receiving chamber. Thus, the flow and sound propagation directions are the same in this facility. It is also important to mention that the two chambers are acoustically untreated, i.e. hard reflective surfaces.

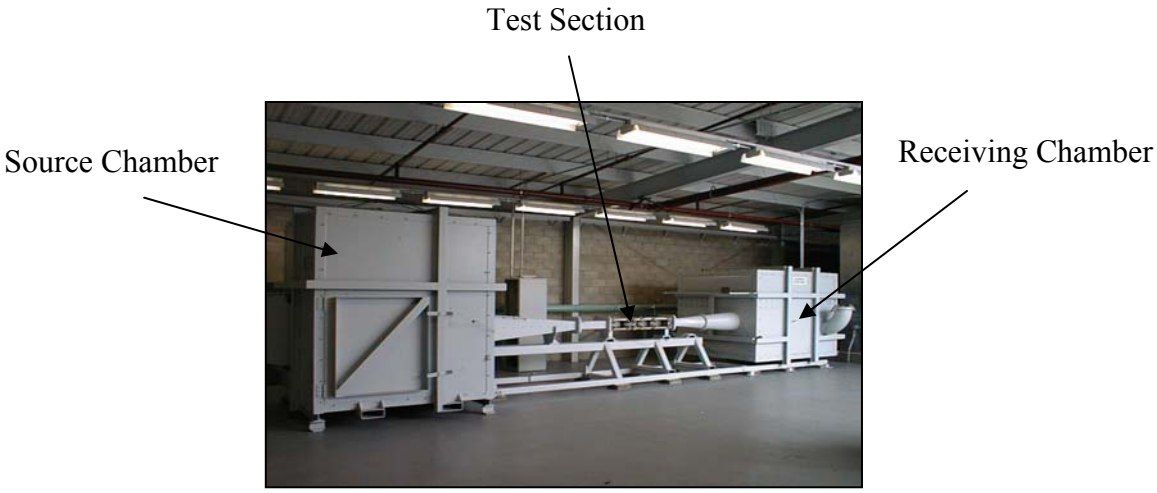

(a)

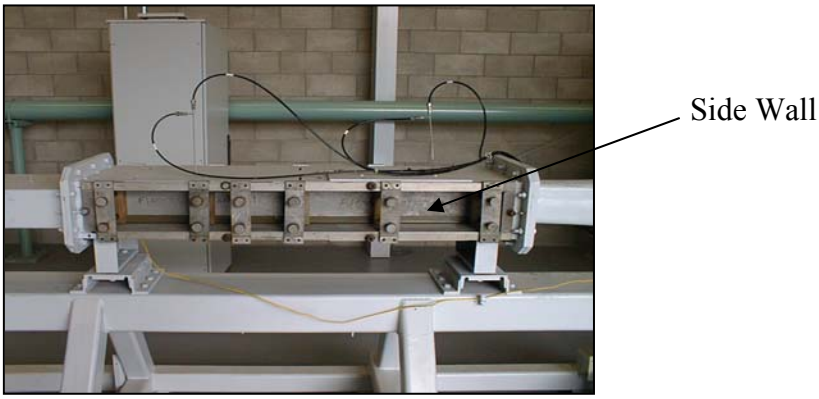

(b)

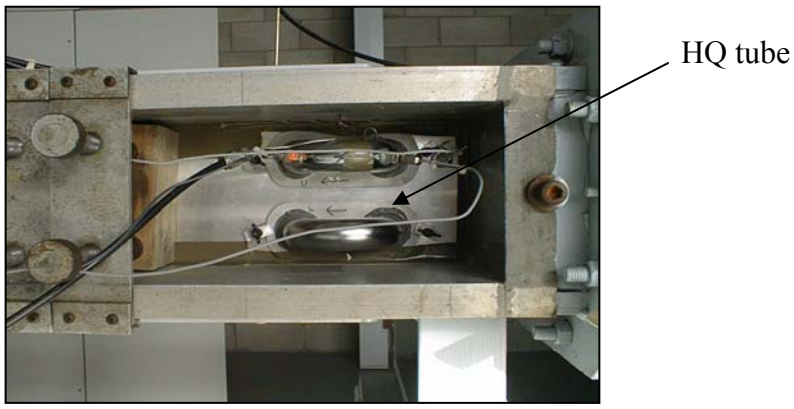

Figure 3.1: (a) Overview of the Air/noise flow duct facility
(b) Test Section of the facility
(c) HQ tubes mounted on the side wall

3.2.2 Experimental Measurement

Three microphones are placed inside the source chamber while a single microphone is located in the receiving chamber. These microphones are used to estimate the average sound pressure levels inside the chambers, which are used to calculate the sound power reduction or insertion loss of the sample tested. The flow speed inside the duct is measured using a Pitot-static Probe.

To calculate the sound power reduction of a test sample, the average sound pressure levels in the source and receiving chambers are first measured for a hard walled test section, i.e. $\overline{L}_{source-HW}$ and $\overline{L}_{receiver-HW}$, respectively. Then, the test sample is installed in the test section and the average sound pressure levels are again measured in both chambers. It is assumed that the average sound pressure in the chambers is directly related to the sound power level. Thus, the difference in the average sound pressure level between the source and receiving chambers is assumed to be directly the difference in sound power level between the chambers. The increase in the average sound pressure difference between the chambers due to a sample tested (as compare to the hard walled case) is considered to be the sound power level reduction due to the sample, i.e. IL. That is, the sound power difference between the chambers is

$$\Delta L_{W-HW} = \overline{L}_{source-HW} - \overline{L}_{receiver-HW} \tag{3.1}$$

for the hard walled test section and

$$\Delta L_{W-sample} = \overline{L}_{source-sample} - \overline{L}_{receiver-sample} \tag{3.2}$$

for the sample tested.

Then, the sound power level reduction due to the test sample is estimated as

$$IL = \Delta L_{W-sample} - \Delta L_{W-HW} \tag{3.3}$$

where *IL* is the insertion loss or sound power level reduction.

The tests were performed for the frequency range of 250-7000 Hz at increments of 50 Hz at six different flow speeds of Mach 0, 0.2, 0.3, 0.4, 0.5 and 0.6.

It is important to remark that direct measurement of the modal amplitudes in the test section was not obtained. The measurement of the modal amplitudes downstream and upstream of the test section would be useful for a better comparison of the numerical and experimental results. The attenuation of individual acoustic modes by the test sample could be determined from the modal information.

3.2.3 Experimental Configurations

The experimental configurations tested consisted of liners only, HQ tubes with hard wall, and HQ tubes with liners. The total number of configurations performed was 66. All configurations tested are described in table 3.1(a) through 3.1(f) and schematics of these test configurations are depicted in figure 3.2. The schematic of the test section in Figure 3.2 is rotated 90° with respect to the pictures in Figure 3.1, i.e. top and bottom walls in 3.1 are side walls in 3.2.

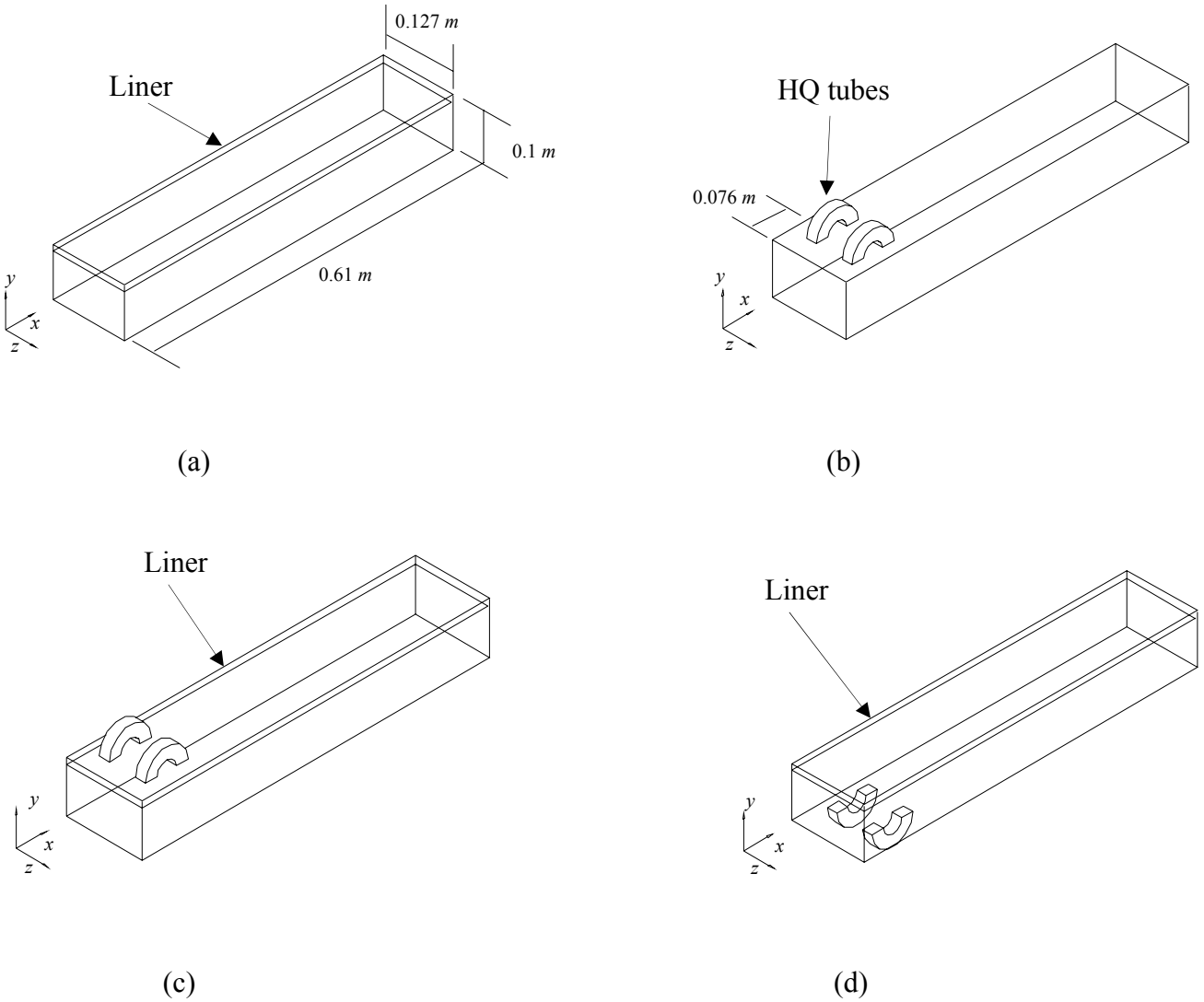

Figure 3.2: Schematic of experimental configurations
(a) Liner only
(b) HQ tubes with hard wall
(c) HQ tubes on the top of rigid plate of lined wall
(d) Hard wall-HQ tubes with a liner at opposite side

The test configurations for the liner only are presented in table 3.1(a). Two types of liners were tested, a perforate liner and a Dynarohr liner which are typically used in turbofan engines. The properties of the perforate liner are 10.5% POA face sheet, 0.001 m (0.039 in) hole diameter, 0.00071 m (0.028 in) plate thickness, and 0.0157 m (0.62 in) core height. The properties of the DynaRohr liner are 34% POA face sheet, 0.00127 m (0.050 in) hole diameter, 0.00064 m (0.025 in) plate thickness, 51.3 rayls wire mesh, and 0.017 m (0.67 in) core height. The liners have a length of 0.61m (24 in) and a width of 0.127m (5 in), respectively. An schematic of the test configuration is shown in figure 3.2 (a).

Table 3.1 (a): Liner Test Configurations

Configuration #	Liner Type	Cross Section Area (in^2)	Total Length (in)
13	Perforate	No Tube	
14	DynaRohr	No Tube	

The test configurations corresponding to HQ tubes on a hard walled duct are presented in table 3.1(b) through 3.1(d). In all tests, two HQ tubes are located at x = 0.076 m (3 in) from the leading edge of the test section as shown in figure 3.2 (b). The implementation of the HQ tubes is shown in figure 3.3.1. The HQ tubes are mounted on a rigid plate, which has a recess machined at the openings. This recess allows for the implementation of screens at the tube-duct interfaces to minimize flow separation effects. The screens are mounted at these tube-duct interfaces using double side tape, i.e. the screens can be easily replaced. Two types of face screens were tested; simple perforate and wire mesh screens. The wire mesh screen consists of a wire mesh bonded on a simple perforate screen. Three different impedances of tube opening screens were tested for perforate and wire mesh screens, respectively. Simple perforated face screen of three different POAs were tested as shown in table 3.1(b) and (c). Three wire mesh face screens were tested as described in Table 3.1(d). The POA of the base perforated plate of the wire mesh screens was 28%. The cross sectional areas of the HQ-waveguides tested were 0.00105 m^2 (1.629 in^2), 0.00101 m^2 (1.568 in^2), 0.000705 m^2 (1.094 in^2), and 0.000658 m^2 (1.021 in^2). Two tube lengths, L= 0.1524 m (6 in) and 0.1397 m (5.5 in) were tested for hard walled ducts with HQ tubes.

Table 3.1 (b): Hard Wall with HQ Tube Tests with Perforate Plate at the Tube Opening

Configuration #	Cross Section Area (in^2)	Face POA (%)	Total Length (in)
1	1.629	12.0	5.50
2	1.094	12.0	5.50
3	1.629	12.0	6.00
4	1.094	12.0	6.00
5	1.629	15.0	5.50
6	1.094	15.0	5.50
7	1.629	15.0	6.00
8	1.094	15.0	6.00
9	1.629	28.0	5.50
10	1.094	28.0	5.50
11	1.629	28.0	6.00
12	1.094	28.0	6.00

Table 3.1 (c): Hard Wall with HQ Tube Tests with Perforate Plate at the Tube Opening

Configuration #	Cross Section Area (in^2)	Face POA (%)	Total Length (in)
55	1.568	12.0	5.50
56	1.021	12.0	5.50
57	1.568	12.0	6.00
58	1.021	12.0	6.00
59	1.568	15.0	5.50
60	1.021	15.0	5.50
61	1.568	15.0	6.00
62	1.021	15.0	6.00
63	1.568	28.0	5.50
64	1.021	28.0	5.50
65	1.568	28.0	6.00
66	1.021	28.0	6.00

Table 3.1 (d): Hard Wall with HQ Tube Tests with Stainless Wire Meshes at the Tube Opening

Configuration #	Cross Section Area (in^2)	Wire Meshes	Total Length (in)
43	1.629	45.88 rayls	5.50
44	1.094	45.88 rayls	5.50
45	1.629	45.88 rayls	6.00
46	1.094	45.88 rayls	6.00
47	1.629	33.07 rayls	5.50
48	1.094	33.07 rayls	5.50
49	1.629	33.07 rayls	6.00
50	1.094	33.07 rayls	6.00
51	1.629	15.97 rayls	5.50
52	1.094	15.97 rayls	5.50
53	1.629	15.97 rayls	6.00
54	1.094	15.97 rayls	6.00

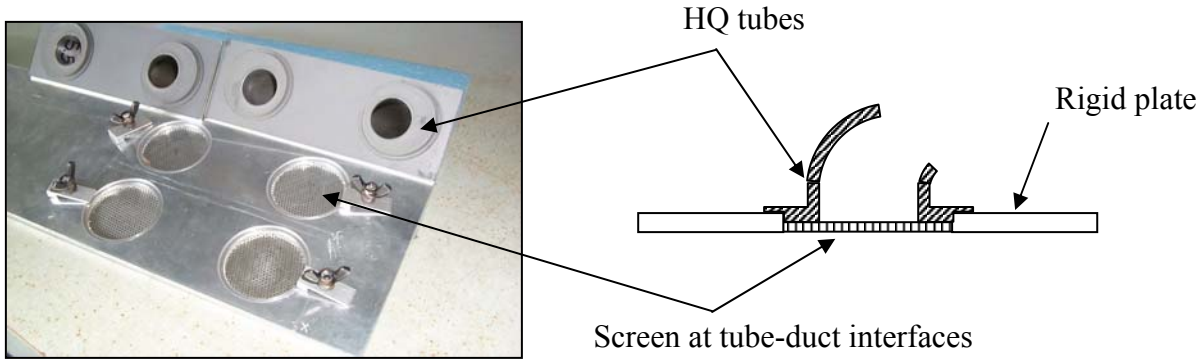

Figure 3.3.1: Implementation of HQ tubes on a hard walled duct

Table 3.1 (e) presents the configurations of the HQ tubes integrated with the liner, as shown in figure 3.2 (c). The HQ-tubes are mounted on the back of the liner and thus the honeycomb structure of the liner is then part of the HQ-tube. The advantage of this implementation is that the manufacturing practice of current liners does not need to be altered, i.e. there are minimum changes of the liner. Though the liner core should not affect acoustically the HQ-tube system, the part of the honeycomb core structure forming the tube was removed, which is indicated as "no core" in configurations 23 through 30 of Table 3.1. Figure 3.3.2 (a) and (b) show implementations of liner-HQ system with and without core.

Table 3.1 (e): Liner with HQ-tube Test Configurations

Configuration #	Liner Type	Cross Section Area (in^2)	Total Length (in)
15	Perforate	1.629	5.5 (with core)
16	Perforate	1.094	5.5 (with core)
17	Perforate	1.629	6.0 (with core)
18	Perforate	1.094	6.0 (with core)
19	DynaRohr	1.629	5.5 (with core)
20	DynaRohr	1.094	5.5 (with core)
21	DynaRohr	1.629	6.0 (with core)
22	DynaRohr	1.094	6.0 (with core)
23	Perforate	1.629	5.5 (no core)
24	Perforate	1.094	5.5 (no core)
25	Perforate	1.629	6.0 (no core)
26	Perforate	1.094	6.0 (no core)
27	DynaRohr	1.629	5.5 (no core)
28	DynaRohr	1.094	5.5 (no core)
29	DynaRohr	1.629	6.0 (no core)
30	DynaRohr	1.094	6.0 (no core)

(a)

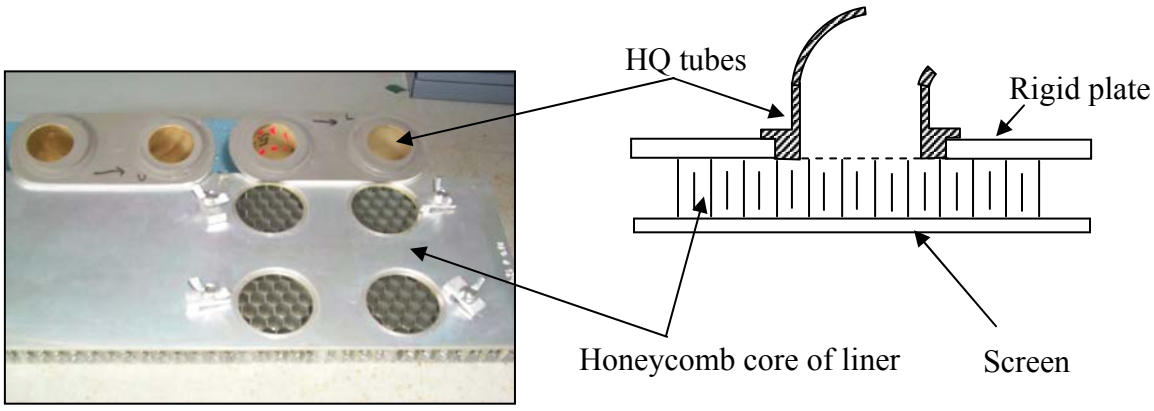

(b)

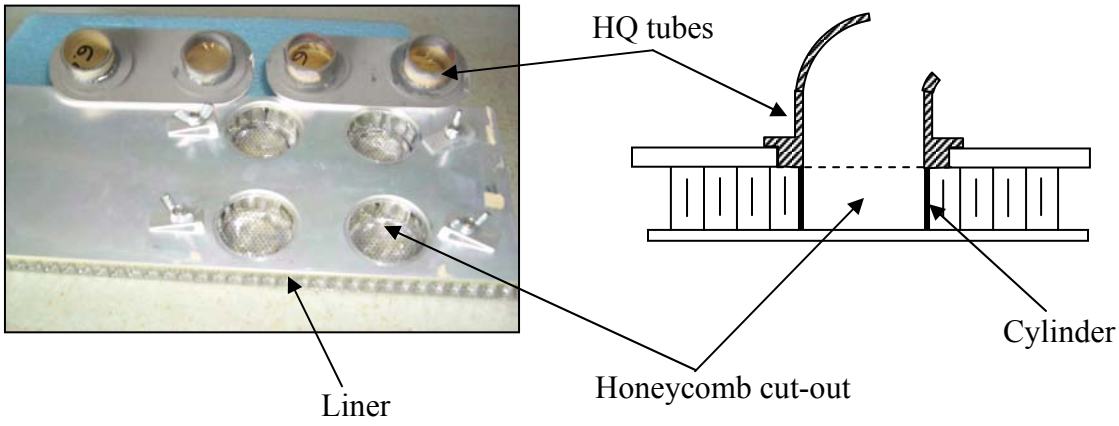

Figure 3.3.2: Implementations of liner HQ configurations
(a) With core cutout mounting method
(b) No core cutout mounting method

Table 3.1 (f) shows the configurations for the DynaRohr liner at the opposite side of the HQ tubes, as shown in figure 3.2 (d). These configurations were tested with three different POAs of tube opening face screens. The performance of these configurations will be compared with the configurations in table 3.1 (e).

Table 3.1 (f): Hard Wall with HQ-tube Tests with a DynaRohr Panel at the Opposite Side

Configuration #	Cross Section Area (in^2)	Face POA (%)	Total Length (in)
31	1.629	12.0	5.50
32	1.094	12.0	5.50
33	1.629	12.0	6.00
34	1.094	12.0	6.00
35	1.629	15.0	5.50
36	1.094	15.0	5.50
37	1.629	15.0	6.00
38	1.094	15.0	6.00
39	1.629	28.0	5.50
40	1.094	28.0	5.50
41	1.629	28.0	6.00
42	1.094	28.0	6.00

It is important to remark that the cross sectional areas of the two HQ-tubes used in conjunction with the liners represents a very small area as compared to the total liner area. The largest HQ-tube cross-sectional area used is 6.516 in^2 ($2\times2\times1.629$ in^2) that represent only 5.4 % of the liner area 120 in^2 (24×5 in^2).

Finally, it is also important to note that the standard deviations of the measurements are not available, which it does not allow for an error analysis of the experimental data. The standard deviation is a very important factor to determine the reliability of the experimental results. Future experimental efforts should consider to include an error analysis of the results.

3.3 Experimental Results

Experimental results for the liners only are presented first in section 3.3.1. The results for the HQ tubes on hard walled duct are described in section 3.3.2. Finally, results for the HQ tubes in combination with a liner follow in section 3.3.3. The experimental results are presented in both narrow (50 Hz resolution) and 1/3 octave frequency bands. In order to have a single metric to describe the attenuation of the different configurations, the overall insertion loss over the 250~7000 Hz band was computed. Appendix B describes the approach and assumptions in the calculation of the overall insertion loss.

In this chapter, only representative test configurations are presented. For the sake of completeness, the measured insertion loss of all configuration tested are presented in Appendix C.

The impedance properties of the liners and face screens used in the experiments were predicted by Goodrich.

3.3.1 Liner configuration results

Since the goal of this research is to determine the performance of HQ tubes with liners as compared to liners only, in this section the performance of the liners alone is presented to define the baseline reference results.

The normalized impedances of the perforate and DynaRohr liners are shown in figure 3.4 and 3.5. The main difference between these liners is that the resistance of the DynaRohr liner is basically independent of the grazing flow speed, whereas the resistance of the perforate liner is a function of flow speed. Another difference between these two liners is that the resistance of the DynaRohr liner at high flow speeds ($M \geq 0.4$) is lower than that of the perforate liner. The reactive components of both liners are very similar.

(a)

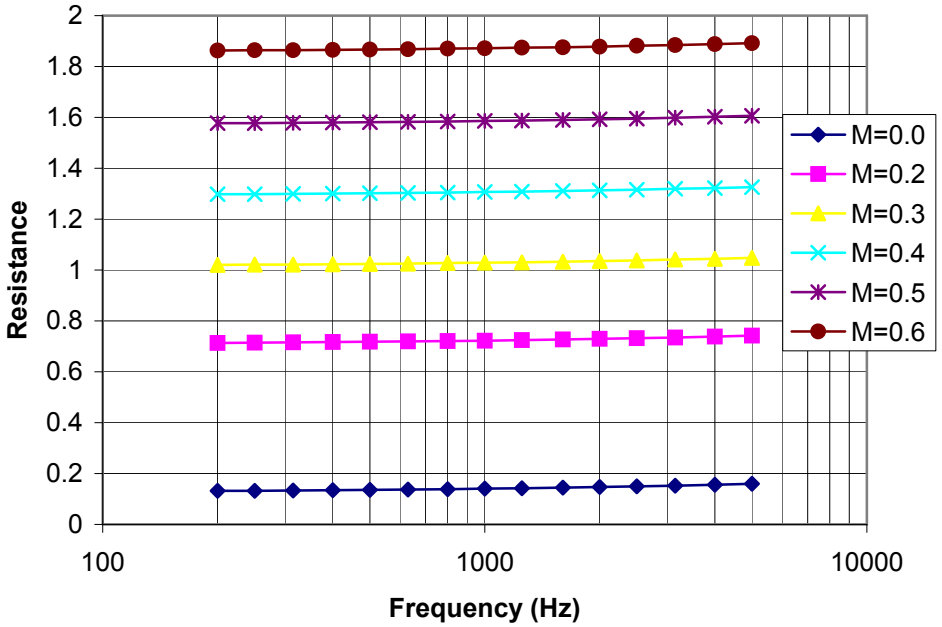

(b)

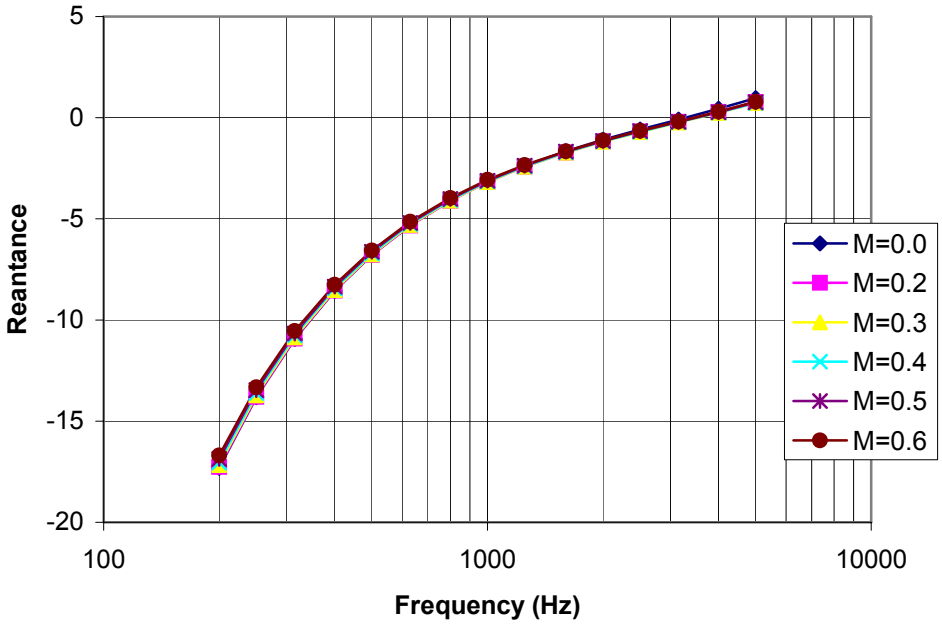

Figure 3.4: Predicted Normalized Impedance of the Perforate Liner

(a) Resistance (b) Reactance

(a)

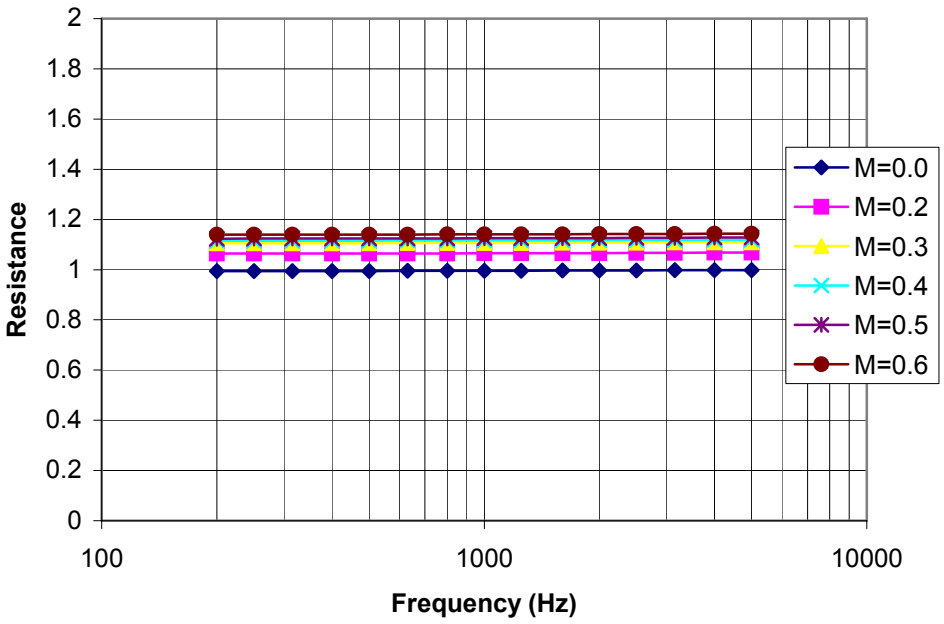

(b)

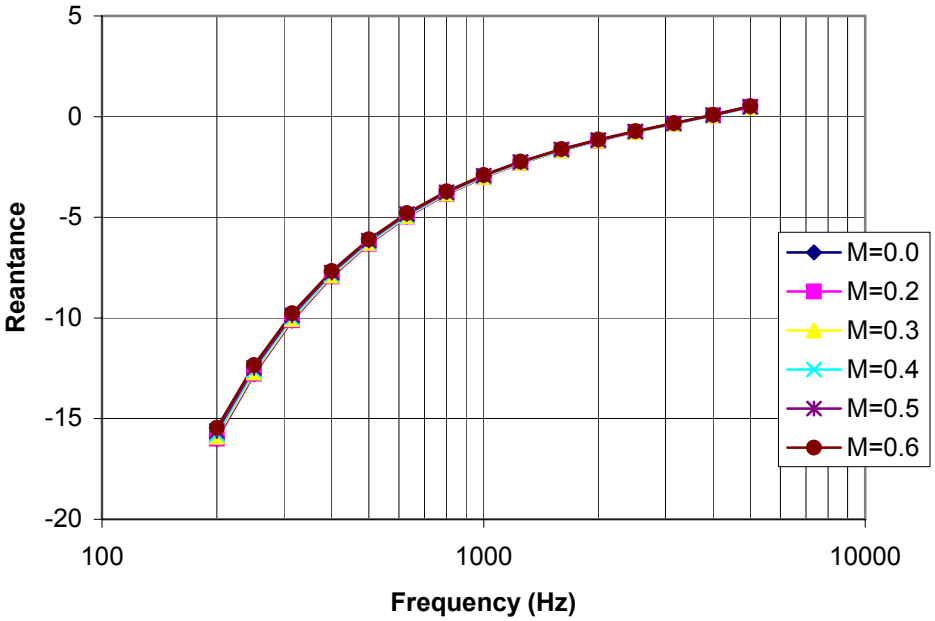

Figure 3.5: Predicted Normalized Impedance of the DynaRohr Liner
(a) Resistance (b) Reactance

The insertion losses for the perforate and DynaRohr liners are plotted in figures 3.6 and 3.7, respectively, in both narrow and 1/3 octave frequency bands. From the test results, maximum attenuations of 14 dB for perforate liner and 20 dB for DynaRohr liner are found around 2000 Hz at M=0.0. The attenuations gradually reduce as the flow speed increases. The maximum

attenuation at the 2000 Hz band is basically the same for both liners at M=0.3, 0.4, 0.5 and 0.6. It is interesting to note that the results show a negative IL at low frequencies, i.e. $\leq$ 400 Hz. It is not clear the reason for this unexpected result.

(a)

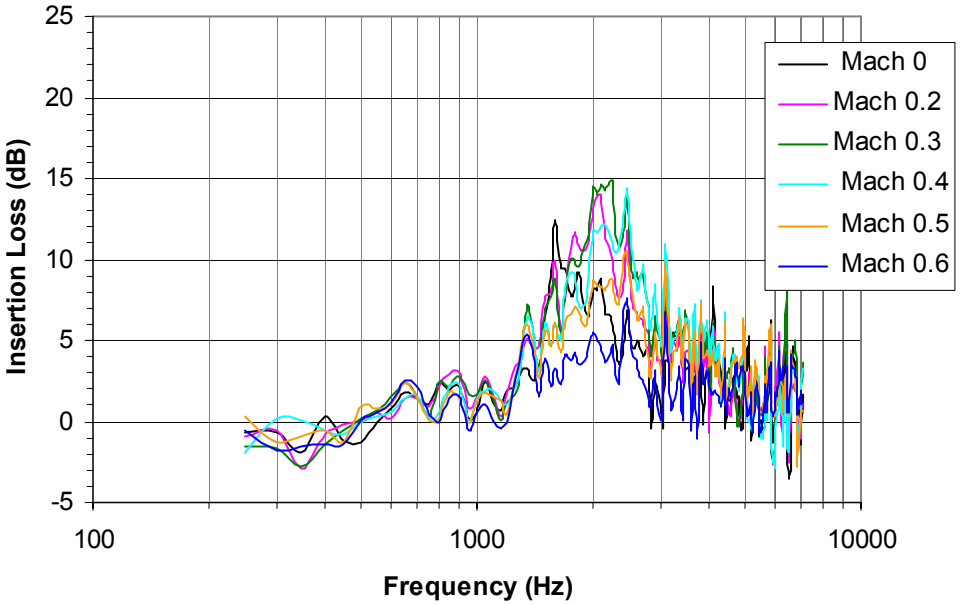

(b)

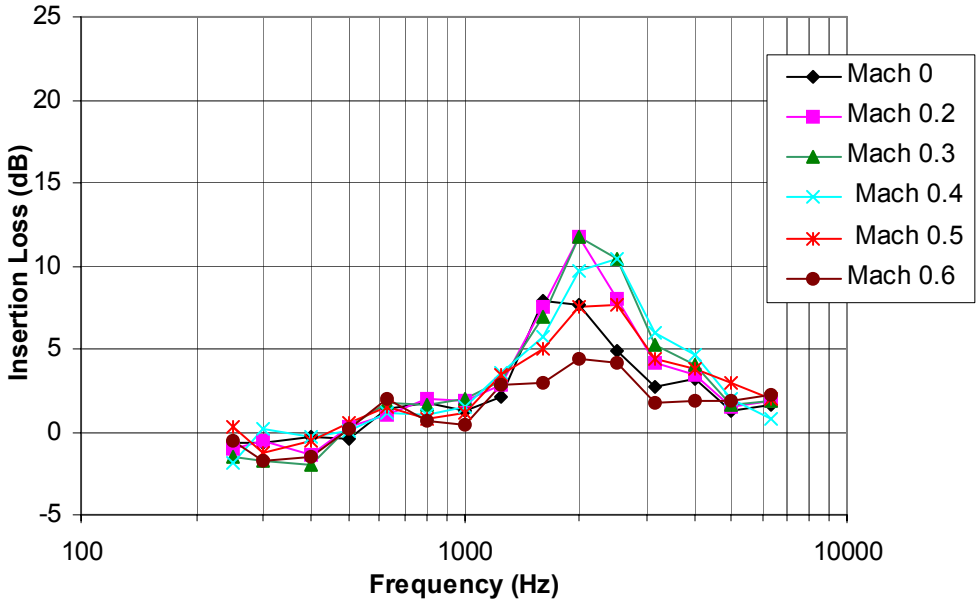

Figure 3.6: Measured insertion loss for perforate liner-configuration 13
(a) narrow (b) 1/3 octave frequency bands.

(a)

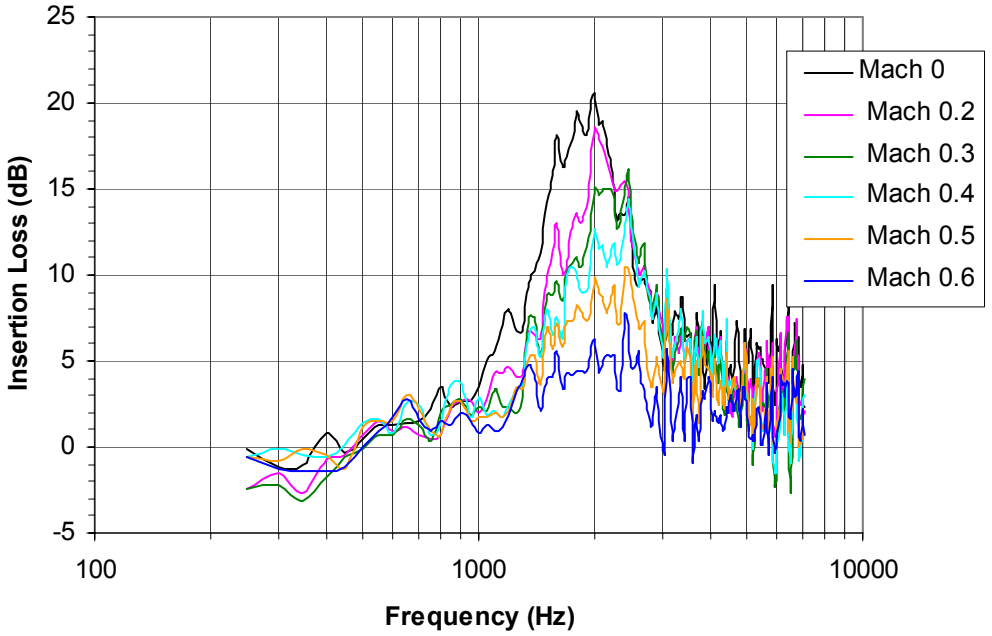

(b)

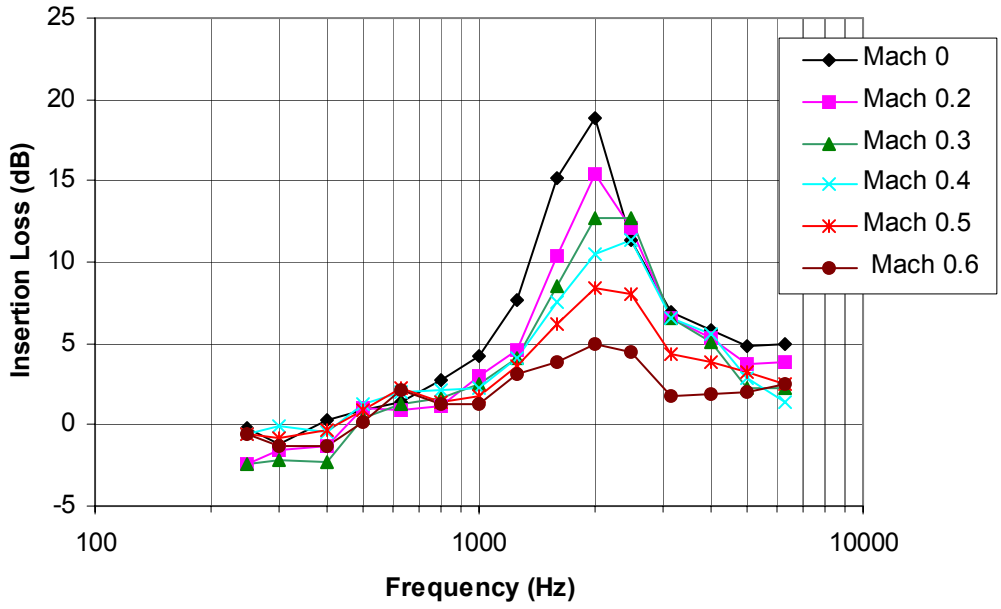

Figure 3.7: Measured insertion loss for DynaRohr liner-configuration 14 (a) narrow (b) 1/3 octave frequency bands.

In figure 3.8, a comparison of overall insertion losses for the perforate and DynaRohr liners is given as a function of flow speed. As shown in figure 3.8, the DynaRohr liner shows slightly better overall sound attenuation than that of the perforate liner at most flow speeds. Specifically, the DynaRohr liner shows a much higher overall attenuation than the perforate liner for M=0.0. However, this case is of no practical relevance.

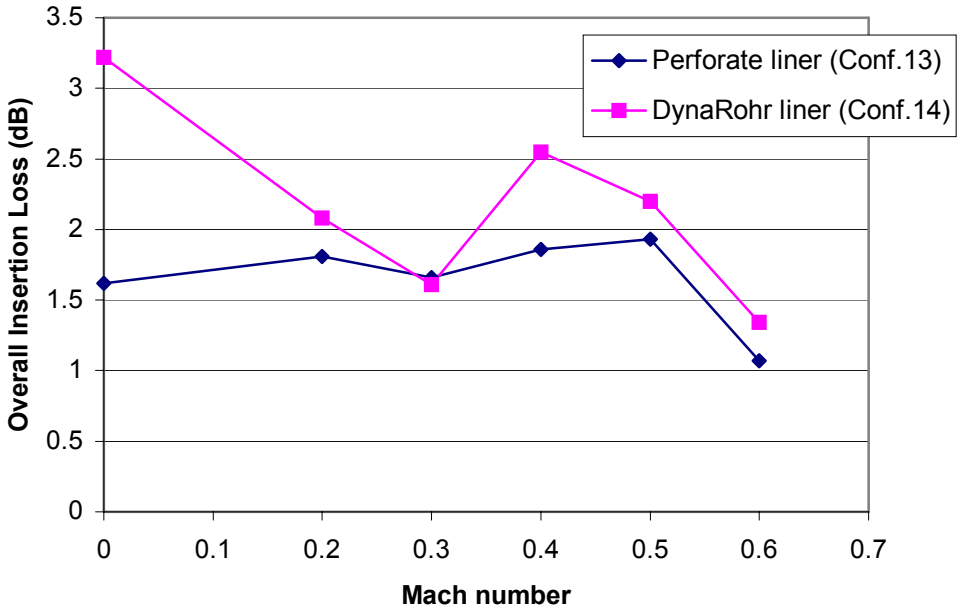

Figure 3.8: Overall insertion loss comparison between the perforate and DynaRohr liners as a function of Mach number (Configurations 13 and 14)

3.3.2 Hard Wall-HQ System Test

In this section, results for the HQ-tube on a hard-walled duct are presented. In particular, results for test configurations 1, 9, 43 and 53 from tables 3.1 (b) and (d) are presented. These configurations are selected to investigate the effect of the face screen placed at the HQ tube-duct interfaces (see figure 3.3.1). Configurations 1 and 9 allow investigating the effect of different POAs (12% and 28%) while configurations 43 and 53 allow investigating the effect of wire mesh resistances (45.88 and 15.97 rayls). All of the selected configurations presented in this section have a tube length of 0.1397 m (5.5 in) and a cross section area of 0.00105 m^2 (1.629 in^2).

The normalized impedances for the perforate (28% and 12% POA) and wire mesh screens (45.88 and 15.97 rayls) are shown in figure 3.9 through 3.12, respectively. Once again the resistance of the perforate screens is very sensitive to flow speed. On the other hand, the resistances of the wire mesh screens are almost independent of flow speed. As expected, the resistance of the 28 % POA is both less sensitive to flow speed and lower than for the 12 % POA screen. The masslike reactances (i.e. positive) for both of the perforate and wire mesh screens are about the same except for the 12 % POA perforate that is slightly higher at higher frequencies.

(a)

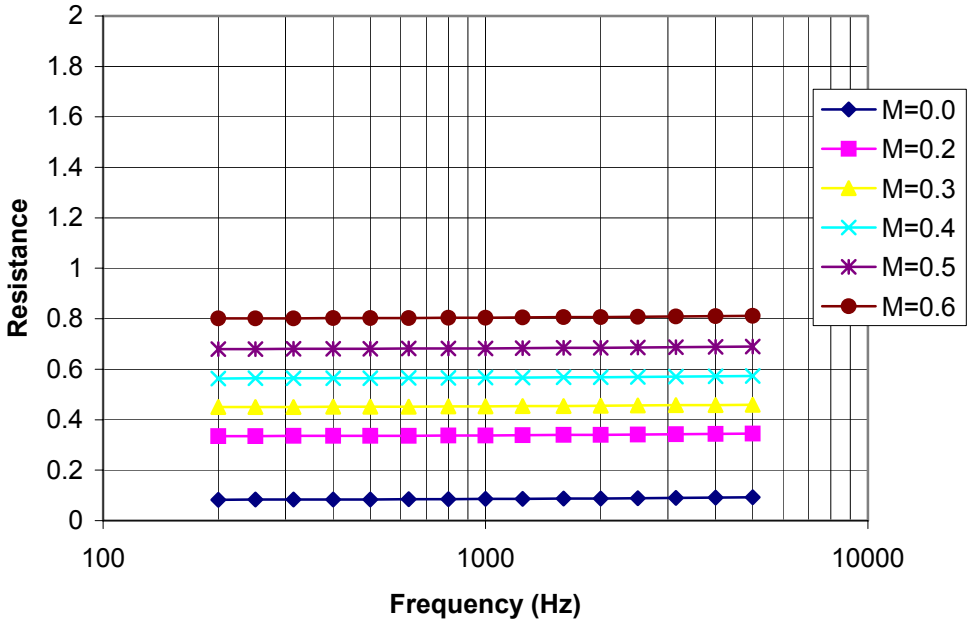

(b)

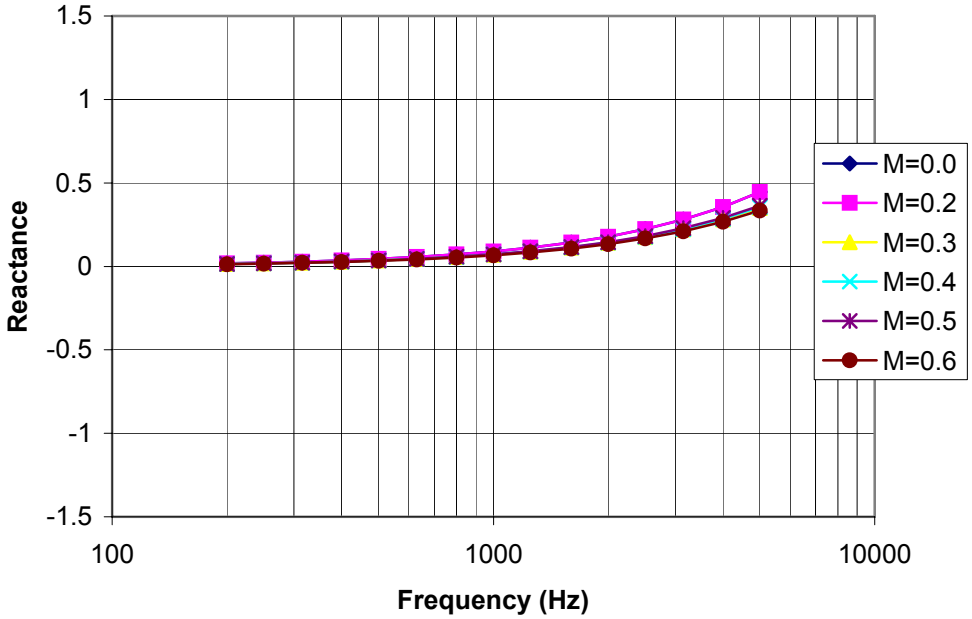

Figure 3.9: Predicted normalized impedance of the perforate screen used at tube duct interface (28 % POA) (a) Resistance (b) Reactance

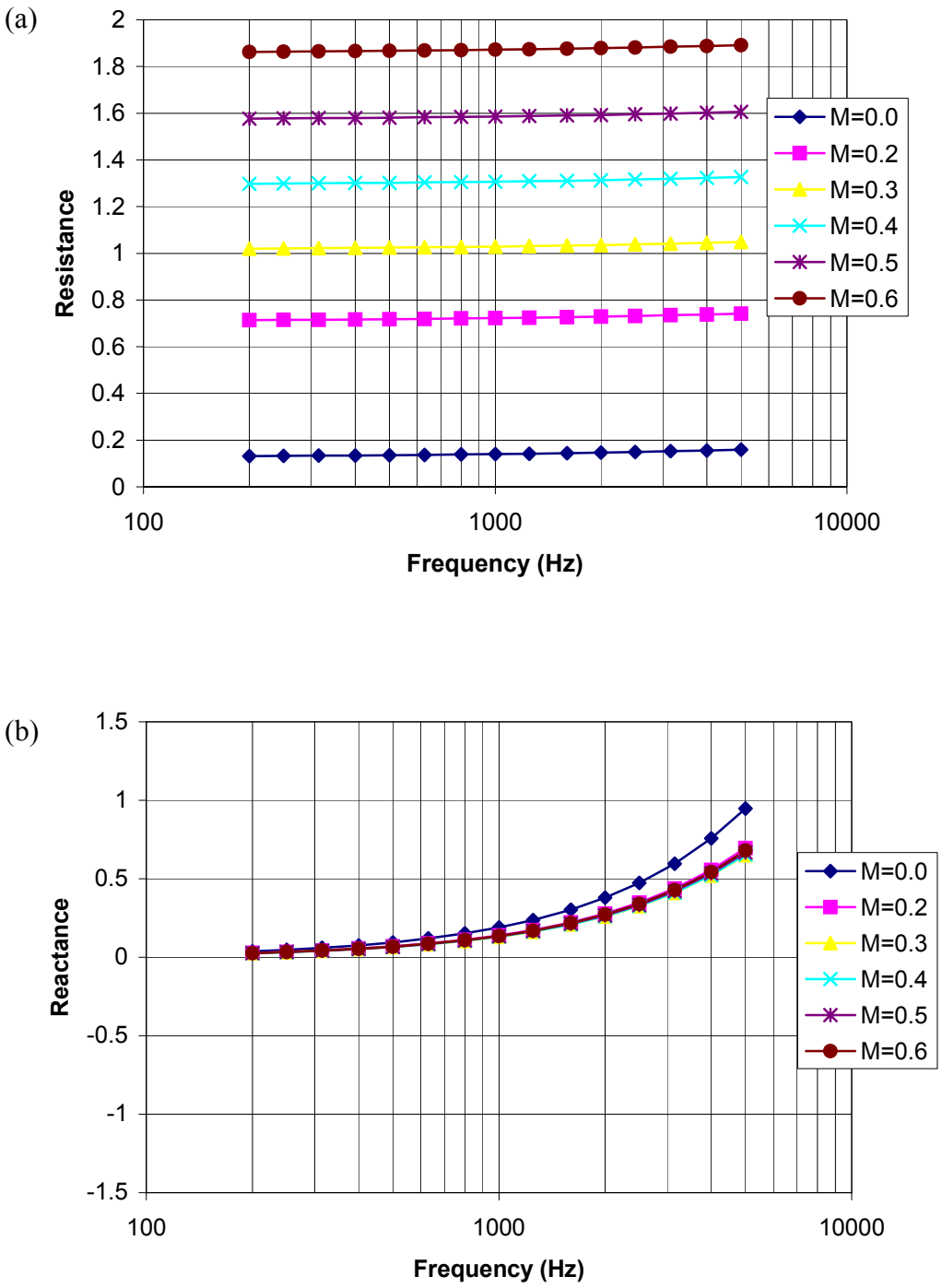

Figure 3.10: Predicted normalized impedance of the perforate screen used at tube duct interface (12 % POA) (a) Resistance (b) Reactance

(a)

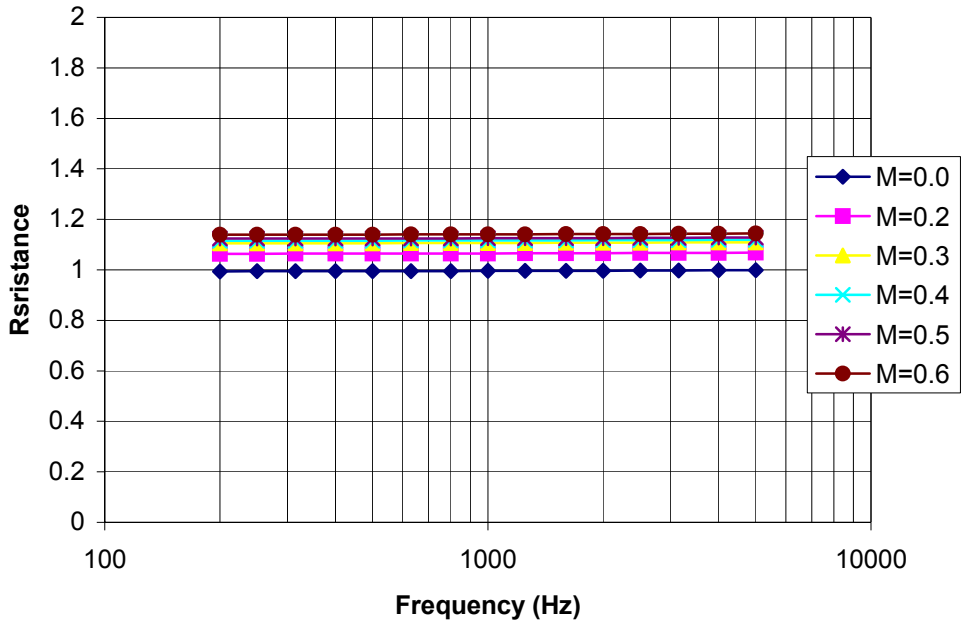

(b)

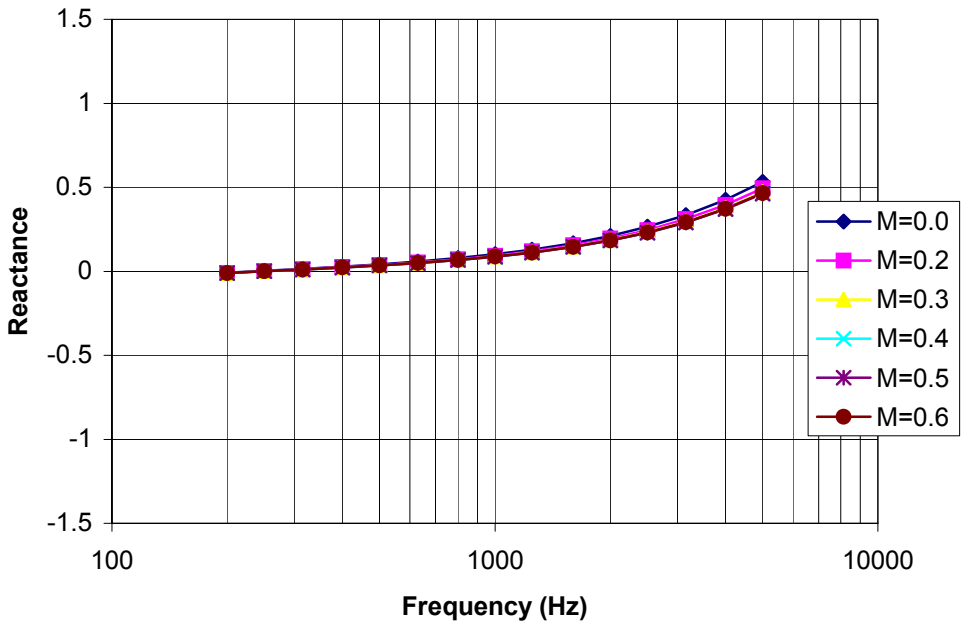

Figure 3.11: Predicted normalized impedance of wire mesh used at tube duct interface (45.88 rayls) (a) Resistance (b) Reactance

(a)

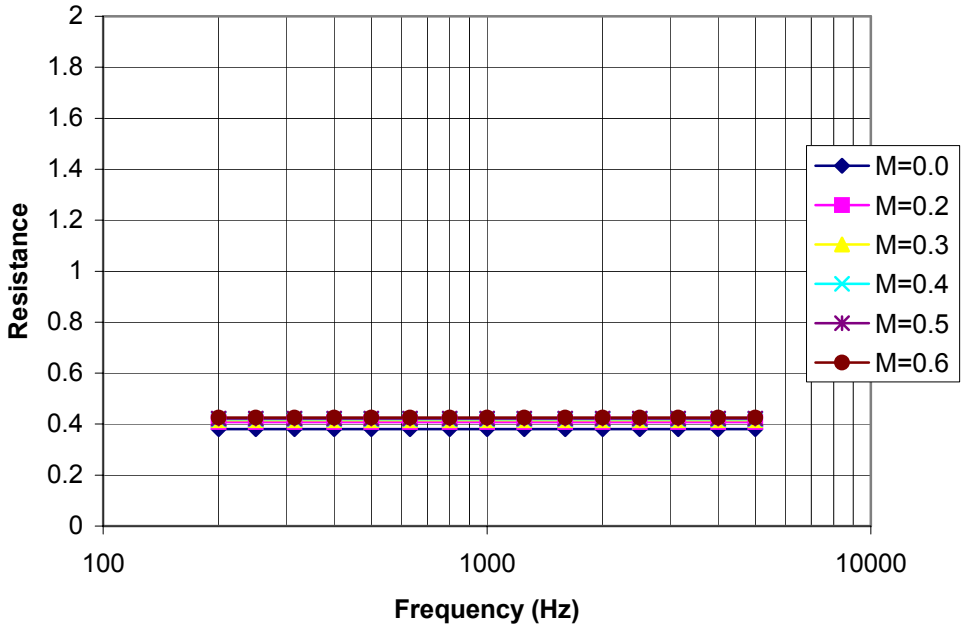

(b)

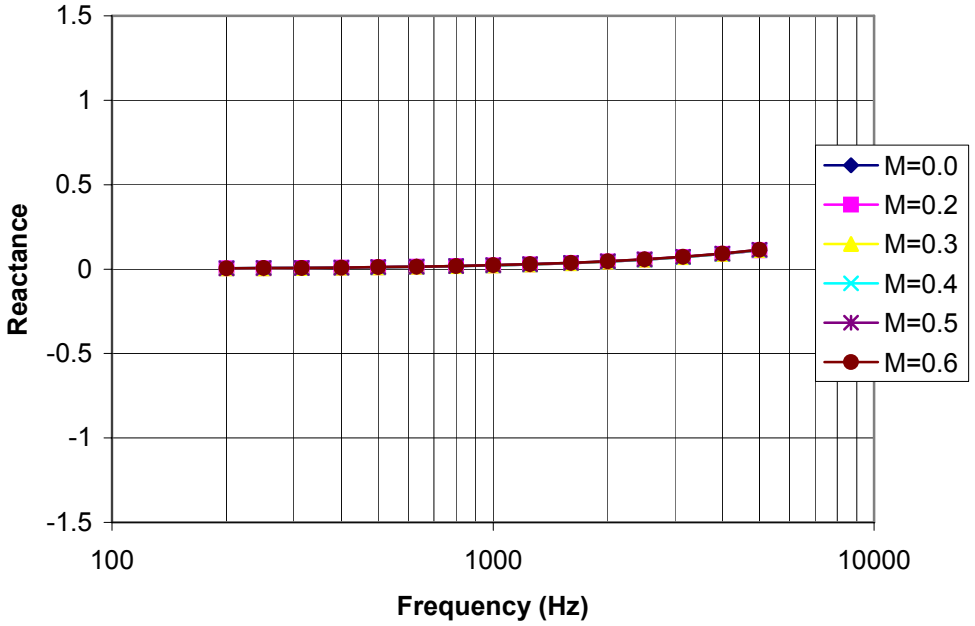

Figure 3.12: Predicted normalized impedance of wire mesh used at tube duct interface (15.97 rayls) (a) Resistance (b) Reactance

The results for configurations 9 and 1 (28% and 12% POA, respectively) are presented in figures 3.13 and 3.14, respectively. The results for configurations 43 and 51 (45.88 and 15.97 rayls, respectively) are presented in figures 3.15 and 3.16, respectively.

From the results, good narrow band attenuations are found around 1000 and 2000 Hz at low speeds for both the 28% and 12% POA screens as shown in figures 3.13 and 3.14. These narrow band attenuations correspond to the 1st and 2nd tube resonances. The frequencies of these narrow band attenuations are slightly lower for the 12% POA screen as compare to that of the 28% POA screen. This is because of the higher reactance of the 12% POA screen. The attenuations at the tube resonances are not evident for the wire mesh screens as shown in figures 3.15 and 3.16. The narrow band sound attenuation results show significant variability at high frequencies for both the perforate and the wire mesh screens.

All four configurations show negative insertion loss at frequencies below 800 Hz and above 2000 Hz. The increase in noise is particularly severe for the high resistance wire mesh (configuration 43). No follow-up experiments were performed to investigate the increase in noise (i.e. negative IL) due to the HQ-tubes. A potential source of the noise generated by the tubes is on the mounting of the HQ-tube screens (see figure 3.3.1). If these screens are not perfectly flush with the duct wall, any irregularity (i.e. step) will probably trigger flow separation and behave as a noise source, in particular at high flow speeds. In general, the HQ tubes with perforate screens result in better attenuation than HQ tubes with wire mesh screens.

(a)

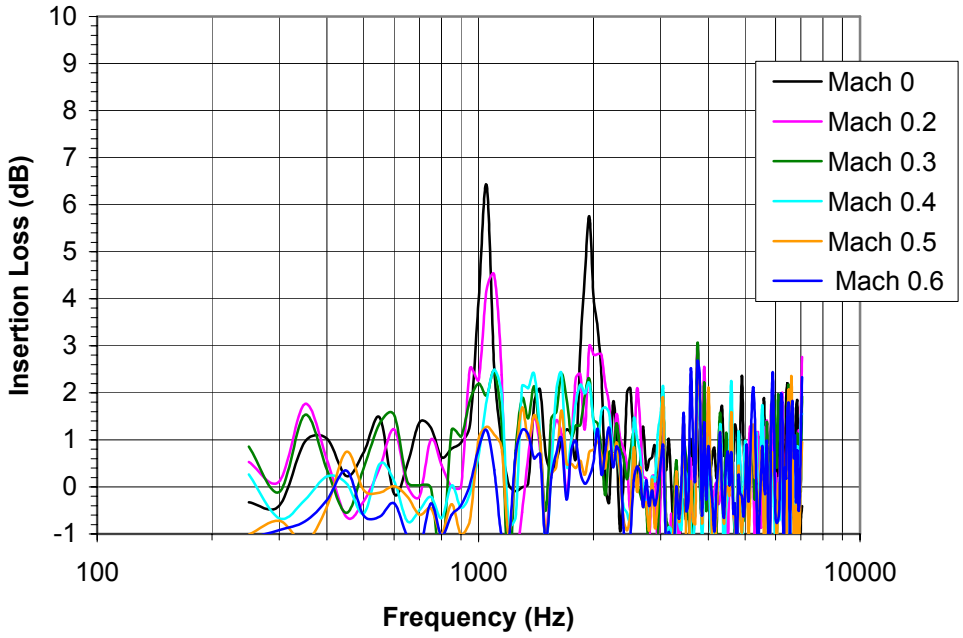

(b)

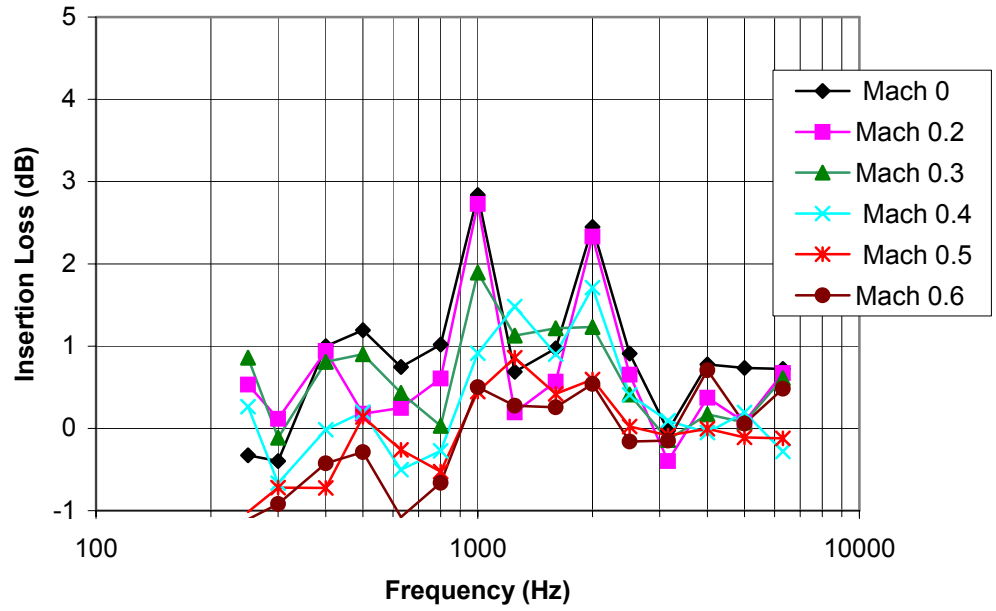

Figure 3.13: Measured insertion loss for hard wall with HQ-configuration 9: (a) narrow (b) 1/3 octave frequency bands. (Screen properties: 28% POA, HQ-tube properties: cross sectional area of 1.629 in^2, tube length of 5.5 in)

(a)

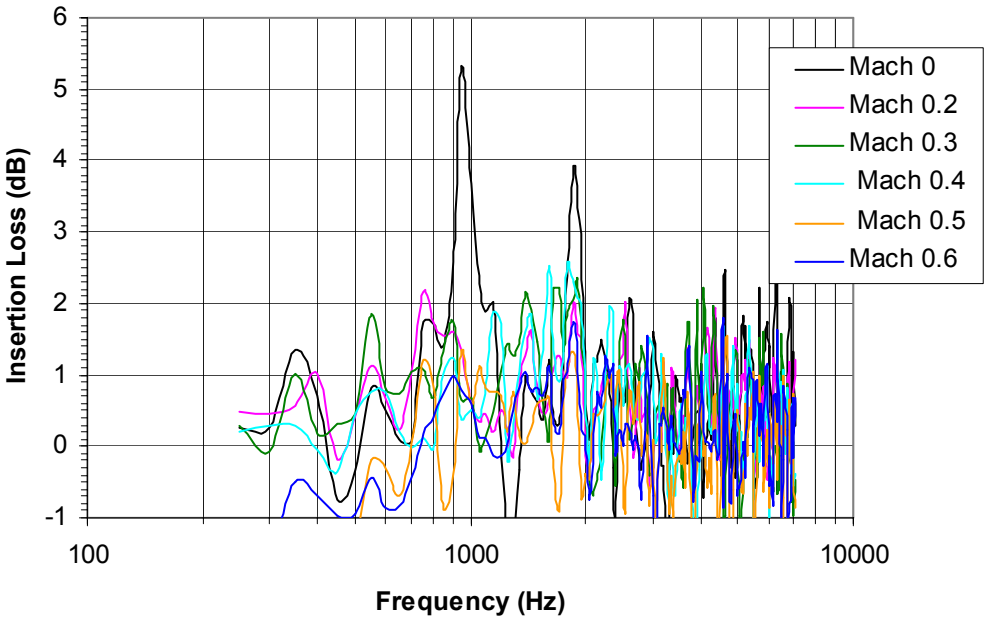

(b)

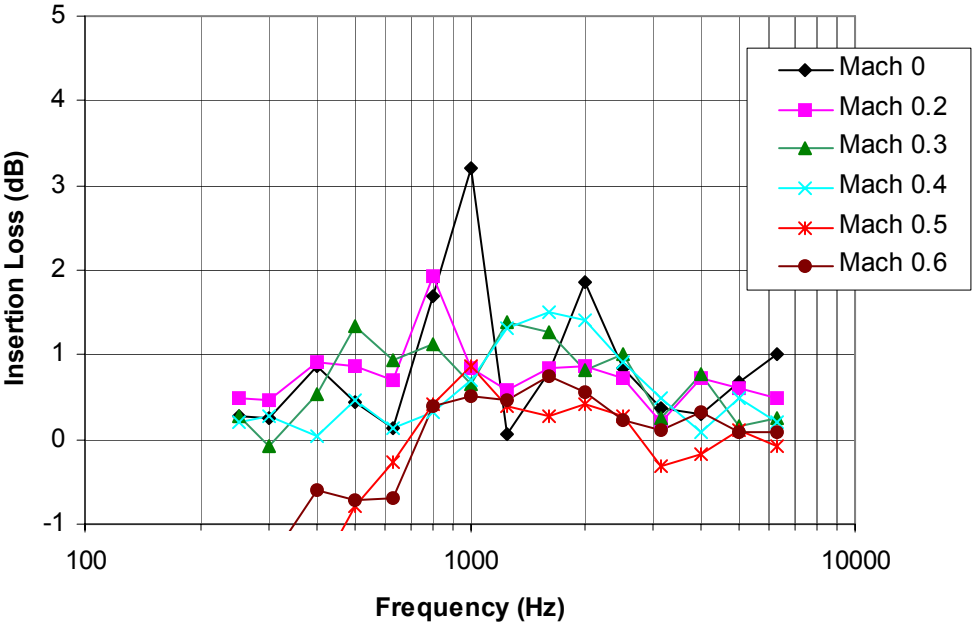

Figure 3.14: Measured insertion loss for hard wall with HQ-configuration 1: (a) narrow (b) 1/3 octave frequency bands. (Screen properties: 12% POA, HQ-tube properties: cross sectional area of 1.629 in^2, tube length of 5.5 in)

(a)

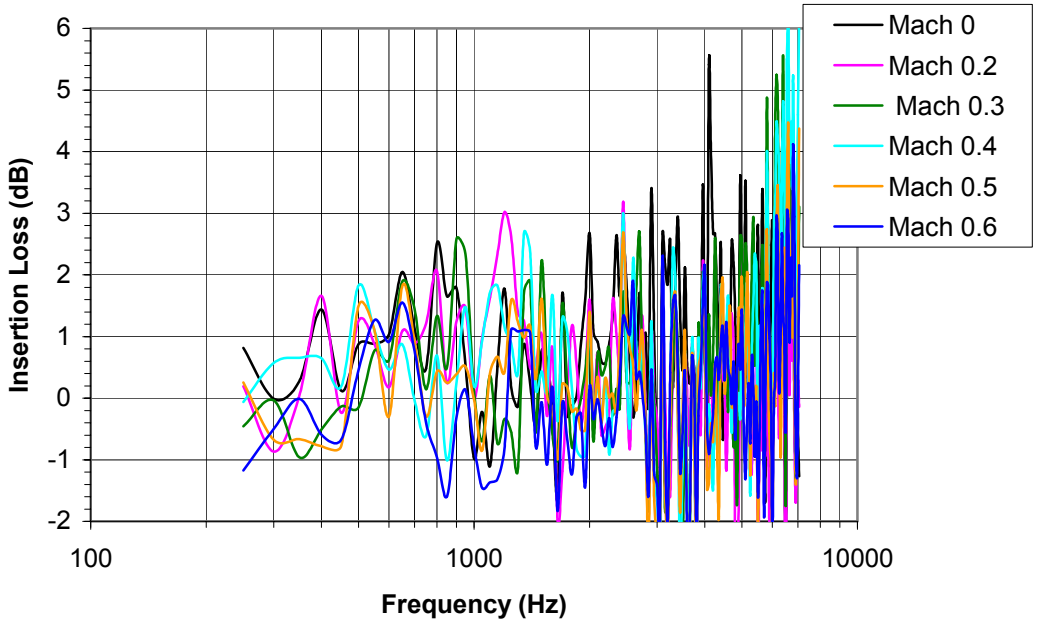

(b)

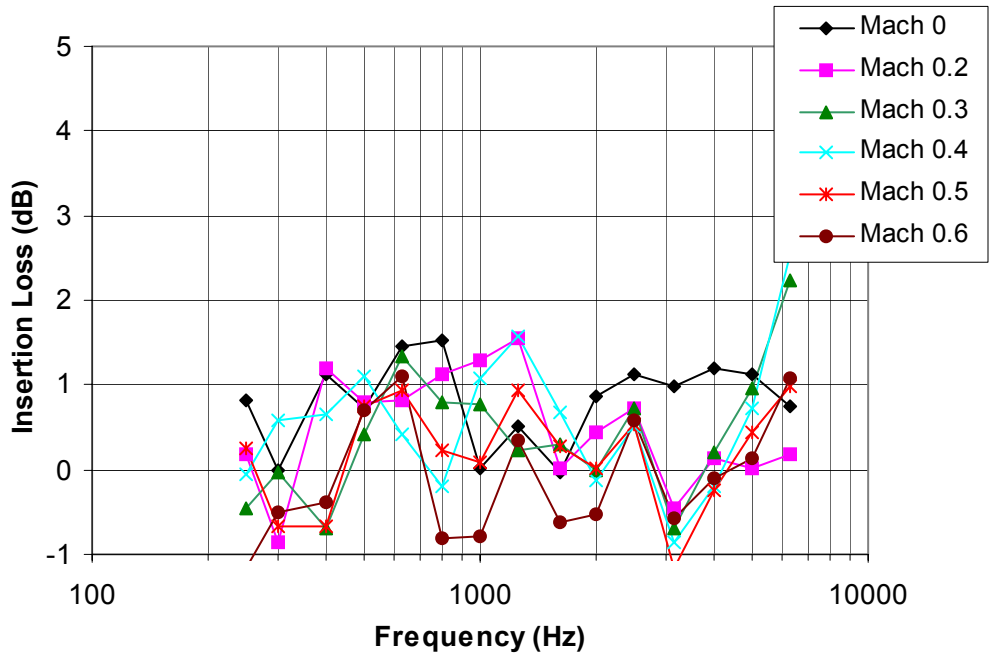

Figure 3.15: Measured insertion loss for hard wall with HQ-configuration 43: (a) narrow (b) 1/3 octave frequency bands. (Screen properties: wire mesh 45.88 rayls on 28 % POA, HQ-tube properties: cross sectional area of 1.629 in^2, tube length of 5.5 in).

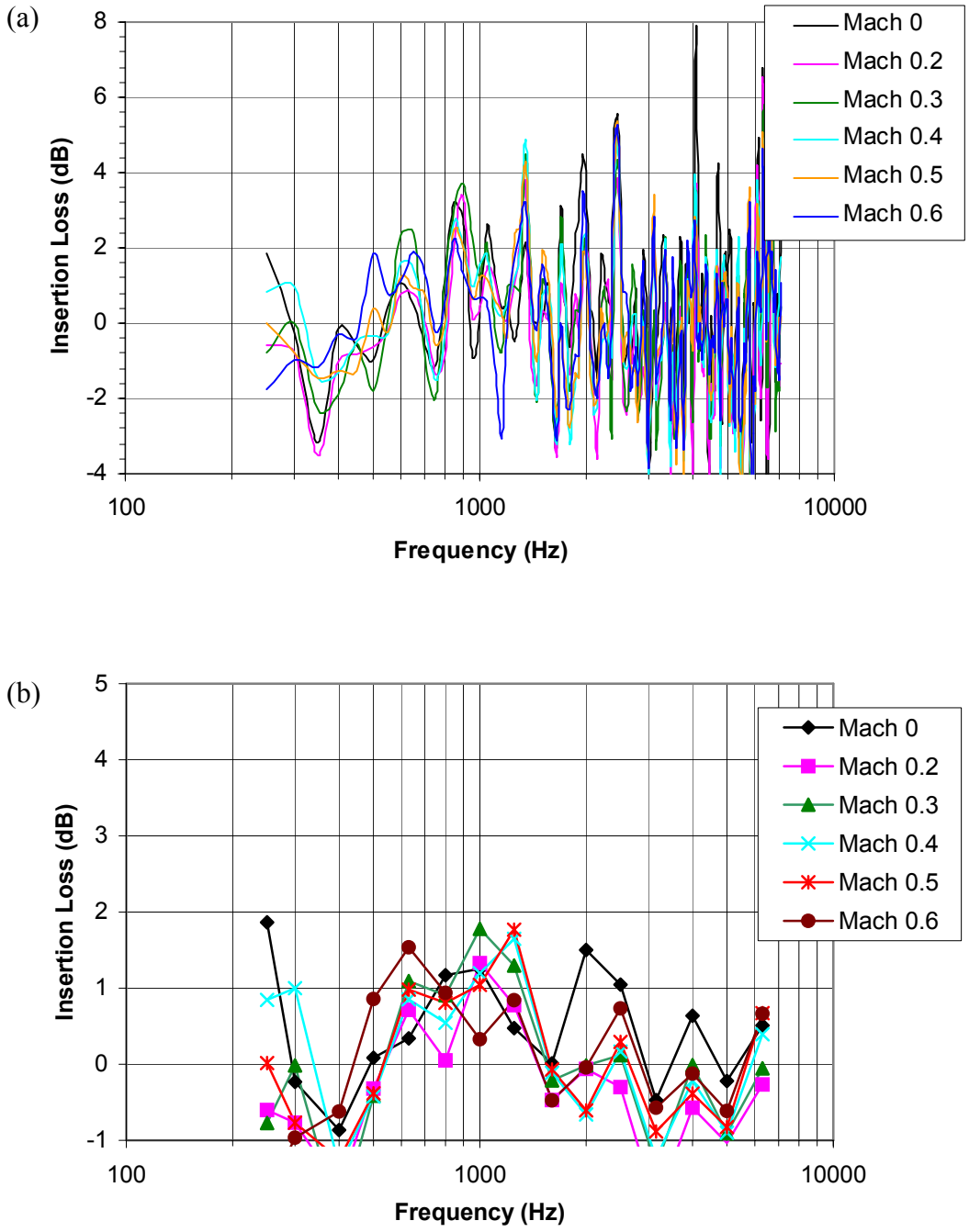

Figure 3.16: Measured insertion loss for hard wall with HQ-configuration 51: (a) narrow (b) 1/3 octave frequency bands. (Screen properties: wire mesh 15.97 rayls on 28 % POA, HQ-tube properties: cross sectional area of 1.629 in^2, tube length of 5.5 in).

The comparison of the overall insertion losses for 28 % and 12 % POA screens is illustrated in figure 3.17. The same comparison for 45.88 and 15.97 rayls wire mesh screens is given in figure 3.18. The 12 % POA screen showed slightly better overall sound attenuations in most flow speeds than the 28% POA screen. However, the high resistance (45.88 rayls) wire mesh screen clearly outperforms the low resistance one. This is a rather unexpected result because in general low resistance is preferable for the HQ systems to yield a highly resonant system and better noise attenuation. The overall insertion losses become insignificant as flow speed increased in both of the comparisons. A main concern in these plots is that the results show an increase in the overall noise levels (negative insertion loss). The reason for this detrimental behavior should be further investigated.

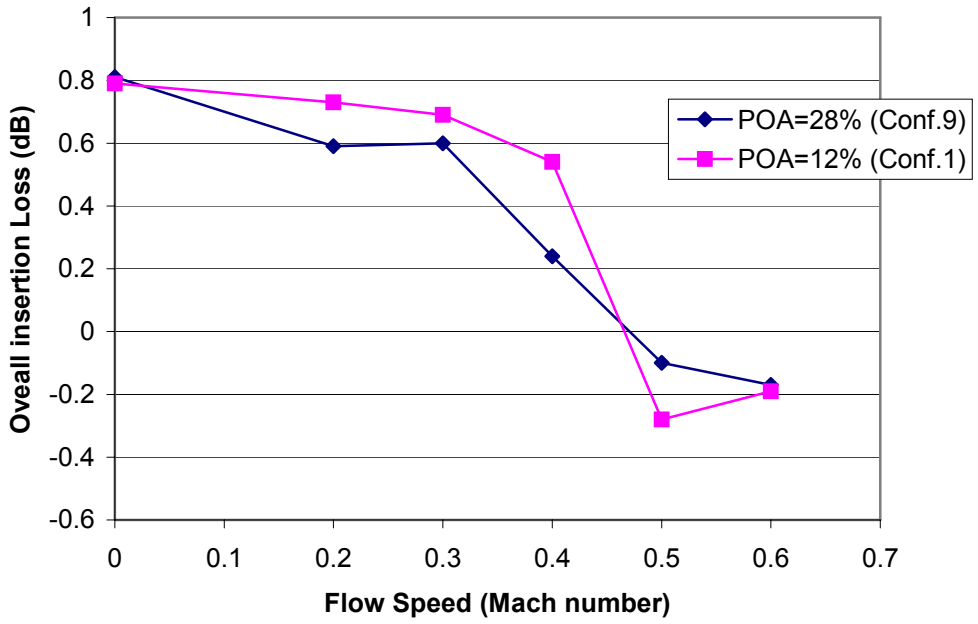

Figure 3.17: Comparison of overall insertion loss for 28 % and 12 % POA screens - configurations 9 and 1 (Tube length of 5.5 in and cross sectional area of 1.629 in^2)

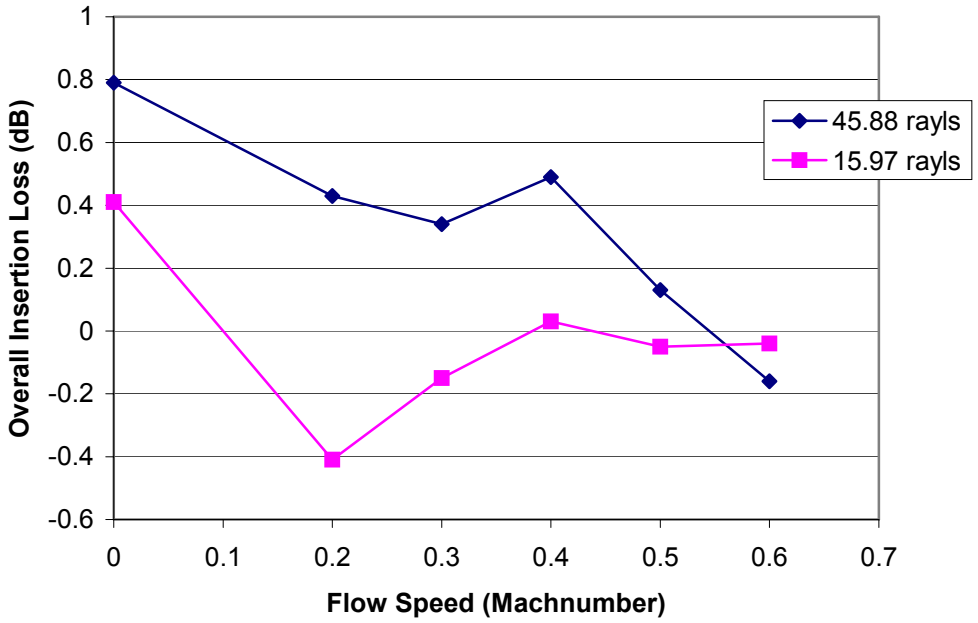

Figure 3.18: Comparison of overall insertion loss for 45.88 and 15.97 rayls wire mesh screens-configurations 43 and 51 (Tube length of 5.5 in and cross section area of 1.629 in^2)

3.3.3 Liner-HQ System Configuration Results

The results of the testing of the liner-HQ configurations 15, 19, 23, 27, 31 and 39 from tables 3.1(e) and 3.1(f) are presented in this section. These configurations are selected because they are representative of the various combinations of liner-HQ system tested. Configurations 15 and 19 correspond to two HQ-tubes mounted on the back plate of the perforate and DynaRohr liners with the liner honeycomb core left in place, respectively. Configurations 23 and 27 are identical to configurations 15 and 19 except that the liner core was removed (see figure 3.3.2b). Thus, the effect of the presence of the core in the HQ-tube can be evaluated. Configurations 31 and 39 correspond to two HQ-tubes mounted at the opposite wall from the lined side of the duct (see figure 3.2d). The HQ-tubes for the six configurations described in this section have the same length (0.1397 m or 5.5 in) and cross sectional area (0.00105 m^2 or 1.629 in^2)

The measured insertion losses for the HQ tubes with perforate and DynaRohr liners with cores are plotted in figures 3.19 and 3.20, respectively. The results in figures 3.21 and 3.22 correspond to the same liners but without the liner core where the HQ tubes are mounted. The insertion losses of the HQ tubes with a DynaRohr liner on opposite side are presented in figures 3.23 and 3.24.

From the test results in figures 3.19 to 3.24, maximum attenuations around 16 dB and 21 dB are found around 2000 Hz for both perforate and DynaRohr liner-HQ systems, respectively. Once again the performance decrease as the Mach number increases. These results have the same trends as for the cases of liner only in section 3.3.1. This is because the attenuation of the liner-HQ system is dominated by the liner performance, i.e. the area of liner is 18 times the area of the tubes. At first inspection, it is difficult from these figures to clearly identify important performance differences between these liner-HQ configurations. The only trend seems to be that the attenuation for 1/3 octave bands $\leq$ 1600 Hz are better for the DynaRohr liner configurations as compared to the perforate liner results. Similarly, comparing the results of the liner-HQ system to the liner alone in figure 3.6 and 3.7 again does not show, at first instance, clear differences.

(a)

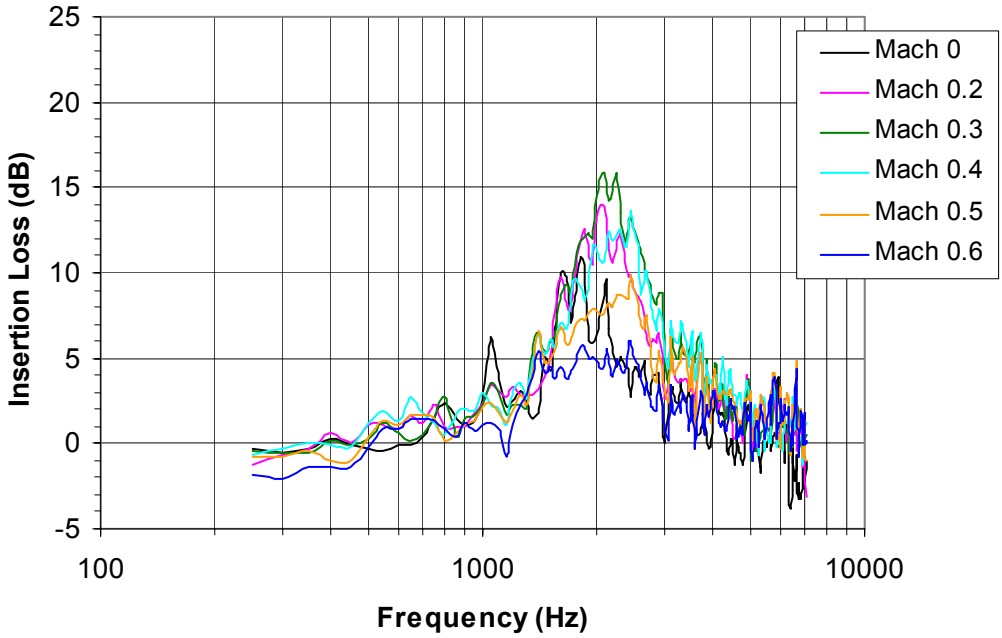

(b)

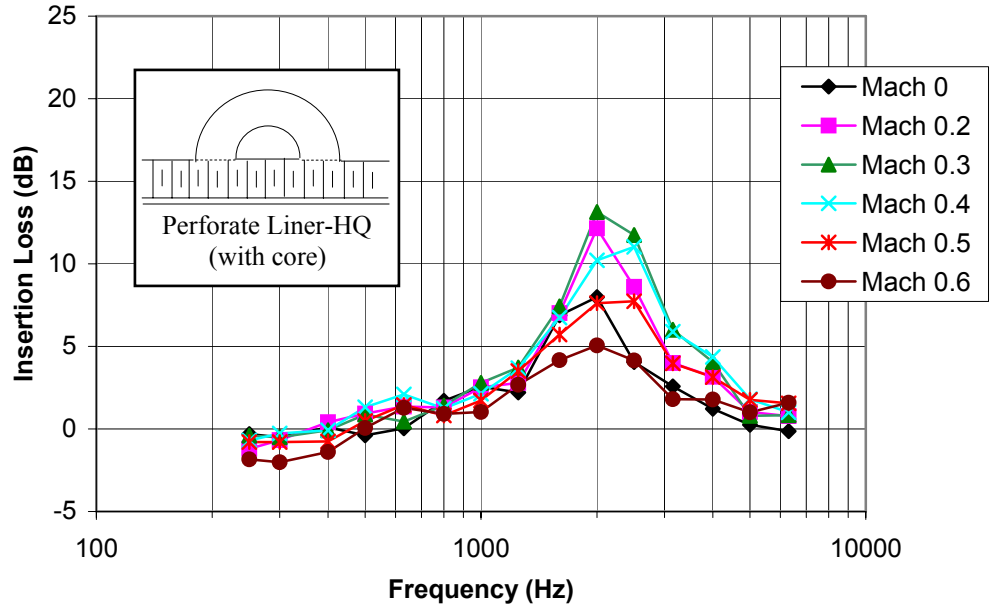

Figure 3.19: Measured insertion loss for perforate liner with HQ-configuration 15: (a) narrow (b) 1/3 octave frequency bands. (HQ-tube properties: cross sectional area of 1.629 in^2, tube length of 5.5 in with core).

(a)

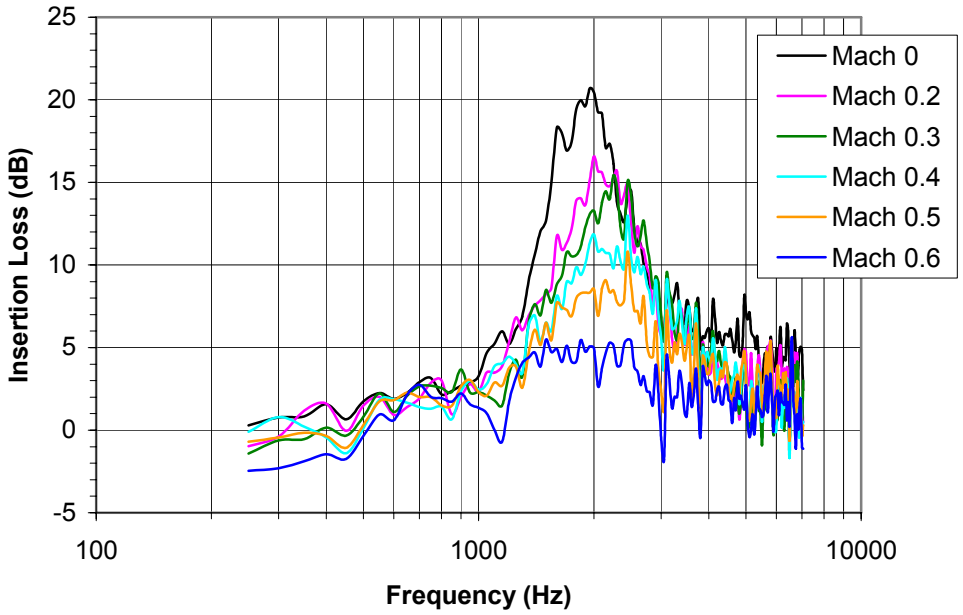

(b)

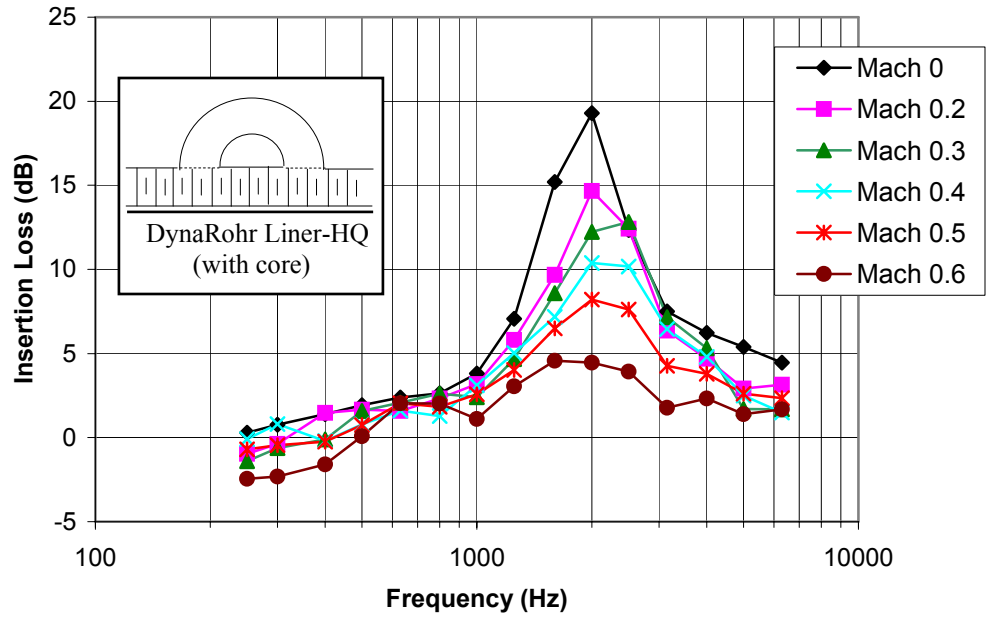

Figure 3.20: Measured insertion loss for DynaRohr liner with HQ-configuration 19: (a) narrow (b) 1/3 octave frequency bands. (HQ-tube properties: cross sectional area of 1.629 in^2, tube length of 5.5 in with core).

(a)

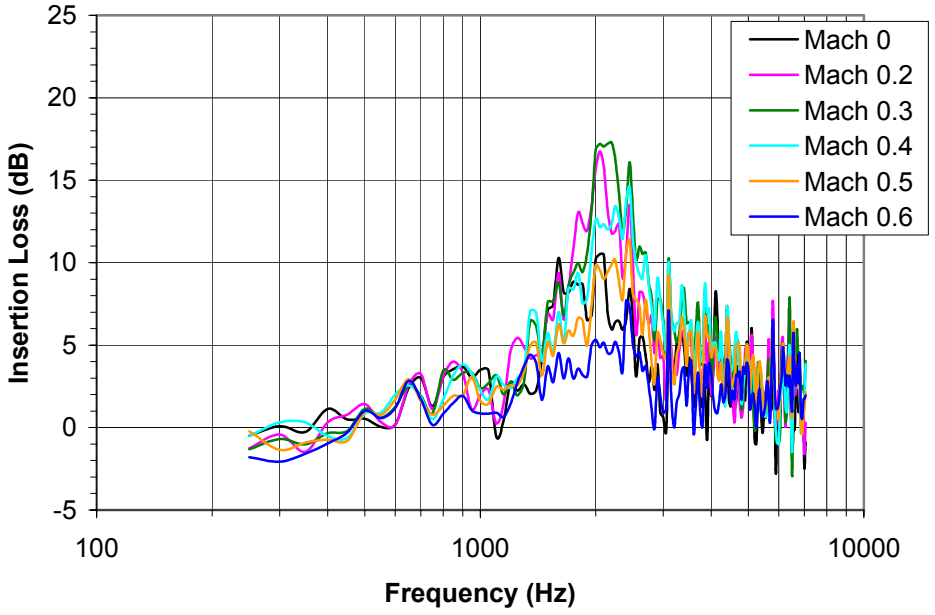

(b)

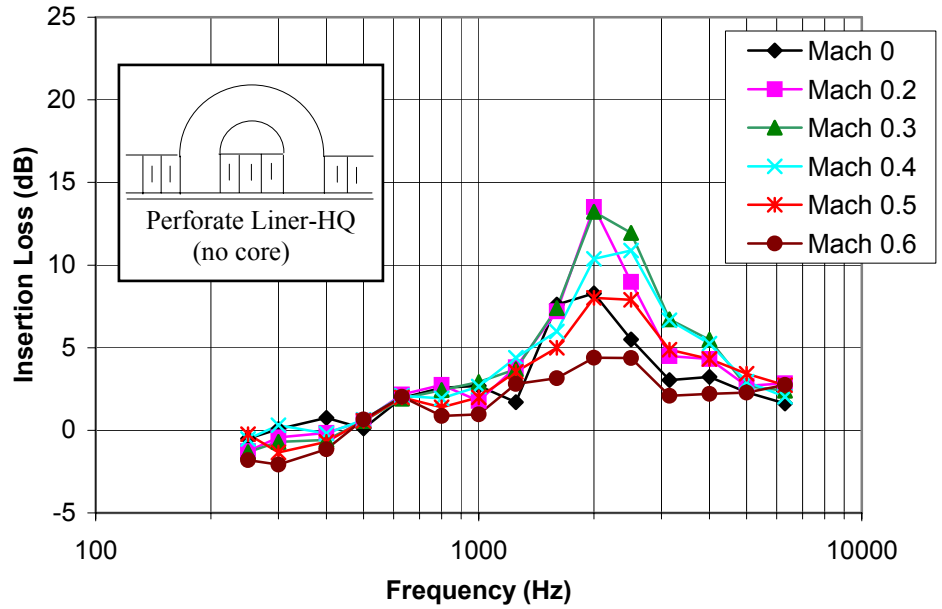

Figure 3.21: Measured insertion loss for perforate liner with HQ-configuration 23: (a) narrow (b) 1/3 octave frequency bands. (HQ-tube properties: cross sectional area of 1.629 in^2, tube length of 5.5 in without core).

(a)

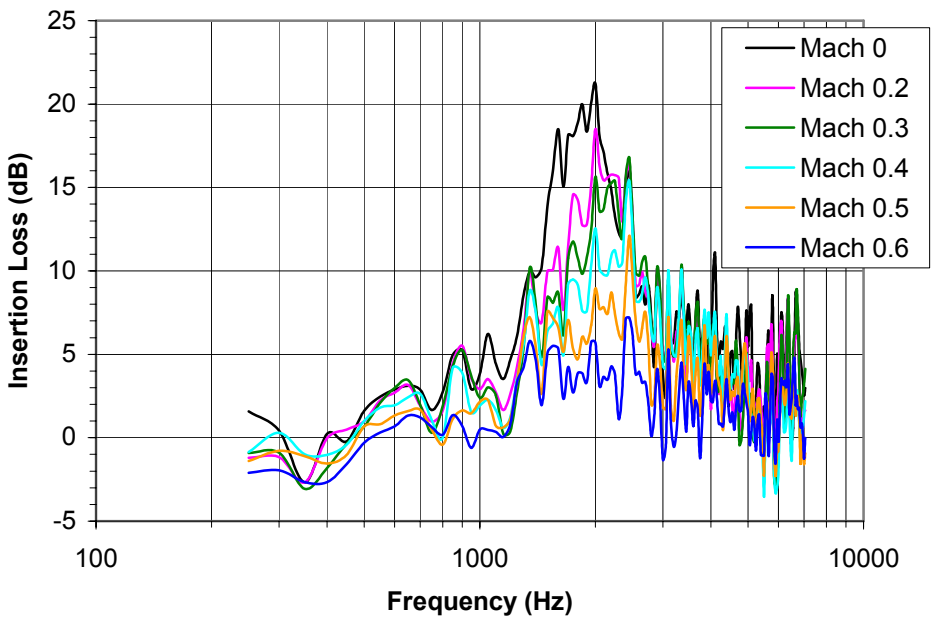

(b)

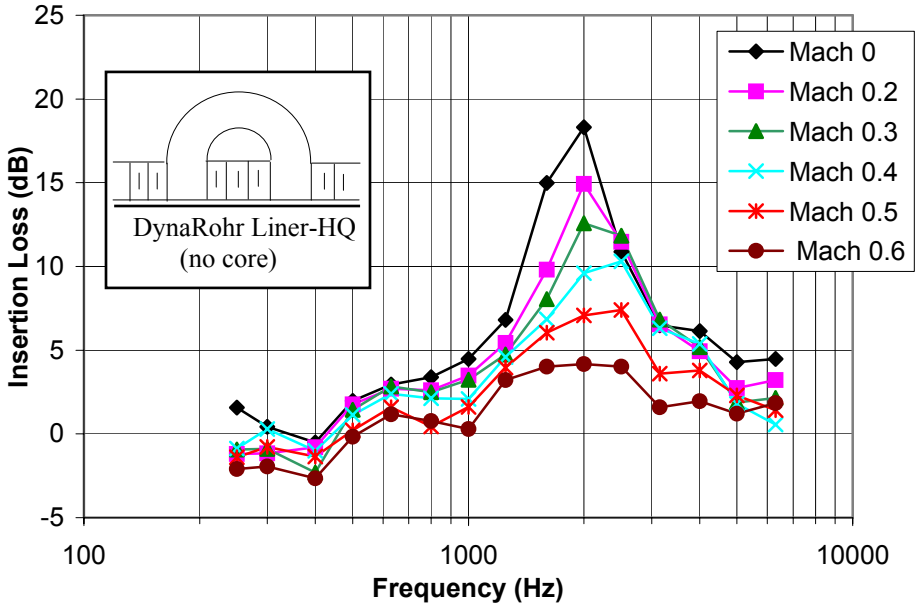

Figure 3.22: Measured insertion loss for DynaRohr liner with HQ-configuration 27: (a) narrow (b) 1/3 octave frequency bands. (HQ-tube properties: cross sectional area of 1.629 in^2, tube length of 5.5 in without core).

(a)

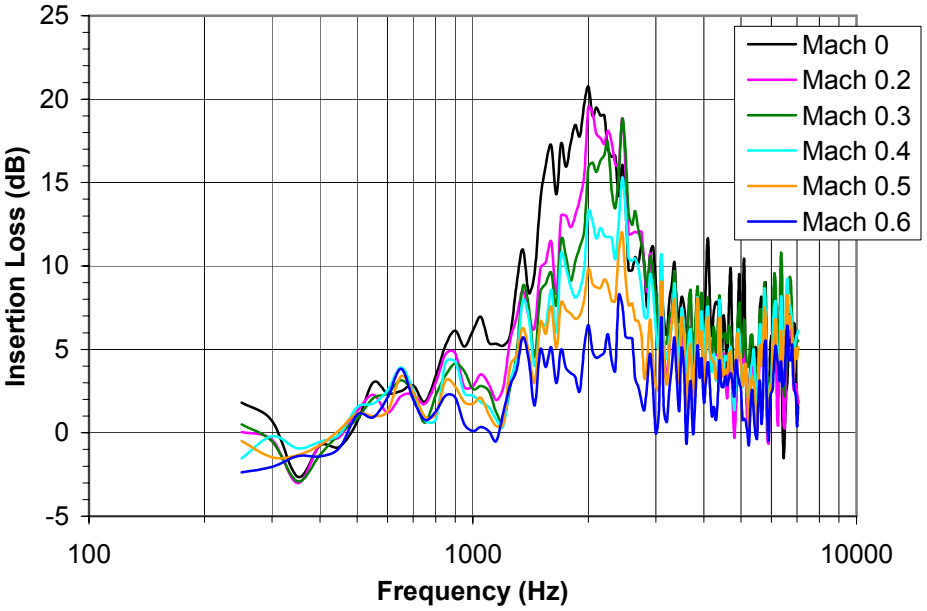

(b)

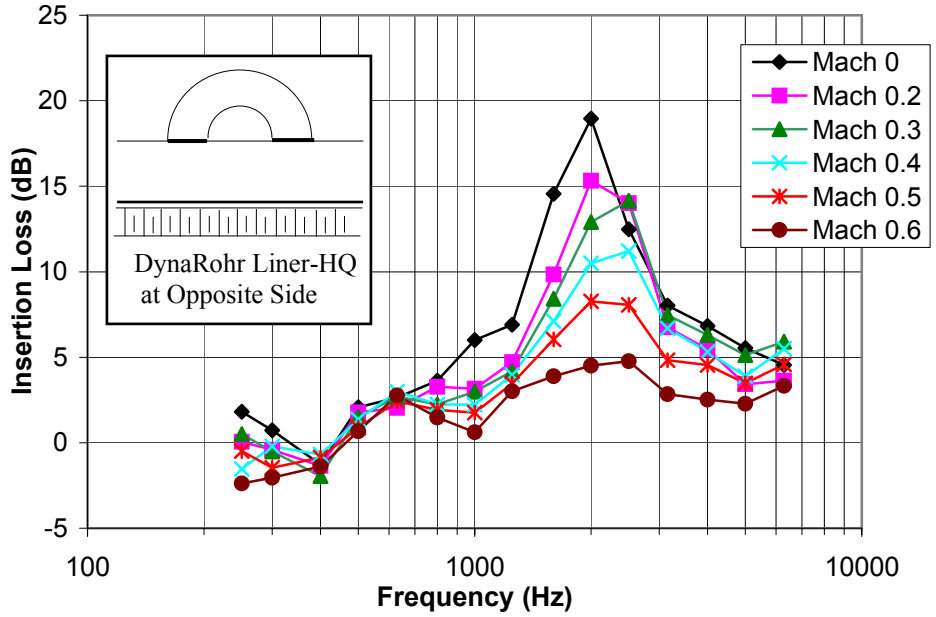

Figure 3.23: Measured insertion loss for DynaRohr liner with HQ at opposite side-configuration 31: (a) narrow (b) 1/3 octave frequency bands. (Screen Property: 12 % POA, HQ-tube properties: cross sectional area of 1.629 in^2, tube length of 5.5 in).

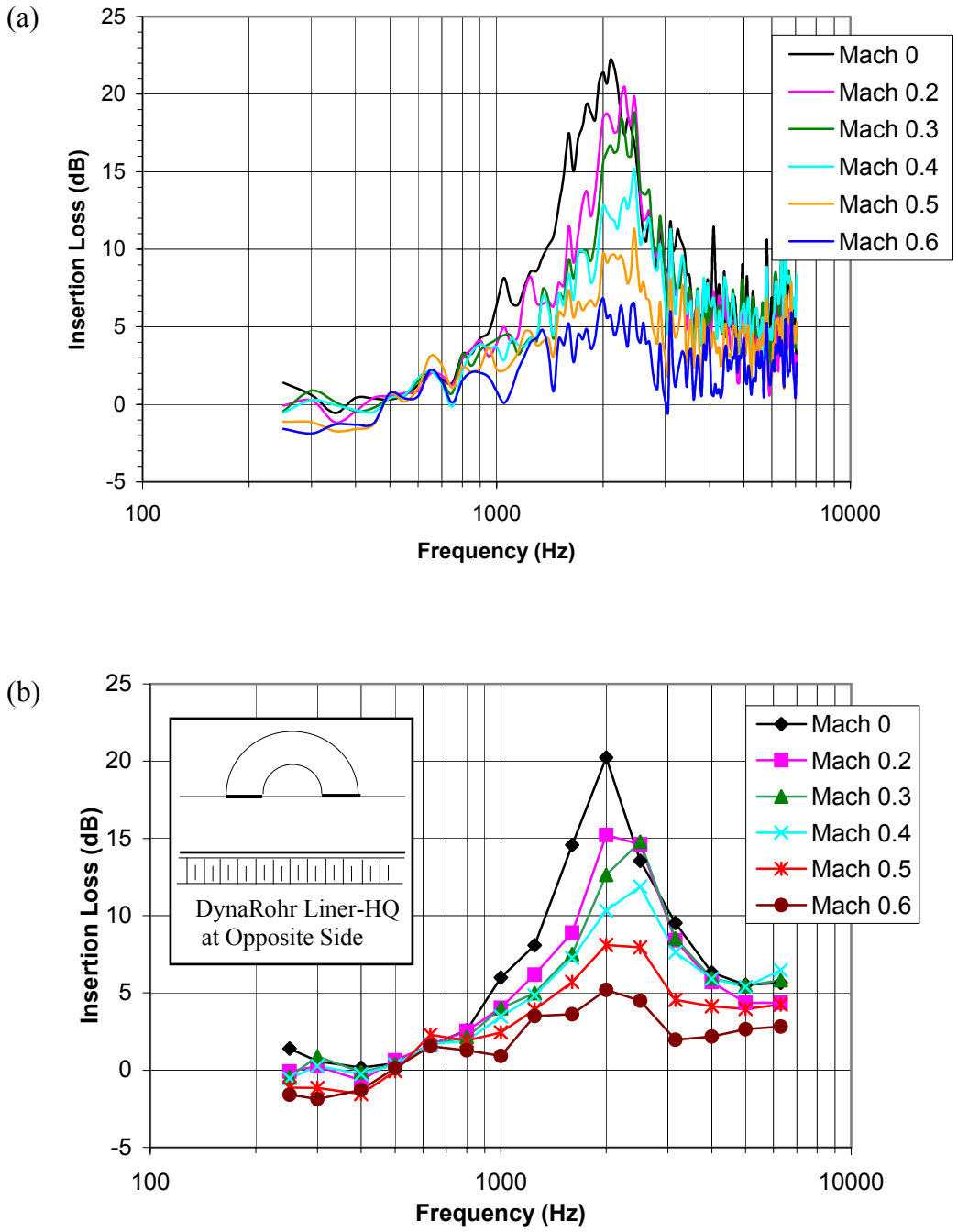

Figure 3.24: Measured insertion loss for DynaRohr liner with HQ at opposite side-configuration 39: (a) narrow (b) 1/3 octave frequency bands. (Screen Property: 28 % POA, HQ-tube properties: cross sectional area of 1.629 in^2, tube length of 5.5 in).

In order to better define the performance of the liner-HQ system, the overall insertion loss of these cases will be compared to both the liner and HQ alone systems. In addition, the difference in insertion loss between the liner-HQ and liner alone systems in 1/3 octave bands will be presented to identify the frequencies of improved performance of the liner-HQ system.

Figure 3.25 shows the overall insertion losses for the perforate liner-HQ system with and without the core cut-out (configurations 15 and 23), the perforate liner alone (configuration 13), and the HQ-tubes alone (configuration 1).

The perforate liner-HQ without core shows better overall sound attenuation than the liner alone at all flow speeds, but as the Mach number increases the insertion loss improvement becomes insignificant. The results also show that the perforate liner-HQ system without a core shows better performance than the system with core. It is also interesting to point out that though the HQ-tubes alone result in a negative IL (increase in noise) at flow Mach of 0.5 and 0.6, when combined with the liner (with the core cut-out) the system, however, outperforms the liner alone.

The insertion loss difference for the perforate liner-HQ system without the core as compared to the liner only system is presented as a function of frequency in figure 3.26. These results do not follow a clear pattern and they seem to indicate that the HQ-tubes improve the performance of the liner over a wide frequency range. This is an expected conclusion since the HQ-tube is expected to provide best performance near its resonances, i.e. ~1000, 2000, …Hz.

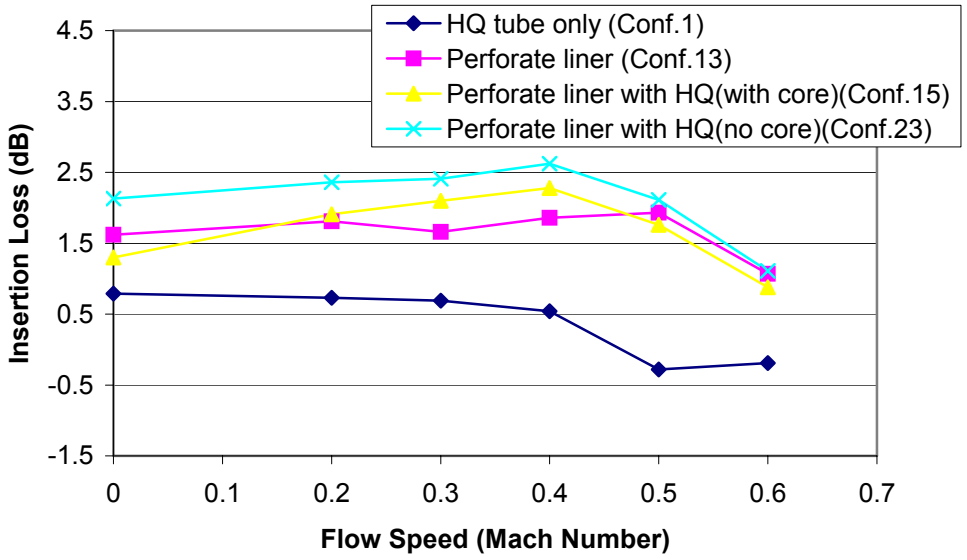

Figure 3.25: Overall insertion loss of perforate liner systems (configurations 1,13,15,23) (HQ-tube properties: cross sectional area of 1.629 in^2, tube length of 5.5 in)

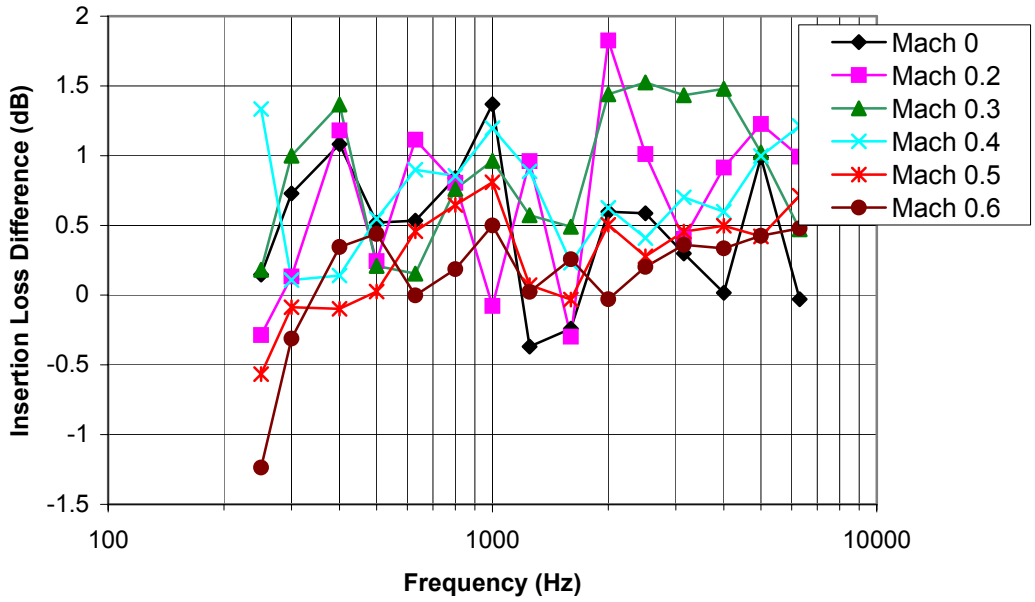

Figure 3.26: Insertion loss difference between perforate liner and liner-HQ system (configurations 23-13)

Similar study is carried out for the DynaRohr liner system. Figure 3.27 shows the insertion losses for the DynaRohr liner-HQ systems with and without the core cut-out (configurations 19 and 27), the DynaRohr liner alone (configuration 14), and the HQ-tubes alone (configuration 9).

The results for the DynaRohr liner shows in general the opposite trends as compared to the perforate liner results. The HQ-tubes mounted on the DynaRohr liner without removing the core outperforms the case where the core was cut-out. In addition, the liner-HQ system does not provide any significant improvement on the liner performance at $M \geq 0.4$.

The insertion loss difference for the DynaRohr liner-HQ system compared with the liner only system as a function of frequency is shown in figure 3.28. The HQ-tubes increase performance of the liner only at low frequencies, i.e. < 600 Hz, which is unexpected because the lowest tube resonance is around 1000 Hz. Increase in noise at many frequency bands is very clear at high flow speeds.

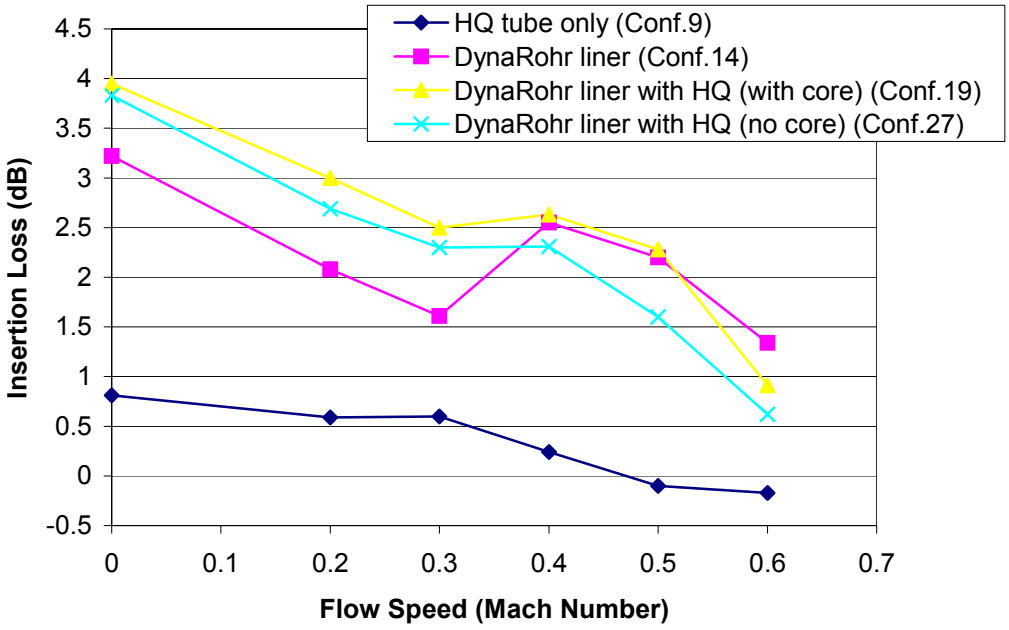

Figure 3.27: Overall insertion loss of DynaRohr liner systems (configurations 9,14,19,27) (HQ-tube properties: cross sectional area of 1.629 in^2, tube length of 5.5 in)

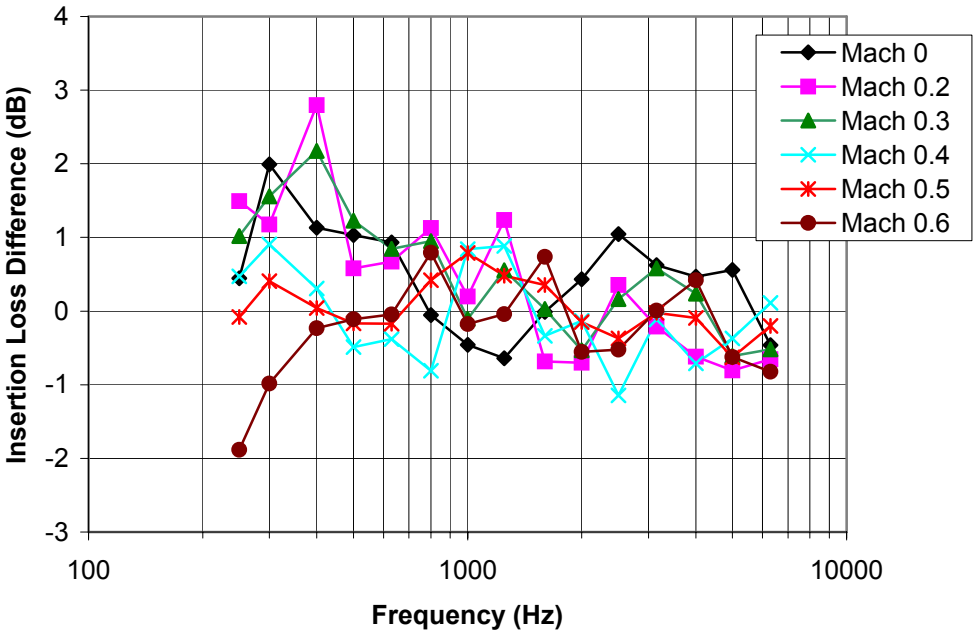

Figure 3.28: Insertion loss difference between DynaRohr liner and liner-HQ system with core (Configurations 19-14)

Figure 3.29 shows the insertion loss for the DynaRohr liner-HQ system with core (configuration 19), HQ tubes mounted opposite to the DynaRohr liner (configuration 39), the DynaRohr liner alone (configuration 14), and the HQ-tubes alone (configuration 9).

The result for the Dynarohr liner with HQ-tubes at the opposite side outperforms the DynaRohr liner-HQ system in the mid range of flow speeds (M= 0.2 and 0.4). At flow speed of M=0.4, the liner-HQ system shows an overall insertion loss of ~3.2 dB as compared to ~1.6 dB of the liner alone, i.e. the HQ yielded a remarkable 1.5 dB improvement.

Figure 3.30 shows the insertion loss difference between the DynaRohr liner and the DynaRohr liner with HQ tubes at the opposite side as a function of frequency. The Dynarohr liner with HQ tubes at the opposite side outperforms the DynaRohr liner system in most frequency ranges.

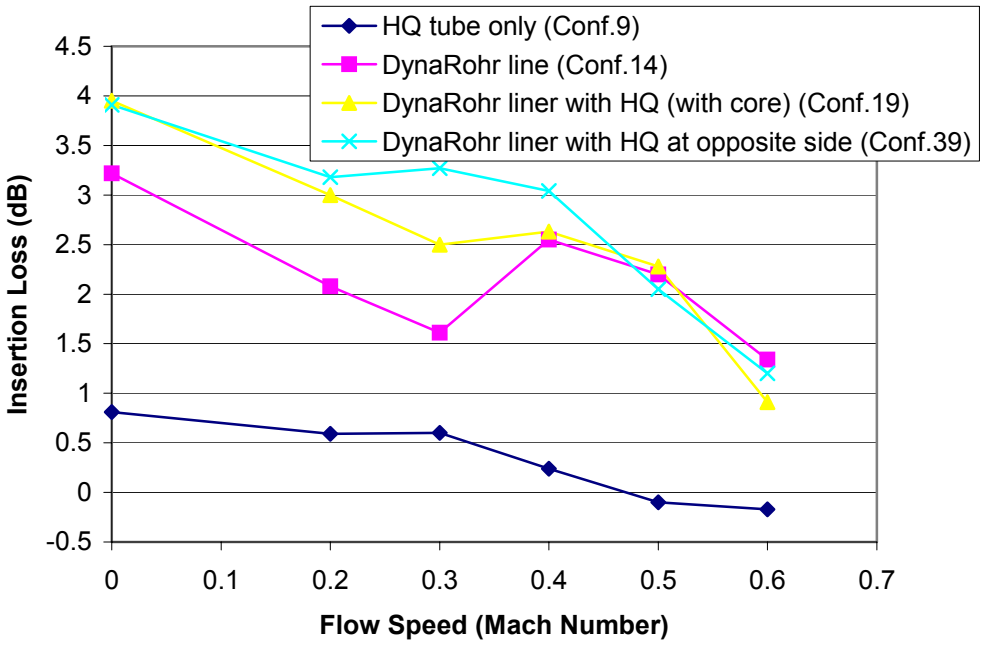

Figure 3.29: Overall insertion losses of DynaRohr liner-HQ systems, DynaRohr liner with HQ at opposite side and HQ tubes alone (configurations 9,14,19,39) (HQ-tube properties: cross sectional area of 1.629 in^2, tube length of 5.5 in)

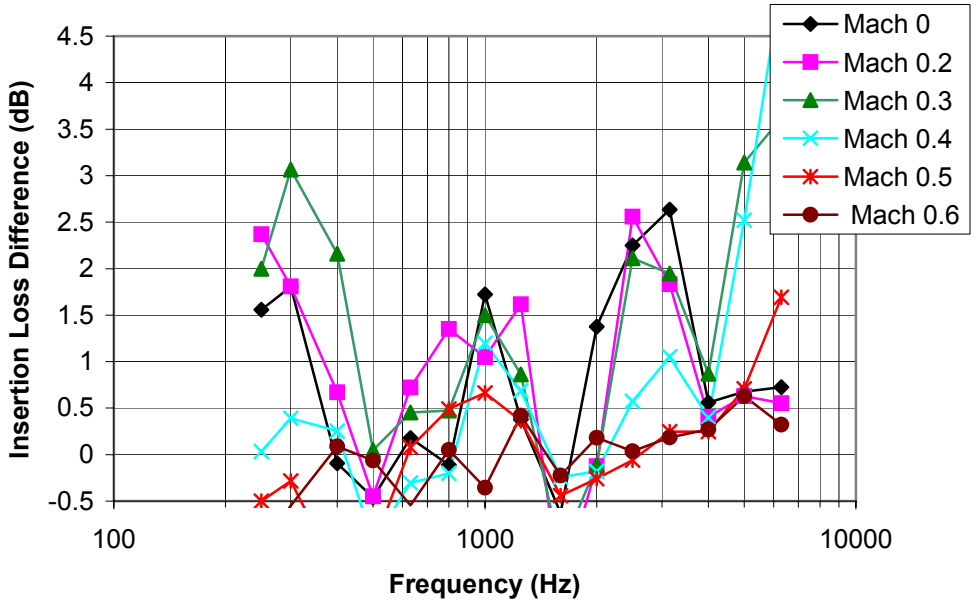

Figure 3.30: Insertion loss difference between DynaRohr with HQ at opposite side and DynaRohr liner (Configurations 39-14)

In order to have a better perspective of the performance of the liner-HQ tube systems as compared to the liner and HQ-tubes separately, the overall attenuations are plotted for all test configurations in figures 3.31 through 3.36 for each flow speed, respectively.

In these figures, the first group of configurations (1~12, 55~66, 43~54) corresponds to the HQ-tubes on a hard walled duct, which are indicated using yellow symbol. The next two configurations (13 and 14) correspond to the perforate and DynaRohr liners. They are identified with a green and red symbol for the perforate and DynaRohr liner, respectively. The final group of configurations corresponds to the liner-HQ-tube systems. For these cases, the same symbols are used as for the liner ones. In these figures, the horizontal green and red dashed lines represents the perforate and DynaRohr liner attenuations. Thus, any symbol on the liner-HQ tube configurations above these lines represents better performance than the liner alone case, i.e. the HQ tubes resulted in improved performance of the liner.

The most important results correspond to flow speeds of $M \geq 0.3$. For M=0.3 and 0.4, all the perforate liner-HQ systems outperform the perforate liner alone while 22 out of 24 DynaRohr liner-HQ tube configurations perform better than the DynaRohr liner alone. At these two flow speeds, it is very clear that mounting the HQ-tubes opposite to the DynaRohr liner is a very effective configuration. However, an issue that needs to be resolved is that if the same trend would be observed with a perforate liner. At M=0.5, about half of the liner-HQ systems result in higher overall insertion loss. Finally, at M=0.6 most of the liner-HQ systems perform poorly as compare to the liner only.

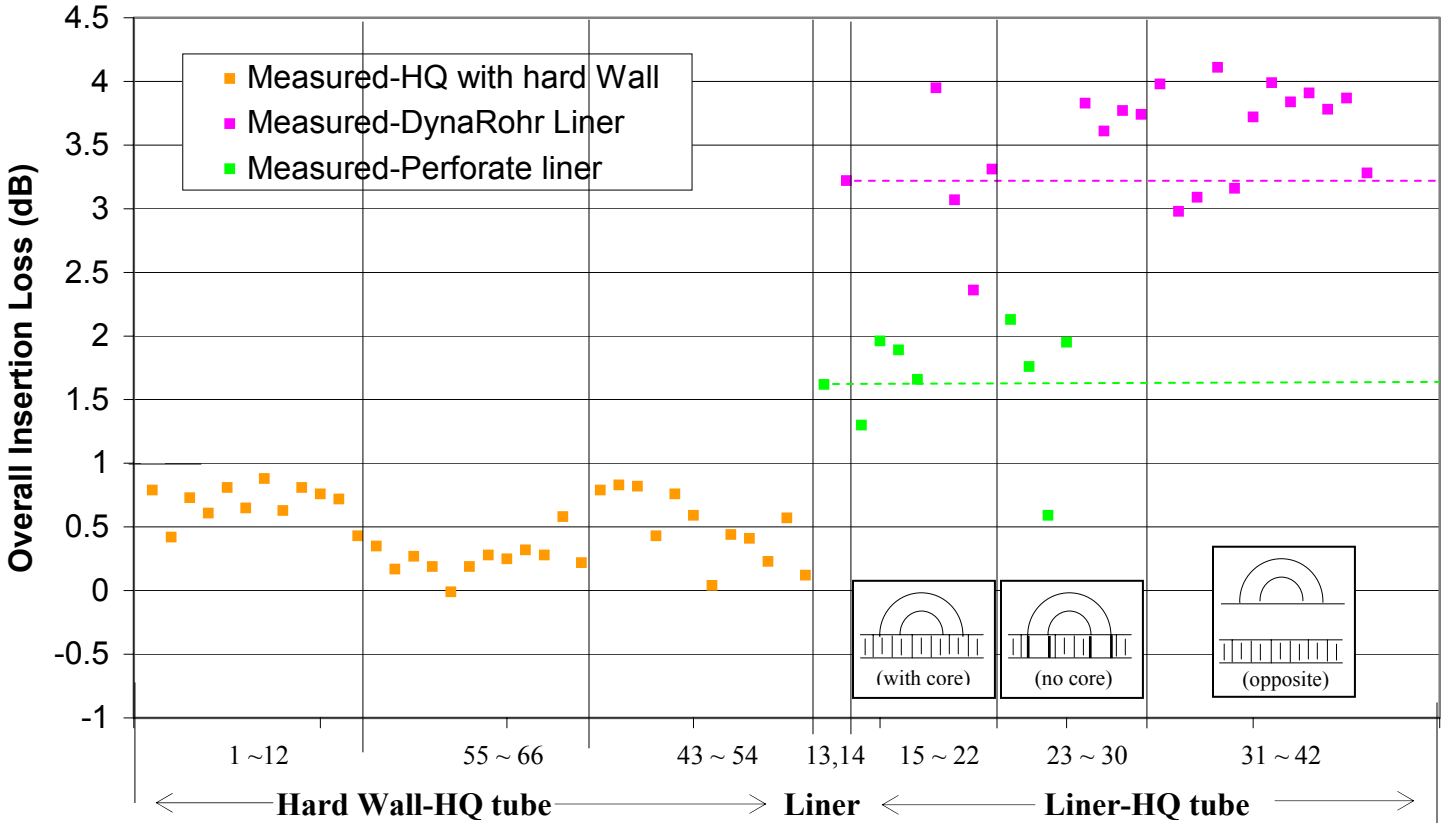

Figure 3.31: Comparison of overall insertion loss of all configurations at Mach 0.0

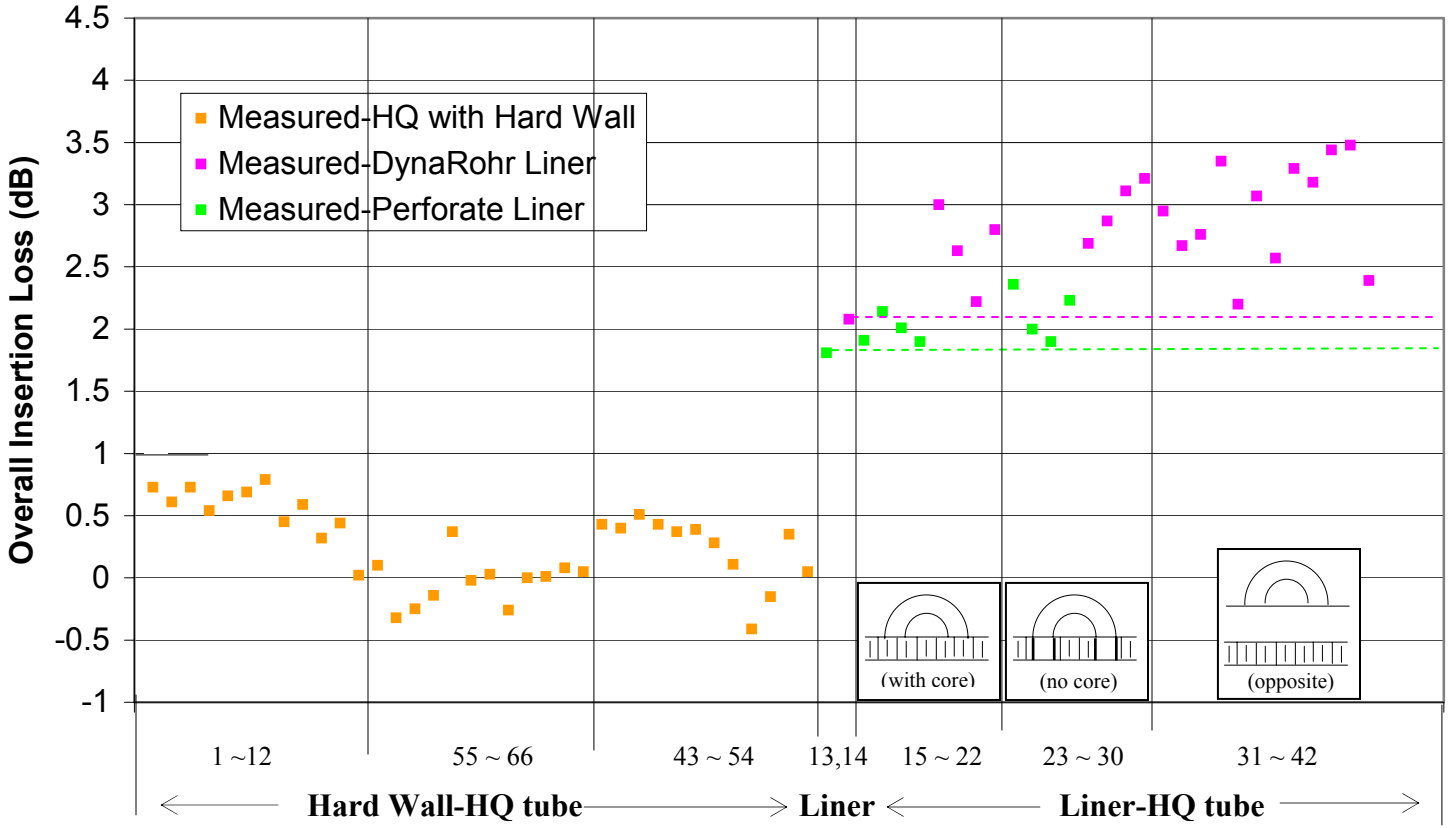

Figure 3.32: Comparison of overall insertion loss of all configurations at Mach 0.2

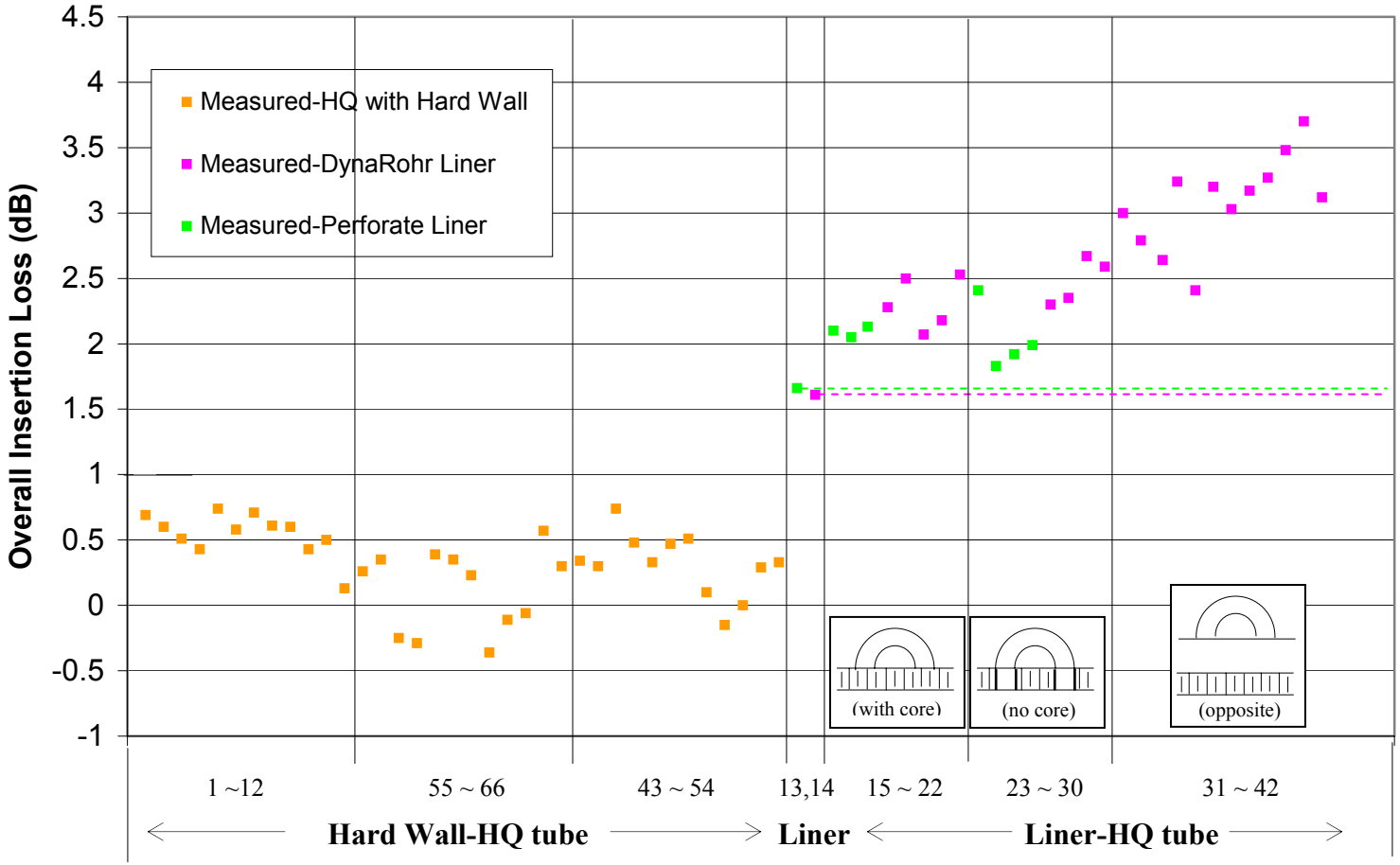

Figure 3.33: Comparison of overall insertion loss of all configurations at Mach 0.3

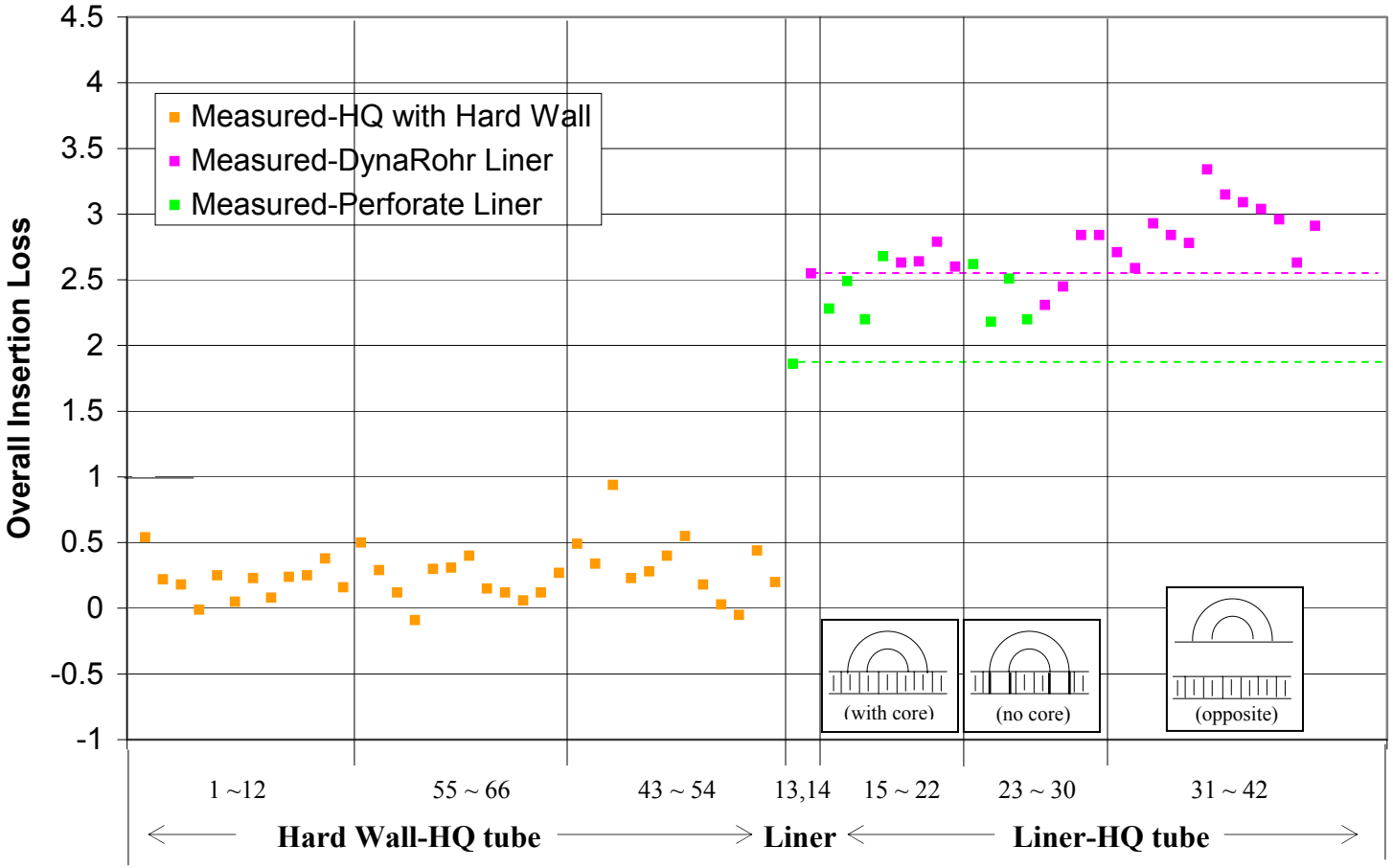

Figure 3.34: Comparison of overall insertion loss of all configurations at Mach 0.4

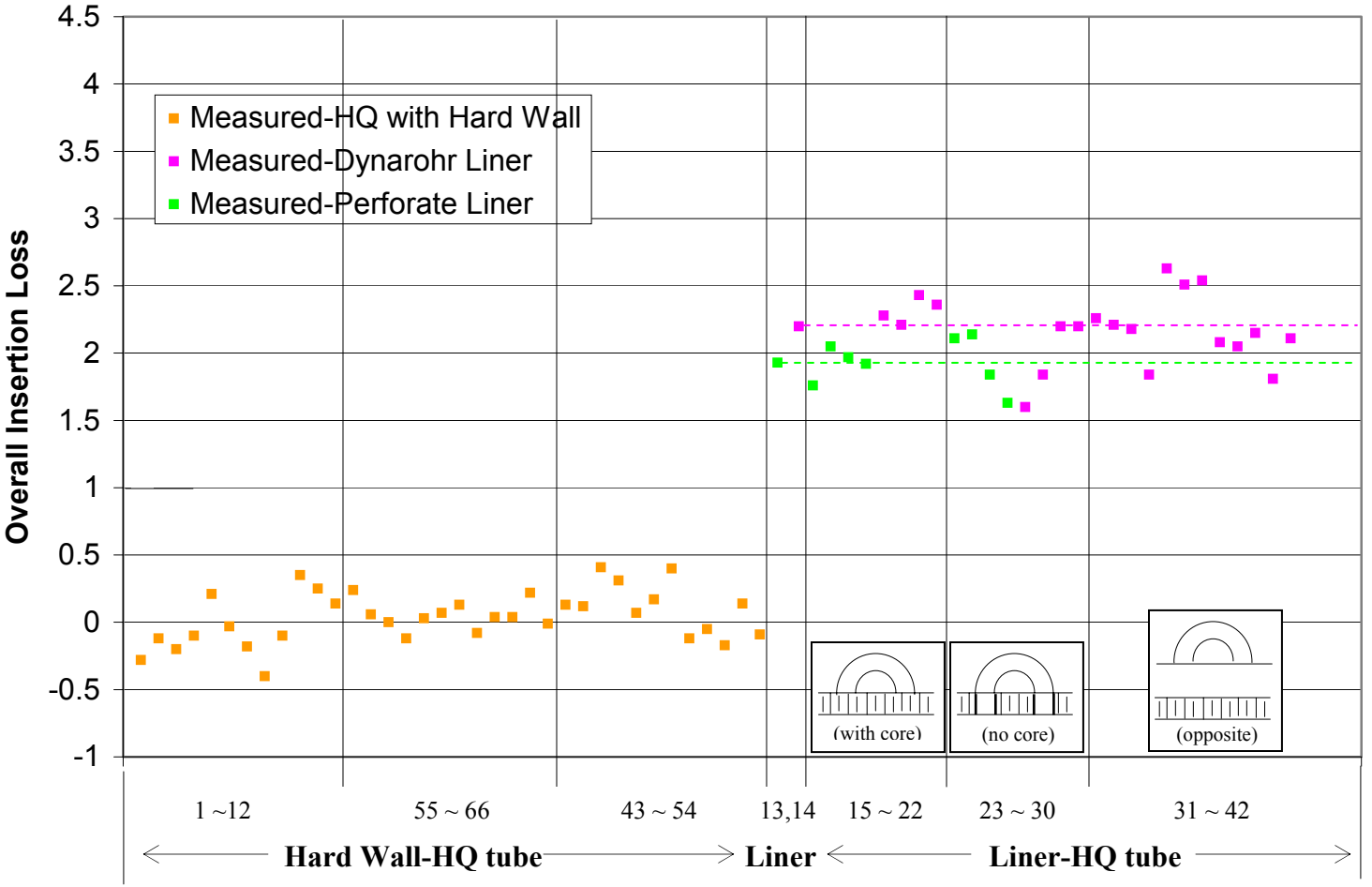

Figure 3.35: Comparison of overall insertion loss of all configurations at Mach 0.5

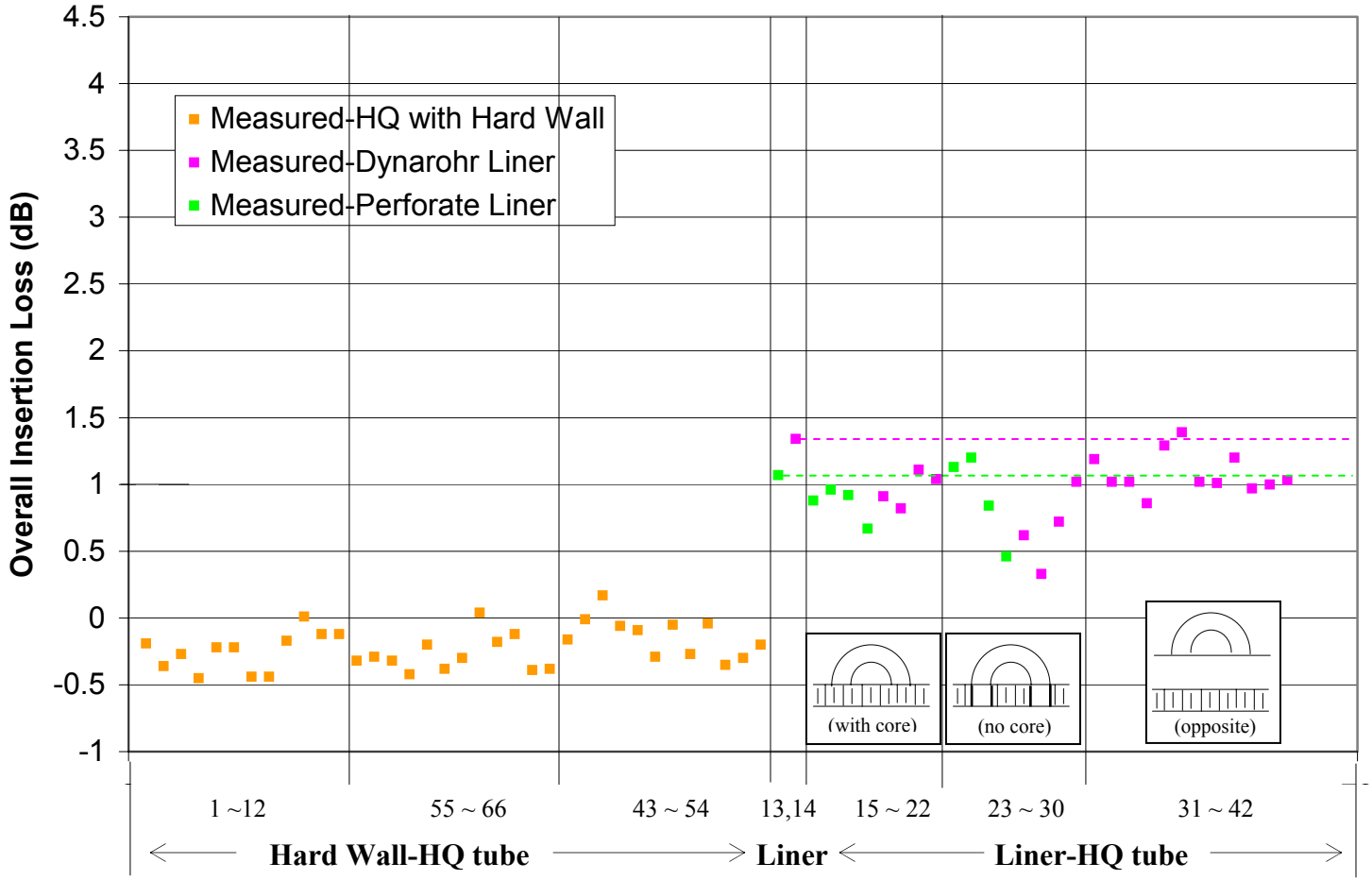

Figure 3.36: Comparison of overall insertion loss of all configurations at Mach 0.6

3.4 Numerical Predictions

In the previous sections, the experimental tests and results were presented and investigated. In this section, the numerical test predictions are presented, including comparisons to the experimental results.

3.4.1 Numerical Description and Results

The numerical model of the rectangular duct was used to predict the sound power level attenuation (insertion loss) of the experimental configurations. The model was used to simulate all the configurations except the cases in table 3.1 (c). The model requires knowing the amplitudes of the incident modes. Because this information is not available, it is common practice to make assumptions about the broadband noise modal structure. The two commonly used approaches to define the amplitude of the modal are equal modal amplitude and equal modal power. Both of these approaches were tested in the numerical simulations and it was found that the equal modal amplitude approach resulted in slightly better agreement to the experimental results. Thus, all numerical simulations presented here were performed with this technique. The phase between the modes was randomly selected. The randomness of the modal phase did not affect the predictions.

In order to determin the modes to be included in the analysis, the cut-off frequencies of the hard-wall rectangular duct were computed for the different flow speeds. They are presented in table 3.2(a) through (f). Because the modeling approach is valid at frequencies below the first cut-off frequency of the HQ-tubes (5588 Hz for 0.001505 m^2), the rectangular duct modes included in the analysis was limited to those having cut-off frequency below 5000 Hz. For example, for the case of M=0.3 the following disturbance modes were considered: (0,0), (0,1), (0,2), (0,3), (1,0), (1,1), (1,2), (2,0), (2,1), (2,2), (3,0), and (3,1).

Finally, the numerical model was executed for a frequency range of 250-5000 Hz at increments of 50 Hz.

Table 3.2 (a): Cut-off frequency (Hz) of rectangular hard wall duct modes at M=0

m \ n	0	1	2	3	4
0	0	1795	3430	5145	6860
1	1350	2182	3686	5319	6991
2	2700	3199	4365	5810	7372
3	4051	4399	5308	6548	7966
4	5401	5667	6398	7459	8731

Table 3.2 (b): Cut-off frequency (Hz) of rectangular hard wall duct modes at M=0.2

m \ n	0	1	2	3	4
0	0	1680	3368	5041	6721
1	1323	2938	3611	5211	6850
2	2646	3134	4277	5693	7223
3	3969	4310	5201	6416	7805
4	5292	5552	6269	7309	8554

Table 3.2 (c): Cut-off frequency (Hz) of rectangular hard wall duct modes at M=0.3

m \ n	0	1	2	3	4
0	0	1636	3272	4908	6544
1	1288	2882	3516	5074	6669
2	2576	3051	4164	5543	7032
3	3864	4196	5063	6246	7599
4	5152	5406	6103	7116	8329

Table 3.2 (d): Cut-off frequency (Hz) of rectangular hard wall duct modes at M=0.4

m \ n	0	1	2	3	4
0	0	1571	3143	4715	6287
1	1237	2000	3378	4875	6408
2	2475	2932	4001	5325	6757
3	3713	4032	4865	6001	7301
4	4950	5194	5864	6837	8002

Table 3.2 (e): Cut-off frequency (Hz) of rectangular hard wall duct modes at M=0.5

m \ n	0	1	2	3	4
0	0	1485	2970	4455	5940
1	1169	1890	3192	4606	6054
2	2339	2770	3780	5032	6384
3	3508	3809	4597	5671	6899
4	4677	4908	5541	6460	7561

Table 3.2 (f): Cut-off frequency (Hz) of rectangular hard wall duct modes at M=0.6

m \ n	0	1	2	3	4
0	0	1372	2744	4116	5488
1	1080	1746	2949	4255	5593
2	2160	2559	3492	4648	5898
3	3240	3519	4246	5238	6373
4	4321	4533	5118	5967	6985

The results of the predictions for the perforate and DynaRohr liners are plotted in figures 3.37 and 3.38 for both narrow and 1/3 octave bands. As in the experimental results, the predicted results for the DynaRohr liner systems show better insertion loss than the results for the perforate liner systems.

However, the model predicts better attenuations than that shown by the experiments (see figures 3.6 and 3.7). The numerical simulation also shows a shift towards high frequencies of the peak reduction as the flow speed increases, which is also present in the experiments. However, the frequency shift is less significant in the measured data.

(a)

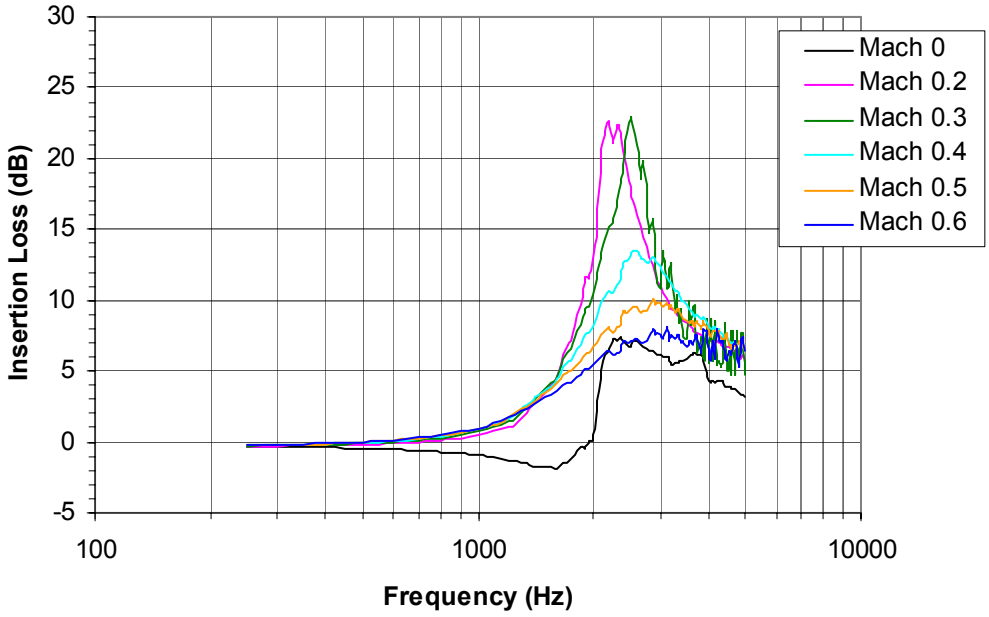

(b)

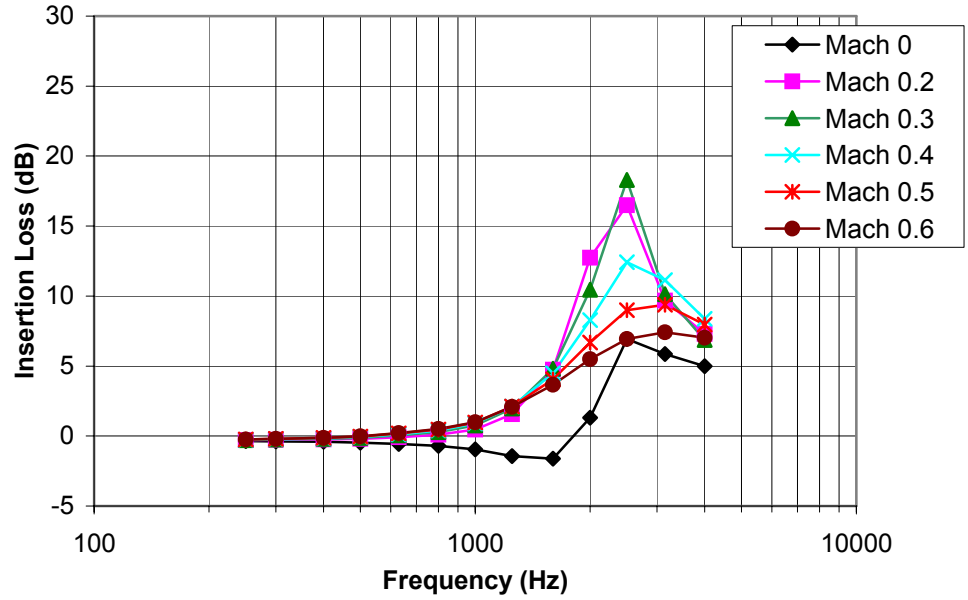

Figure 3.37: Predicted insertion loss for perforate liner-configuration 13: (a) narrow (b) 1/3 octave frequency bands.

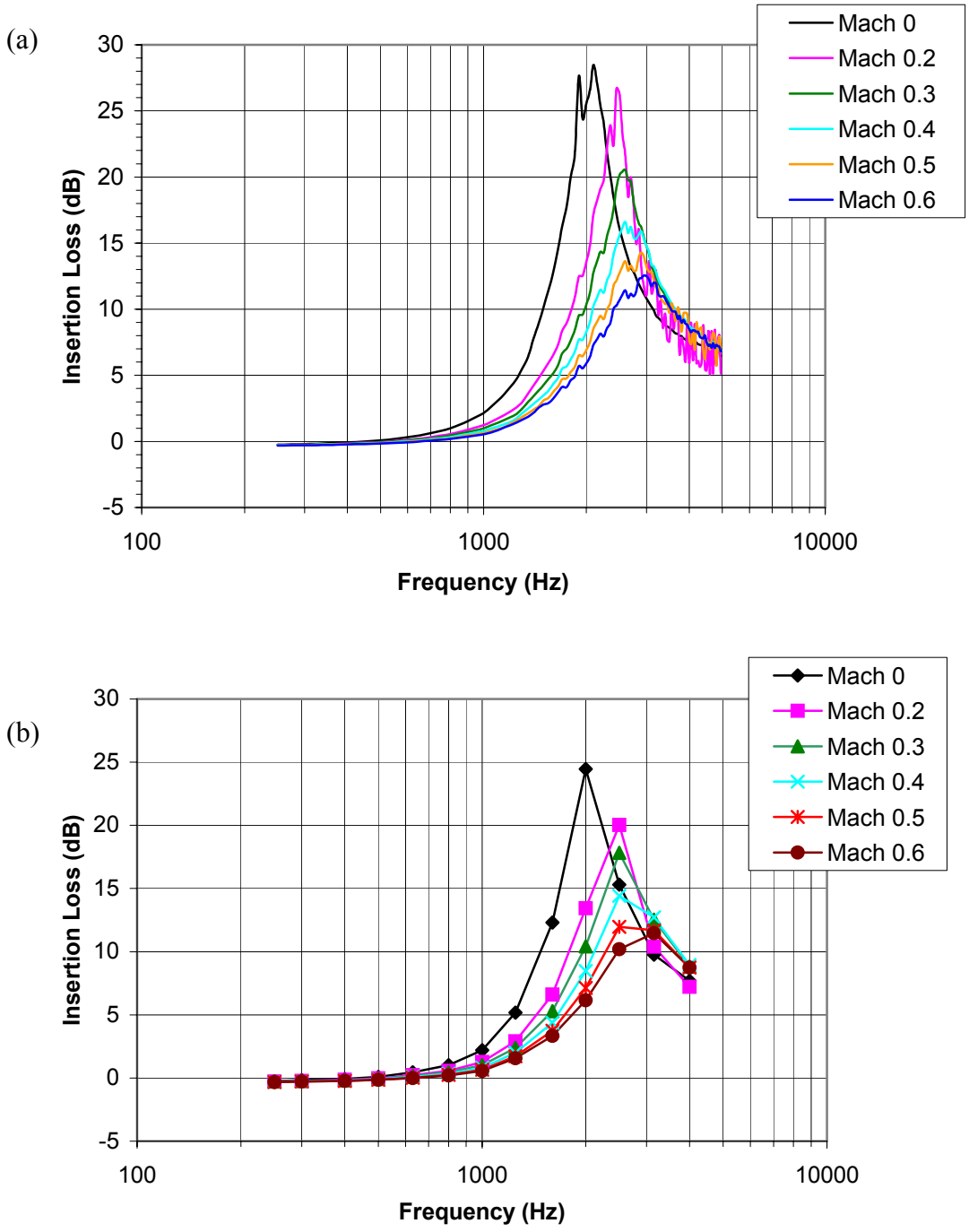

Figure 3.38: Predicted insertion loss for DynaRohr liner-configuration 14: (a) narrow (b) 1/3 octave frequency bands.

The results of the predictions for the hard wall with HQ tubes are plotted in figure 3.39 and 3.40 for both narrow and 1/3 octave bands. The performance for perforate face screens with 28% and 12% POA were predicted. As in the experimental results, the numerical result for 28% POA screen shows better insertion loss than the results for 12% POA screen. However, the model predicts better attenuation than that shown by the experiments (see figures 3.13 and 3.14).

(a)

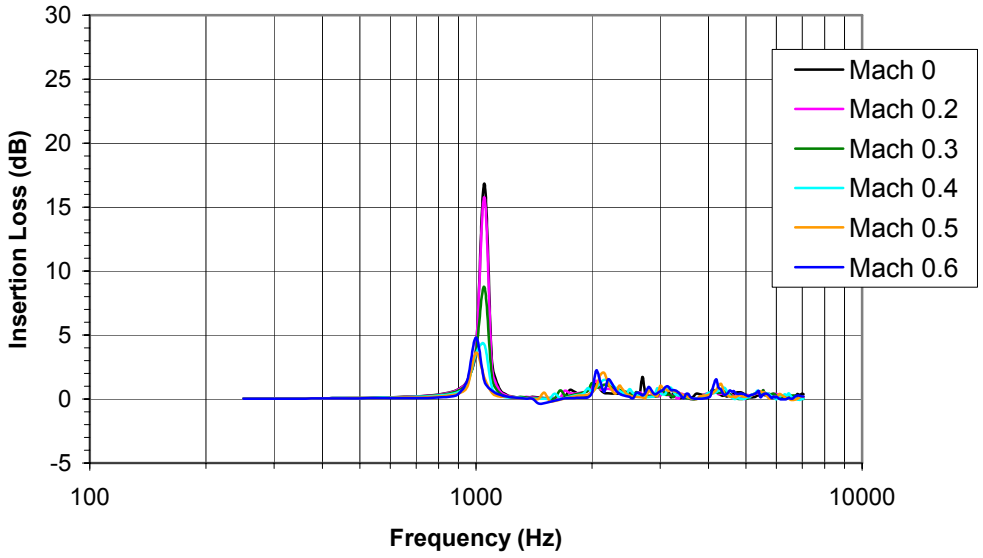

(b)

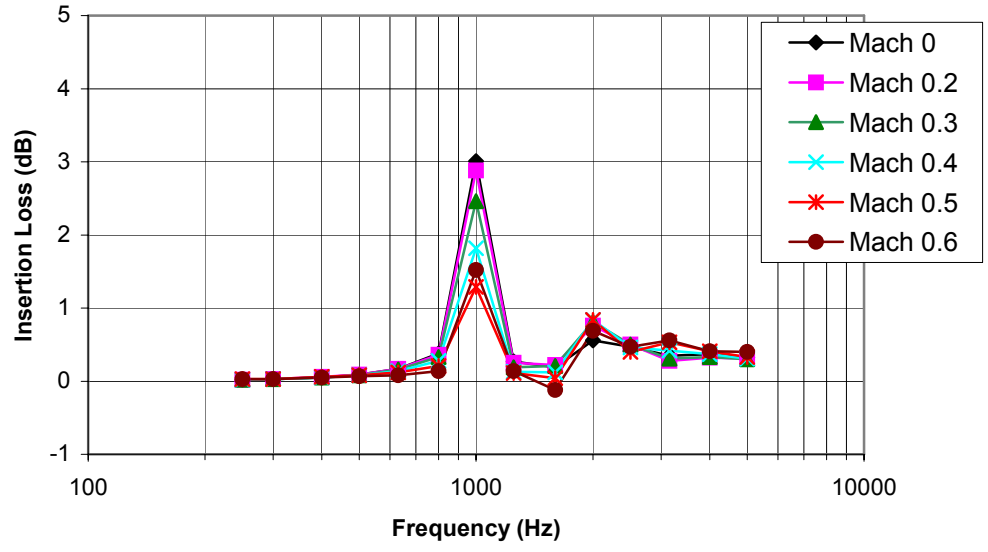

Figure 3.39: Predicted insertion loss for hard wall with HQ-configuration 9: (a) narrow (b) 1/3 octave frequency bands. (Screen Property: 28 % POA, HQ-tube properties: cross sectional area of 1.629 in^2, tube length of 5.5 in).

(a)

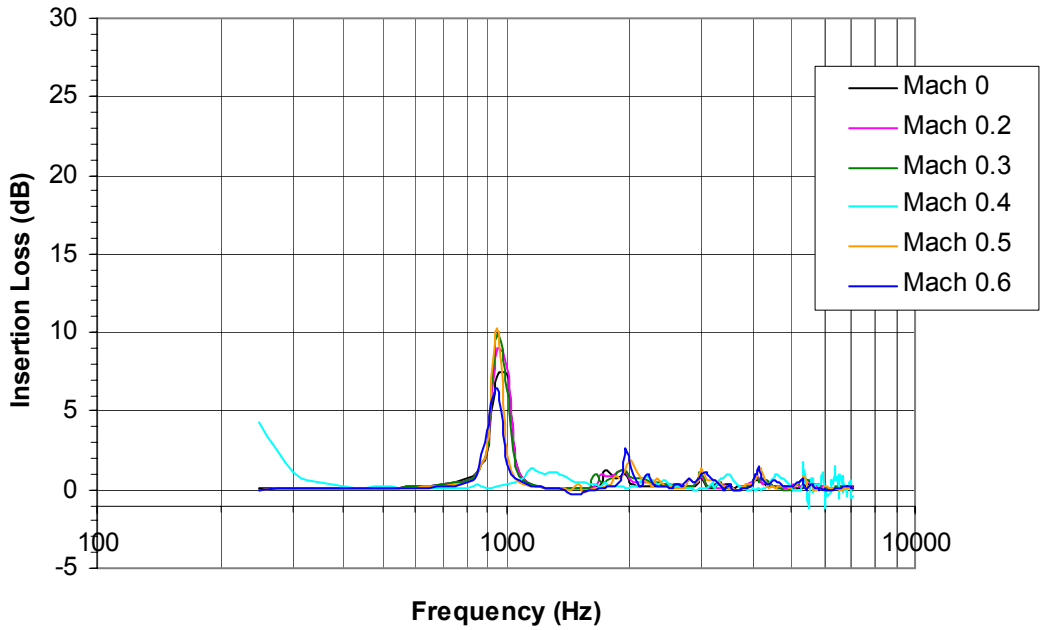

(b)

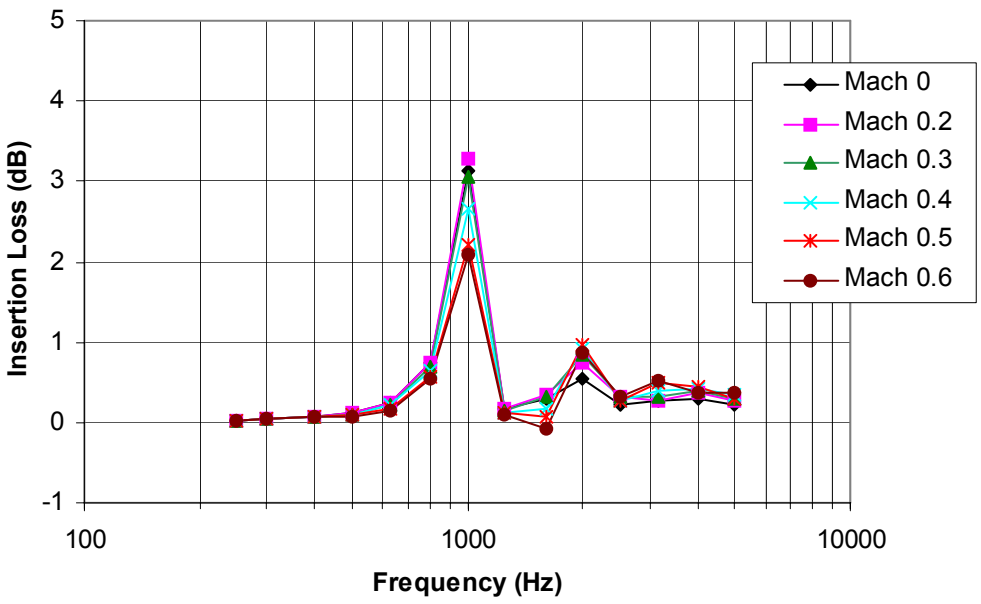

Figure 3.40: Predicted insertion loss for hard wall with HQ-configuration 1: (a) narrow (b) 1/3 octave frequency bands. (Screen Property: 12 % POA, HQ-tube properties: cross sectional area of 1.629 in^2, tube length of 5.5 in).

The results of the predictions for the perforate liner with HQ tubes and the DynaRohr liner with HQ tubes are plotted in figure 3.41 and 3.42 for both narrow and 1/3 octave bands. As in the experimental results, the predicted result for the DynaRohr liner with HQ tubes shows better insertion loss than the results for the perforate liner with HQ tubes. However, the model predicts again better attenuation than those shown by the experiments (see fig 3.19 and 3.20). The results for the perforate liner with HQ tubes at M=0 show power increases at some frequencies. These results are unexpected and are attributed to numerical errors in the solution of the mode eigenproperties.

(a)

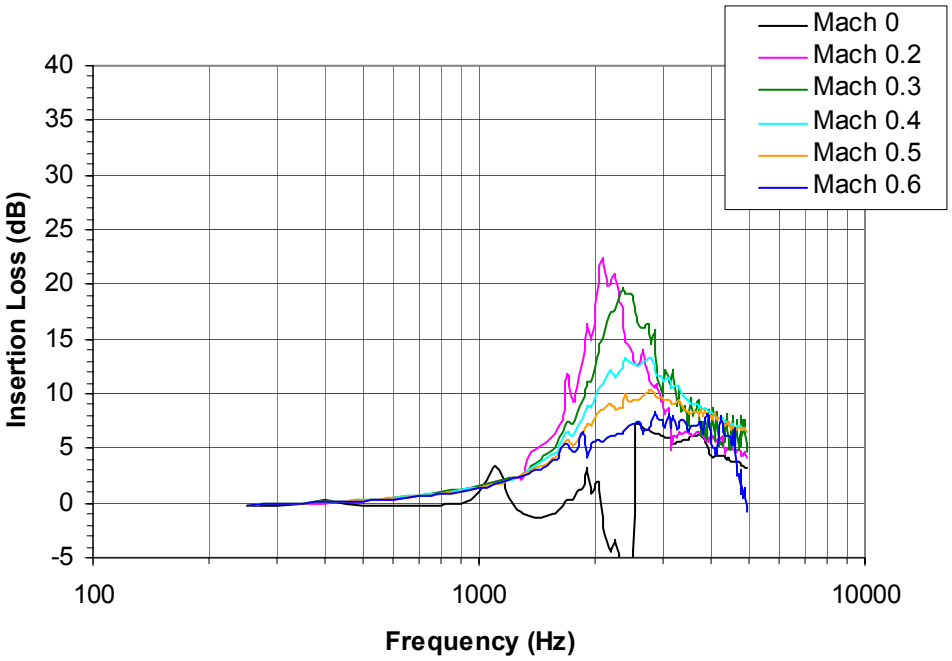

(b)

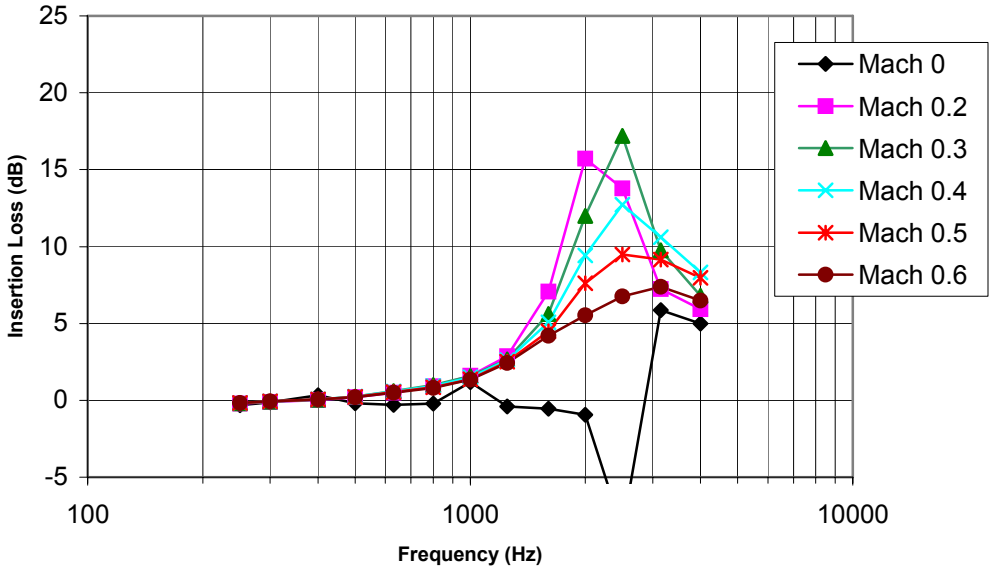

Figure3.41: Predicted insertion loss for perforate liner with HQ-configuration 15: (a) narrow (b) 1/3 octave frequency bands. (HQ-tube properties: cross sectional area of 1.629 in^2, tube length of 5.5 in).

(a)

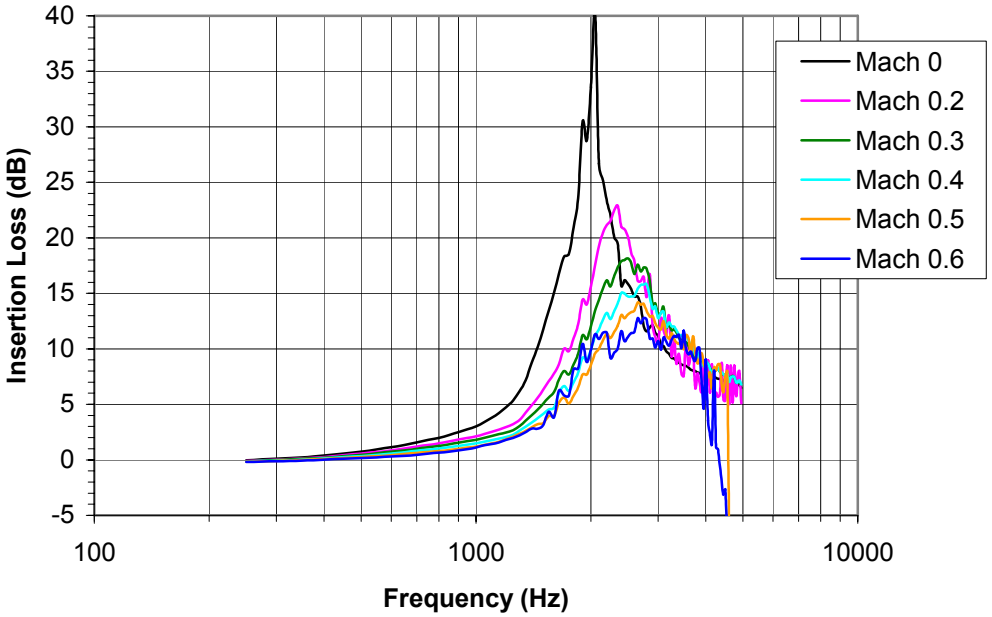

(b)

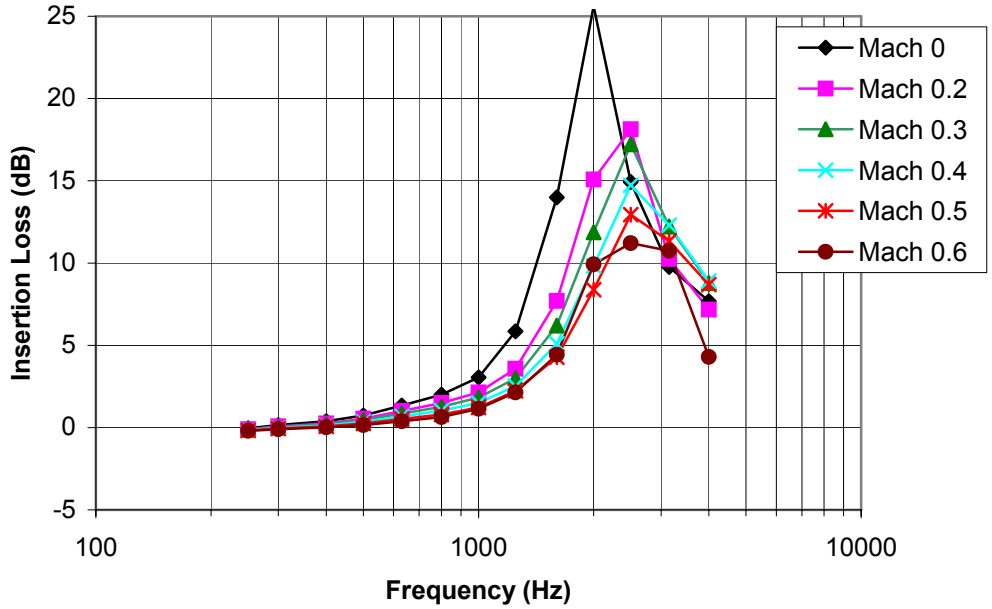

Figure 3.42: Predicted insertion loss for DynaRohr liner with HQ-configuration 19: (a) narrow (b) 1/3 octave frequency bands. (HQ-tube properties: cross sectional area of 1.629 in^2, tube length of 5.5 in).

3.4.2 Numerical and Experimental Comparisons

Comparisons of the numerical and experimental results are presented here for typical cases on 1/3 octave bands and overall insertion losses. The comparisons for the perforate and DynaRohr liners for all Mach numbers are plotted in figures 3.43 and 3.44, respectively. The 1/3 octave band shows reasonable good agreement between predictions and measurements. For both liners, there are two main differences between numerical and experimental results. The numerical results predict better performance than the experiments and the band of optimum attenuation is 2500 Hz for the analysis as compared to the 2000 Hz band shown in the experiments.

Comparison of the overall insertion losses shows again reasonable agreement between the analysis and experiments, in particular for the DynaRohr liner with difference within ± 0.5 dB (see figure 3.44c).

(a)

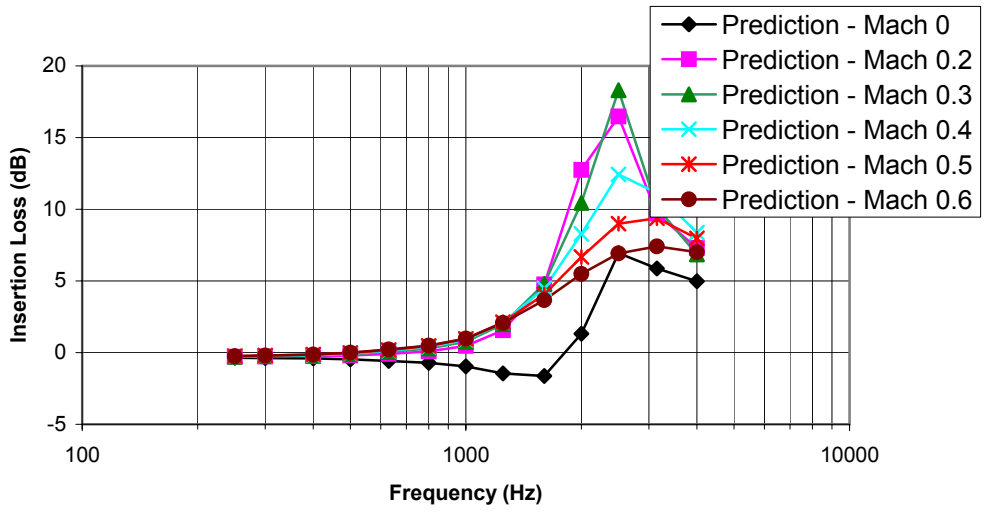

(b)

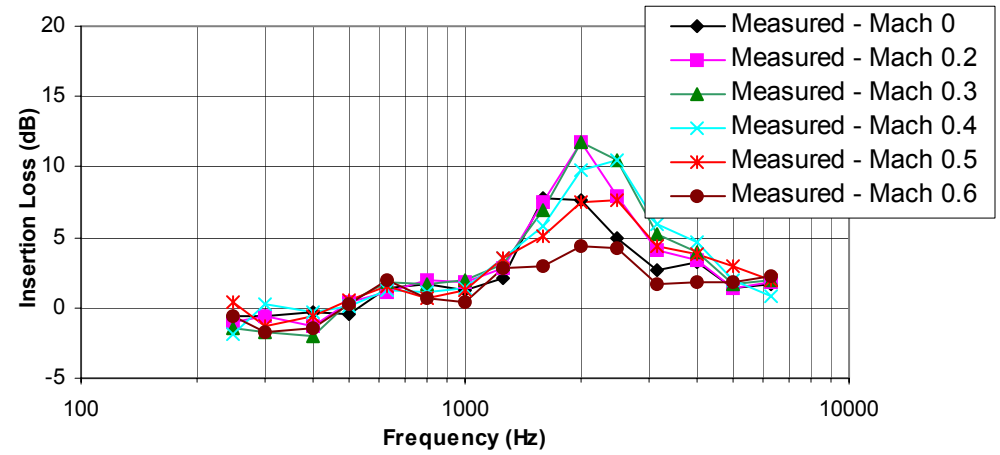

(c)

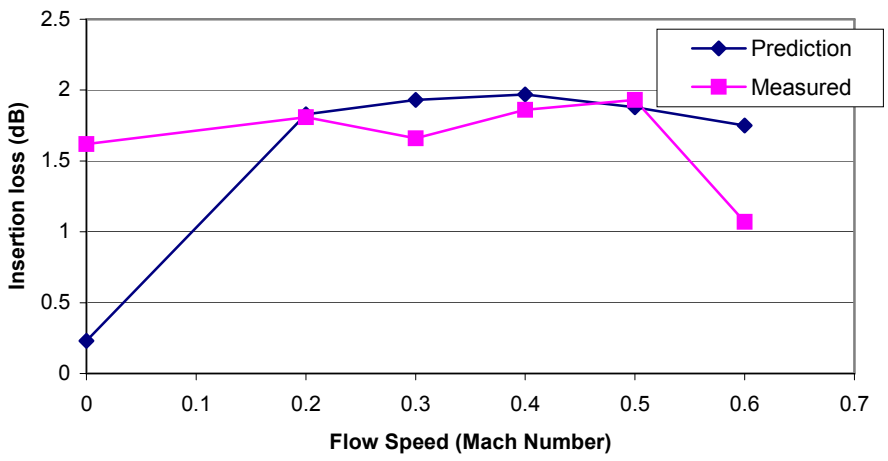

Figure 3.43: Insertion loss for perforate liner-configuration 13
(a) prediction (b) measurement (c) overall insertion loss

(a)

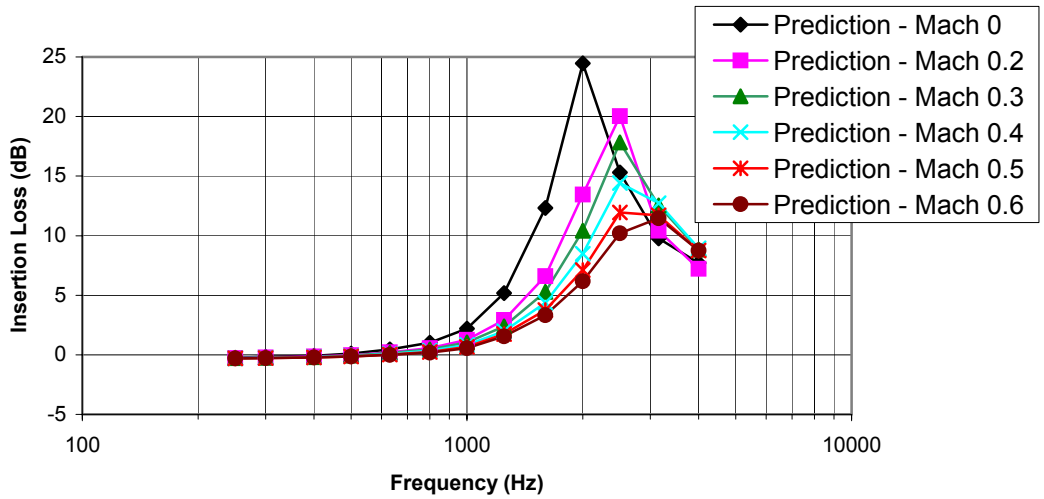

(b)

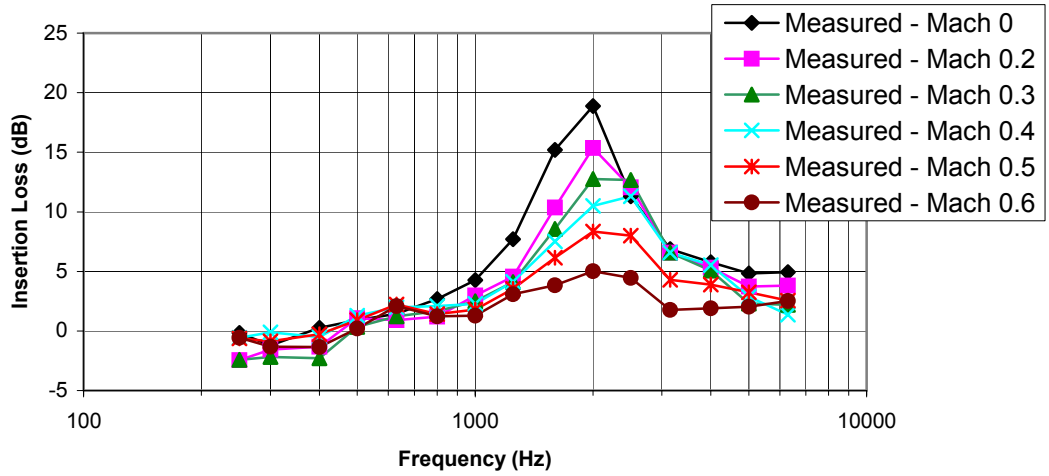

(c)

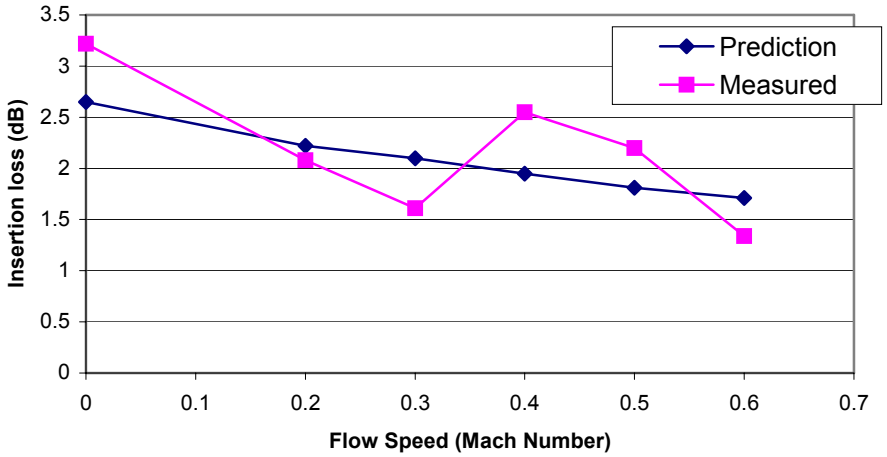

Figure 3.44: Insertion loss for DynaRohr liner-configuration 14

(a) prediction (b) measurement (c) overall insertion loss

The typical results of prediction and measurement for HQ tube with hard walled duct for all Mach numbers are plotted in figures 3.45 and 3.46. The comparisons for the configurations that have a HQ tube length of 0.1397 m (5.5 in), a cross section area of 0.00105 m^2 (1.629 in^2), and 28% and 12% POA perforate screens were carried out. The results in the figures show poor agreement between predictions and measurements. The only trend predicted by both the model and experiment is the good attenuation of the HQ-tubes at the 1000 and 2000 Hz bands. That is, maximum attenuations are found at the first two HQ-waveguide resonance frequencies near 1000 and 2000 Hz. In general, the measured results show better attenuations than the predictions at the second HQ-tube resonance frequency, as shown in figures 3.45 and 3.46 (a) and (b).

The comparisons for the overall insertion loss show again poor agreement for both cases as shown in figures 3.45 and 3.46 (c). The measured overall insertion loss is reduced dramatically for $M \geq 0.5$, which is a trend not predicted by the model. It is possible that there are other physical noise mechanisms taken place not accounted for in the model.

(a)

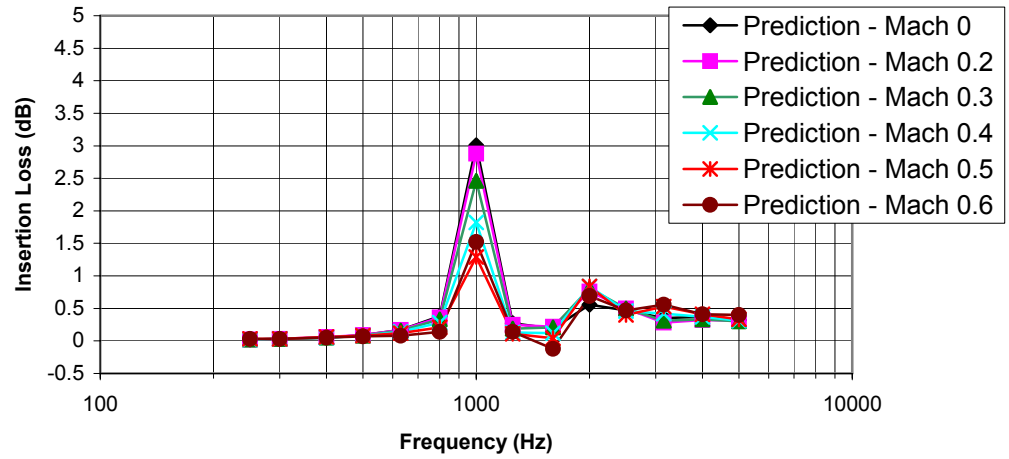

(b)

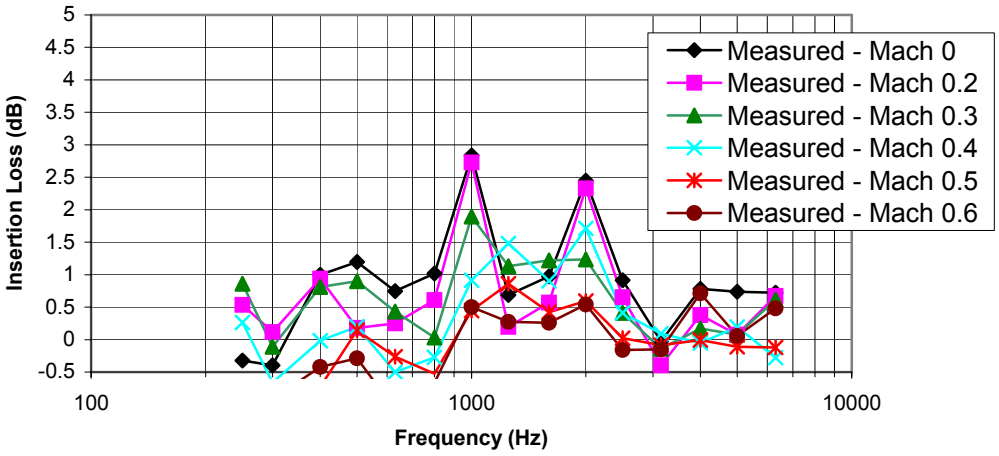

(c)

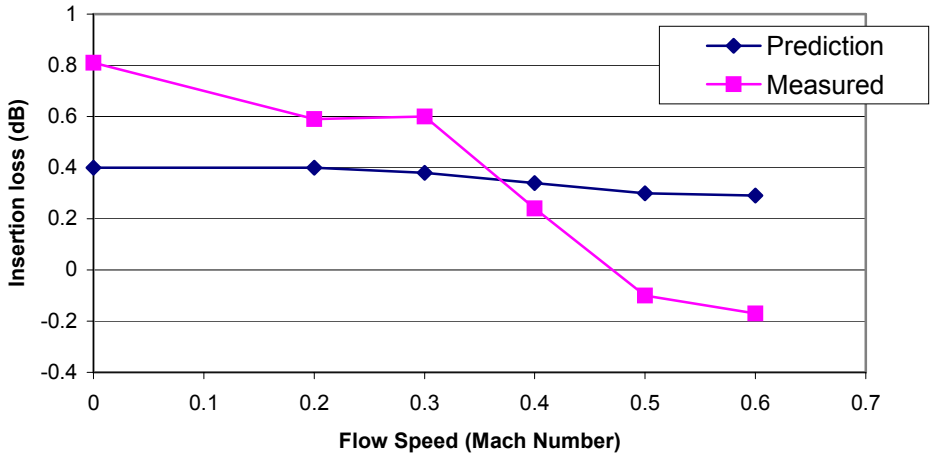

Figure 3.45: Insertion loss for hard wall with HQ-configuration 9: (a) prediction (b) measurement (c) overall insertion loss (28% POA screen, cross sectional area of 1.629 in^2, tube length of 5.5 in)

(a)

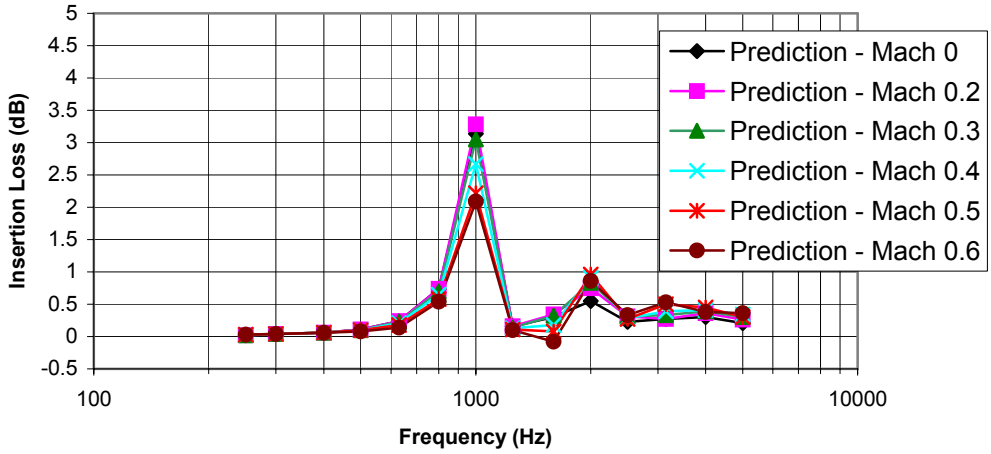

(b)

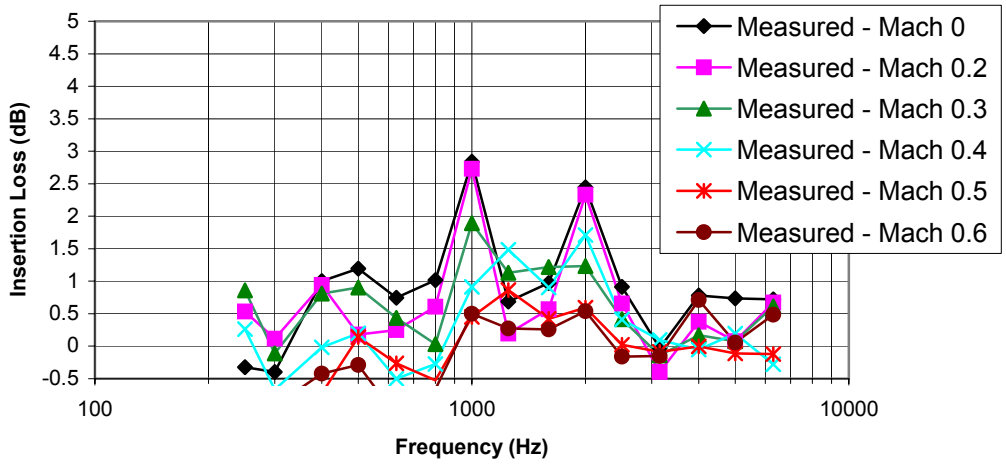

(c)

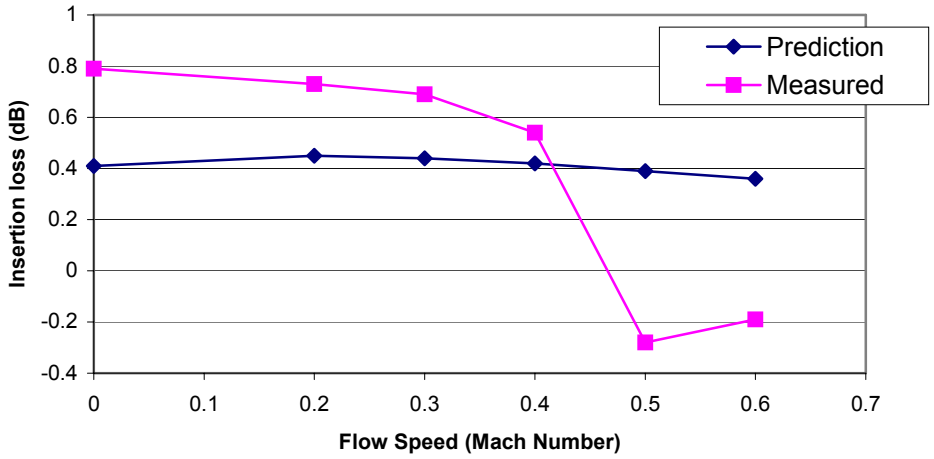

Figure 3.46: Insertion loss for hard wall with HQ-configuration 1: (a) prediction (b) measurement (c) insertion loss (12% POA screen, cross sectional area of 1.629 in^2, tube length of 5.5 in)

The comparison of the predicted and measured results for perforate and DynaRohr liners with two HQ tubes for all Mach numbers are plotted in figures 3.47 and 3.48. The configurations compared have a tube length of 0.1397 m (5.5 in) and a cross section area of 0.00105 m^2 (1.629 in^2). The 1/3 octave band results show good agreement between prediction and measurement, except for M=0 and 0.6, as shown in figures 3.47 and 3.48 (a) and (b). The overall insertion losses of both cases are also in good agreement between prediction and measurement, particularly, in mid range of flow speeds as shown in figures 3.47 and 3.48 (c). For the flow speed range between 0.2 and 0.5, the predicted overall attenuations are well within $\pm$ 0.5 dB from the experimental values.

(a)

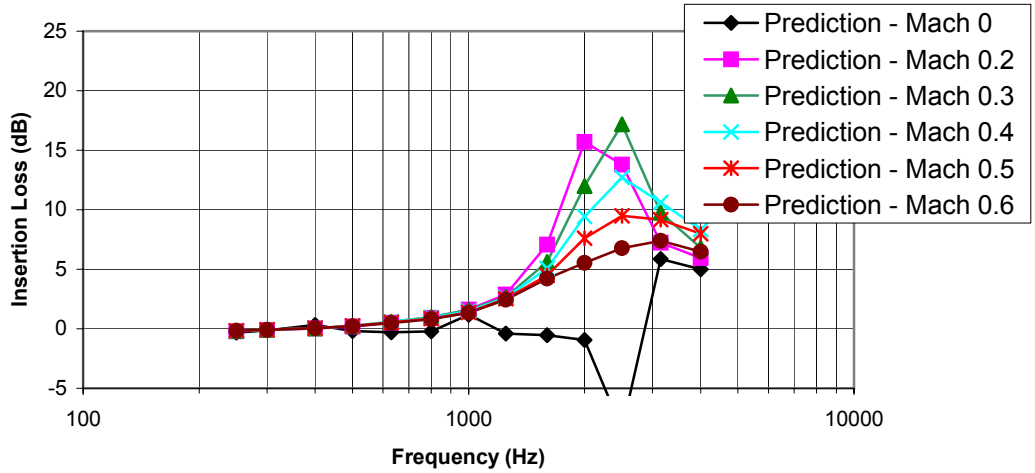

(b)

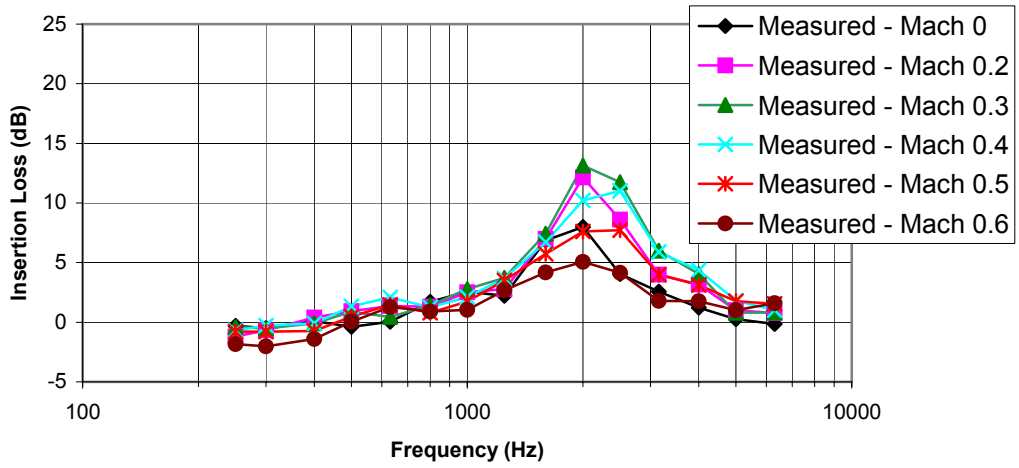

(c)

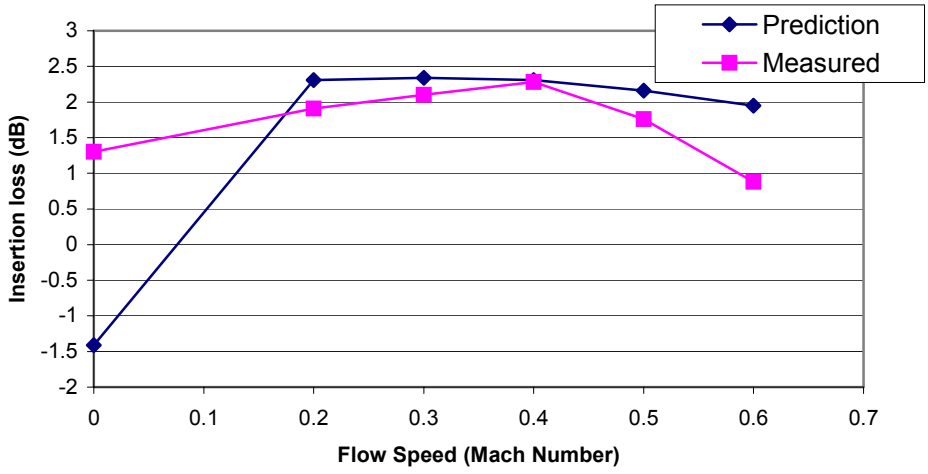

Figure 3.47: Insertion loss for perforate liner with HQ-configuration 15: (a) prediction (b) measurement (c) insertion loss (cross sectional area of 1.629 in^2, tube length of 5.5 in with core)

(a)

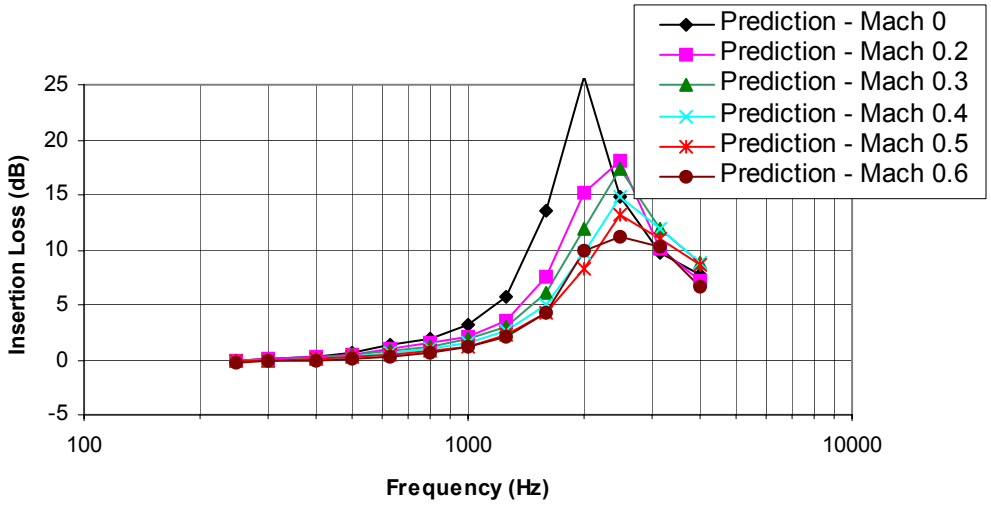

(b)

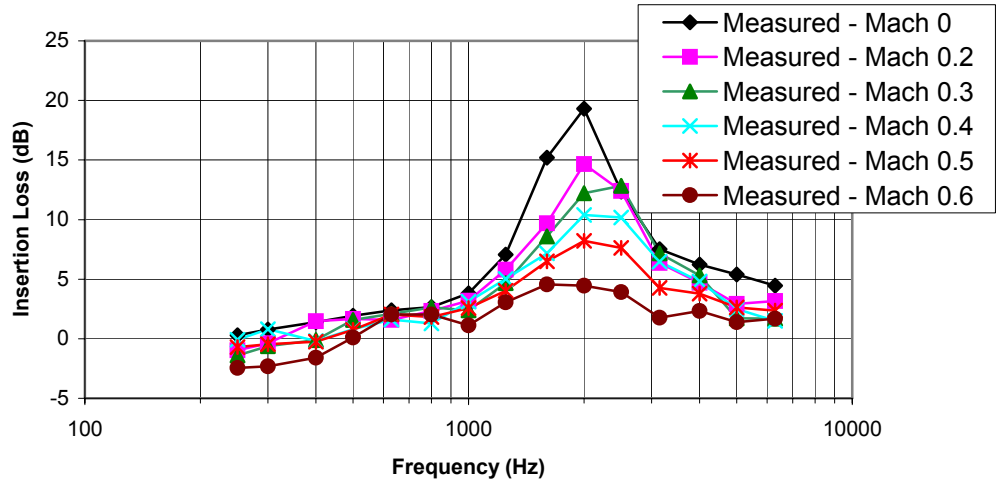

(c)

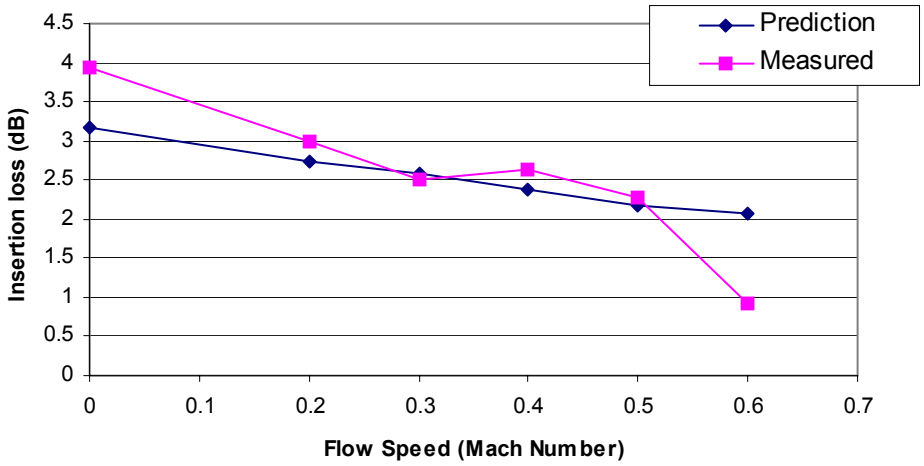

Figure 3.48: Insertion loss for DynaRohr liner with HQ-configuration19: (a) prediction (b) measurement (c) insertion loss (cross sectional area of 1.629 in^2, tube length of 5.5 in with core)

Finally, comparisons between the predicted and measured overall insertion losses for all cases are presented in figures 3.49 through 3.53. The predicted results are indicated using a black symbol.

The predicted results show reasonable agreement with measured results at $M \leq 0.5$. However, at M=0.6 most of the predicted results show poor agreement with the measurements. The measured results for liner-HQ configurations show better attenuation than the predicted values at low flow speeds (M=0.2, 0.3 and 0.4), but vice versa at high flow speeds (M > 0.4). In general, the predicted results are less sensitive to flow speed for all configurations. That is, the measured overall insertion losses decrease dramatically at M > 0.3. Finally, the overall data show the liner-HQ systems have better attenuation than the liner only systems for both predictions and measurements.

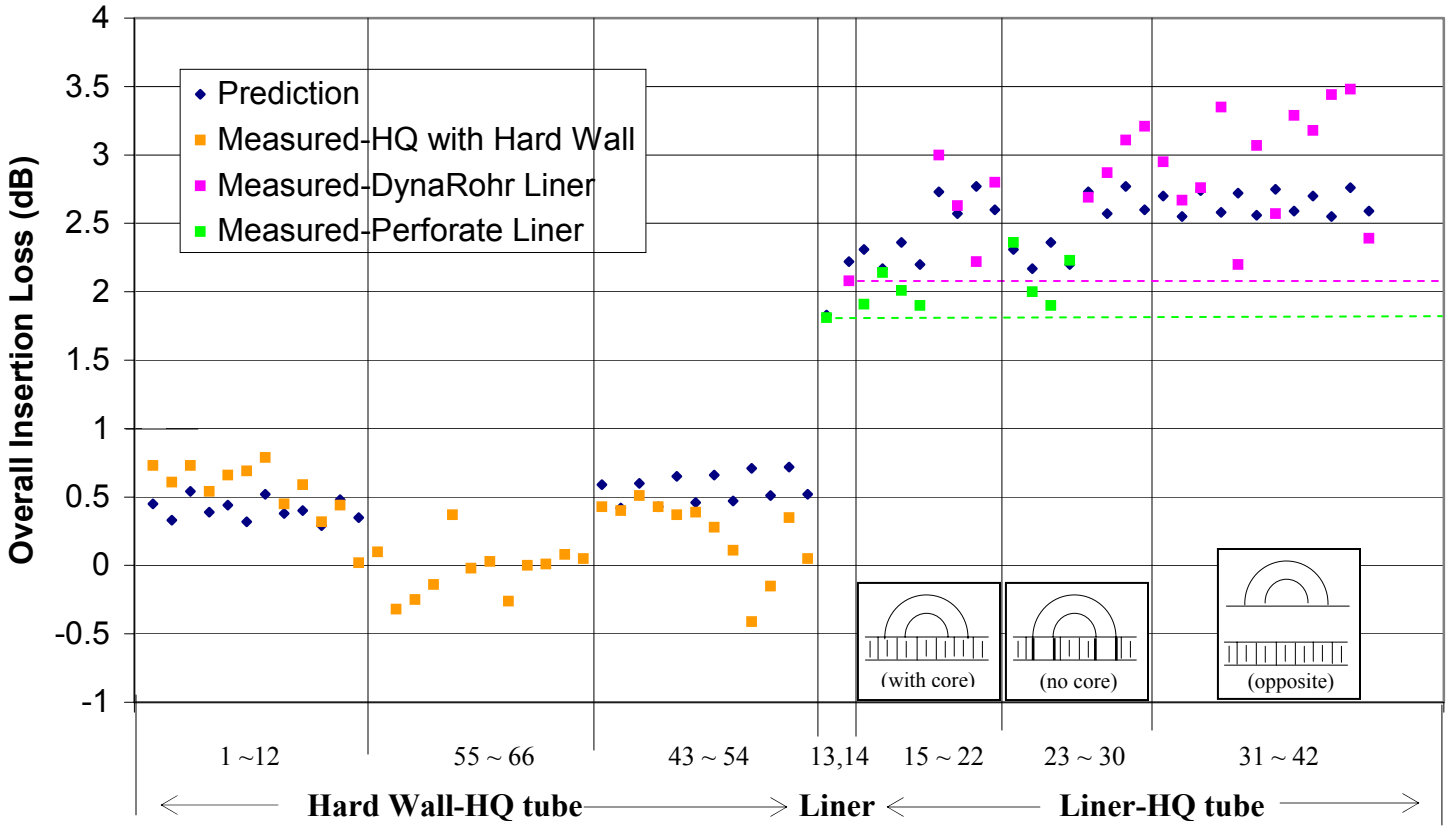

Figure 3.49: Comparison of overall insertion loss of all configurations at Mach 0.2

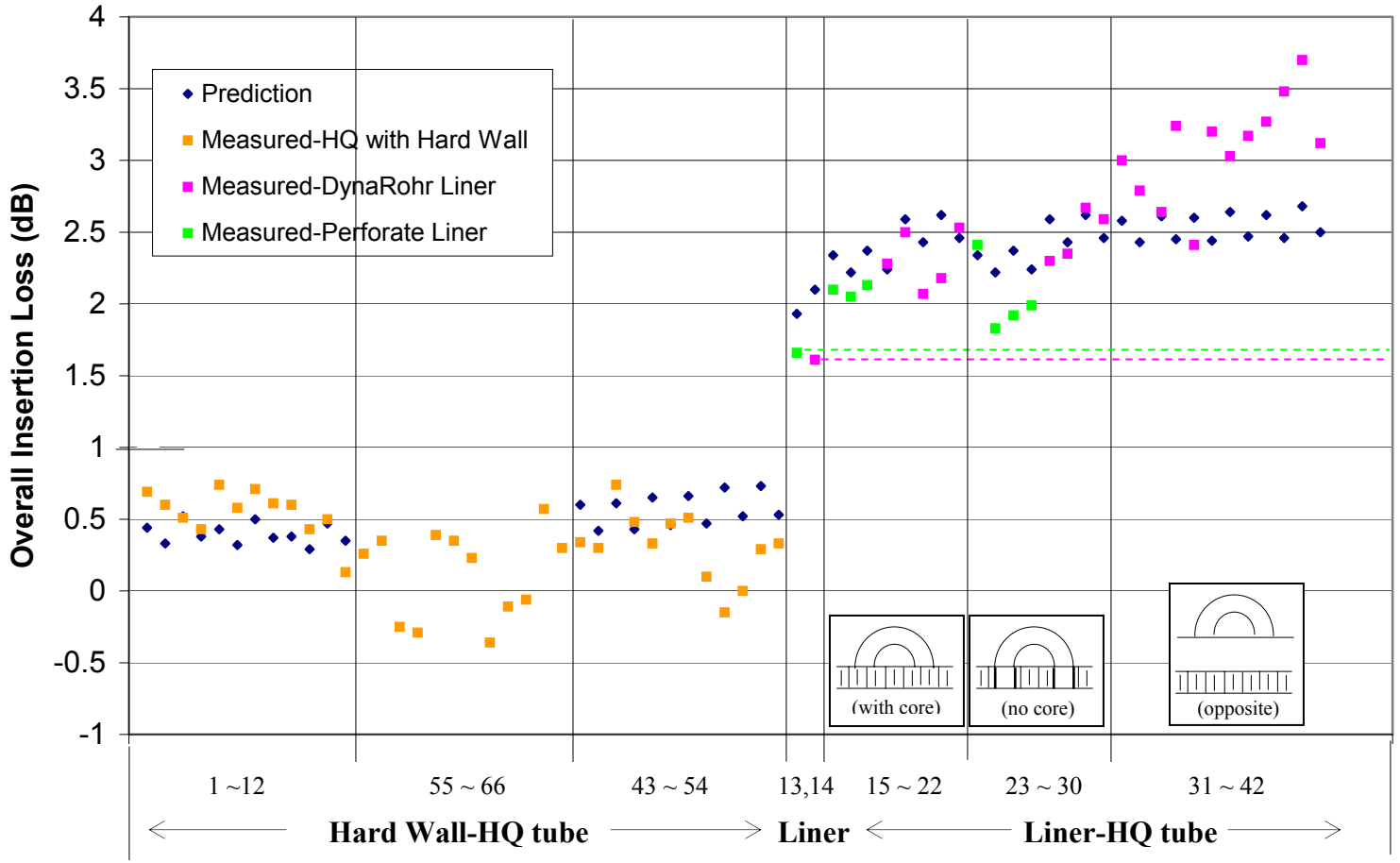

Figure 3.50: Comparison of overall insertion loss of all configurations at Mach 0.3

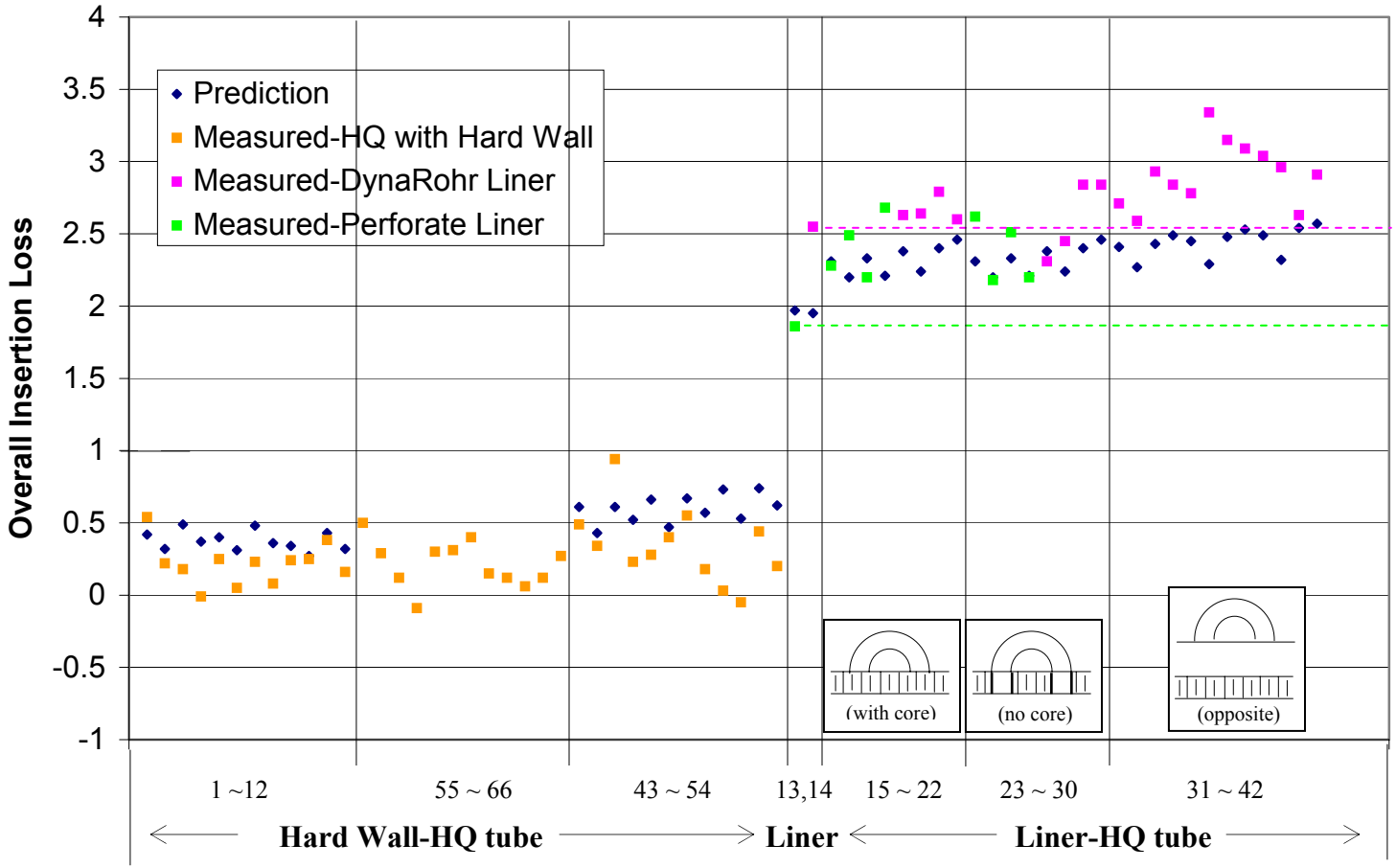

Figure 3.51: Comparison of overall insertion loss of all configurations at Mach 0.4

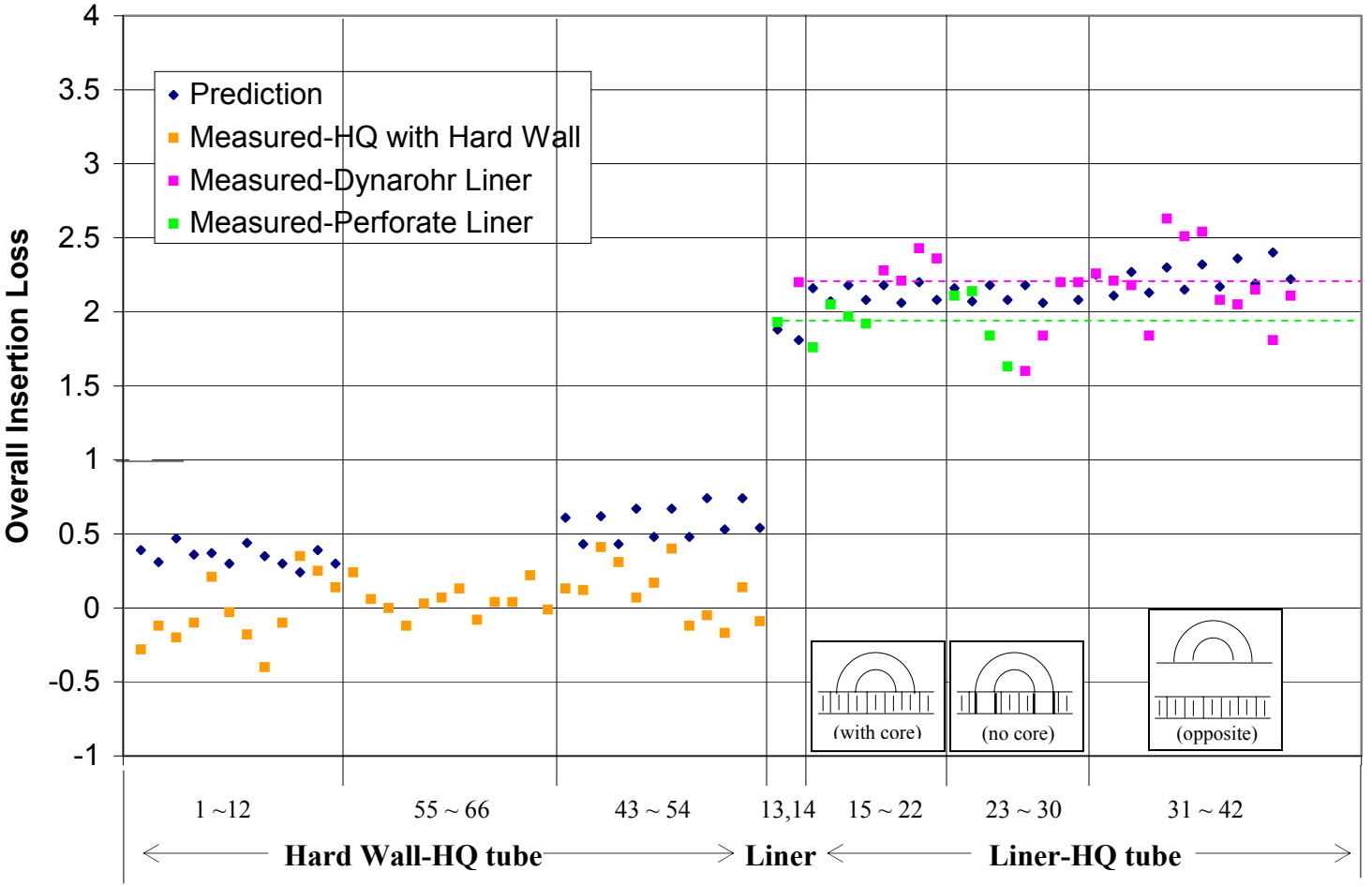

Figure 3.52: Comparison of overall insertion loss of all configurations at Mach 0.5

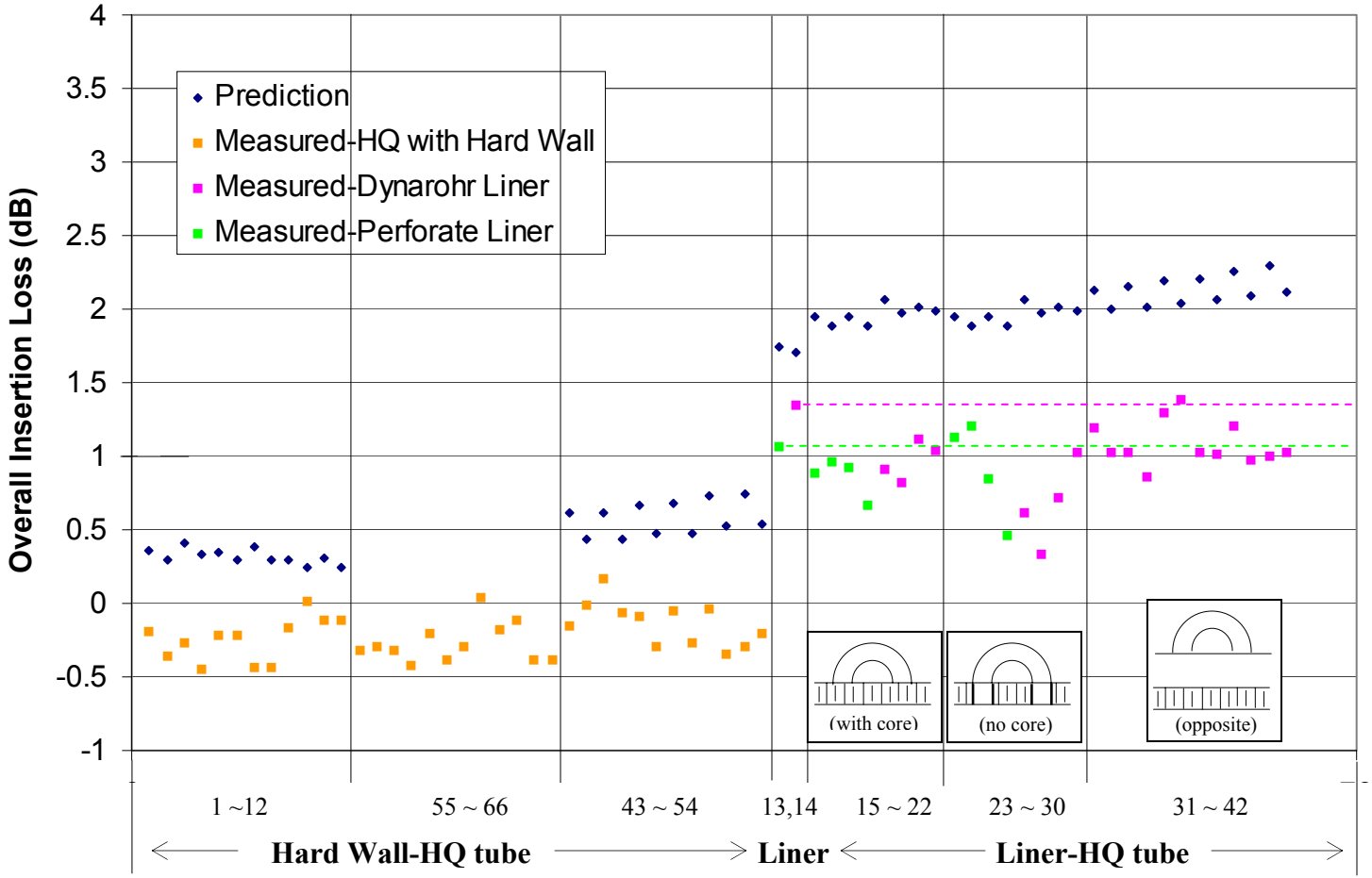

Figure 3.53: Comparison of overall insertion loss of all configurations at Mach 0.6

In the previous section, the numerical and experimental results considered the case of a only two HQ-tube place in parallel. The two tubes took only a small percentage (~ 5%) of the available liner surface area and for many configurations resulted in improved attenuation over the one provided by the liner alone. However, in practice the HQ-tubes will probably take even more percentage area of the liner. Thus, it is important to have an estimate of the performance of the liner-HQ system for higher number of HQ-tubes implemented. To this end, predictions for increase number of tubes combined with the DynaRohr liner are presented in figure 3.54. In this figure, an array implies two parallel HQ-tubes. Thus, an array corresponds to the cases previously investigated. The results shows the performance of the liner-HQ system to be directly related to the number of HQ-tubes used.

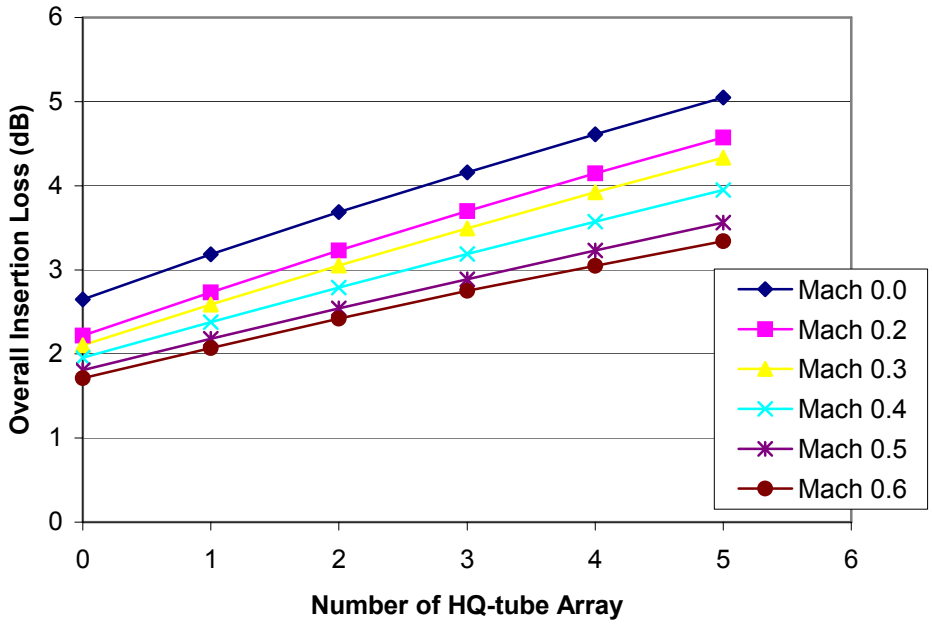

Figure 3.54: Overall insertion loss by increasing the number of HQ tube array, i.e. two parallel tubes per array.

Chapter 4. Conclusions and Recommendations

4.1 Conclusions

In this thesis, an innovative implementation of the Herschel-Quincke tubes concept combined with a passive liner for the reduction of noise was investigated using a lined rectangular duct. One of the main objectives of this work was to develop a model of the HQ-tubes on a lined rectangular duct with flow. This model allows the prediction of the sound power attenuation of liner-HQ in the presence of higher-order modes in a uniform flow. The analytical technique involved the modeling the HQ tube-duct interfaces as finite piston sources that couple the acoustic field inside the duct with the acoustic field within the HQ tubes. The performance of the liner-HQ tube systems was numerically evaluated by computing the acoustic power reduction, referred in this thesis as insertion loss.

Another objective of this research was to validate the accuracy of the model. To this end, the results predicted by the model were compared to the experimental data taken on different configurations of the lined-HQ systems.

The test configurations investigated included liner, HQ tubes on a hard walled duct, and liner-HQ tube systems. Two type of single-degree-of-freedom liners commonly used in treatment of turbofan engines were tested; i.e. a perforate liner and a linear liner (Dynarohr). Then, HQ-tubes mounted on a hard walled duct were tested. In these

configurations, several type of tube opening screens were tested that included perforate plate with different POAs and wire mesh screens with different resistance values. Finally, the configurations of the lined wall with HQ tubes were tested to investigate the performance of the HQ tubes in conjunction with liners. In the liner-HQ configurations, the HQ-tube was mounted on the backside of the liner, which is a potential practical implementation of this concept. Since the liner core forms part of the HQ-waveguide, tests were performed to investigate its effect, i.e. in some configurations the liner core was removed. Finally, test configurations where the HQ-tubes were placed on the opposite side of the lined walled (DynaRohr liner) were also tested.

For the liner alone tests, the DynaRohr liner showed slightly better attenuation than the perforate liner at most flow speeds. The results of the HQ-tubes on a hard walled duct showed that the 12% POA and 45.88 rayls wire mesh face screens showed slightly better overall sound attenuation than the 28% POA and 15.97 rayls wire mesh, respectively. These results indicate that face screen with high resistance at the tube-duct interfaces yields better sound attenuations as compared to lower resistance ones. This conclusions is opposite to the general belief that the low resistance was preferred to allow for a highly resonant tube. Finally, the insertion loss produced by the HQ-tubes became insignificant as flow speed was increased, in particular for M=0.6.

The results of the liner-HQ configurations showed that in general the DynaRohr liner-HQ outperformed the perforate liner-HQ systems. This conclusion is in part due to the fact that the DynaRohr produced better attenuation than the perforated one.

By comparing the attenuation of the liner-HQ to the liner alone system, the impact of the HQ-tubes can be assessed. The overall sound attenuation results show that the HQ-tubes significantly improves the performance of the liner alone in particular at low flow speeds, i.e. $M \leq 0.4$, for both liners. In a number of configurations, the increase in noise reduction due to the tubes is remarkable in view of the fact they take only 5% of the liner area. However, the performance degrades as the flow speed increases. In particular, the effect of the HQ-tubes is detrimental (decreases liner performance) at the high flow speeds, i.e. $M \geq 0.5$.

The results also show no clear advantages by removing the part of the liner core that forms part of the HQ-tube. The overall insertion losses basically show the same

attenuations with and without the core for both liners. On the other hand, it is clear that placing the HQ-tubes on the opposite wall to the liner (rather than on the back of the liner) results in much better attenuation.

A model for the HQ-tubes integrated with liners was developed. The numerical results were compared to the experimental data to validate this model. There are several factors that do not allow a direct comparison between the numerical and experimental results. The model requires knowing the complex amplitudes of the modes present in the duct. This information was not available experimentally and some assumptions were made to obtain this required data. The model predicts the performance by computing the sound power upstream and downstream of the test section ignoring reflection effects, i.e. infinity duct theory. On the other hand, the noise reduction in the experiments is indirectly estimated from monitoring the average sound levels in the upstream and downstream chambers. Even though the above differences in the numerical and experimental approaches, the results indicated good agreement between the numerical predictions and the experimental results, and therefore validated the numerical modeling technique. However, the agreement degrades dramatically at the high flow speed of M=0.6, which needs to be investigated.

4.2 Recommendations for Future Research

Based on the results presented in this work, suggestions for future work are as follows:

- In this research only two HQ tubes were mounted on the rectangular duct taking only 5% of the available area. In practice, most probably the tubes will take a higher percentage of this area. Thus, future experiments should include increasing number of HQ tubes in the systems.

- The two liner used in the experiments were representative of typical treatment applied to turbofan engines. The HQ-tubes were then added to the liners. It would be useful to investigate what combination of liner and HQ-tube parameters would yield optimum sound attenuation for the combined system. In other words, it is important to determine how the HQ-tubes impact the current design practices of liners.

- It is very important to investigate the reasons for the increase in noise resulting from the HQ-tube implementation. To this end, it would be useful to measure the modal amplitudes in the duct rather than average pressure in the chambers.

- Multiple testing of the configurations is needed to be able to perform an error analysis of the data. This will provide confidence limit or error bounds for the measurements.

Bibliography

[1 Raphael F. Hallez, “Investigation of the Herschel-Quincke Tube Concept as a Noise control Device for Turbofan Engines,” M.S. thesis, Virginia Polytechnic Institute and State University, 5-6, January (2001).

[2] Kantola, R.A., and Gliebe, P.R., “Effects of Vane/Blade Ratio and Spacing on Fan Noise,” AIAA Paper no. 81-2033, Oct. (1981).

[3] Dittmar, J. H. and Woodward, R. P., “An Evaluation of some Alternative Approaches for Reducing Fan Tone Noise,” NASA Technical Memorandum 105356, February (1992).

[4] Mangiarotty, R. A., “The Reduction of Aircraft Engine Fan-Compressor Noise Using Acoustic Linings,” Journal of Sound and Vibration, 18 (4), 565-576, (1971).

[5] Walker, B. E., and Hersh, A. S., "Application of active Helmholz resonator technology to plane wave duct acoustics," CEAS/AIAA-95-163, presented at the 1st Joint CEAS/AIAA Aeroacoustic Conference, Munich, Germany, vol. 2, June 1995, pp. 1115-1120.

[6] Smith, J. P. and Burdisso, R. A., “Active Control of Inlet Noise From a Turbofan Engine Using Inlet Wavenumber Sensors,” CEAS/AIAA-99-1808, presented at the 5th CEAS/AIAA Aeroacoustics Conference, Seattle, WA, May 1999.

[7] Burdisso, R.A., Fuller, C.R., Smith, J.P., "Experiments on the Active Control of a Turbofan Inlet Noise using Compact, Lightweight Inlet Control and Error Transducers," CEAS/AIAA-95-028, 1995, pp. 177-185.

[8] Smith, J.P., Burdisso, R.A., and Fuller, C.R., "Experiments on the Active Control of Inlet Noise From Turbofan Jet Engine Using Multiple Circumferential Control Arrays," AIAA 96-1792, 1996.

[9] Joseph, P., Nelson, P.A., and Fisher, M.J., "Active Control of Turbofan Radiation Using an In-Duct Error Sensor Array," *Proceedings of Active 97,* pp. 273-286, August 21-23, Budapest, Hungary 1997.

[10] Kraft, R. E., Janardan, B. A., Kontos, G. C., and Gliebe, P. R., "Active Control of Fan Noise – Feasibility Study. Volume 1: Flyover System Noise Studies," NASA CR 195392, October, 1994.

[11] Kraft, R. E., Janardan, B. A., Gliebe, P. R., and Kontos, G. C., "Active Control of Fan Noise – Feasibility Study. Volume 4: Flyover System Noise Studies, Part 2," NASA CR 198512, September 1996.

[12] Herschel, J. F. W. ,"On the absorption of light by coloured media, viewed in connexion with the undulatory theory," *Philosophical Magazine and Journal of Science*, **3**, 401-412, (1833).

[13] Quincke, G., "Ueber interferenzapparate fur schallwellen," *Annalen der Physik und Chemie*, **128**, 177-192, (1866)

[14] Stewart, G. W., "The theory of the Herschel-Quincke tube," *Physical Review*, **31**, 696-698, (1928)

[15] Selamet, A., Dickey, N. S., and Novak, J. M., "The Hershcel-Quincke tube: a theoretical, computational, and experimental investigation," *J. Acoust. Soc. Am.*, **96** (5), 3177-3185, (1994)

[16] Zhichi, Z., Song, L. , Rui, T., Rui, G., Genhua, D., and Peizi, L., “Application of Quincke tubes to flow ducts as a sound attenuation device,” Noise Control Eng. J., 46(6), 245-255, Nov-Dec (1998)

[17] Brady, L. A., Burdisso, R. A., and Smith, J. P., "Investigation of the Herschel-Quincke Tube Concept for the Suppression of Higher-order Modes in a Duct," Proceedings of Internoise 99, pp. 545-550, Fort Lauderdale Florida, December (1999).

[18] Burdisso, R.A. and Smith, J.P., “Control of Inlet Noise from Turbofan Engines Using Herschel-Quincke Waveguides,” 6th AIAA/CEAS 2000-1994, (2000).

[19] Walter Eversman and M. Dean Nelsen, “Design of Acoustic Linings for Ducts with Flow,” Journal of Aircraft, Vol. 9, No.8, August, 1972, PP 548-550.

[20] Morse, P. M. and Ingard, K. U., “Theoretical Acoustics,” Princeton University

[21] Goldstein, Marvin E., “Aeroacoustics”, McGraw-Hill, 1976

APPENDIX A

In appendix, the eigenvalue problem was solved for the rectangular hard walled and lined duct, respectively, in section A.1. The Green's function is developed in section A.2. The sound field generated by a finite piston source radiation is derived for each condition in section A.3. The expression for average pressure over sources due to disturbance is derived in section A.4. Modeling of HQ tubes is presented in section A.5. Finally, the expression for transmitted acoustic power is derived in sections A.6.

A.1. The Eigenvalue Problem

The acoustic wave equation in a moving media is given as [20].

$$\nabla^2 p = \frac{1}{c^2}\left(\frac{\partial}{\partial t} + \vec{V}\cdot\nabla\right)^2 p \tag{A.1.1}$$

where $\nabla^2(\ )$ is the Laplacian operator, c is the speed of sound, $p(x,y,z)$ is the acoustic pressure, and $\vec{V}$ is the flow velocity field vector.

The equilibrium equation is given as

$$-\frac{\partial p}{\partial \ell} = \rho\left(\frac{\partial}{\partial t} + \vec{V}\cdot\nabla\right) v_\ell \qquad \ell = x, y, z \tag{A.1.2}$$

where v_ℓ is the acoustic particle velocity in the ℓ-direction.

Assuming a uniform flow field in the positive x-direction, i.e. $\vec{V} = cM\,\vec{i}$ where M is the Mach flow number ($M=V/c$), and considering harmonic motion, i.e. $e^{i\omega t}$ time dependence, equations (A.1.1) and (A.1.2) in cartesian coordinates become

$$\frac{\partial^2 p}{\partial x^2} + \frac{\partial^2 p}{\partial y^2} + \frac{\partial^2 p}{\partial z^2} = -k_o^2 p + 2ik_o M\frac{\partial p}{\partial x} + M^2\frac{\partial^2 p}{\partial x^2} \tag{A.1.3}$$

and

$$-\frac{\partial p}{\partial \ell} = i\omega\rho v_\ell + \rho c M \frac{\partial v_\ell}{\partial x} \qquad \ell = x, y, z \tag{A.1.4}$$

respectively, k_o is the free-field acoustic wavenumber,i.e. , $k_o = \omega / c$, and $i = \sqrt{-1}$.

Using the separation of variables, the solution to the partial differential equation is assumed to have the form

$$p(x, y, z, t) = \Phi(y, z)\, e^{-ik_x x} e^{i\omega t} \tag{A.1.5}$$

The time function $e^{i\omega t}$ is omitted for the rest of the derivations.

Replacing (A.1.5) into (A.1.3) gives

$$-k_x^2\Phi + \frac{\partial^2\Phi}{\partial y^2} + \frac{\partial^2\Phi}{\partial z^2} = -k_o^2\Phi + 2k_o k_x M\Phi - M^2 k_x^2\Phi \tag{A.1.6}$$

where the term $e^{-ik_x x}$ is canceled out.

Reordering Eq.(A.1.6) gives

$$\frac{\partial^2\Phi}{\partial y^2} + \frac{\partial^2\Phi}{\partial z^2} + \left\{k_o^2 - k_x^2\left(1 - M^2\right) - 2k_o k_x M\right\}\Phi = 0 \tag{A.1.7}$$

To find $\Phi(y, z)$, we need to satisfy Eq.(A.1.7) and the duct wall boundary conditions. The solution of this eigenvalue problem will be carried out for the hard walled and lined duct cases, respectively, in the next two subsections.

A.1.1 The Rigid Wall Duct Case

The first case will consist of a rigid-walled duct as shown in figure A.1.1. Thus, the boundary conditions are written as

$$\left.\frac{\partial p}{\partial y}\right|_{y=0} = \left.\frac{\partial p}{\partial y}\right|_{y=a} = 0 \tag{A.1.8a}$$

$$\left.\frac{\partial p}{\partial z}\right|_{z=0} = \left.\frac{\partial p}{\partial z}\right|_{z=b} = 0 \tag{A.1.8b}$$

The solution to the equation (A.1.7) with the boundary conditions in (A.1.8a) and (A.1.8b) is now derived using separation of variables as

$$\Phi(y,z) = Y(y)Z(z) \tag{A.1.9}$$

Replacing (A.1.9) into (A.1.7) and dividing by $Y(y)Z(z)$ gives

$$\frac{1}{Y}\frac{d^2Y}{dy^2} + \frac{1}{Z}\frac{d^2Z}{dz^2} + k_{nm}^2 = 0 \tag{A.1.10}$$

where

$$k_{nm}^2 = k_o^2 - k_x^2(1-M^2) - 2k_o k_x M \tag{A.1.11}$$

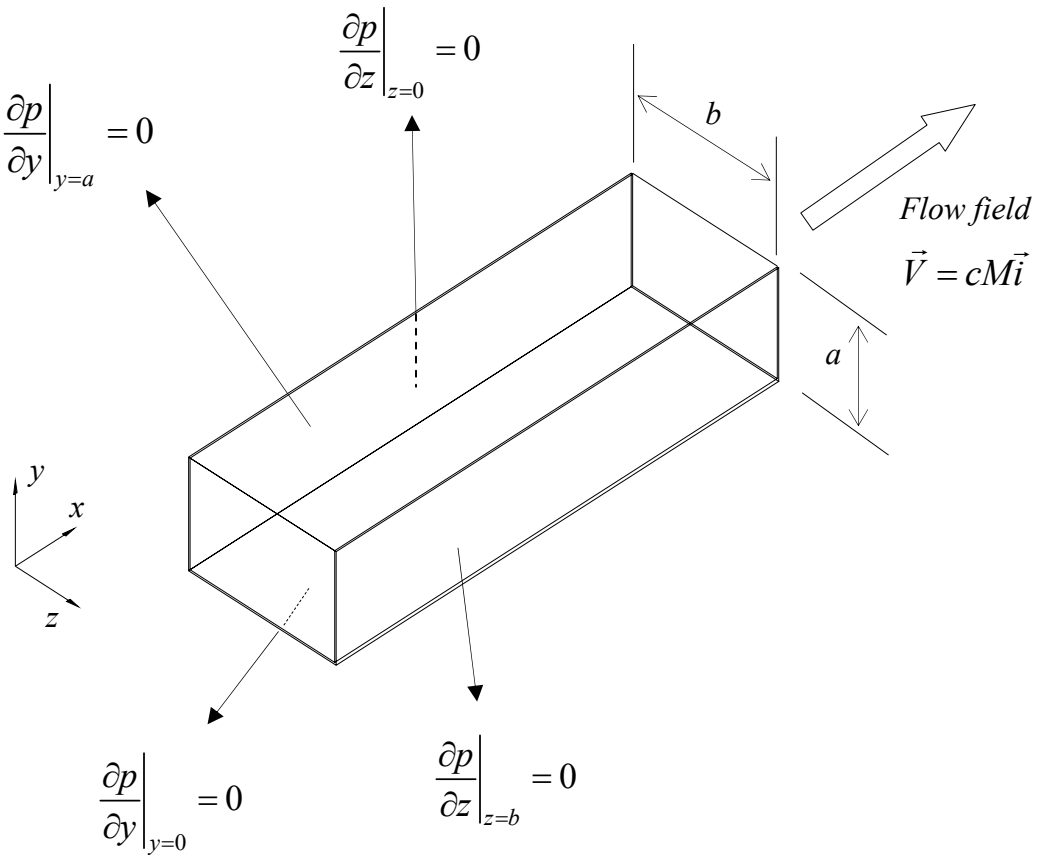

Figure A.1.1: Rectangular hard wall duct

Replacing (A.1.9) into the boundary conditions in (A.1.8a-b) leads to

$$\left.\frac{dY}{dy}\right|_{y=0} = \left.\frac{dY}{dy}\right|_{y=a} = 0 \tag{A.1.12}$$

$$\left.\frac{dZ}{dz}\right|_{z=0} = \left.\frac{dZ}{dz}\right|_{z=b} = 0 \tag{A.1.13}$$

The solution to (A.1.10) implies that

$$\frac{1}{Y}\frac{d^2Y}{dy^2} = -k_y^2 \tag{A.1.14}$$

and

$$\frac{1}{Z}\frac{d^2Z}{dz^2} = -k_z^2 \tag{A.1.15}$$

where k_y^2 and k_z^2 are constants. Thus,

$$k_{nm}^2 = k_y^2 + k_z^2 = k_o^2 - k_x^2\left(1 - M^2\right) - 2k_o k_2 M \tag{A.1.16}$$

Thus, the differential equation in (A.1.14) with the boundary conditions in (A.1.12) results in the solution

$$Y\left(y\right) = A\cos\left(k_y y\right) \tag{A.1.17}$$

where

$$k_y = \frac{n\pi}{a} \qquad n = 0,1,2,\ldots \tag{A.1.18}$$

In the same way, the solution to (A.1.15) with boundary conditions (A.1.13) yields

$$Z(z) = B\cos(k_y z) \tag{A.1.19}$$

where

$$k_z = \frac{m\pi}{b} \qquad m = 0,1,2,\ldots \tag{A.1.20}$$

Thus, the function $\Phi(y,z)$ becomes

$$\Phi_{nm}(y,z) = A_{nm}\cos(k_y y)\cos(k_z z) \tag{A.1.21}$$

where A_{nm} is an arbitrary constant.

Using these wavenumbers, we can also solve for the wavenumber k_x using

$$k_y^2 + k_z^2 = k_o^2 - k_x^2\left(1 - M^2\right) - 2k_o\, k_x M \tag{A.1.22}$$

Equation (A.1.22) is referred as the dispersion relation, and allows us to solve for the value of the wavenumber k_x. The function $\Phi_{nm}(y,z)$ is the (*n,m*) mode that propagates as a wave with the axial wavenumber k_x and A_{nm} is the amplitude of the (*n,m*) mode. The case (*n*=0, *m*=0) represents the plane wave case. Thus, the axial wavenumber k_x is a function of "*n*" and "*m*". The (*n,m*) mode eigenvalue is given as

$$k_{nm}^2 = k_y^2 + k_z^2 = \left(\frac{n\pi}{a}\right)^2 + \left(\frac{m\pi}{b}\right)^2 \qquad n = 0, 1, 2,\ldots \quad m = 0, 1, 2,\ldots \tag{A.1.23}$$

Solving for k_x in eq. (A.1.22) yields

$$k_x = \left\{-Mk_o \pm \sqrt{k_o^2 - \left(1-M^2\right)k_{nm}^2}\right\} \;/\; \left(1-M^2\right) \tag{A.1.24}$$

Thus, there are two k_x values as

$$k_x^{(+)} = \left\{-Mk_o + \sqrt{k_o^2 - \left(1-M^2\right)k_{nm}^2}\right\} \;/\; \left(1-M^2\right) \tag{A.1.25}$$

and

$$k_x^{(-)} = \left\{-Mk_o - \sqrt{k_o^2 - \left(1-M^2\right)k_{nm}^2}\right\} \;/\; \left(1-M^2\right) \tag{A.1.26}$$

which represent positive and negative traveling waves, respectively.

From equations (A.1.25) and (A.1.26), the modes can be propagating or decaying depending on the following conditions

(i) If $k_o > k_{nm}\sqrt{\left(1-M^2\right)}$ the mode will propagate

and

(ii) If $k_o < k_{nm}\sqrt{\left(1-M^2\right)}$ the mode will decay

Based on the above conditions, there are four possible cases for the axial wavenumber:

i) Positive traveling mode;

$$k_x^{(+)} = \left\{-Mk_o + \sqrt{k_o^2 - \left(1-M^2\right)k_{nm}^2}\right\} \;/\; \left(1-M^2\right) \tag{A.1.27}$$

ii) Positive decaying mode;

$$k_x^{(+)} = \left\{-Mk_o - i\sqrt{\left(1-M^2\right)k_{nm}^2 - k_o^2}\right\} \;/\; \left(1-M^2\right) \tag{A.1.28}$$

where the negative root was selected to have the wave decaying in the positive *x*-direction.

iii) Negative traveling mode;

$$k_x^{(-)} = \left\{ -Mk_o - \sqrt{k_{\mathrm{o}}^2 - \left(1-M^2\right)k_{nm}^2} \right\} / \left(1-M^2\right) \qquad \text{(A.1.29)}$$

iv) Negative decaying mode;

$$k_x^{(-)} = \left\{ -Mk_o + i\sqrt{\left(1-M^2\right)k_{\mathrm{nm}}^2 - k_{\mathrm{o}}^2} \right\} / \left(1-M^2\right) \qquad \text{(A.1.30)}$$

where the positive root was selected to have the wave decaying in the negative *x*-direction.

Finally, the pressure field in the duct can be expressed as a linear combination of the acoustic modes as

$$p(x,y,z) = \sum_{n=0}^{Ny} \sum_{m=0}^{Nz} \left[A_{nm}^{(+)} \Phi_{nm}(y,z) e^{-ik_x^{(+)}x} + A_{nm}^{(-)} \Phi_{nm}(y,z) e^{-ik_x^{(-)}x} \right] \qquad \text{(A.1.31)}$$

where $A_{nm}^{(+)}$ and $A_{nm}^{(-)}$ are the amplitude of the positive and negative waves, respectively; and N_y and N_z are the number of modes used in the expansion.

A.1.2 Duct With One Side Lined

We want to consider the same duct, but in this case the upper wall i.e. $y = a$, has a liner with impedance Z_w (see figure A.1.2). The impedance is commonly written in terms of the specific admittance as

$$z_w = \rho c / \beta_w \tag{A.1.32}$$

where β_w is the specific admittance.

Assuming again a solution as in (A.1.9) will lead to equation (A.1.10). Assuming the solution as in eq.(A.1.5), the boundary conditions in terms of $\Phi(y,z)$ becomes

$$\left.\frac{\partial \Phi}{\partial y}\right|_{y=0} = 0 \tag{A.1.33a}$$

$$-\left.\frac{\partial \Phi}{\partial y}\right|_{y=a} = i\rho c\left(k_o - Mk_x\right)v_y\left(a,z\right) \tag{A.1.33b}$$

$$\left.\frac{\partial \Phi}{\partial z}\right|_{z=0} = 0 \tag{A.1.33c}$$

$$\left.\frac{\partial \Phi}{\partial z}\right|_{z=b} = 0 \tag{A.1.33d}$$

Replacing (A.1.9) into the boundary conditions in (A.1.33a-d), gives

$$\left.\frac{dY}{dy}\right|_{y=0} = 0 \tag{A.1.34a}$$

$$-Z\left.\frac{dY}{dy}\right|_{y=a} = i\rho c(k_o - k_x M)v_y(a,z) \tag{A.1.34b}$$

$$\left.\frac{dZ}{dz}\right|_{z=0} = 0 \tag{A.1.34c}$$

$$\left.\frac{dZ}{dz}\right|_{z=b} = 0 \tag{A.1.34d}$$

Equation (A.1.15) and the boundary conditions (A.1.34c) and (A.1.34d) results in the solution in (A.1.19) and (A.1.20). This implies that the variation of the particle velocity $v_y(a,z)$ with respect to z has to be the same as $Z(z)$. Thus,

$$v_y\left(y,z\right) = \hat{v}_y\left(y\right)Z\left(z\right) \tag{A.1.35}$$

Thus, the boundary conditions (A.1.34a-b) becomes

$$\left.\frac{dY}{dy}\right|_{y=0} = 0 \tag{A.1.36a}$$

$$-\left.\frac{dY}{dy}\right|_{y=a} = i\rho c\left(k_o - Mk_x\right)\hat{v}_y\left(a\right) \tag{A.1.36b}$$

The function $\hat{v}_y(y)$ is obtained by matching the particle displacement in the *y*-direction inside the liner and in the duct at $y = a$. That is

$$\frac{\hat{v}^{\ell}}{i\omega} = \frac{\hat{v}_y(a)}{i\omega\left(1 - M\frac{k_x}{k_o}\right)} = \frac{\hat{v}_y(a)}{i\omega(k_o - Mk_x)/k_o} \tag{A.1.37}$$

where $\hat{v}^{\ell}$ is the particle velocity in the liner. The particle velocity and the pressure are related through the liner specific admittance as

$$\hat{v}^{\ell} = \frac{p^{\ell}}{Z_w} = \beta_w \frac{p^{\ell}}{\rho c} \tag{A.1.38}$$

where p^{ℓ} is the pressure in the liner.

Replacing $\hat{v}_y(a)$ from (A.1.36b) and $\hat{v}^{\ell}$ from (A.1.38) into (A.1.37) gives

$$\beta_w \frac{p^{\ell}}{\rho c} = -\frac{1}{i\rho c\left(k_o - Mk_x\right)^2/k_o}\frac{dY}{dy}\bigg|_{y=a} \tag{A.1.39}$$

The pressure in the liner ("locally reacting") has to match the pressure in the duct, i.e. $p^{\ell} = Y(a)$. Thus, the boundary condition at $y = a$ becomes

$$\beta_w Y(a)\frac{i\left(k_o - Mk_x\right)^2}{k_o} = -\frac{dY}{dy}\bigg|_{y=a} \tag{A.1.40}$$

The differential equation in (A.1.14) and the boundary conditions in (A.1.36a) and (A.1.40) needs to be solved.

The solution to (A.1.14) is assumed as

$$Y(y) = A\cos(k_y y) + B\sin(k_y y) \tag{A.1.41}$$

Replacing (A.1.41) into (A.1.36a), it is found that B = 0. Equation (A.1.41) is now replaced into (A.1.40) to yield

$$i\beta_w \frac{(k_0 - Mk_x)^2}{k_o}\cos(k_y a) = k_y \sin(k_y a) \tag{A.1.42}$$

or

$$k_y a \tan(k_y a) = i\beta_w k_o a\left(1 - M\frac{k_x a}{k_o a}\right)^2 \tag{A.1.43}$$

Note that the solution to (A.1.43) will yield the values for k_y. However, eq.(A.1.43) depend on the value of k_x in the presence of flow, i.e. $M \neq 0$, which is obtained from (A.1.16). That is

$$k_{nm}^2 = k_y^2 + k_z^2 = k_o^2 - k_x^2(1 - M^2) - 2k_o k_x M \tag{A.1.44}$$

The two values for k_x were previously obtained in equation (A.1.25) and (A.1.26) as

$$k_x^{(+)} = \frac{-Mk_o + \sqrt{k_o^2 - (1 - M^2)(k_y^2 + k_z^2)}}{(1 - M^2)} \tag{A.1.45}$$

and

$$k_x^{(-)} = \frac{-Mk_o - \sqrt{k_o^2 - \left(1-M^2\right)\left(k_y^2 + k_z^2\right)}}{\left(1-M^2\right)} \tag{A.1.46}$$

where $k_x^{(+)}$ and $k_x^{(-)}$ corresponds to positive and negative *x*-direction propagating waves. This implies that the value of k_y and $Y\left(y\right)$ will depend on the direction of wave propagation. Equation (A.1.25) is replaced into (A.1.43) to give

$$k_y^{(+)} a \tan\left(k_y^{(+)} a\right) = i\beta_w k_o a \left[1 + \frac{M^2 - M\sqrt{1-\left(1-M^2\right)\left[\left(\frac{k_y^{(+)} a}{k_o a}\right)^2 + \left(\frac{k_z a}{k_o a}\right)^2\right]}}{\left(1-M^2\right)}\right]^2 \tag{A.1.47}$$

and eq.(A.1.26) is replaced into (A.1.43) to give

$$k_y^{(-)} a \tan\left(k_y^{(-)} a\right) = i\beta_w k_o a \left[1 + \frac{M^2 + M\sqrt{1-\left(1-M^2\right)\left[\left(\frac{k_y^{(-)} a}{k_o a}\right)^2 + \left(\frac{k_z a}{k_o a}\right)^2\right]}}{\left(1-M^2\right)}\right]^2 \tag{A.1.48}$$

Thus, solving (A.1.47) will yield $k_y^{(+)}$ and

$$Y^{(+)}\left(y\right) = A\cos\left(k_y^{(+)} y\right) \tag{A.1.49}$$

that is valid for the mode propagating in the positive *x*-direction.

On the other hand, solving (A.1.48) will yield $k_y^{(-)}$ and

$$Y^{(-)}\left(y\right) = A\cos\left(k_y^{(-)} y\right) \tag{A.1.50}$$

that is valid for the mode propagating in the negative x-direction.

The modes are then given as

$$\Phi_{nm}^{(+)}\left(y,z\right) = A_{nm}\cos\left(k_y^{(+)} y\right)\cos\left(\frac{m\pi}{b}z\right) \tag{A.1.51a}$$

and

$$\Phi_{nm}^{(-)}\left(y,z\right) = A_{nm}\cos\left(k_y^{(-)} y\right)\cos\left(\frac{m\pi}{b}z\right) \tag{A.1.51b}$$

for positive and negative x-direction propagation, respectively. The wavenumber k_{nm} will also depend on the direction of propagation. Thus, replacing $k_y^{(+)}$ and $k_y^{(-)}$ in (A.1.23) will give $k_{nm}^{(+)}$ and $k_{nm}^{(-)}$, respectively.

Then, the pressure field is given as

$$p\left(x,y,z\right) = \sum_{n=0}^{N_y}\sum_{m=0}^{N_z}\left[A_{nm}^{(+)}\Phi_{nm}^{(+)}\left(y,z\right)e^{-ik_x^{(+)}x} + A_{nm}^{(-)}\Phi_{nm}^{(-)}\left(y,z\right)e^{-ik_x^{(-)}x}\right] \tag{A.1.52}$$

where $A_{nm}^{(+)}$ and $A_{nm}^{(-)}$ are the complex modal amplitudes of the positive and negative propagating modes, respectively.

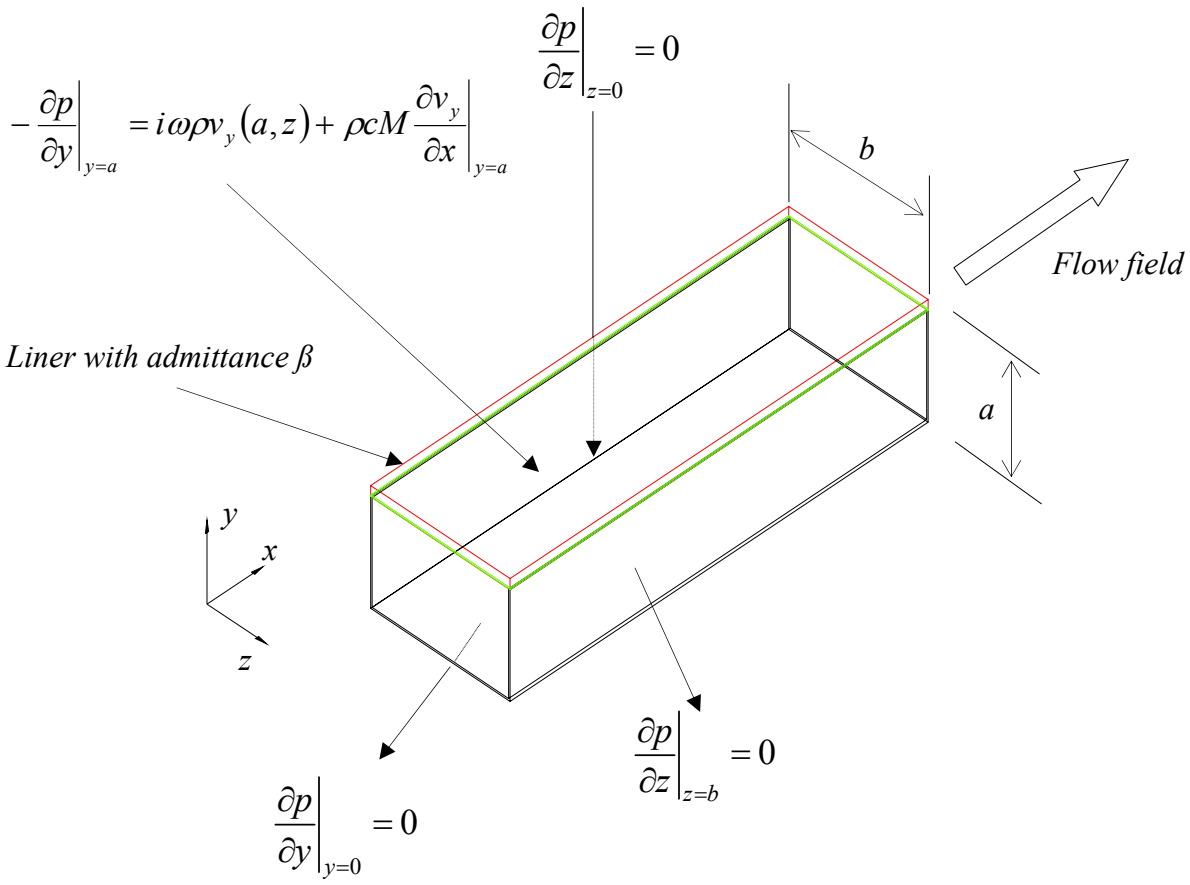

Figure A.1.2: Infinite rectangular duct with a liner on the upper wall

A.2 Green's Function

The Green's function is the pressure field generated by a source located at (x_o, y_o, z_o) defined by the generalized Dirac function. To this end, the following differential equation needs to be solved .

$$\frac{\partial^2 g}{\partial x^2} + \frac{\partial^2 g}{\partial y^2} + \frac{\partial^2 g}{\partial z^2} + k_o^2 g - M^2 \frac{\partial^2 g}{\partial x^2} - 2Mik_o \frac{\partial g}{\partial x} = \delta(x - x_o)\delta(y - y_o)\delta(z - z_o) \tag{A.2.1a}$$

where $g(x, y, z \mid x_o, y_o, z_o)$ is the Green's function.

Equation (A.2.1a) can be rewritten as

$$\frac{\partial^2 g}{\partial x^2}\left(1 - M^2\right) - 2iMk_o \frac{\partial g}{\partial x} + \frac{\partial^2 g}{\partial y^2} + \frac{\partial^2 g}{\partial z^2} + k_o^2 g = \delta(x - x_o)\delta(y - y_o)\delta(z - z_o) \tag{A.2.1b}$$

A.2.1 The Hard-Wall Case

The first case to consider is the rigid-walled duct. The solution to eq.(A.2.1b) is expanded in terms of the rigid-walled duct modes $\Phi_{nm}(y, z)$ as

$$g(x, y, z \mid x_o, y_o, z_o) = \sum_{n=0}^{Ng} \sum_{m=0}^{Mg} F_{nm}(x)\Phi_{nm}(y, z) \tag{A.2.2}$$

where N_g and M_g indicate the number of modes included in the Green's function. Note

that for the rigid wall duct case, the modes are the same for the positive and negative *x*-direction propagation.

Replacing eq.(A.2.2) into (A.2.1b) gives

$$\sum_{n=0}^{N_g}\sum_{m=0}^{M_g}\left\{\frac{d^2F_{nm}}{dx^2}(1-M^2)-2iMk_o\frac{dF_{nm}}{dx}-k_{nm}^2F_{nm}+k_o^2F_{nm}\right\}\Phi_{nm}(y,z)$$

$$=\delta(x-x_o)\delta(y-y_o)\delta(z-z_o) \tag{A.2.3}$$

Premultiplying eq.(A.2.3) by the (*r,s*) mode $\Phi_{rs}(y,z)$, integrating over the duct cross section, and considering the orthogonality condition.

$$\int_0^a\int_0^b\Phi_{rs}(y,z)\Phi_{nm}(y,z)dydz=ab\Lambda_{nm}\delta_{rn}\delta_{sm} \tag{A.2.4}$$

where $\Lambda_{nm}=\varepsilon_n\varepsilon_m$ with $\varepsilon_n(\varepsilon_m)$ is 1 for $n(m)=0$ and ½ for $n(m)\geq 1$ gives

$$\frac{d^2F_{nm}}{dx^2}(1-M^2)-2iMk_o\frac{dF_{nm}}{dx}-\left(k_{nm}^2-k_o^2\right)F_{nm}=\delta(x-x_o)\frac{\Phi_{nm}(y_o,z_o)}{ab\Lambda_{nm}} \tag{A.2.5}$$

Equation (A.2.5) is an ordinary differential equation in *x* which is solved assuming the solutions for positions upstream and downstream of the source to be as

$$F_{nm}(x)=\mathrm{A}_{nm}e^{-ik_x^{(+)}(x-x_o)} \qquad x\geq x_o \tag{A.2.6a}$$

$$F_{nm}(x)=\mathrm{A}_{nm}e^{-ik_x^{(-)}(x-x_o)} \qquad x\leq x_o \tag{A.2.6b}$$

Note that by selecting the same amplitude A_{nm} for both solutions, the sound field is uniquely defined at $x = x_o$.

To solve for the unknown amplitude A_{nm}, the following integral needs to be solved

$$\lim_{\alpha\to 0}\int_{x_o-\alpha}^{x_o+\alpha}\left[\frac{d^2F_{nm}}{dx^2}(1-M^2)-2iMk_o\frac{dF_{nm}}{dx}-\left(k_{nm}^2-k_o^2\right)F_{nm}\right]dx = \delta(x-x_o)\frac{\Phi_{nm}(y_o,z_o)}{ab\Lambda_{nm}} \tag{A.2.7}$$

that results in

$$\lim_{\alpha\to 0}\left\{(1-M^2)\left[\left.\frac{dF_{nm}}{dx}\right|_{x_o+\alpha}-\left.\frac{dF_{nm}}{dx}\right|_{x_o-\alpha}\right]\right\}=\frac{\Phi_{nm}(y_o,z_o)}{ab\Lambda_{nm}} \tag{A.2.8}$$

Replacing eqs.(A.2.6a) and (A.2.6b) for the upper and lower limits respectively in (A.2.8) yields

$$\lim_{\alpha\to 0}\left(1-M^2\right)\left[A_{nm}\left(-ik_x^{(+)}\right)e^{ik_x^{(+)}\alpha}-A_{nm}\left(-ik_x^{(-)}\right)e^{ik_x^{(-)}\alpha}\right]=\frac{\Phi_{nm}(y_o,z_o)}{ab\Lambda_{nm}} \tag{A.2.9}$$

Taking the limit yields

$$-A_{nm}i\left(1-M^2\right)\left(k_x^{(+)}-k_x^{(-)}\right)=\frac{\Phi_{nm}(y_o,z_o)}{ab\Lambda_{nm}} \tag{A.2.10}$$

Solving for A_{nm} and replacing back into (A.2.6a) and (A.2.6b) and then into (A.2.2) gives

$$g^{(+)}\left(x,y,z\,|\,x_o,y_o,z_o\right)=\frac{i}{ab}\sum_{n=0}^{N_g}\sum_{m=0}^{M_g}\frac{\Phi_{nm}(y,z)\Phi_{nm}(y_o,z_o)}{\Lambda_{nm}\left(1-M^2\right)\left(k_x^{(+)}-k_x^{(-)}\right)}e^{-ik_x^{(+)}(x-x_o)}$$

$$x\geq x_o \quad \text{(2.2.11a)}$$

and

$$g^{(-)}\left(x,y,z\,|\,x_o,y_o,z_o\right)=\frac{i}{ab}\sum_{n=0}^{N_g}\sum_{m=0}^{M_g}\frac{\Phi_{nm}(y,z)\Phi_{nm}(y_o,z_o)}{\Lambda_{nm}\left(1-M^2\right)\left(k_x^{(+)}-k_x^{(-)}\right)}e^{-ik_x^{(-)}(x-x_o)}$$

$$x\le x_o \quad \text{(A.2.11b)}$$

which are the Green's function for the positive and negative *x*-propagation directions, respectively.

A.2.2 The Lined Duct Case

For the case of a duct with a wall admittance β_w and in the presence of flow, the acoustic modes in the positive and negative directions are different. Thus, we assume a solution to (A.2.1b) of the form

$$\begin{aligned}g^{(+)}\left(x,y,z\,|\,x_o,y_o,z_o\right)&=\sum_{n=0}^{N_g}\sum_{m=0}^{M_g}F_{nm}^{(+)}\Phi_{nm}^{(+)}\left(y,z\right)\\&=\sum_{n=0}^{N_g}\sum_{m=0}^{M_g}\mathrm{A}_{nm}^{(+)}\Phi_{nm}^{(+)}\left(y,z\right)e^{-ik_x^{(+)}(x-x_o)}\end{aligned}\qquad \text{for } x\ge x_0 \quad \text{(A.2.12a)}$$

and

$$\begin{aligned}g^{(-)}\left(x,y,z\,|\,x_o,y_o,z_o\right)&=\sum_{n=0}^{N_g}\sum_{m=0}^{M_g}F_{nm}^{(-)}\Phi_{nm}^{(-)}(y,z)\\&=\sum_{n=0}^{N_g}\sum_{m=0}^{M_g}\mathrm{A}_{nm}^{(-)}\Phi_{nm}^{(-)}(y,z)e^{-ik_x^{(-)}(x-x_o)}\end{aligned}\qquad \text{for } x\le x_0 \quad \text{(A.2.12b)}$$

In addition, we need to satisfy that (A.2.12a) and (A.2.12b) must be the same at $x=x_o$. That is

$$\sum_{n=0}^{N_g}\sum_{m=0}^{M_g} \mathrm{A}_{nm}^{(+)}\Phi_{nm}^{(+)}\left(y,z\right)=\sum_{n=0}^{N_g}\sum_{m=0}^{M_g} \mathrm{A}_{nm}^{(-)}\Phi_{nm}^{(-)}(y,z) \qquad \text{(A.2.13)}$$

where $\Phi_{nm}^{(+)}\left(y,z\right)$ and $\Phi_{nm}^{(-)}\left(y,z\right)$ are the duct modes for the positive and negative *x*-propagation directions with amplitudes $\mathrm{A}_{nm}^{(+)}$ and $\mathrm{A}_{nm}^{(-)}$, respectively.

The differential equation of motion in (A.2.1b) is premultiplied by each of the positive (or negative) propagating modes $\Phi_{re}^{(+)}\left(y,z\right)$ and integrated over a volume as

$$\lim_{\varepsilon\to 0}\int_0^a\int_0^b\int_{x_0-\varepsilon}^{x_0+\varepsilon}\Phi_{re}^{(+)}\left(y,z\right)\left\{\frac{\partial^2 g}{\partial x^2}\left(1-M^2\right)-2iMk_o\frac{\partial g}{\partial x}+\frac{\partial^2 g}{\partial y^2}+\frac{\partial^2 g}{\partial z^2}+k_o^2 g\right\}dxdydz$$
$$=\Phi_{re}^{(+)}\left(y_o,z_o\right) \qquad \text{(A.2.14)}$$

Equation (A.2.14) will reduce to

$$\lim_{\varepsilon\to 0}\int_0^a\int_0^b\int_{x_o-\varepsilon}^{x_o+\varepsilon}\Phi_{re}^{(+)}\left(y,z\right)\left(1-M^2\right)\frac{\partial^2 g}{\partial x^2}dxdydz=\Phi_{re}^{(+)}\left(y_o,z_o\right) \qquad \text{(A.2.15)}$$

Replacing (A.2.12a) and (A.2.12b) into (A.2.15) gives

$$\lim_{\varepsilon\to 0}\sum_{n=0}^{N_g}\sum_{m=0}^{M_g}\left\{\int_0^a\int_0^b\Phi_{re}^{(+)}\Phi_{nm}^{(+)}dydz\left.\frac{dF_{nm}^{(+)}}{dx}\right|_{x_o+\varepsilon}-\int_0^a\int_0^b\Phi_{re}^{(+)}\Phi_{nm}^{(-)}dydz\left.\frac{dF_{nm}^{(-)}}{dx}\right|_{x_o-\varepsilon}\right\}\left(1-M^2\right)$$

$$=\Phi_{re}^{(+)}\left(y_o,z_o\right) \qquad r=0,\ 1,\ 2,\ldots\ e=0,\ 1,\ 2,\ldots \quad \text{(A.2.16)}$$

The integration of the product of the modes in (A.2.16) will vanish only for, $e\neq m$, i.e. the modes are orthogonal with respect to the *z*-component. However, the modes are not

orthogonal with respect to the *y*-direction. Thus, evaluating the derivatives and taking the limit yields

$$\sum_{n=0}^{N_g}\left\{k_x^{(+)}A_{nm}^{(+)}\int_0^a\int_0^b\Phi_{rm}^{(+)}\Phi_{nm}^{(+)}dydz-k_x^{(-)}A_{nm}^{(-)}\int_0^a\int_0^b\Phi_{rm}^{(+)}\Phi_{nm}^{(-)}dydz\right\}=\frac{\Phi_{rm}^{(+)}\left(y_o,z_o\right)i}{\left(1-M^2\right)}$$

$r = 0, 1, 2, \ldots \quad m = 0, 1, 2, \ldots$ (A.2.17)

Equation (A.2.17) can be written in matrix form as

$$\left[\Lambda_{rn,m}^{(+)}\right]\left[k_x^{(+)}\right]\left\{A_{nm}^{(+)}\right\}-\left[\Lambda_{rn,m}^{(-)}\right]\left[k_x^{(-)}\right]\left\{A_{nm}^{(-)}\right\}=\left\{\Psi_r\right\} \qquad m = 0, 1, 2, \ldots$$ (A.2.18)

The (*r,n*) element of the matrices in (A.2.18) are

$$\Lambda_{rn,m}^{(+)}=\frac{1}{ab}\int_0^a\int_0^b\Phi_{rm}^{(+)}\Phi_{nm}^{(+)}dydz$$

and

$$\Lambda_{rn,m}^{(-)}=\frac{1}{ab}\int_0^a\int_0^b\Phi_{rm}^{(+)}\Phi_{nm}^{(-)}dydz$$

while the elements of the independent vector $\left\{\Psi_r\right\}$ are

$$\Psi_r=\frac{i\Phi_{rm}^{(+)}\left(y_o,z_o\right)}{ab\left(1-M^2\right)}$$

Matrices $\left[k_x^{(+)}\right]$ and $\left[k_x^{(-)}\right]$ are diagonal where the elements are the axial wavenumber $k_x^{(+)}$

and $k_x^{(-)}$ for the (*n,m*) mode, respectively.

The next step is to premultiply (A.2.13) by $\Phi_{re}^{(+)}$ and integrate over the duct cross section. Once again, it is easy to show that this leads to

$$\left[\Lambda_{rn,m}^{(+)}\right]\left\{A_{nm}^{(+)}\right\}=\left[\Lambda_{rn,m}^{(-)}\right]\left\{A_{nm}^{(-)}\right\} \qquad m = 0, 1, 2, \ldots \tag{A.2.19}$$

Equations (A.2.18) and (A.2.19) can now be used to solve for the amplitude of the vectors $\left\{A_{nm}^{(+)}\right\}$ and $\left\{A_{nm}^{(-)}\right\}$ needed to define the Green's functions in eqs.(A.2.12a) and (A.2.12b).

To find $\left\{A_{nm}^{(+)}\right\}$ it is convenient to solve for $\left\{A_{nm}^{(-)}\right\}$ from (A.2.19) as

$$\left\{A_{nm}^{(-)}\right\}=\left[\Lambda_{rn,m}^{(-)}\right]^{-1}\left[\Lambda_{rn,m}^{(+)}\right]\left\{A_{nm}^{(+)}\right\} \tag{A.2.20}$$

and then replacing this into (A.2.18) to yield

$$\left(\left[\Lambda_{rn,m}^{(+)}\right]\left[k_x^{(+)}\right]-\left[\Lambda_{rn,m}^{(-)}\right]\left[k_x^{(-)}\right]\left[\Lambda_{rn,m}^{(-)}\right]^{-1}\left[\Lambda_{rn,m}^{(+)}\right]\right)\left\{A_{nm}^{(+)}\right\}=\left\{\Psi_r\right\} \tag{A.2.21}$$

Inverting the matrix in (A.2.21) results in

$$\left\{A_{nm}^{(+)}\right\}=\left[T_{rn,m}^{(+)}\right]\left\{\Psi_r\right\} \tag{A.2.22}$$

where

$$\left[T_{rn,m}^{(+)}\right]=\left(\left(\left[\Lambda_{rn,m}^{(+)}\right]\left[k_x^{(+)}\right]-\left[\Lambda_{rn,m}^{(-)}\right]\left[k_x^{(-)}\right]\left[\Lambda_{rn,m}^{(-)}\right]^{-1}\left[\Lambda_{rn,m}^{(+)}\right]\right)\right)^{-1}$$

Equation (A.2.22) can be expressed as

$$A_{nm}^{(+)} = \sum_{r=0}^{N_g} \frac{T_{rn,m}^{(+)} i\Phi_{rm}^{(+)}\left(y_o, z_o\right)}{ab\left(1-M^2\right)} \tag{A.2.23}$$

where $T_{rn,m}^{(+)}$ in (A.2.23) represents the elements of the n^{th} row of matrix $\left[T_{rn,m}^{(+)}\right]$.

The vector $\left\{A_{nm}^{(-)}\right\}$ can be solved with a similar approach. From eq.(A.2.19) we solve for $\left\{A_{nm}^{(+)}\right\}$ as

$$\left\{A_{nm}^{(+)}\right\} = \left[\Lambda_{rn,m}^{(+)}\right]^{-1}\left[\Lambda_{rn,m}^{(-)}\right]\left\{A_{nm}^{(-)}\right\} \tag{A.2.24}$$

That is replaced into (A.2.18) to yield

$$\left(\left[\Lambda_{rn,m}^{(+)}\right]\left[k_x^{(+)}\right]\left[\Lambda_{rn,m}^{(+)}\right]^{-1}\left[\Lambda_{rn,m}^{(-)}\right] - \left[\Lambda_{rn,m}^{(-)}\right]\left[k_x^{(-)}\right]\right)\left\{A_{nm}^{(-)}\right\} = \left\{\Psi_r\right\} \tag{A.2.25}$$

Inverting the matrix in (A.2.25) results in

$$\left\{A_{nm}^{(-)}\right\} = \left[T_{rn,m}^{(-)}\right]\left\{\Psi_r\right\} \tag{A.2.26}$$

where

$$\left[T_{rn,m}^{(-)}\right] = \left(\left(\left[\Lambda_{rn,m}^{(+)}\right]\left[k_x^{(+)}\right]\left[\Lambda_{rn,m}^{(+)}\right]^{-1}\left[\Lambda_{rn,m}^{(-)}\right] - \left[\Lambda_{rn,m}^{(-)}\right]\left[k_x^{(-)}\right]\right)\right)^{-1}$$

Once again eq.(A.2.26) can be expanded as

$$A_{nm}^{(-)} = \sum_{r=0}^{N_g} \frac{T_{rn,m}^{(-)} i\Phi_{rm}^{(+)}\left(y_o, z_o\right)}{ab\left(1-M^2\right)} \tag{A.2.27}$$

where $T_{rn,m}^{(-)}$ in (A.2.27) represents the elements of the n^{th} row of matrix $\left[T_{rn,m}^{(-)}\right]$.

Replacing (A.2.23) and (A.2.27) into (A.2.12a) and (A.2.12b), the Green's function are given as

$$g^{(+)}\left(\vec{x}\middle|\vec{x}_o\right) = \frac{i}{ab}\sum_{n=0}^{N_g}\sum_{m=0}^{M_g}\left(\sum_{r=0}^{N_g}\frac{T_{rn,m}^{(+)}\Phi_{rm}^{(+)}\left(y_o, z_o\right)}{\left(1-M^2\right)}\right)\Phi_{nm}^{(+)}e^{-ik_x^{(+)}(x-x_o)} \qquad x \geq x_o \tag{A.2.28a}$$

and

$$g^{(-)}\left(\vec{x}\middle|\vec{x}_o\right) = \frac{i}{ab}\sum_{n=0}^{N_g}\sum_{m=0}^{M_g}\left(\sum_{r=0}^{N_g}\frac{T_{rn,m}^{(-)}\Phi_{rm}^{(+)}\left(y_o, z_o\right)}{\left(1-M^2\right)}\right)\Phi_{nm}^{(-)}e^{-ik_x^{(-)}(x-x_o)} \qquad x \leq x_o \tag{A.2.28b}$$

for positive and negative *x*-direction propagations, respectively.

It is interesting to note that if we assume that matrices $\left[\Lambda_{rn,m}^{(+)}\right]$ and $\left[\Lambda_{rn,m}^{(-)}\right]$ are diagonal (such as for a hard or lined duct with no flow), equation (A.2.18) and (A.2.19) will reduce to

$$\Lambda_{nn,m}^{(+)}k_x^{(+)}A_{nm}^{(+)} - \Lambda_{nn,m}^{(-)}k_x^{(-)}A_{nm}^{(-)} = \frac{i\Phi_{nm}^{(+)}\left(y_o, z_o\right)}{ab\left(1-M^2\right)} \tag{A.2.29a}$$

$$\Lambda_{nn,m}^{(+)}A_{nm}^{(+)} = \Lambda_{nn,m}^{(-)}A_{nm}^{(-)} \tag{A.2.29b}$$

that can be used to solve for $A_{nm}^{(+)}$ and $A_{nm}^{(-)}$ as follows

$$A_{nm}^{(+)} = \frac{i\Phi_{nm}^{(+)}\left(y_o, z_o\right)}{\Lambda_{nn,m}^{(+)}\left(1-M^2\right)\left(k_x^{(+)} - k_x^{(-)}\right)ab} \tag{A.2.30a}$$

$$A_{nm}^{(-)} = \frac{i\Phi_{nm}^{(-)}\left(y_o, z_o\right)}{\Lambda_{nn,m}^{(-)}\left(1-M^2\right)\left(k_x^{(+)} - k_x^{(-)}\right)ab} \tag{A.2.30b}$$

A.3 Finite Source Radiation

In this section, the sound field generated by a finite piston source, as illustrated in Figure A.3.1 is derived. The sound field generated by a finite piston source with a surface area *S* and velocity *v* radiating into the duct is obtained using the Green's function derived in the previous section.

A.3.1 The Hard Wall Case

The Green's function for a point source positioned on the hard wall duct at $(\tilde{x},\tilde{y},\tilde{z})$ is given as

$$g(x,y,z|\tilde{x},\tilde{y},\tilde{z}) = \frac{i}{ab}\sum_{n}^{N_g}\sum_{m}^{M_g}\frac{\Phi_{nm}(y,z)\Phi_{nm}(\tilde{y},\tilde{z})}{\Lambda_{nm}\left(1-M^2\right)\left(k_x^{(+)}-k_x^{(-)}\right)}e^{-ik_x^{(+)}(x-\tilde{x})}$$

for $x > \tilde{x}$ (A.3.1a)

where $k_x^{(+)}$ is

$$k_x^{(+)} = \begin{cases} \left\{-Mk_o + \sqrt{k_o^2-(1-M^2)k_{nm}^2}\right\}/(1-M^2) & k_0 > \sqrt{(1-M^2)}k_{nm} \\ \left\{-Mk_o - i\sqrt{(1-M^2)k_{nm}^2-k_o^2}\right\}/(1-M^2) & k_0 < \sqrt{(1-M^2)}k_{nm} \end{cases}$$

and

$$g(x,y,z|\tilde{x},\tilde{y},\tilde{z}) = \frac{i}{ab}\sum_{n}^{N_g}\sum_{m}^{M_g}\frac{\Phi_{nm}(y,z)\Phi_{nm}(\tilde{y},\tilde{z})}{\Lambda_{nm}\left(1-M^2\right)\left(k_x^{(+)}-k_x^{(-)}\right)}e^{-ik_x^{(-)}(x-\tilde{x})}$$

for $x < \tilde{x}$ (A.3.1b)

where $k_x^{(-)}$ is

$$k_x^{(-)} = \begin{cases} \left\{ -Mk_o - \sqrt{k_o^2 - (1-M^2)k_{nm}^2} \right\} / (1-M^2) & k_0 > \sqrt{(1-M^2)}k_{nm} \\ \left\{ -Mk_o + i\sqrt{(1-M^2)k_{nm}^2 - k_o^2} \right\} / (1-M^2) & k_0 < \sqrt{(1-M^2)}k_{nm} \end{cases}$$

and the eigenfunction is given as

$$\Phi_{nm}(y,z) = \cos\left(\frac{n\pi}{a}y\right)\cos\left(\frac{m\pi}{b}z\right) \qquad \text{(A.3.2)}$$

and N_g and M_g are the number of modes included in the Green's function.

The modes normalization factor Λ_{nm} is given as

$$ab\Lambda_{nm} = \int_0^a \int_0^b \cos^2\left(\frac{n\pi}{a}y\right)\cos^2\left(\frac{m\pi}{b}z\right)dydz \qquad \text{(A.3.3)}$$

Thus, this leads to

$$\Lambda_{nm} = \begin{array}{ll} 1 & \text{for } n=0 \text{ and } m=0 \\ ½ & \text{for } n=0 \text{ and } m \neq 0 \\ ½ & \text{for } n \neq 0 \text{ and } m=0 \\ ¼ & \text{for } n \neq 0 \text{ and } m \neq 0 \end{array} \qquad \text{(A.3.4)}$$

The pressure at (*x, y, z*) due to the n^{th} finite piston source with source velocity v_n is then obtained by integrating the Green's function over the surface of the source as

$$p(x,y,z|x_n,y_n,z_n) = -i\omega\rho v_n \int_{x_n-d}^{x_n+d}\int_{z_n-d}^{z_n+d} g(x,y,z\,|\,\tilde{x},\tilde{y},\tilde{z})d\tilde{x}d\tilde{z} \qquad \text{(A.3.5)}$$

where the dimension d of the source is given in terms of the source area as $d = \sqrt{S}/2$ and (x_n, y_n, z_n) is the location of the source center as defined in figure A.3.1. Note that $y_n = \tilde{y}$ can take the value of "0" or "*a*" depending on whether the piston source is in the lower or upper wall.

Replacing (A.3.1a) or (A.3.1b) into (A.3.5), it is clear that there are two integrals that need to be solved. The first one is with respect to the coordinate *z*, which is easily obtained as

$$\int_{z_n-d}^{z_n+d} \cos\left(\frac{m\pi\tilde{z}}{b}\right)d\tilde{z} = 2d\frac{\sin(m\pi d/b)}{m\pi d/b}\cos\left(\frac{m\pi}{b}z_n\right) = \kappa_z(d)\cos\left(\frac{m\pi}{b}z_n\right) \qquad \text{(A.3.6)}$$

where $\kappa_z(d) = 2d\dfrac{\sin(m\pi d/b)}{m\pi d/b}$

For the special case of *m*=0 eq. (A.3.6) gives 2*d*.

The second integral is along the *x*-direction and depends on the position of the observation point *x* relative to the source position x_n. There are three cases to consider, as illustrated in figures A.3.2a-c.

CASE 1: The observation point is upstream of the source, i.e. $x > x_n + d$. This case is illustrated in Figure A.3.2a and implies that $x > \tilde{x}$ and eq.(A.3.1a) need to be replaced in (A.3.5). Thus, the following integral needs to be solved

$$\int_{x_n-d}^{x_n+d} e^{-ik_x^{(+)}(x-\tilde{x})} d\tilde{x} \qquad\qquad x > \tilde{x}$$

that leads to

$$\int_{x_n-d}^{x_n+d} e^{-ik_x^{+}(x-\tilde{x})} d\tilde{x} = e^{-ik_x^{(+)}(x-x_n)} \frac{\sin(k_x^{(+)}d)}{k_x^{(+)}d} 2d \tag{A.3.7}$$

The pressure due to the source positioned at (x_n, y_n, z_n) (See figure A.3.1) is now obtained by replacing eq.(A.3.1a) into (A.3.5) and considering the solution to integrals in (A.3.6) and (A.3.7). That is

$$\begin{aligned} &p(x,y,z \mid x_n, y_n, z_n) \\ &= v_n \frac{k_0 \rho c}{ab} \sum_{n}^{N_g} \sum_{n}^{M_g} \frac{\Phi_{nm}(y,z)\Phi_{nm}(y_n,z_n)}{(1-M^2)\Lambda_{nm}(k_x^{(+)} - k_x^{(-)})} \kappa_z(d) e^{-ik_x^{(+)}(x-x_n)} \frac{\sin(k_x^{(+)}d)}{k_x^{(+)}d} 2d \end{aligned} \tag{A.3.8}$$

CASE 2: The observation point is downstream of the source, i.e. $x < x_n - d$. This case is illustrated in Figure A.3.2b and implies that $x < \tilde{x}$ and eq.(A.3.1b) need to be replaced in (A.3.5). Thus, the following integral needs to be solved

$$\int_{x_n-d}^{x_n+d} e^{-ik_x^{(-)}(x-\tilde{x})} d\tilde{x} \qquad\qquad x < \tilde{x}$$

that leads to

$$\int_{x_n-d}^{x_n+d} e^{-ik_x^{(-)}(x-\tilde{x})}d\tilde{x} = e^{-ik_x^{(-)}(x-x_n)}\frac{2\sin(k_x^{(-)}d)}{k_x^{(-)}d}2d \tag{A.3.9}$$

The pressure due to the source is now obtained by replacing eq.(A.3.1b) into (A.3.5) and considering the solution to integrals in (A.3.6) and (A.3.9). That is

$$\begin{aligned} &p(x,y,z\,|\,x_n,y_n,z_n) \\ &= v_n\frac{k_0\rho c}{ab}\sum_n^{N_g}\sum_n^{M_g}\frac{\Phi_{nm}(y,z)\Phi_{nm}(y_n,z_n)}{(1-M^2)\Lambda_{nm}(k_x^{(+)}-k_x^{(-)})}\kappa_z(d)e^{-ik_x^{(-)}(x-x_n)}\frac{\sin(k_x^{(-)}d)}{k_x^{(-)}d}2d \end{aligned} \tag{A.3.10}$$

CASE 3: The observation point is on the surface of the source, i.e. $x_n - d < x < x_n + d$. This case is illustrated in Figure A.3.2c and requires that eq. (A.3.1a) be used for $x_n - d < \tilde{x} < x$ and that eq.(A.3.1b) be used for $x < \tilde{x} < x_n + d$ into (A.3.5), respectively. Thus, we need to solve this integral

$$\int_{x_n-d}^{x} e^{-ik_x^{(+)}(x-\tilde{x})}d\tilde{x} + \int_{x}^{x_n+d} e^{-ik_x^{(-)}(x-\tilde{x})}d\tilde{x}$$

Solving the integrals leads to

$$\frac{1-e^{-ik_x^{(+)}(x-x_n+d)}}{ik_x^{(+)}} - \frac{1-e^{-ik_x^{(-)}(x-x_n-d)}}{ik_x^{(-)}} \tag{A.3.11}$$

The pressure due to the piston is then given as

$$p(x,y,z\,|\,x_n,y_n,z_n) = v_n \frac{k_0\rho c}{ab}\sum_{n}^{N_g}\sum_{n}^{M_g}\frac{\Phi_{nm}(y,z)\Phi_{nm}(y_n,z_n)}{(1-M^2)\Lambda_{nm}(k_x^{(+)}-k_x^{(-)})} \times \kappa_z(d)\left(\frac{1-e^{-ik_x^{(+)}(x-x_n+d)}}{ik_x^{(+)}} - \frac{1-e^{-ik_x^{(-)}(x-x_n-d)}}{ik_x^{(-)}}\right) \tag{A.3.12}$$

In the next section, it is necessary to compute the average pressure over a source due to another piston source with unit velocity, i.e. impedance function. To compute these impedance functions, the average pressure over a piston source "*r*" due to another source "*s*" with unit velocity is simply given as

$$Z_{rs} = \frac{1}{v_s S_r}\int_{x_r-d_r}^{x_r+d_r}\int_{z_r-d_r}^{z_r+d_r} p(x,y_r,z\,|\,x_s,y_s,z_s)\,dxdz \tag{A.3.13}$$

The solution of (A.3.13) once again requires solving two integrals. The first integral is

$$\int_{z_r-d_r}^{z_r+d_r}\cos\left(\frac{m\pi}{b}z\right)dz = \kappa_z(d_r)\cos\left(\frac{m\pi}{b}z_r\right) \tag{A.3.14}$$

while the second integral is with respect to the *x*-coordinate that the solution to (A.3.14) depends on the location of the observation source "*r*" relative to the source "*s*". Once again three cases are possible as illustrated in figure A.3.3a-c.

CASE 1: The observation source "*r*" is downstream of source "*s*", i.e. $x_r - d_r > x_s + d_s$. In this case, equation (A.3.8) is replaced into (A.3.13) and the following integral needs to be solved.

$$\int_{x_r-d_r}^{x_r+d_r} e^{-ik_x^{(+)}(x-x_s)} \frac{\sin(k_x^{(+)}d_s)}{k_x^{(+)}d_s} 2d_s dx$$

that yields

$$e^{-ik_x^{(+)}(x_r-x_s)} \frac{\sin(k_x^{(+)}d_r)}{k_x^{(+)}d_r} 2d_r \frac{\sin(k_x^{(+)}d_s)}{k_x^{(+)}d_s} 2d_s$$

and in turn the impedance function becomes

$$\begin{aligned} Z_{rs} = & \frac{k_o \rho c}{S_r ab} \sum_{n=0}^{N_g} \sum_{n=0}^{M_g} \frac{\Phi_{nm}(y_s, z_s)\Phi_{nm}(y_r, z_r)}{(1-M^2)\Lambda_{nm}(k_x^{(+)} - k_x^{(-)})} \kappa_z(d_r)\kappa_z(d_s) \\ & \times e^{-ik_x^{(+)}(x_r-x_s)} \frac{\sin(k_x^{(+)}d_r)}{k_x^{(+)}d_r} 2d_r \frac{\sin(k_x^{(+)}d_s)}{k_x^{(+)}d_s} 2d_s \end{aligned} \tag{A.3.15}$$

CASE 2: The observation source "*r*" is upstream of source "*s*", i.e. $x_r + d_r < x_s - d_s$. In this case, equation (A.3.10) is replaced into (A.3.13) and the following integral needs to be solved.

$$\int_{x_r-d_r}^{x_r+d_r} e^{-ik_x^{(-)}(x-x_s)} \frac{\sin(k_x^{(-)}d_s)}{k_x^{(-)}d_s} 2d_s dx$$

that yields

$$e^{-ik_x^{(-)}(x_r-x_s)} \frac{\sin(k_x^{(-)}d_r)}{k_x^{(-)}d_r} 2d_r \frac{\sin(k_x^{(-)}d_s)}{k_x^{(-)}d_s} 2d_s$$

and in turn the impedance function becomes

$$Z_{rs} = \frac{k_o \rho c}{S_r ab} \sum_{n=0}^{N_g} \sum_{n=0}^{M_g} \frac{\Phi_{nm}(y_s, z_s)\Phi_{nm}(y_r, z_r)}{(1-M^2)\Lambda_{nm}(k_x^{(+)} - k_x^{(-)})} \kappa_z(d_r)\kappa_z(d_s) \times e^{-ik_x^{(-)}(x_r - x_s)} \frac{\sin(k_x^{(-)} d_r)}{k_x^{(-)} d_r} 2d_r \frac{\sin(k_x^{(-)} d_s)}{k_x^{(-)} d_s} 2d_s \tag{A.3.16}$$

CASE 3: The observation source "*r*" is at the same location as source "*s*". In addition, we assume that they have the same dimensions, i.e. $d_r = d_s$. In this case, equation (A.3.12) is replaced into (A.3.13) and solving

$$\int_{x_r - d_r}^{x_r + d_r} \left[\frac{1 - e^{-ik_x^{(+)}(x - x_s + d_s)}}{ik_x^{(+)}} - \frac{1 - e^{-ik_x^{(-)}(x - x_s - d_s)}}{ik_x^{(-)}} \right] dx$$

yielding

$$\frac{2d_r}{ik_x^{(+)}} - \frac{2d_r}{ik_x^{(-)}} + \frac{1 - e^{-ik_x^{(+)} 2d_r}}{\left(k_x^{(+)}\right)^2} + \frac{1 - e^{ik_x^{(-)} 2d_r}}{\left(k_x^{(-)}\right)^2}$$

Thus, the impedance Z_{rs} is

$$Z_{rs} = \frac{k_0 \rho c}{S_r ab} \sum_{n}^{N_g} \sum_{m}^{M_g} \frac{\Phi_{nm}(y_r, z_r)\Phi_{nm}(y_s, z_s)}{(1-M^2)\Lambda_{nm}(k_x^{(+)} - k_x^{(-)})} \kappa_z(d_r)\kappa_z(d_s) \times \frac{2d_r}{ik_x^{(+)}} - \frac{2d_r}{ik_x^{(-)}} + \frac{1 - e^{-ik_x^{(+)} 2d_r}}{\left(k_x^{(+)}\right)^2} + \frac{1 - e^{ik_x^{(-)} 2d_r}}{\left(k_x^{(-)}\right)^2} \tag{A.3.17}$$

A.3.2 The Lined Wall Case

In this section, the sound field generated by a finite piston sources for a lined duct as illustrated in Figure A.3.4 is derived. The sound field generated by a finite piston source of surface area *S* into the duct is obtained, again using the Green's functions for the lined duct. The Green's functions for a point source positioned on the duct at $(\tilde{x},\tilde{y},\tilde{z})$ is given as

$$g^{(+)}\left(x,y,z\middle|\tilde{x},\tilde{y},\tilde{z}\right)=\frac{i}{ab}\sum_{n=0}^{N_g}\sum_{m=0}^{M_g}\left(\sum_{r=0}^{N_g}\frac{T_{rn,m}^{(+)}\Phi_{rm}^{(+)}\left(\tilde{y},\tilde{z}\right)}{\left(1-M^2\right)}\right)\Phi_{nm}^{(+)}\left(y,z\right)e^{-ik_x^{(+)}(x-\tilde{x})} \qquad \text{(A.3.18a)}$$

where $k_x^{(+)}$ is

$$k_x^{(+)}=\left\{-Mk_o+\sqrt{k_o^2-(1-M^2)k_{nm}^2}\right\}/(1-M^2)$$

and

$$g^{(-)}\left(x,y,z\middle|\tilde{x},\tilde{y},\tilde{z}\right)=\frac{i}{ab}\sum_{n=0}^{N_g}\sum_{m=0}^{M_g}\left(\sum_{r=0}^{N_g}\frac{T_{rn,m}^{(-)}\Phi_{rm}^{(+)}\left(\tilde{y},\tilde{z}\right)}{\left(1-M^2\right)}\right)\Phi_{nm}^{(-)}\left(y,z\right)e^{-ik_x^{(-)}(x-\tilde{x})} \qquad \text{(A.3.18b)}$$

where $k_x^{(-)}$ is

$$k_x^{(-)}=\left\{-Mk_o-\sqrt{k_o^2-(1-M^2)k_{nm}^2}\right\}/(1-M^2)$$

In equations (A.3.18a) and (A.3.18b) the eigenfunctions are

$$\Phi_{nm}^{(+)}(y,z)=\cos\left(k_y^{(+)}y\right)\cos\left(\frac{m\pi}{b}z\right) \qquad \text{(A.3.19)}$$

$$\Phi_{nm}^{(-)}(y,z)=\cos\left(k_y^{(-)}y\right)\cos\left(\frac{m\pi}{b}z\right) \tag{A.3.20}$$

where $k_y^{(+)}$, $k_y^{(-)}$ and k_z are the mode eigennumbers, and N_g and M_g are the number of modes included in the Green's functions. It is important to note that the modes are not orthogonal.

The pressure at (*x, y, z*) due to the n^{th} finite piston source with source velocity v_n is then obtained by integrating the Green's function over the surface of the source as

$$p(x,y,z\big|x_n,y_n,z_n)=-i\omega\rho v_n\int_{x_n-d}^{x_n+d}\int_{z_n-d}^{z_n+d}g(x,y,z\,|\,\tilde{x},\tilde{y},\tilde{z})d\tilde{x}d\tilde{z} \tag{A.3.21}$$

where the dimension d of the source is given in terms of the source area as $d=\sqrt{s}/2$ and (x_n,y_n,z_n) is the location of the source center as defined in Figure A.3.4. Note that $y_n=\tilde{y}$ can take the value of "0" or "*a*" depending on whether the piston source is in the lower or upper wall.

Replacing (A.3.18a) or (A.3.18b) into (A.3.21), it is clear that there are again two integrals that need to be solved. The first one is with respect to the coordinate *z*, and is the same as in eq.(A.3.6) for the hard wall case.

$$\int_{z_n-d}^{z_n+d}\cos\left(\frac{m\pi\tilde{z}}{b}\right)d\tilde{z}=\kappa_z(d)\cos\left(\frac{m\pi}{b}z_n\right) \tag{A.3.22}$$

The second integral is along the *x*-direction and again is similar to the hard wall case except that the axial wavenumbers $k_x^{(+)}$ and $k_x^{(-)}$ are different.

The solution of these integrals depends on the position of the observation point x relative to the piston source position x_n. The same three cases are considered as illustrated in Figure A.3.2a-c. They are:

CASE 1: The observation point is upstream of the source, i.e. $x > x_n + d$. This case is illustrated in Figure A.3.2a and implies that $x > \tilde{x}$ and the following integral needs to be solved

$$\frac{p(x,y,z|x_n,y_n,z_n)}{v_n} = -i\omega\rho \int_{x_n-d}^{x_n+d}\int_{z_n-d}^{z_n+d} g^{(+)}\left(x,y,z|\tilde{x},y_n,\tilde{z}\right)d\tilde{x}d\tilde{z} \tag{A.3.23}$$

Replacing (A.3.18a) into (A.3.23) and considering (A.3.22) and (A.3.7) results in

$$\begin{aligned}\frac{p(x,y,z|x_n,y_n,z_n)}{v_n} = \frac{k_o\rho c}{ab}\sum_{n=0}^{N_g}\sum_{m=0}^{M_g}\left(\sum_{r=0}^{N_g}\frac{T_{rn,m}^{(+)}\Phi_{rm}^{(+)}\left(y_n,z_n\right)}{\left(1-M^2\right)}\right) \\ \times\ \Phi_{nm}^{(+)}\left(y,z\right)\kappa_z\left(d\right)e^{-ik_x^{(+)}(x-x_n)}\frac{\sin\left(k_{\mathrm{x}}^{(+)}d\right)}{k_{\mathrm{x}}^{(+)}d}2d\end{aligned} \tag{A.3.24}$$

CASE 2: The observation point is downstream of the source, i.e. $x < x_n - d$. This case is illustrated in Figure A.3.2b and implies that $x < \tilde{x}$ and the following integral needs to be solved

$$\frac{p(\vec{x}|\vec{x}_n)}{v_n} = -i\omega\rho \int_{x_n-d}^{x_n+d}\int_{z_n-d}^{z_n+d} g^{(-)}\left(x,y,z|\tilde{x},y_n,\tilde{z}\right)d\tilde{x}d\tilde{z} \tag{A.3.25}$$

Replacing (A.3.18b) into (A.3.25) and considering (A.3.22) and (A.3.9) results in

$$\frac{p(x,y,z|x_n,y_n,z_n)}{v_n} = \frac{k_o \rho c}{ab} \sum_{n=0}^{N_g} \sum_{m=0}^{M_g} \left(\sum_{r=0}^{N_g} \frac{T_{rn,m}^{(-)} \Phi_{rm}^{(+)}(y_n,z_n)}{\left(1-M^2\right)} \right) \times \Phi_{nm}^{(-)}(y,z) \kappa_z(d) e^{-ik_x^{(-)}(x-x_n)} \frac{\sin\left(\mathrm{k}_\mathrm{x}^{(-)} d\right)}{\mathrm{k}_\mathrm{x}^{(-)} d} 2d \tag{A.3.26}$$

CASE 3: The observation point is on the surface of the source, i.e., $x_n - d < x < x_n + d$. This case is illustrated in Figure A.3.2c and requires the separation of the integral into two parts as

$$\frac{p(\vec{x}|\vec{x}_n)}{v_n} = -i\omega\rho \int_{z_n-d}^{z_n+d} \left\{ \int_{x_n-d}^{x} g^{(+)}\left(x,y,z|\tilde{x},y_n,\tilde{z}\right) d\tilde{x} + \int_{x}^{x_n+d} g^{(-)}\left(x,y,z|\tilde{x},y_n,\tilde{z}\right) d\tilde{x} \right\} d\tilde{z} \tag{A.3.27}$$

To solve (A.3.27), it is required to find the following integrals as follows

$$\int_{x_n-d}^{x} e^{-ik_x^{(+)}(x-\tilde{x})} d\tilde{x} = \frac{1-e^{-ik_x^{(+)}(x-x_n+d)}}{ik_x^{(+)}} \tag{A.3.28a}$$

and

$$\int_{x}^{x_n+d} e^{-ik_x^{(-)}(x-\tilde{x})} d\tilde{x} = -\frac{1-e^{-ik_x^{(-)}(x-x_n-d)}}{ik_x^{(-)}} \tag{A.3.28b}$$

Thus, replacing (A.3.18a) and (A.3.18b) into (A.3.27) and considering (A.3.22), (A.3.28a) and (A.3.29b) results in

$$\frac{p(x,y,z|x_n,y_n,z_n)}{v_n}$$

$$= \frac{k_o \rho c}{ab} \sum_n^{N_g} \sum_m^{M_g} \left\{ \left(\sum_{r=0}^{N_g} \frac{T_{rn,m}^{(+)} \Phi_{rm}^{(+)}(y_n,z_n)}{\left(1-M^2\right)} \right) \Phi_{nm}^{(+)}(y,z) \kappa_z(d) \left(\frac{1-e^{-ik_x^{(+)}(x-x_n+d)}}{ik_x^{(+)}} \right) - \right.$$

$$\left. \left(\sum_{r=0}^{N_g} \frac{T_{rn,m}^{(-)} \Phi_{rm}^{(+)}(y_n,z_n)}{\left(1-M^2\right)} \right) \Phi_{nm}^{(-)}(y,z) \kappa_z(d) \left(\frac{1-e^{-ik_x^{(-)}(x-x_n+d)}}{ik_x^{(-)}} \right) \right\} \qquad \text{(A.3.29)}$$

As for the hard wall case, it is necessary to compute the average pressure over a source due to another position source with unit velocity, i.e. impedance function. That is, we need to solve eq.(A.3.13) again. As in section A.3.1, there are three cases to solve for the integration in the *x*-direction. They are

CASE 1: The observation source "*r*" is downstream of the source "*s*" as shown in figure A.3.3a. That is $x_n - d_r > x_s + d_s$. Replacing (A.3.24) into (A.3.13) and solving the following integral as

$$\begin{aligned} &\int_{x_r-d_r}^{x_r+d_r} e^{-ik_x^{(+)}(x-x_s)} \frac{\sin(k_x^{(+)}d_s)}{k_x^{(+)}d_s} 2d_s dx \\ &= e^{-ik_x^{(+)}(x_r-x_s)} \frac{\sin(k_x^{(+)}d_r)}{k_x^{(+)}d_r} 2d_r \frac{\sin(k_x^{(+)}d_s)}{k_x^{(+)}d_s} 2d_s \end{aligned} \qquad \text{(A.3.30a)}$$

results in

$$Z_{rs} = \frac{k_o \rho c}{S_r ab} \sum_{n=0}^{N_g} \sum_{m=0}^{M_g} \left(\sum_{r=0}^{N_g} \frac{T_{rn,m}^{(+)} \Phi_{rm}^{(+)}(y_r, z_r)}{\left(1 - M^2\right)} \right) \Phi_{nm}^{(+)}(y_s, z_s)$$
$$\times \ \kappa_z(d_r) \kappa_z(d_s) e^{-ik_x^{(+)}(x_r - x_s)} \frac{\sin(k_x^{(+)} d_r)}{k_x^{(+)} d_r} 2d_r \frac{\sin(k_x^{(+)} d_s)}{k_x^{(+)} d_s} 2d_s \tag{A.3.31}$$

CASE 2: The observation source "*r*" is upstream of the source "*s*" as shown in figure A.3.3b. That is $x_r + d_s < x_s - d_s$. Replacing (A.3.26) into (A.3.13) and solving the following integral as

$$\int_{x_r - d_r}^{x_r + d_r} e^{-ik_x^{(-)}(x - x_s)} \frac{\sin(k_x^{(-)} d_s)}{k_x^{(-)} d_s} 2d_s dx$$
$$= e^{-ik_x^{(-)}(x_r - x_s)} \frac{\sin(k_x^{(-)} d_r)}{k_x^{(-)} d_r} 2d_r \frac{\sin(k_x^{(-)} d_s)}{k_x^{(-)} d_s} 2d_s \tag{A.3.32}$$

that yields

$$Z_{rs} = \frac{k_o \rho c}{S_r ab} \sum_{n=0}^{N_g} \sum_{m=0}^{M_g} \left(\sum_{r=0}^{N_g} \frac{T_{rn,m}^{(-)} \Phi_{rm}^{(+)}(y_r, z_r)}{\left(1 - M^2\right)} \right) \Phi_{nm}^{(-)}(y_s, z_s)$$
$$\times \ \kappa_z(d_r) \kappa_z(d_s) e^{-ik_x^{(-)}(x_r - x_s)} \frac{\sin(k_x^{(-)} d_r)}{k_x^{(-)} d_r} 2d_r \frac{\sin(k_x^{(-)} d_s)}{k_x^{(-)} d_s} 2d_s \tag{A.3.33}$$

CASE 3: The observation source "*r*" and the source "*s*" are at the same axial location , i.e. $x_r = x_s$. Replacing (A.3.29) into (A.3.13) and solving the following integrals

$$\int_{x_r - d_r}^{x_r + d_r} \frac{1 - e^{-jk_x^{(+)}(x - x_s + d_s)}}{ik_x^{(+)}} dx = \frac{2d_r}{ik_x^{(+)}} + \frac{1 - e^{-ik_x^{(+)} 2d_r}}{\left(k_x^{(+)}\right)^2} \tag{A.3.34a}$$

and

$$\int_{x_r-d_r}^{x_r+d_r} -\frac{1-e^{-jk_x^{(-)}(x-x_s-d_s)}}{ik_x^{(+)}}dx = -\frac{2d_r}{ik_x^{(-)}} + \frac{1-e^{-ik_x^{(-)}2d_r}}{\left(k_x^{(-)}\right)^2} \tag{A.3.34b}$$

results in

$$\frac{\overline{p}}{v_s} = \frac{k_o \rho c}{S_r ab} \sum_{n=0}^{N_g} \sum_{m=0}^{M_g} \left\{ \left(\sum_{r=0}^{N_g} \frac{T_{rn,m}^{(+)} \Phi_{rm}^{(+)}\left(y_r, z_r\right)}{\left(1-M^2\right)} \right) \right.$$
$$\times\ \Phi_{nm}^{(+)}\left(y_s, z_s\right) \kappa_z\left(d_r\right) \kappa_z\left(d_s\right) \left(\frac{2d_r}{ik_x^{(+)}} + \frac{1-e^{-ik_x^{(+)}2d_r}}{\left(k_x^{(+)}\right)^2} \right) +$$
$$\left. \left(\sum_{r=0}^{N_g} \frac{T_{rn,m}^{(-)} \Phi_{rm}^{(+)}\left(y_r, z_r\right)}{\left(1-M^2\right)} \right) \Phi_{nm}^{(-)}\left(y_s, z_s\right) \kappa_z\left(d_r\right) \kappa_z\left(d_s\right) \left(-\frac{2d_r}{ik_x^{(-)}} + \frac{1-e^{-ik_x^{(-)}2d_r}}{\left(k_x^{(-)}\right)^2} \right) \right\} \tag{A.3.35}$$

It is important to note that in eqs.(A.3.34a-b) we have assumed that $d_r = d_s$. This implies that the formulation developed here is valid only for tubes of the same cross-sectional area.

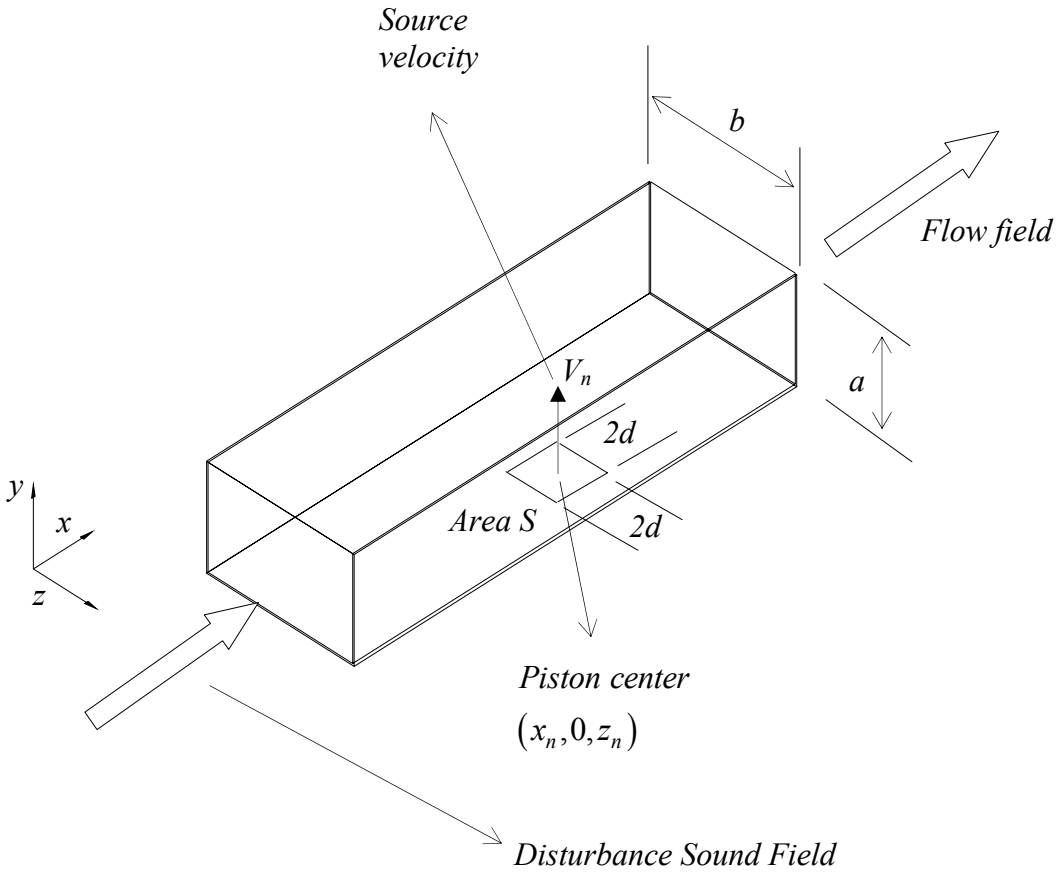

Figure A.3.1: Piston sources

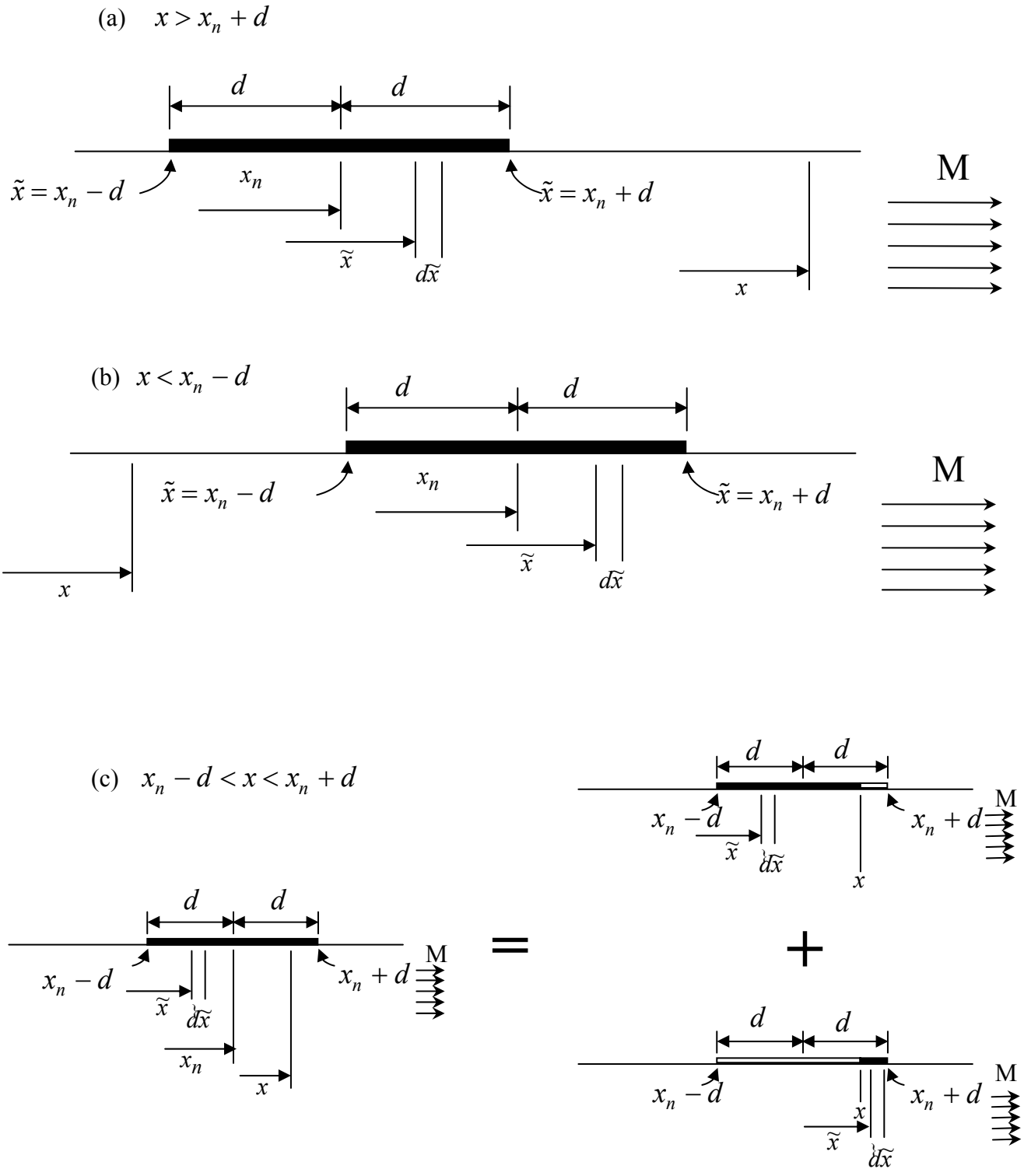

Figure A.3.2 : Elements of integration over the source surface
(a) case 1: observation point x is downstream of the source
(b) case 2: observation point x is upstream of the source
(c) case 3: observation point x is on the surface of the source.

(a) $x_r - d_r > x_s + d_s$

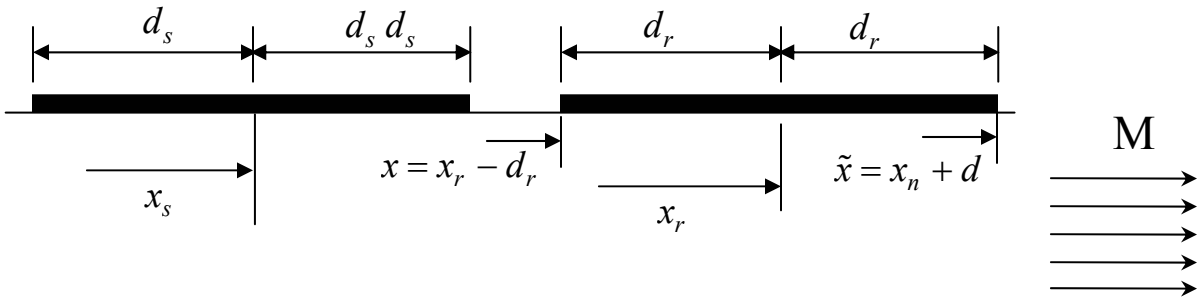

(b) $x_r + d_r < x_s - d_s$

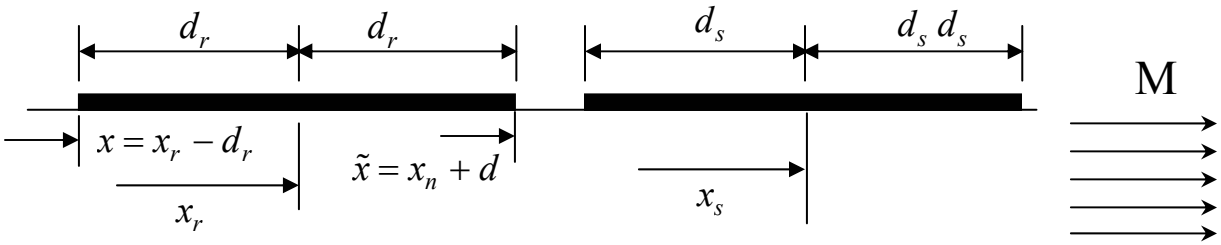

(c) $x_r = x_s \quad d_r = d_s$

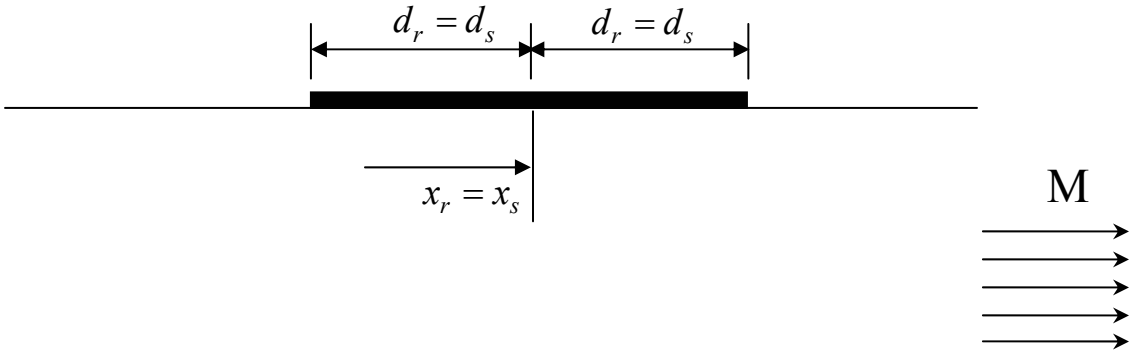

Figure A.3.3: (a) case 1: observation source *"r"* is downstream of the source *"s"*
(b) case 2: observation source *"r"* is upstream of the source *"s"*
(c) case 3: observation source *"r"* and source *"s"* at the same axial location

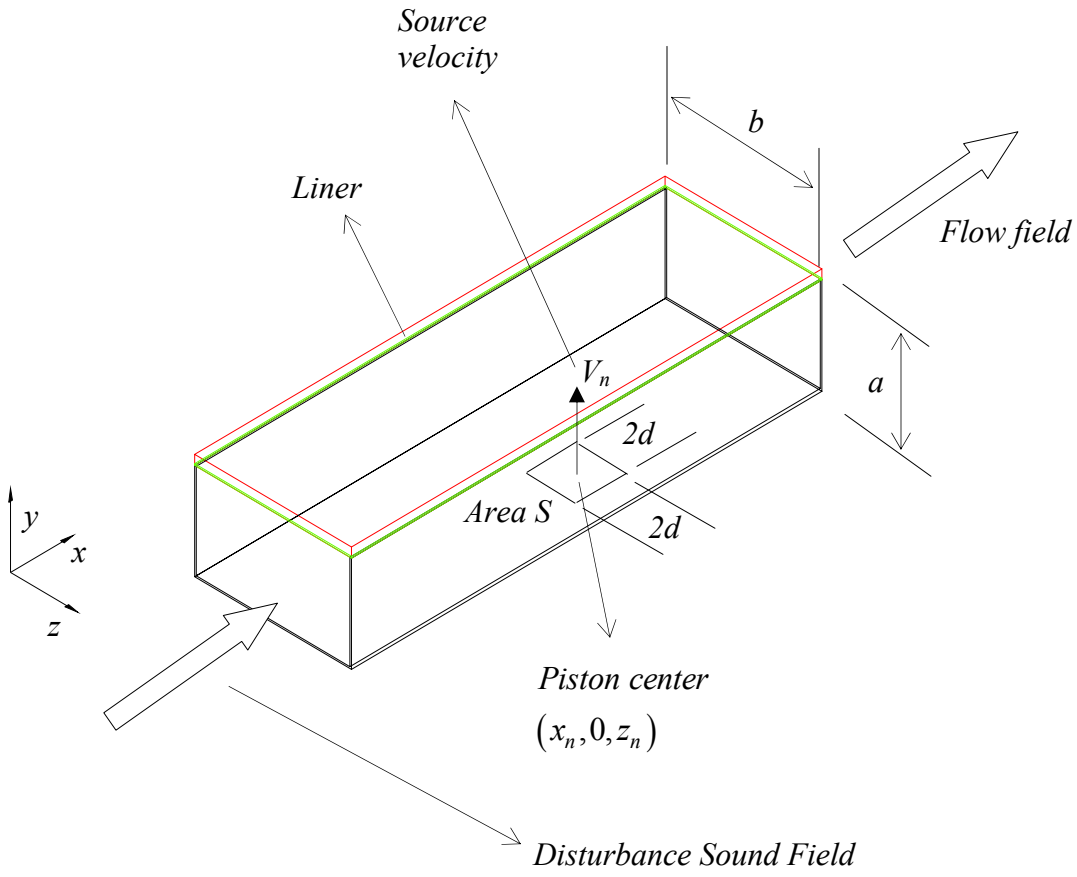

Figure A.3.4: Piston source in a lined duct

A.4 Average Pressure over Sources due to Disturbance

The average pressure over a piston source located at (x_n, y_n, z_n) due to the disturbance given as

$$\overline{P}_d(x_n, y_n, z_n) = \frac{1}{S}\int_{x_n-d}^{x_n+d}\int_{z_n-d}^{z_n+d} p_d(x,y,z)dxdz \tag{A.4.1}$$

where the piston source has area $S = (2d)^2$. Note that y_n can take the value of "0" or "a".

Replacing eqs.(2.1) and (A.1.51a) into (A.4.1) gives

$$\overline{p}_d(x_n, y_n, z_n) = \frac{1}{S}\sum_{n=0}^{N_d}\sum_{m=0}^{M_d} A_{nm}^d \cos\left(k_y^{(+)} y_n\right)\int_{z_n-d}^{z_n+d}\cos\left(\frac{m\pi}{b}z\right)dz\int_{x_n-d}^{x_n+d} e^{-ik_x^{(+)}x}dx \tag{A.4.2}$$

Solving the integrals as

$$\int_{z_n-d}^{z_n+d}\cos\left(\frac{m\pi}{b}z\right)dz = \cos\left(\frac{m\pi}{b}z_n\right)\frac{2d\sin\left(\frac{m\pi}{b}d\right)}{\left(\frac{m\pi}{b}d\right)}$$

and

$$\int_{x_n-d}^{x_n+d} e^{-ik_x^{(+)}x}dx = e^{-ik_x^{(+)}x_n}\frac{2d\sin(k_x^{(+)}d)}{k_x^{(+)}d}$$

Thus, equation (A.4.2) becomes

$$\overline{p}_d\left(x_n, y_n, z_n\right) = \sum_{n=0}^{N_d}\sum_{m=0}^{M_d} A_{nm}^{d}\Phi_{nm}^{(+)}\left(y_n, z_n\right)e^{-ik_x^{(+)}x_n}\frac{\sin\left(\frac{m\pi}{b}d\right)}{\left(\frac{m\pi}{b}d\right)}\frac{\sin\left(k_x^{(+)}d\right)}{k_x^{(+)}d} \qquad \text{(A.4.3)}$$

where $\Phi_{nm}^{(+)}$ is the positive *x*-propagating mode.

The average pressure over the sources due to the disturbance is easily computed. The general expression for the average pressure over the n^{th} source due to the disturbance is

$$\overline{p}_d\left(x_n, y_n, z_n\right) = \sum_{n=0}^{N_d}\sum_{m=0}^{M_d} A_{nm}^{d}\Phi_{nm}^{(+)}\left(y_n, z_n\right)e^{-ik_x^{(+)}x_n}\frac{\sin\left(\frac{m\pi}{b}d\right)}{\left(\frac{m\pi}{b}d\right)}\frac{\sin\left(k_x^{(+)}d\right)}{k_x^{(+)}d} \qquad \text{(A.4.4)}$$

A.5 Modeling of HQ-Tubes

In practice, the HQ-tubes are constructed as a semi-circle or other smooth shapes. However, for modeling purposes they are considered as straight tubes with uniform cross-sections, as shown in figure A.5.1.

The sound fields inside the tubes are assumed to consist of plane waves only, a valid assumption well below the first cut-on frequency of the tubes. The sound field inside a tube is expressed in terms of a positive and a negative traveling plane wave of amplitudes A and B, respectively. If ξ is the local tube coordinate, the pressure and particle velocity are given as

$$p'(\xi,t) = Ae^{-ik_o\xi} + Be^{+ik_o\xi} \tag{A.5.1}$$

and

$$v'(\xi,t) = \frac{Ae^{-ik_o\xi} - Be^{+ik_o\xi}}{\rho c} \tag{A.5.2}$$

The acoustic pressure and particle velocity at the ends of the tube are expressed in the following matrix form:

$$\begin{Bmatrix} p'_{\ell i} \\ \rho c v'_{\ell i} \end{Bmatrix} = [T_t] \begin{Bmatrix} p'_{\ell o} \\ \rho c v'_{\ell o} \end{Bmatrix} = \begin{bmatrix} \cos(k_o L) & i\sin(k_o L) \\ i\sin(k_o L) & \cos(k_o L) \end{bmatrix} \begin{Bmatrix} p'_{\ell o} \\ \rho c v'_{\ell o} \end{Bmatrix} \tag{A.5.3}$$

where L is the centerline length of the tubes.

A perforated screen is placed at the ends of each tube to limit the effect of discontinuities (vortex shedding) in the duct, which could create an additional noise source. The effect of these perforated screens is included as

$$\begin{Bmatrix} p^t_{\ell i} \\ \rho c v^t_{\ell i} \end{Bmatrix} = \begin{bmatrix} T_{ps} \end{bmatrix} \begin{Bmatrix} p'_{\ell i} \\ \rho c v'_{\ell i} \end{Bmatrix} \text{ and } \begin{Bmatrix} p'_{\ell o} \\ \rho c v'_{\ell o} \end{Bmatrix} = \begin{bmatrix} T_{ps} \end{bmatrix} \begin{Bmatrix} p^t_{\ell o} \\ \rho c v^t_{\ell o} \end{Bmatrix} \tag{A.5.4}$$

where the transfer matrix of the perforated screen T_{ps} is

$$\begin{bmatrix} T_{ps} \end{bmatrix} = \begin{bmatrix} 1 & \dfrac{Z_{ps}}{\rho c} \\ 0 & 1 \end{bmatrix} \tag{A.5.5}$$

where Z_{ps} is the impedance of the perforated screen. The impedances of the perforate screens are provided by Goodrich aerostructure group for this investigation.

Including the effects of the perforated screens, the matrix that relates the pressure and particle velocity at the tube ends is

$$\begin{Bmatrix} p^t_{\ell i} \\ \rho c v^t_{\ell i} \end{Bmatrix} = \begin{bmatrix} T_{ps} \end{bmatrix} \begin{bmatrix} T_t \end{bmatrix} \begin{bmatrix} T_{ps} \end{bmatrix} \begin{Bmatrix} p^t_{\ell o} \\ \rho c v^t_{\ell o} \end{Bmatrix} = \begin{bmatrix} T_{11} & T_{12} \\ T_{21} & T_{22} \end{bmatrix} \begin{Bmatrix} p^t_{\ell o} \\ \rho c v^t_{\ell o} \end{Bmatrix} \tag{A.5.7}$$

Then, rearranging eq.(A.5.7), the impedance matrix for the ℓ^{th} tube can be expressed as

$$\begin{Bmatrix} p^t_{\ell i} \\ p^t_{\ell o} \end{Bmatrix} = \rho c \begin{bmatrix} \dfrac{T_{11}}{T_{21}} & \dfrac{T_{12}T_{21} - T_{11}T_{22}}{T_{21}} \\ \dfrac{1}{T_{21}} & -\dfrac{T_{22}}{T_{21}} \end{bmatrix} \begin{Bmatrix} v^t_{\ell i} \\ v^t_{\ell o} \end{Bmatrix} = \begin{bmatrix} Z^{t\ell}_{ii} & Z^{t\ell}_{io} \\ Z^{t\ell}_{oi} & Z^{t\ell}_{oo} \end{bmatrix} \begin{Bmatrix} v^t_{\ell i} \\ v^t_{\ell o} \end{Bmatrix} \tag{A.5.8}$$

where the impedance matrix in (A.5.8) relates the pressure to the particle velocity at the two ends of the ℓ^{th} tube, including the effect of the perforated screen.

It is important to note that in the process of matching the source velocity to the corresponding tube particle velocity, a consistent convention for the positive direction must be kept. To this end, the positive particle velocity in the entrance end of the tube at $\xi = 0$, which is opposite to the positive source velocity, is reversed by changing the sign of the first column of the matrix in (A.5.8). This will then yield

$$\begin{Bmatrix} p_{\ell i}^{t} \\ p_{\ell o}^{t} \end{Bmatrix} = \rho c \begin{bmatrix} -\dfrac{T_{11}}{T_{21}} & \dfrac{T_{12}T_{21} - T_{11}T_{22}}{T_{21}} \\ -\dfrac{1}{T_{21}} & -\dfrac{T_{22}}{T_{21}} \end{bmatrix} \begin{Bmatrix} v_{\ell i}^{t} \\ v_{\ell o}^{t} \end{Bmatrix} = \begin{bmatrix} Z_{ii}^{t\ell} & Z_{io}^{t\ell} \\ Z_{oi}^{t\ell} & Z_{oo}^{t\ell} \end{bmatrix} \begin{Bmatrix} v_{\ell i}^{t} \\ v_{\ell o}^{t} \end{Bmatrix} \tag{A.5.9}$$

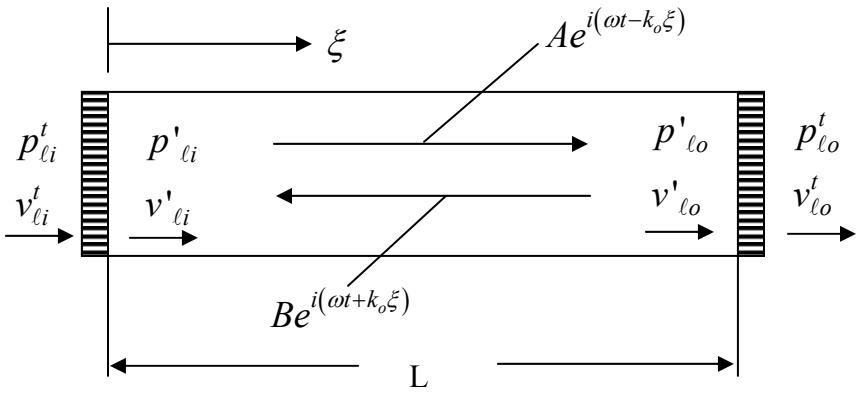

Figure A.5.1: Simplified model of HQ-tube

A.6. Transmitted Acoustic Power

A.6.1 Intensity Field

From sound intensity the total acoustic power can be calculated . The sound intensity in the *x*-direction in the presence of a uniform flow is given as [1]

$$I_x = \frac{1}{2} real\left[\left(\frac{p}{\rho} + v_x cM\right)\left(\rho v_x + p\frac{M}{c}\right)^*\right] \tag{A.6.1}$$

that can also be written as

$$I_x = \frac{1}{2} Real\left[pv_x^* + \rho c\left|v_x\right|^2 M + \frac{\left|p\right|^2}{\rho c} M + v_x p^* M^2 \right] \tag{A.6.2}$$

where v_x is the particle velocity in the *x*-direction, and an asterisk (*) denotes the complex conjugate.

To compute the intensity, the particle velocity in the *x*-direction is obtained from Euler's equation as

$$-\frac{\partial p}{\partial x} = i\omega\rho v_x + \rho cM\frac{\partial v_x}{\partial x} \tag{A.6.3}$$

Since, the particle velocity is given as

$$v_x\left(x,y,z\right) = v_x\left(y,z\right)e^{-ik_x^{(+)}x} \tag{A.6.4}$$

equation (A.6.3) becomes

$$-\frac{\partial p}{\partial x} = i\rho c\left(k_o - k_x^{(+)}M\right)v_x\left(y,z\right)e^{-ik_x^{(+)}x} \tag{A.6.5}$$

that can be solved for the particle velocity as

$$v_x\left(y,z\right)e^{-ik_x^{(+)}x} = -\frac{1}{i\rho c\left(k_o - k_x^{(+)}M\right)}\frac{\partial p}{\partial x} \tag{A.6.6}$$

Replacing the transmitted pressure from (A.4.19) into (A.4.6) results

$$v_x(x,y,z)=\sum_{n=0}^{N_g}\sum_{m=0}^{N_g}\frac{A_{nm}^{(+)}\Phi_{nm}^{(+)}(y,z)k_x^{(+)}e^{-ik_x^{(+)}x}}{\rho c\left(k_o-k_x^{(+)}M\right)} \tag{A.6.7}$$

A.6.2 Acoustic Power

The acoustic power is obtained by integrating the intensity as

$$W=\int_0^a\int_0^b I_x\,dydx \tag{A.6.8}$$

The transmitted acoustic power is obtained by replacing (A.6.7) into (A.6.2). Note that in this process we need to change the indices (*n,m*) by (*r,s*) in eq. (A.6.7).
It is clear that the following integral needs to be solved

$$\int_0^a\int_0^b \Phi_{nm}^{(+)}(y,z)\Phi_{rs}^{*(+)}(y,z)\,dydz \tag{A.6.9}$$

For the case of hard wall conditions, the mode shapes are real and the integral in eq. (A.6.9) was previously solved in (A.2.4) as

$$\int_0^a\int_0^b \Phi_{nm}(y,z)\Phi_{rs}(y,z)\,dydz=ab\Lambda_{nm}\delta_{nr}\delta_{ms} \tag{A.6.10}$$

where $\Lambda_{nm}=\varepsilon_n\varepsilon_m$ with $\varepsilon_n(\varepsilon_m)=1$ for $n(m)=0$ and $\varepsilon_n(\varepsilon_m)=1/2$ for $n(m)\geq 1$. Using the orthogonality property of the modes, the total transmitted power is given as

$$W = \sum_{n=0}^{N_g} \sum_{m=0}^{M_g} W_{nm}^{(+)} \tag{A.6.11}$$

where

$$W_{nm}^{(+)} = \frac{\left| \left(A_{nm}^{(+)} \right)_{hq} \right|^2}{\rho c} ab\Lambda_{nm} \left\{ \left(1 + M^2\right) Real\left[\frac{\left(k_x^{(+)}\right)^*}{\left(k_o - k_x^{(+)} M\right)^*} \right] + \frac{M \left| k_x^{(+)} \right|^2}{\left| k_o - k_x^{(+)} M \right|^2} + M \right\} \tag{A.6.12}$$

is the (n,m) modal power.

For the case of a lined duct, the computation of the acoustic power is more involved because the modes are not orthogonal. The integral in (A.6.9) is solved, and is given as

$$\int_0^a \int_0^b \Phi_{nm}^{(+)}(y,z) \Phi_{rm}^{*(+)}(y,z) dzdy = ab\hat{\Lambda}_{nr,m}^{(+)} \tag{A.6.13}$$

Note that we have taken advantage of the fact that the modes are orthogonal with respect to the "m" index, i.e. $m=s$.

The acoustic power is then given as

$$W = \frac{1}{2} real \left[\sum_{m=0}^{M_g} \sum_{n=0}^{N_g} \sum_{r=0}^{N_g} \frac{A_{nm}^{(+)} A_{rm}^{(+)^*} ab \hat{\Lambda}_{nr,m}^{(+)}}{\rho c} \frac{\left(k_x^{(+)}\right)_{rm}^*}{k_o - \left(k_x^{(+)}\right)_{rm}^* M} + \right.$$

$$\sum_{m=0}^{M_g} \sum_{n=0}^{N_g} \sum_{r=0}^{N_g} \frac{A_{nm}^{(+)^*} A_{rm}^{(+)} ab \hat{\Lambda}^{*(+)}_{nr,m}}{\rho c} M^2 \frac{\left(k_x^{(+)}\right)_{rm}}{k_o - \left(k_x^{(+)}\right)_{rm} M} +$$

$$\sum_{m=0}^{M_g} \sum_{n=0}^{N_g} \sum_{r=0}^{N_g} \frac{A_{nm}^{(+)} A_{rm}^{(+)^*} ab \hat{\Lambda}_{nr,m}^{(+)}}{\rho c} M \frac{\left(k_x^{(+)}\right)_{nm} \left(k_x^{(+)}\right)_{rm}^*}{\left(k_o - \left(k_x^{(+)}\right)_{nm} M\right)\left(k_o - \left(k_x^{(+)}\right)_{rm}^* M\right)} +$$

$$\left. \sum_{m=0}^{M_g} \sum_{n=0}^{N} \sum_{r=0}^{N_g} \frac{A_{nm}^{(+)} A_{rm}^{(+)^*} ab \hat{\Lambda}_{nr,m}^{(+)}}{\rho c} M \right]$$

(A.6.14)

APPENDIX B

It is useful to calculate the overall insertion loss to compare the overall performance of the configurations tested in this research using a single metric. To this end, the calculation of the overall insertion loss is presented in section B.1 of this Appendix. The overall insertion loss is determined based on the measured insertion loss at the 1/3 octave band frequencies. The predicted overall insertion loss for all the configuration, using both the predicted and measured data, are tabulated in section B.2.

B.1 Calculation of Overall Insertion Loss

As indicated before, the approach is to compute the overall insertion loss from the insertion loss at the 1/3 octave bands. Thus, the overall sound power for the reference hard wall configuration is given as

$$L_{W-HW} = 10Log_{10}\left[\sum_{i=1}^{N_B} 10^{\frac{L_{Wi}}{10}}\right] dB \qquad \text{(B.1)}$$

where N_B is the number of 1/3 octave bands and L_{Wi} is the sound power level for each 1/3 octave band frequency. Assuming that all bands have the same power levels, i.e. $L_{Wi} = \hat{L}_W$ for *i =1, 2, ...N_B*, equation (B.1) reduces to

$$L_{W-HW} = 10Log_{10}\left[N_B 10^{\frac{\hat{L}_W}{10}}\right] dB \qquad \text{(B.2)}$$

The overall sound power level for liner-HQ or HQ on a hard-walled duct system can be obtained by subtracting the insertion loss at each band from the original sound power level of the hard wall condition given in equation (B.2). Figure B.1 (b) illustrated

the approach. Thus, the overall sound power of the a particular configuration, e.g. liner-HQ, is given as

$$L_{W-(liner-HQ)} = 10Log_{10}\left[\sum_{i=1}^{N_B} 10^{\frac{(L_{Wi}-\Delta_i)}{10}}\right] = 10Log_{10}\left[10^{\frac{\hat{L}_W}{10}}\sum_{i=1}^{N_B} 10^{\frac{-\Delta_i}{10}}\right] dB \qquad \text{(B.3)}$$

where Δ_i is the insertion loss (sound power reduction) of the i^{th} 1/3 octave band.

Thus, overall insertion loss or sound power reduction is then given as

$$\left(\Delta L_W\right)_{overall} = L_{W-HW} - L_{W-(liner-HQ)} \qquad \text{(B.4)}$$

Replacing equations (B.2) and (B.3) into (B.4), the overall insertion loss (or sound power reduction) is obtained as

$$\left(\Delta L_W\right)_{overall} = 10Log_{10}\left[N_B 10^{\frac{\hat{L}_W}{10}}\right] - 10Log_{10}\left[10^{\frac{\hat{L}_W}{10}}\sum_{i=1}^{N_B} 10^{\frac{-\Delta_i}{10}}\right] dB \qquad \text{(B.5)}$$

or

$$\left(\Delta L_W\right)_{overall} = -10Log_{10}\left[\sum_{i=1}^{N_B}\frac{10^{\left(\frac{-\Delta_i}{10}\right)}}{N_B}\right] \qquad \text{(B.6)}$$

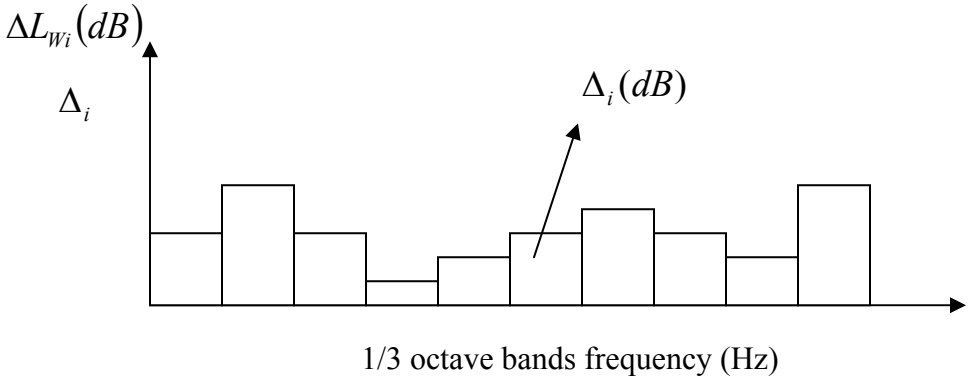

(a)

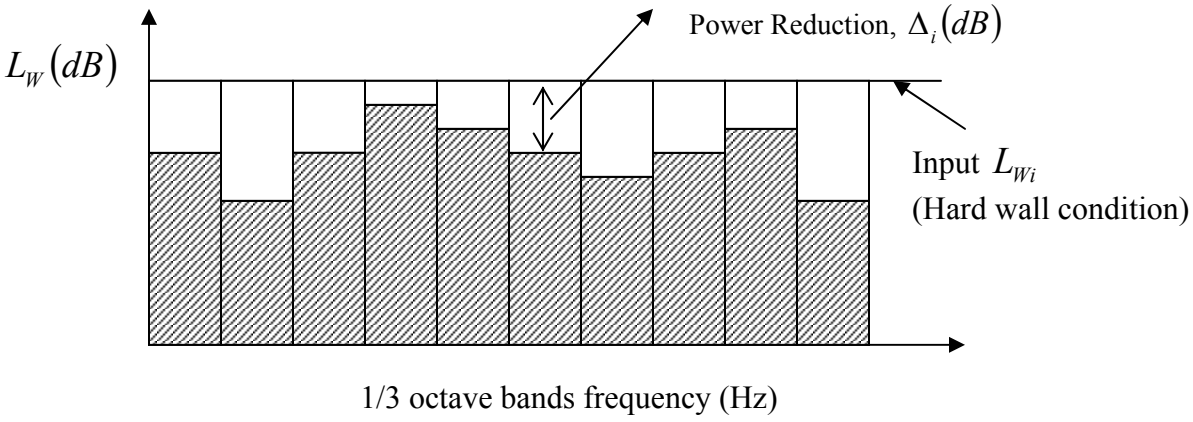

(b)

Figure B.1: Schematic of sound power reduction on 1/3 octave frequency bands

(a) Insertion loss or sound power reduction in i^{th} band

(b) Illustration of sound power reduction and hard wall condition power level

B.2 Overall Insertion Loss Results

Table B.1: Overall insertion loss of predicted and measured data for each configuration.

Conf #	Mach 0.0		Mach 0.2		Mach 0.3		Mach 0.4		Mach 0.5		Mach 0.6	
	Pre.	Mea.	Pre.	Mea.	Pre.	Mea.	Pre.	Mea.	Pre.	Mea.	Pre.	Mea.
1	0.41	0.79	0.45	0.73	0.44	0.69	0.42	0.54	0.39	-0.28	0.36	-0.19
2	0.29	0.41	0.33	0.61	0.33	0.60	0.32	0.22	0.31	-0.12	0.30	-0.36
3	0.51	0.73	0.54	0.73	0.52	0.51	0.49	0.18	0.47	-0.20	0.41	-0.27
4	0.36	0.61	0.39	0.54	0.38	0.43	0.37	-0.01	0.36	-0.10	0.33	-0.45
5	0.40	0.81	0.44	0.66	0.43	0.74	0.40	0.25	0.37	0.21	0.34	-0.22
6	0.29	0.65	0.32	0.69	0.32	0.58	0.31	0.05	0.30	-0.03	0.29	-0.22
7	0.49	0.88	0.52	0.79	0.50	0.71	0.48	0.23	0.44	-0.18	0.38	-0.44
8	0.34	0.63	0.38	0.45	0.37	0.61	0.36	0.08	0.35	-0.40	0.30	-0.44
9	0.40	0.81	0.40	0.59	0.38	0.60	0.34	0.24	0.30	-0.10	0.29	-0.17
10	0.28	0.76	0.29	0.32	0.29	0.43	0.27	0.25	0.24	0.35	0.25	0.01
11	0.45	0.72	0.48	0.44	0.47	0.50	0.43	0.38	0.39	0.25	0.31	-0.12
12	0.32	0.43	0.35	0.02	0.35	0.13	0.32	0.16	0.30	0.14	0.25	-0.12
13	0.23	1.62	1.83	1.81	1.93	1.66	1.97	1.86	1.88	1.93	1.75	1.07
14	2.65	3.22	2.22	2.08	2.10	1.61	1.95	2.55	1.81	2.20	1.71	1.34
15	-1.41	1.30	2.31	1.91	2.34	2.10	2.31	2.28	2.16	1.76	1.95	0.88
16	-0.72	1.96	2.17	2.14	2.22	2.05	2.20	2.49	2.07	2.05	1.89	0.96
17	-0.96	1.89	2.36	2.01	2.37	2.13	2.33	2.20	2.18	1.97	1.95	0.92
18	-0.23	1.66	2.20	1.90	2.24	2.28	2.21	2.68	2.08	1.92	1.89	0.68
19	3.18	3.95	2.73	3.00	2.59	2.50	2.38	2.63	2.18	2.28	2.07	0.91
20	3.01	3.07	2.57	2.63	2.43	2.07	2.24	2.64	2.06	2.21	1.98	0.82
21	3.21	2.36	2.77	2.22	2.62	2.18	2.40	2.79	2.20	2.43	2.01	1.11
22	3.04	3.31	2.60	2.80	2.46	2.53	2.46	2.60	2.08	2.36	1.99	1.04
23	-1.41	2.13	2.31	2.36	2.34	2.41	2.31	2.62	2.16	2.11	1.95	1.11
24	-0.72	1.76	2.17	2.00	2.22	1.83	2.20	2.18	2.07	2.14	1.89	1.20
25	-0.96	0.59	2.36	1.90	2.37	1.92	2.33	2.51	2.18	1.84	1.95	0.84
26	-0.23	1.95	2.20	2.23	2.24	1.99	2.21	2.20	2.08	1.63	1.89	0.46
27	3.18	3.83	2.73	2.69	2.59	2.30	2.38	2.31	2.18	1.60	2.07	0.62
28	3.01	3.61	2.57	2.87	2.43	2.33	2.24	2.45	2.06	1.84	1.98	0.33
29	3.21	3.77	2.77	3.11	2.62	2.67	2.40	2.84	2.20	2.20	2.01	0.72
30	3.04	3.74	2.60	3.21	2.46	2.59	2.46	2.84	2.08	2.20	1.99	1.02
31	3.06	3.98	2.70	2.95	2.58	3.00	2.41	2.71	2.25	2.26	2.13	1.19
32	2.93	2.98	2.55	2.67	2.43	2.79	2.27	2.59	2.11	2.21	2.00	1.02
33	3.11	3.09	2.74	2.76	2.61	2.64	2.43	2.93	2.27	2.18	2.15	1.02
34	2.97	4.11	2.58	3.35	2.45	3.24	2.49	2.84	2.13	1.84	2.01	0.86

Table B.1: Overall insertion loss (Continue)

Conf #	Mach 0.0		Mach 0.2		Mach 0.3		Mach 0.4		Mach 0.5		Mach 0.6	
	Pre.	Mea.	Pre.	Mea.	Pre.	Mea.	Pre.	Mea.	Pre.	Mea.	Pre.	Mea.
35	3.03	3.16	2.72	2.20	2.60	2.41	2.45	2.78	2.30	2.63	2.19	1.29
36	2.91	3.72	2.56	3.07	2.44	3.20	2.29	3.34	2.15	2.51	2.04	1.39
37	3.08	3.99	2.75	2.57	2.64	3.03	2.48	3.15	2.32	2.52	2.21	1.02
38	2.94	3.84	2.59	3.29	2.47	3.17	2.53	3.09	2.17	2.08	2.06	1.01
39	2.96	3.91	2.70	3.18	2.62	3.27	2.49	3.04	2.36	2.05	2.26	1.20
40	2.86	3.78	2.55	3.44	2.46	3.48	2.32	2.96	2.19	2.15	2.09	0.97
41	3.00	3.87	2.76	3.48	2.68	3.70	2.54	2.63	2.40	1.81	2.30	1.00
42	2.89	3.28	2.59	2.39	2.50	3.12	2.57	2.91	2.22	2.11	2.12	1.03
43	0.58	0.79	0.59	0.43	0.60	0.34	0.61	0.49	0.61	0.13	0.61	-0.16
44	0.41	0.83	0.42	0.40	0.42	0.30	0.43	0.34	0.43	0.12	0.43	-0.01
45	0.59	0.82	0.60	0.51	0.61	0.74	0.61	0.94	0.62	0.41	0.62	0.17
46	0.42	0.43	0.43	0.43	0.43	0.48	0.52	0.23	0.43	0.31	0.44	-0.06
47	0.63	0.76	0.65	0.37	0.65	0.33	0.66	0.28	0.67	0.07	0.67	-0.09
48	0.45	0.59	0.46	0.39	0.46	0.47	0.47	0.40	0.48	0.17	0.47	-0.29
49	0.64	0.04	0.66	0.28	0.66	0.51	0.67	0.55	0.67	0.40	0.68	-0.05
50	0.46	0.44	0.47	0.11	0.47	0.10	0.57	0.18	0.48	-0.12	0.48	-0.27
51	0.67	0.41	0.71	-0.41	0.72	-0.15	0.73	0.03	0.74	-0.05	0.73	-0.04
52	0.49	0.23	0.51	-0.15	0.52	0.00	0.53	-0.05	0.53	-0.17	0.53	-0.35
53	0.69	0.57	0.72	0.35	0.73	0.29	0.74	0.44	0.74	0.14	0.75	-0.30
54	0.50	0.12	0.52	0.05	0.53	0.33	0.62	0.20	0.54	-0.09	0.54	-0.20
55	0.00	0.35	0.00	0.10	0.00	0.26	0.00	0.50	0.00	0.24	0.00	-0.32
56	0.00	0.17	0.00	-0.32	0.00	0.35	0.00	0.29	0.00	0.06	0.00	-0.29
57	0.00	0.27	0.00	-0.25	0.00	-0.25	0.00	0.12	0.00	0.00	0.00	-0.32
58	0.00	0.19	0.00	-0.14	0.00	-0.29	0.00	-0.09	0.00	-0.12	0.00	-0.42
59	0.00	-0.01	0.00	0.37	0.00	0.39	0.00	0.30	0.00	0.03	0.00	-0.20
60	0.00	0.19	0.00	-0.02	0.00	0.35	0.00	0.31	0.00	0.07	0.00	-0.38
61	0.00	0.28	0.00	0.03	0.00	0.23	0.00	0.40	0.00	0.13	0.00	-0.30
62	0.00	0.25	0.00	-0.26	0.00	-0.36	0.00	0.15	0.00	-0.08	0.00	0.04
63	0.00	0.32	0.00	0.00	0.00	-0.11	0.00	0.12	0.00	0.04	0.00	-0.18
64	0.00	0.28	0.00	0.01	0.00	-0.06	0.00	0.06	0.00	0.04	0.00	-0.12
65	0.00	0.58	0.00	0.08	0.00	0.57	0.00	0.12	0.00	0.22	0.00	-0.39
66	0.00	0.22	0.00	0.05	0.00	0.30	0.00	0.27	0.00	-0.01	0.00	-0.38

APPENDIX C

In this appendix, the measured insertion loss is presented for all configurations tested. For convenience they are presented in the same order of table 3.1.

Configuration #13

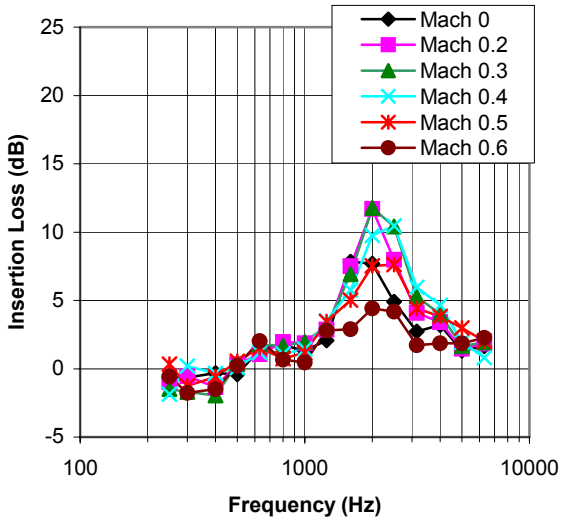

Configuration #14

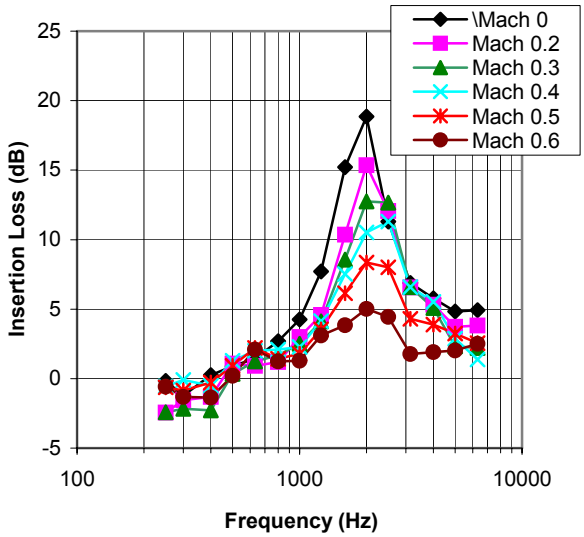

Configuration #1

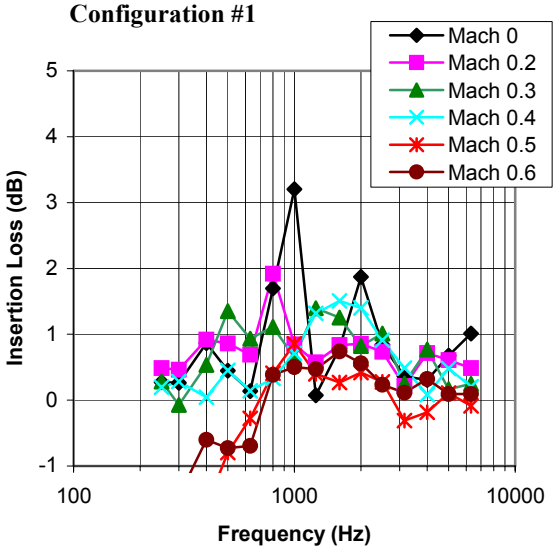

Configuration #2

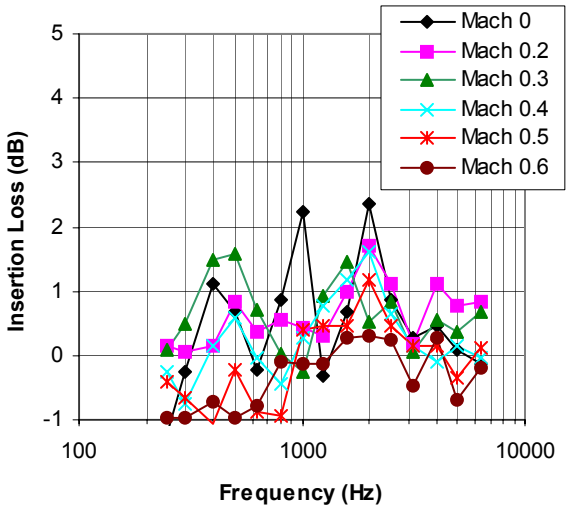

Configuration #3

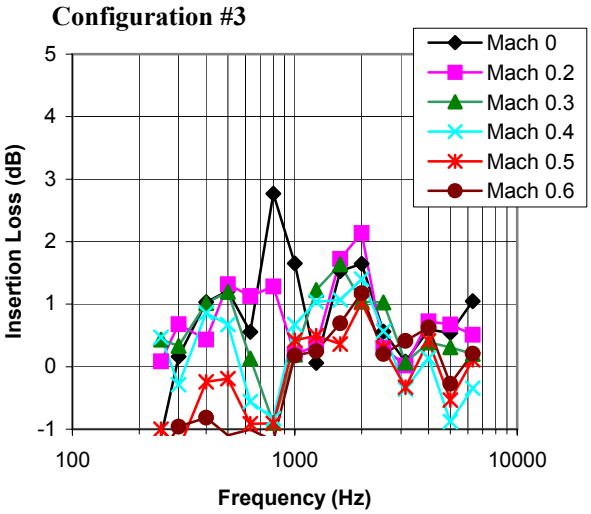

Configuration #4

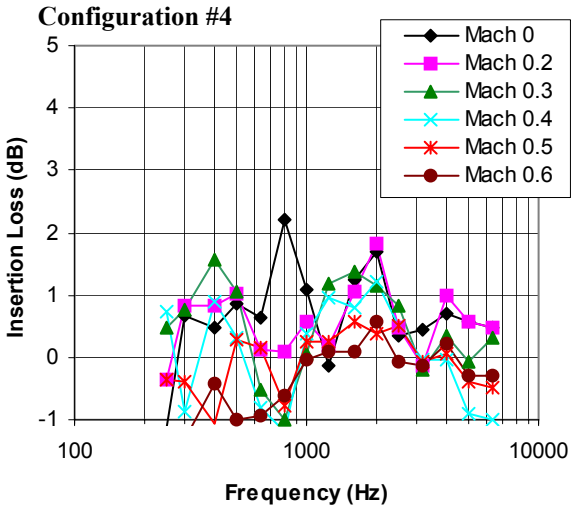

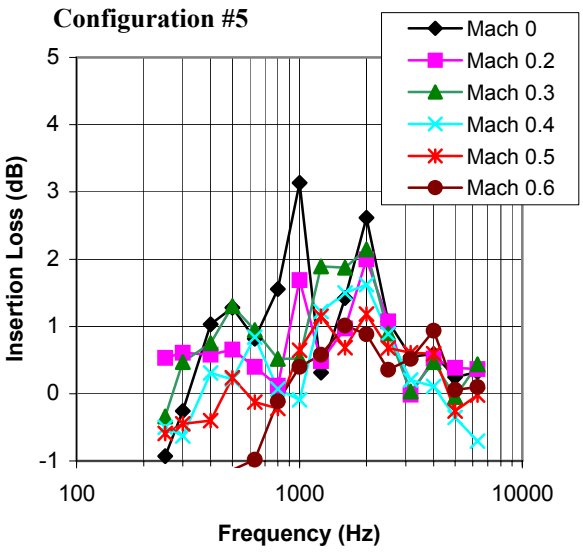
Configuration #5
Mach 0
Mach 0.2
Mach 0.3
Mach 0.4
Mach 0.5
Mach 0.6
Insertion Loss (dB)
5
4
3
2
1
0
-1
100
1000
10000
Frequency (Hz)

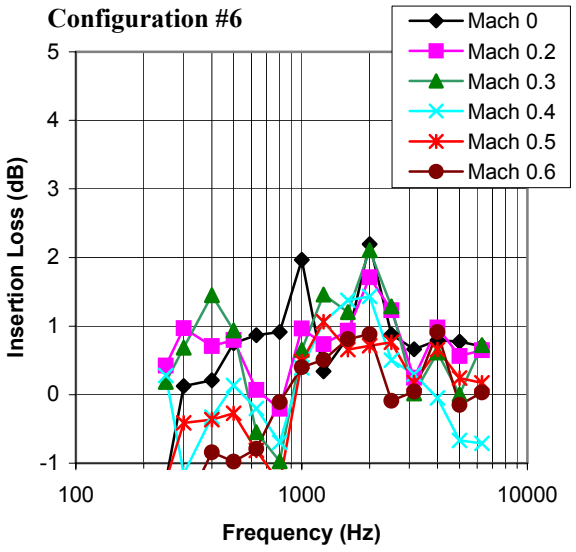
Configuration #6
Mach 0
Mach 0.2
Mach 0.3
Mach 0.4
Mach 0.5
Mach 0.6
Insertion Loss (dB)
5
4
3
2
1
0
-1
100
1000
10000
Frequency (Hz)

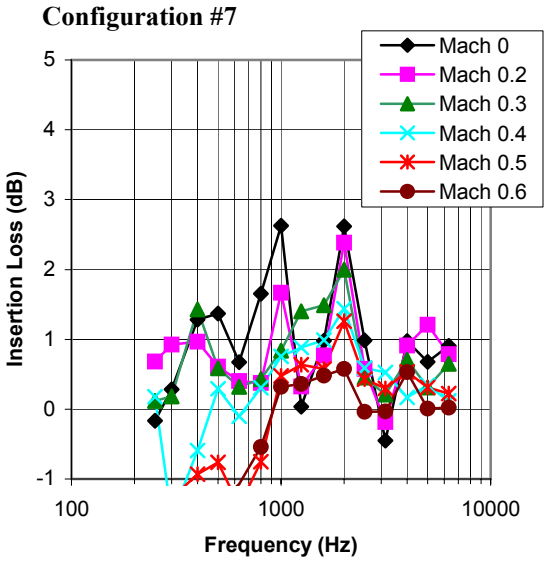
Configuration #7
Mach 0
Mach 0.2
Mach 0.3
Mach 0.4
Mach 0.5
Mach 0.6
Insertion Loss (dB)
5
4
3
2
1
0
-1
100
1000
10000
Frequency (Hz)

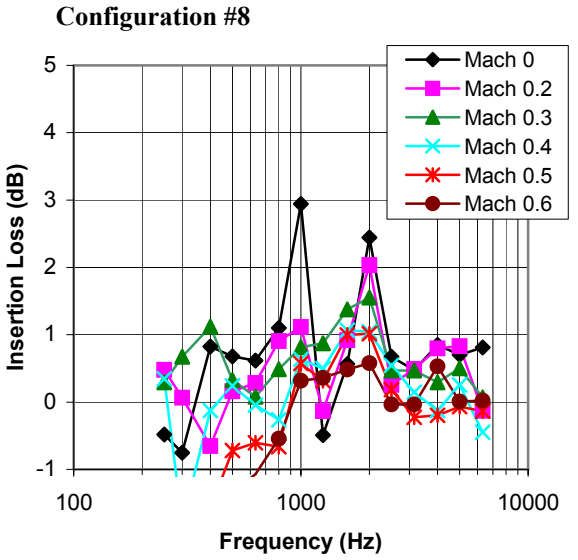
Configuration #8
Mach 0
Mach 0.2
Mach 0.3
Mach 0.4
Mach 0.5
Mach 0.6
Insertion Loss (dB)
5
4
3
2
1
0
-1
100
1000
10000
Frequency (Hz)

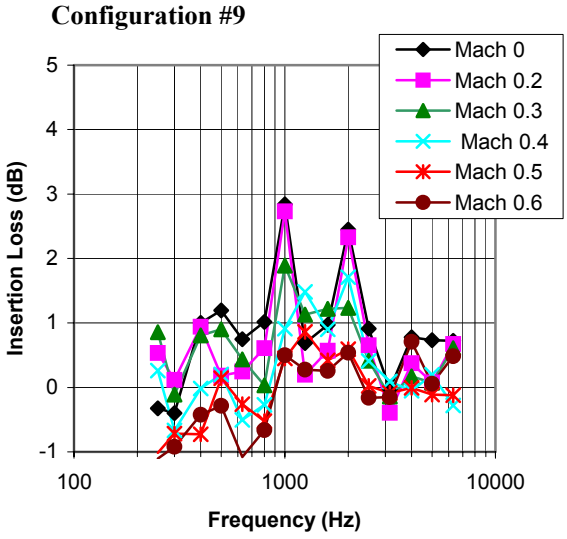
Configuration #9
Mach 0
Mach 0.2
Mach 0.3
Mach 0.4
Mach 0.5
Mach 0.6
Insertion Loss (dB)
5
4
3
2
1
0
-1
100
1000
10000
Frequency (Hz)

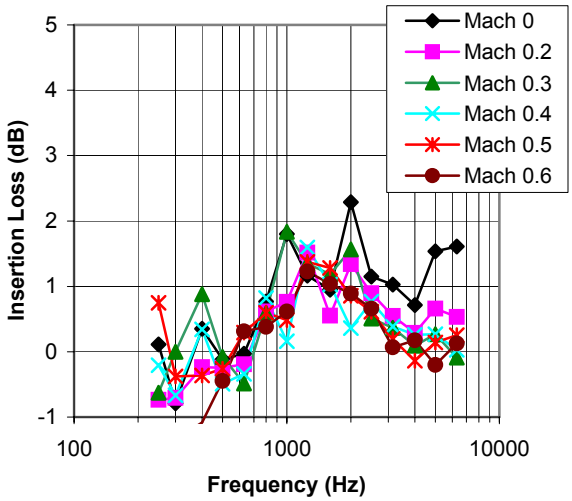
Configuration #10
Mach 0
Mach 0.2
Mach 0.3
Mach 0.4
Mach 0.5
Mach 0.6
Insertion Loss (dB)
5
4
3
2
1
0
-1
100
1000
10000
Frequency (Hz)

Configuration #11

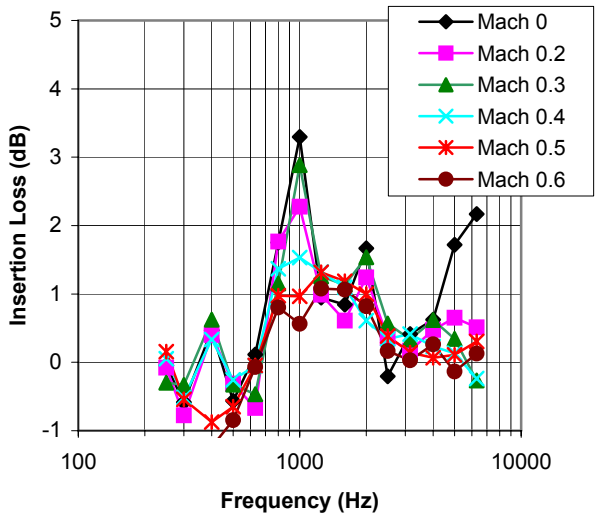

Configuration #12

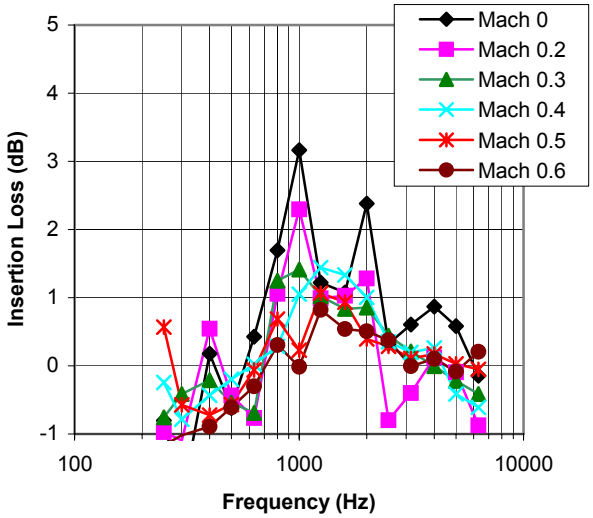

Configuration #55

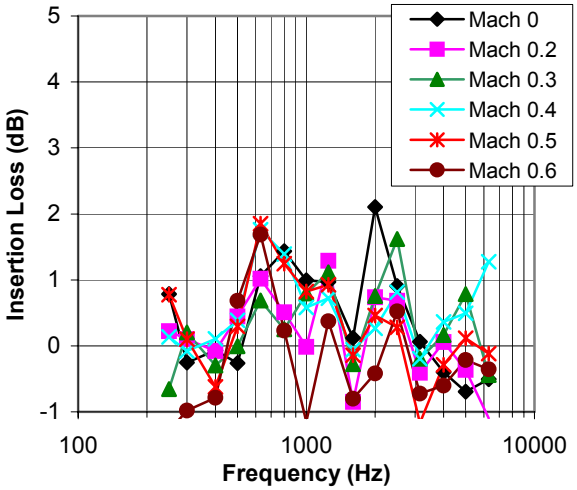

Configuration #56

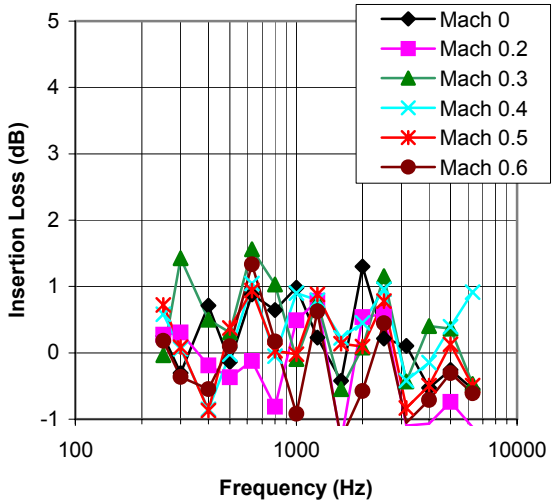

Configuration #57

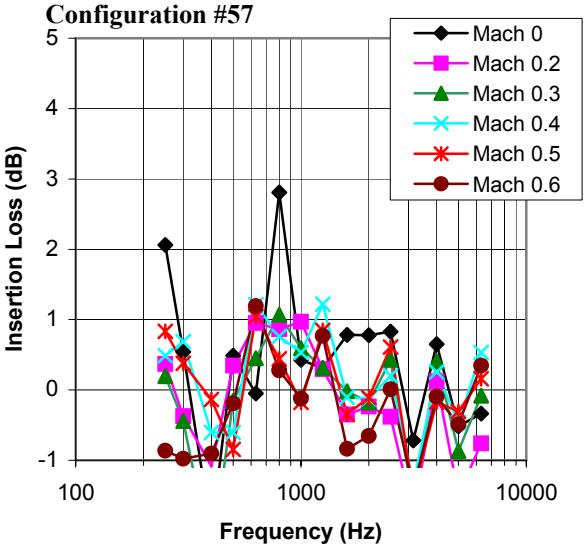

Configuration #58

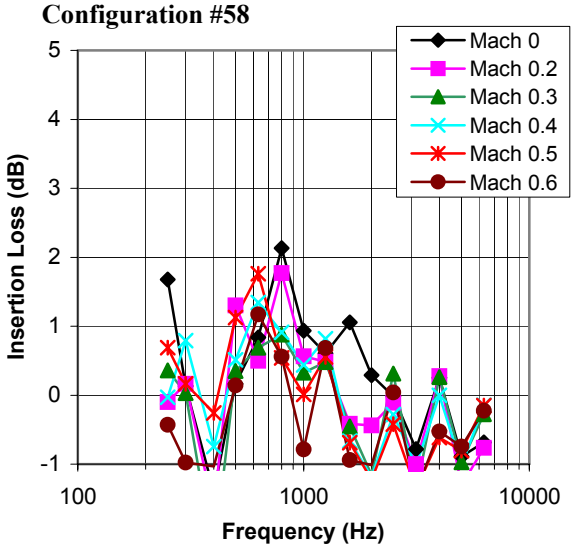

Configuration #59

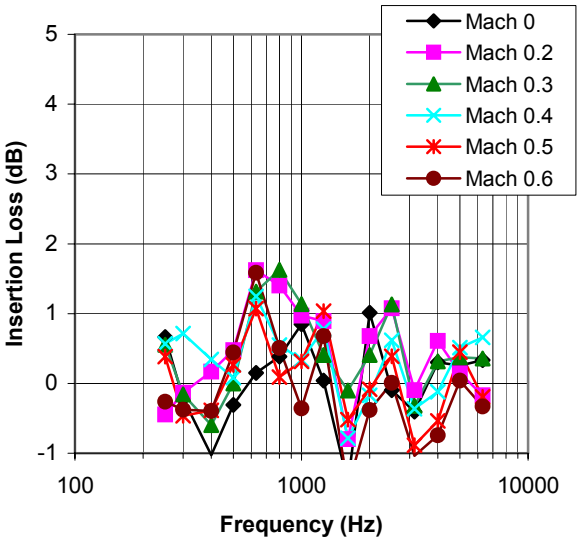

Configuration #60

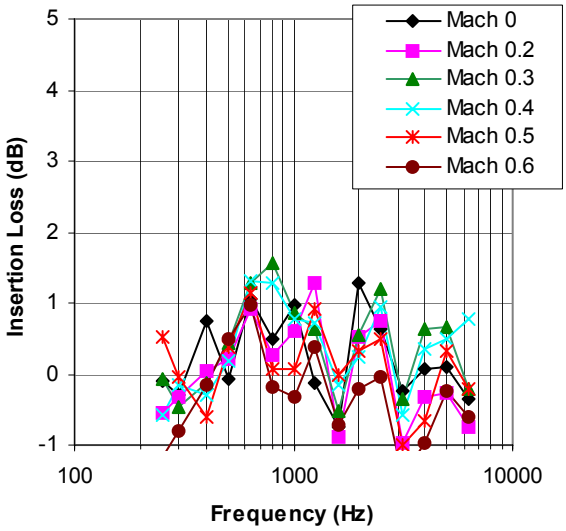

Configuration #61

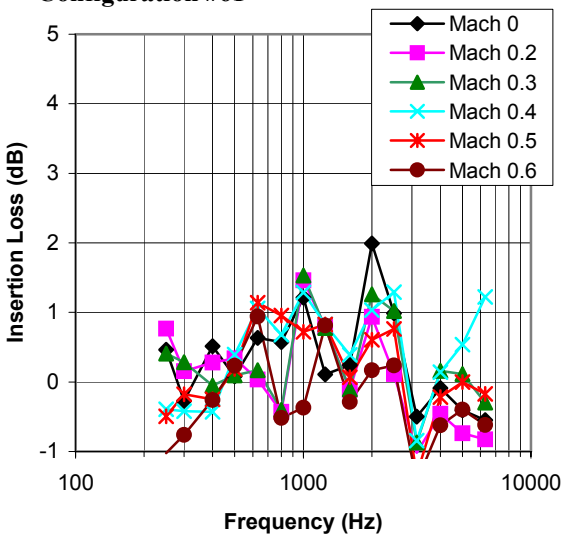

Configuration #62

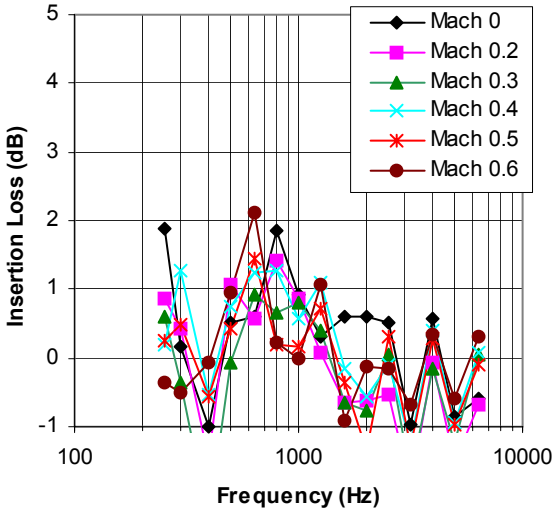

Configuration #63

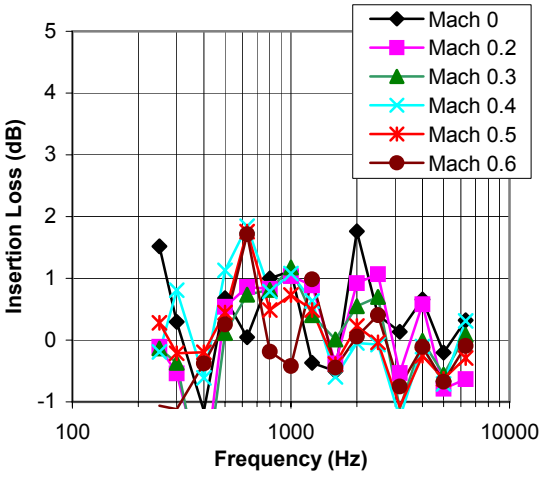

Configuration #64

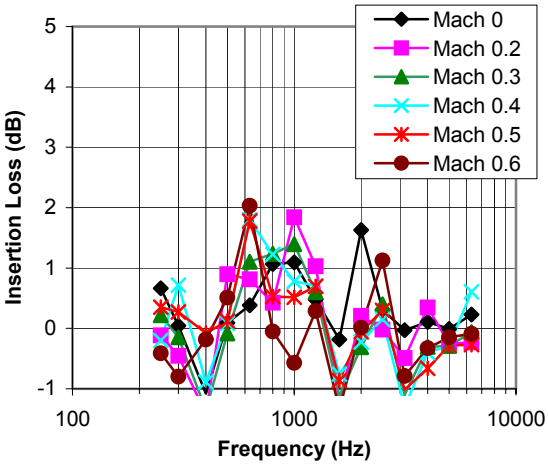

Configuration #65

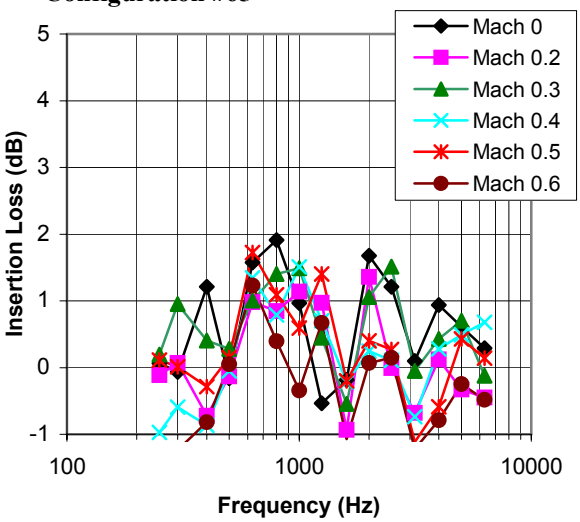

Configuration #66

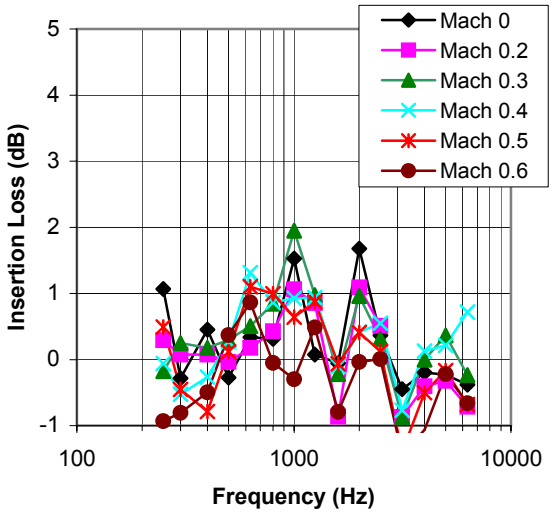

Configuration #43

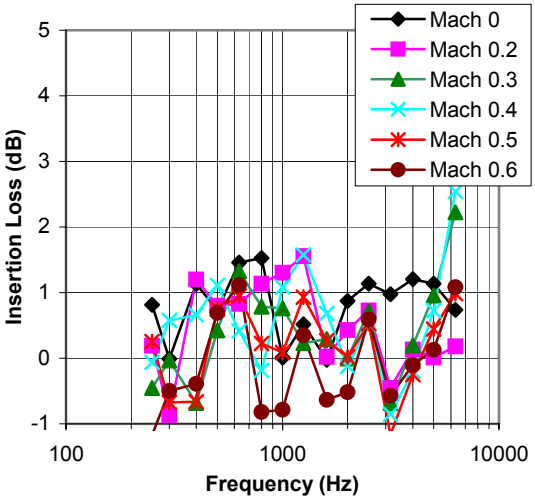

Configuration #44

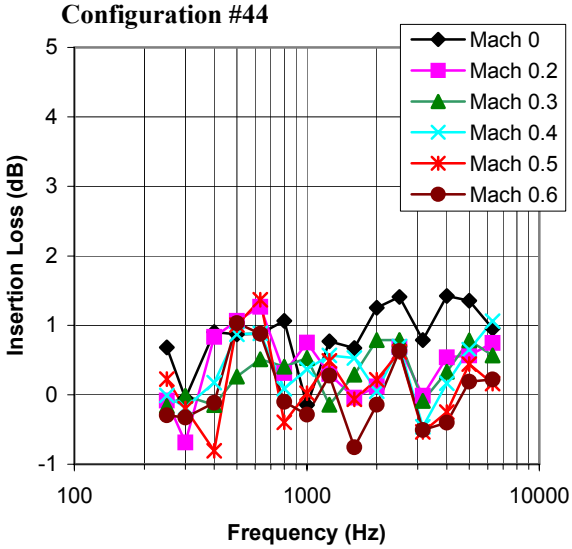

Configuration #45

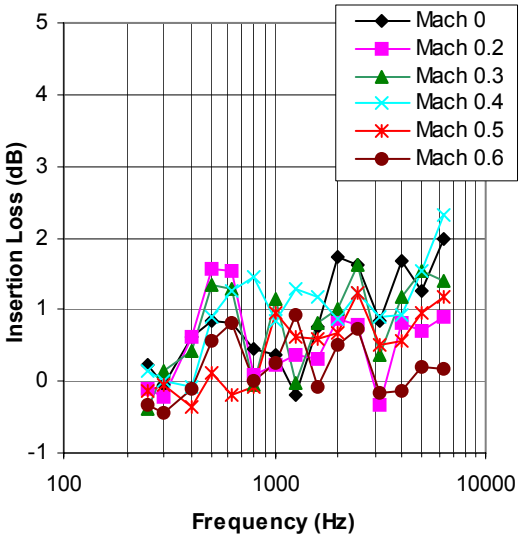

Configuration #46

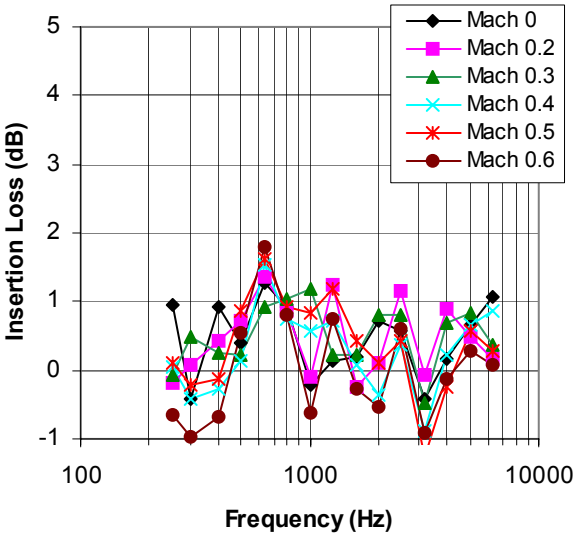

Configuration #47

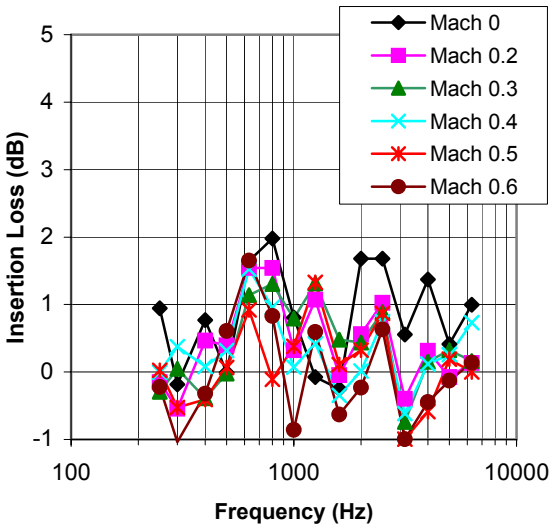

Configuration #48

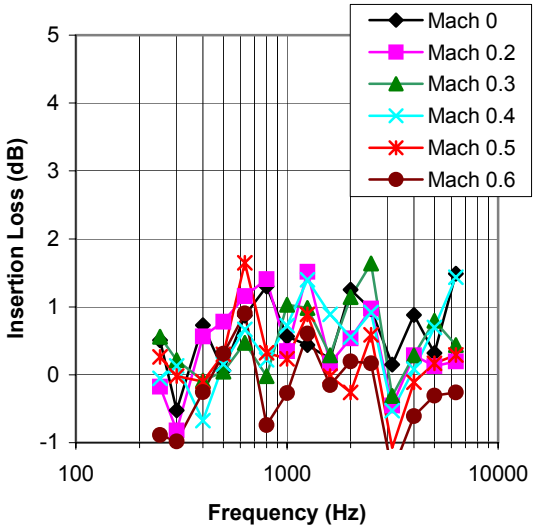

Configuration #49

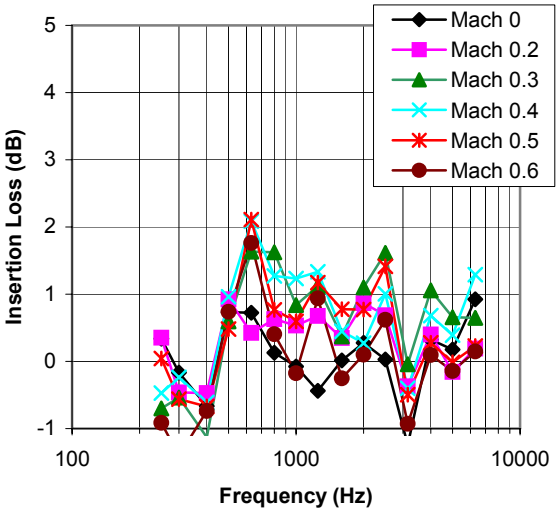

Configuration #50

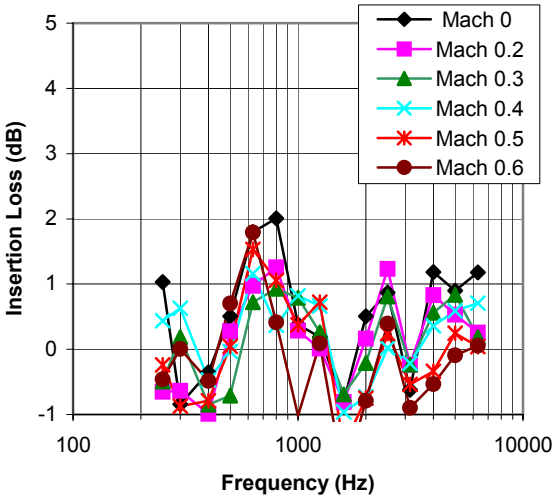

Configuration #51

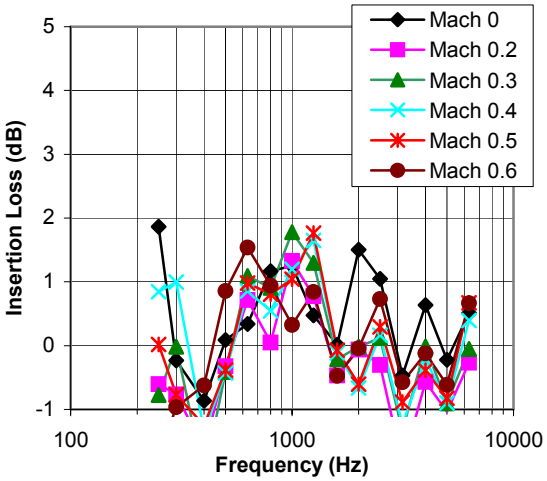

Configuration #52

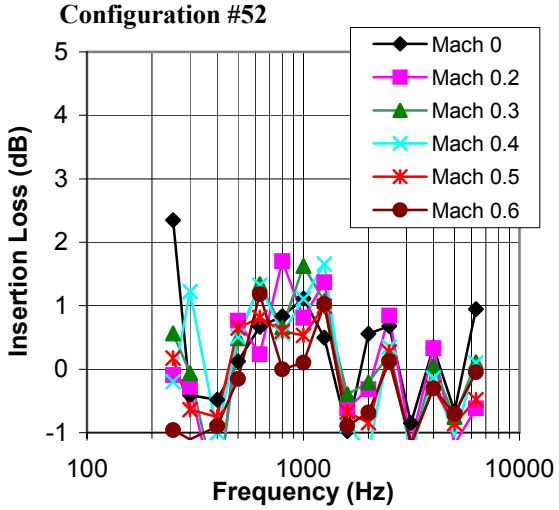

Configuration #53

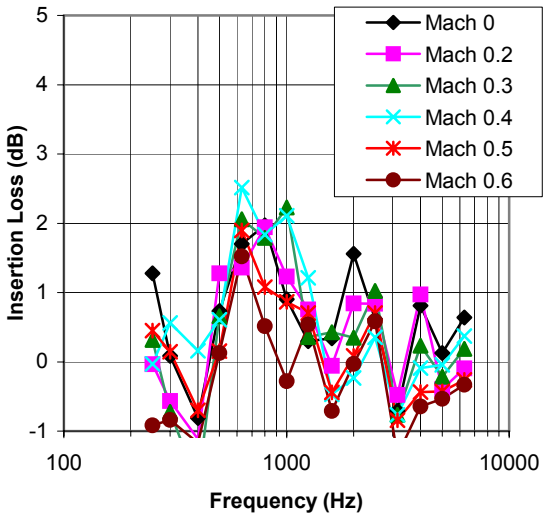

Configuration #54

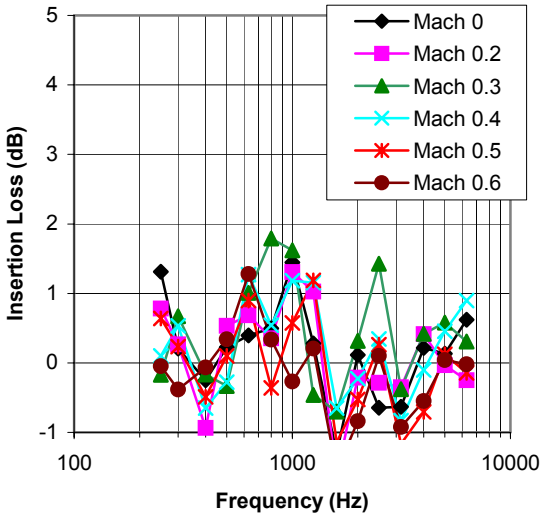

Configuration #15

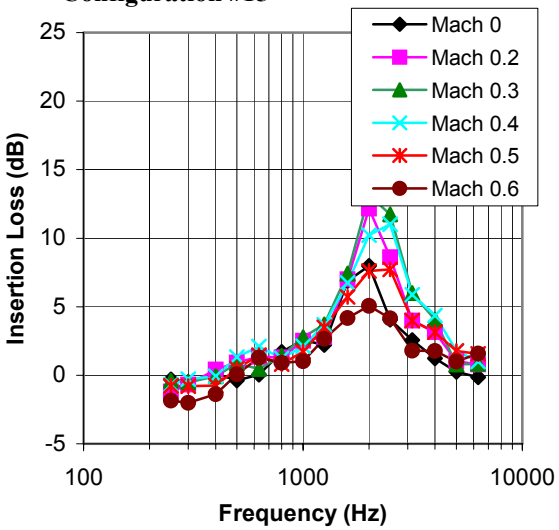

Configuration #16

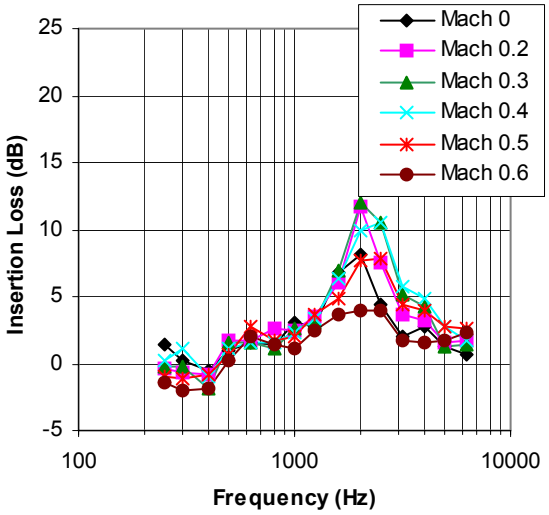

Configuration #17

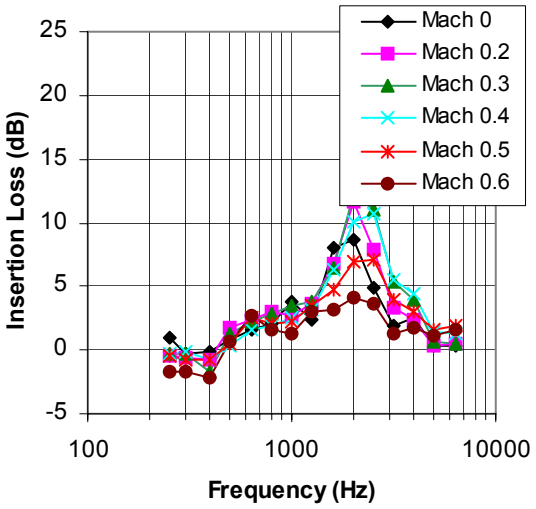

Configuration #18

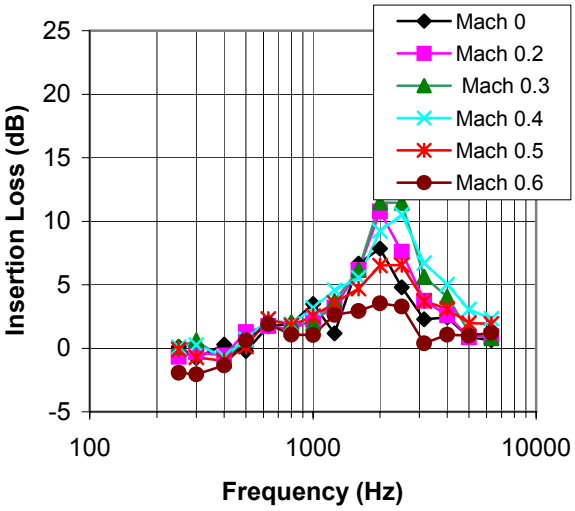

Configuration #19

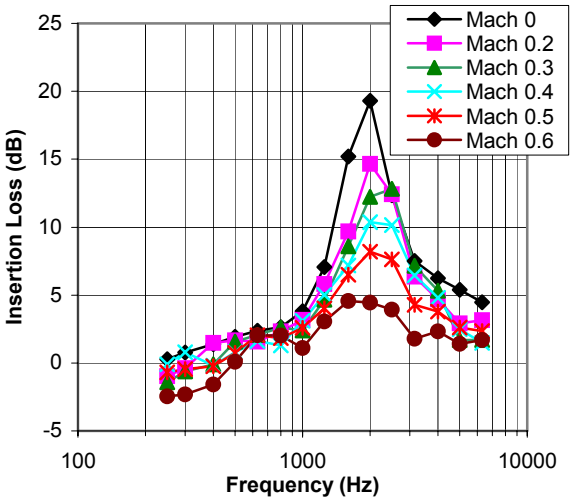

Configuration #20

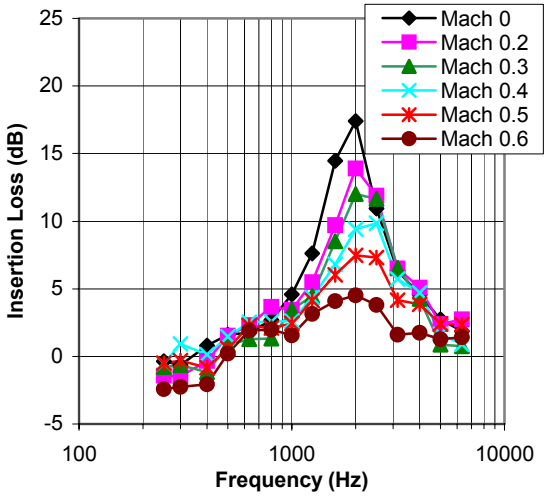

Configuration #21

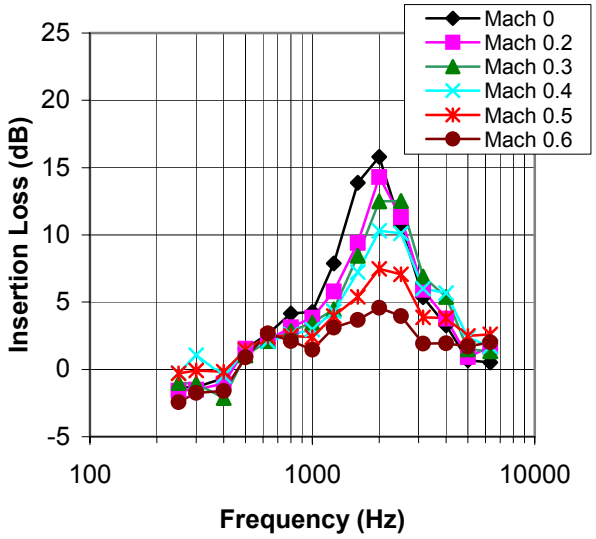

Configuration #22

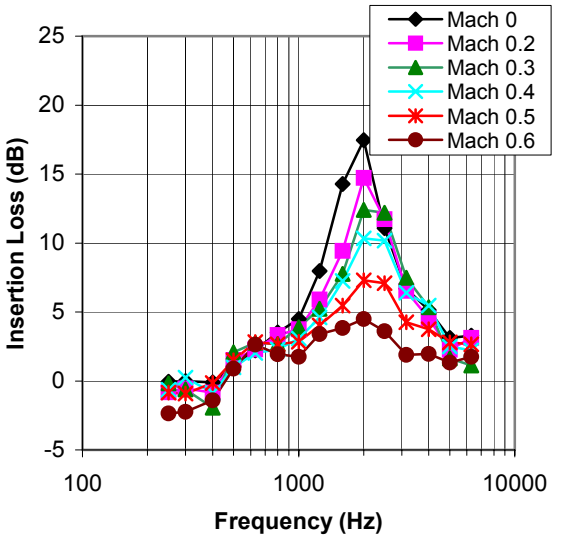

Configuration #23

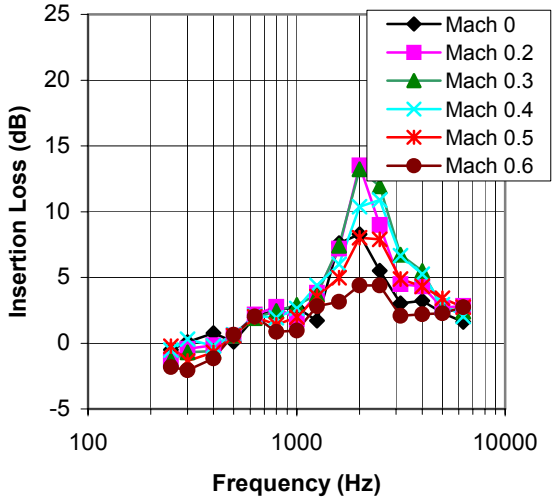

Configuration #24

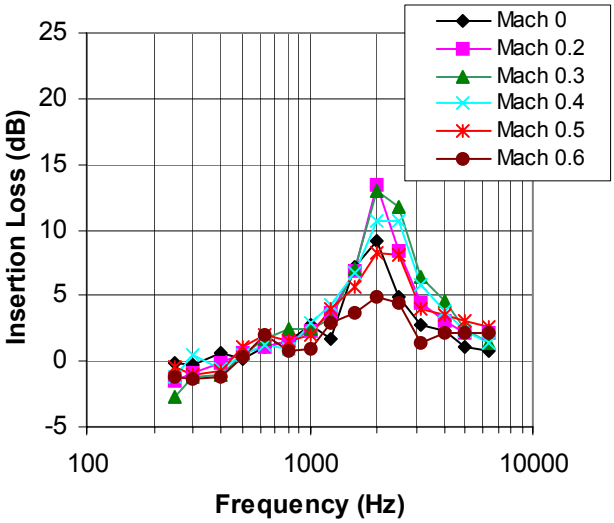

Configuration #25

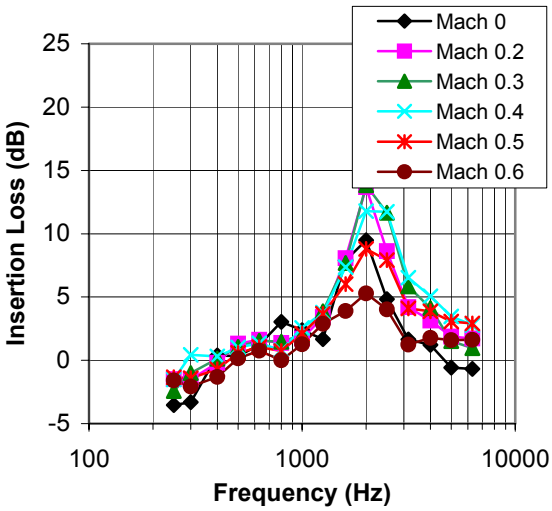

Configuration #26

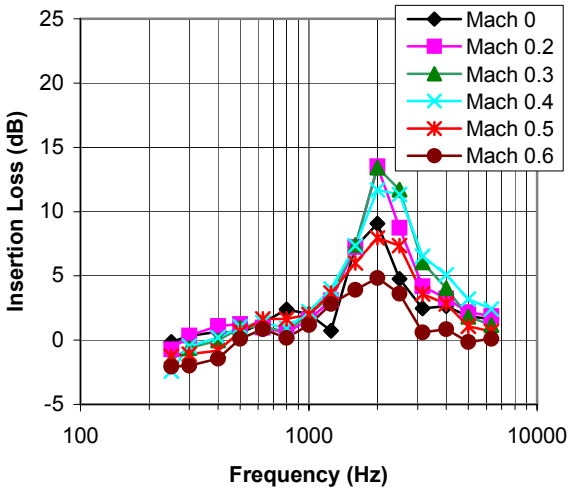

Configuration #27

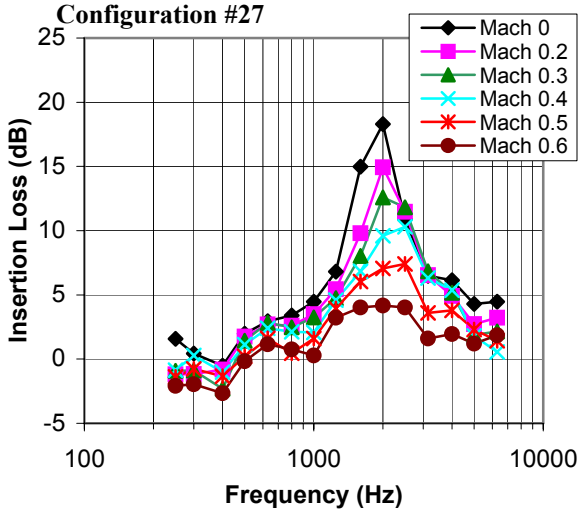

Configuration #28

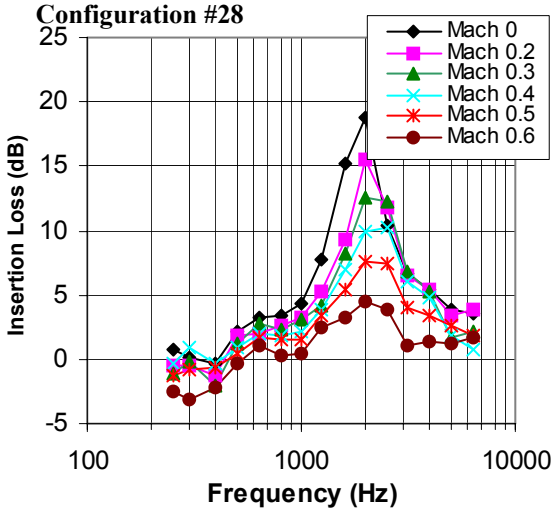

Configuration # 29

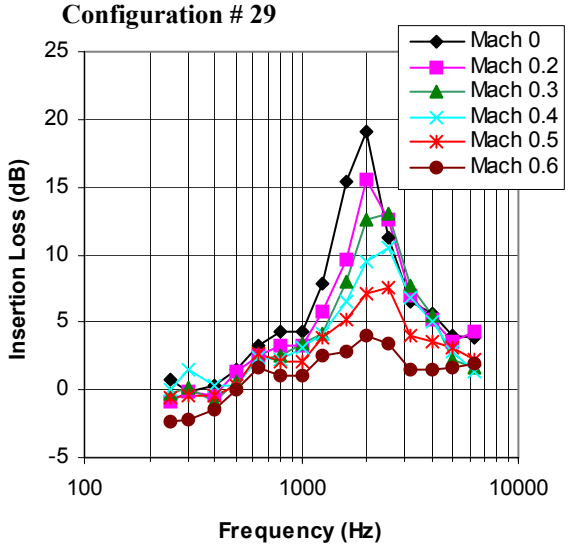

Configuration # 30

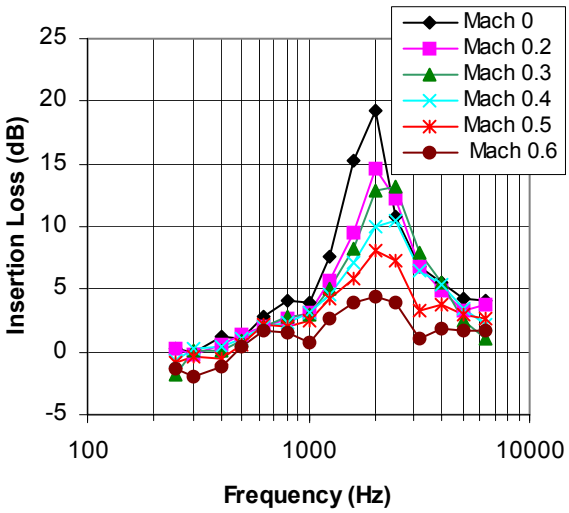

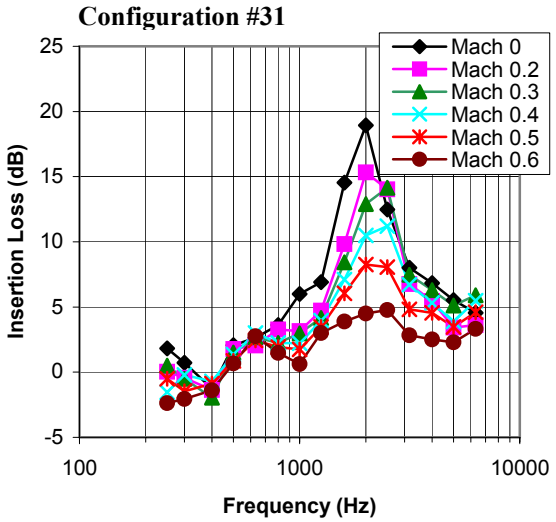
Configuration #31
Mach 0
Mach 0.2
Mach 0.3
Mach 0.4
Mach 0.5
Mach 0.6
Insertion Loss (dB)
25
20
15
10
5
0
-5
100
1000
10000
Frequency (Hz)

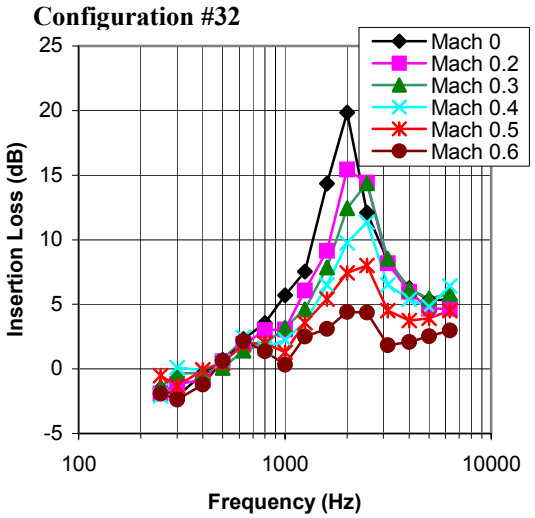
Configuration #32
Mach 0
Mach 0.2
Mach 0.3
Mach 0.4
Mach 0.5
Mach 0.6
Insertion Loss (dB)
25
20
15
10
5
0
-5
100
1000
10000
Frequency (Hz)

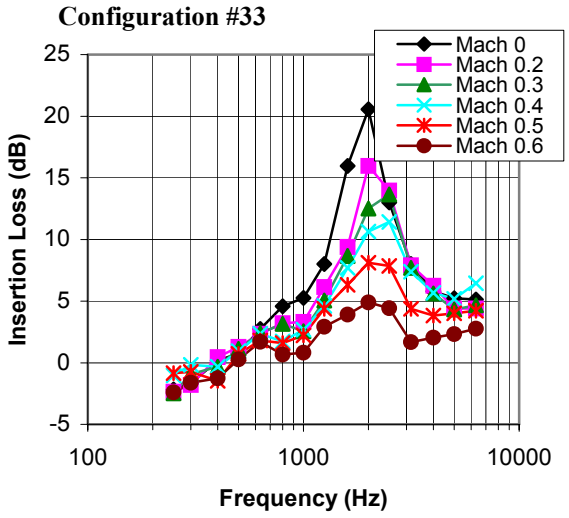
Configuration #33
Mach 0
Mach 0.2
Mach 0.3
Mach 0.4
Mach 0.5
Mach 0.6
Insertion Loss (dB)
25
20
15
10
5
0
-5
100
1000
10000
Frequency (Hz)

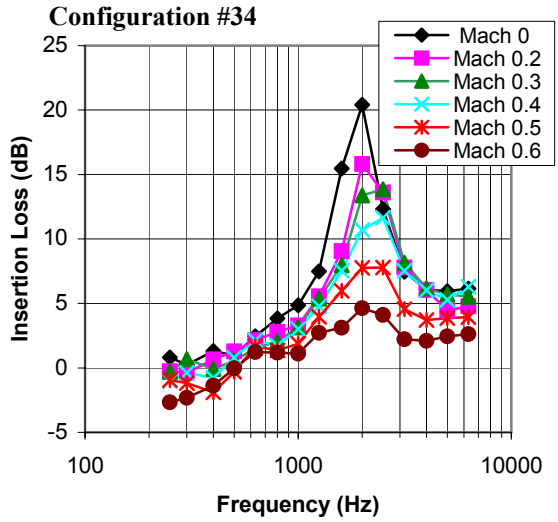
Configuration #34
Mach 0
Mach 0.2
Mach 0.3
Mach 0.4
Mach 0.5
Mach 0.6
Insertion Loss (dB)
25
20
15
10
5
0
-5
100
1000
10000
Frequency (Hz)

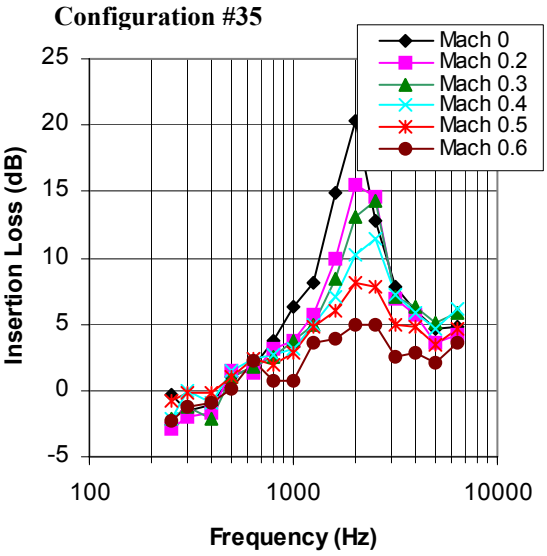
Configuration #35
Mach 0
Mach 0.2
Mach 0.3
Mach 0.4
Mach 0.5
Mach 0.6
Insertion Loss (dB)
25
20
15
10
5
0
-5
100
1000
10000
Frequency (Hz)

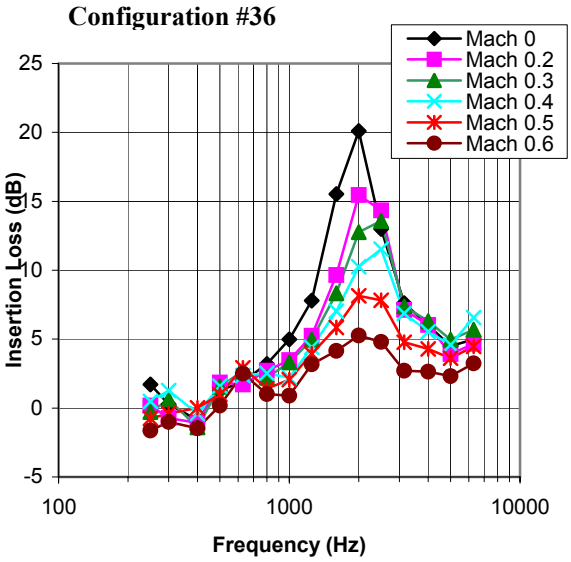
Configuration #36
Mach 0
Mach 0.2
Mach 0.3
Mach 0.4
Mach 0.5
Mach 0.6
Insertion Loss (dB)
25
20
15
10
5
0
-5
100
1000
10000
Frequency (Hz)

Configuration #37

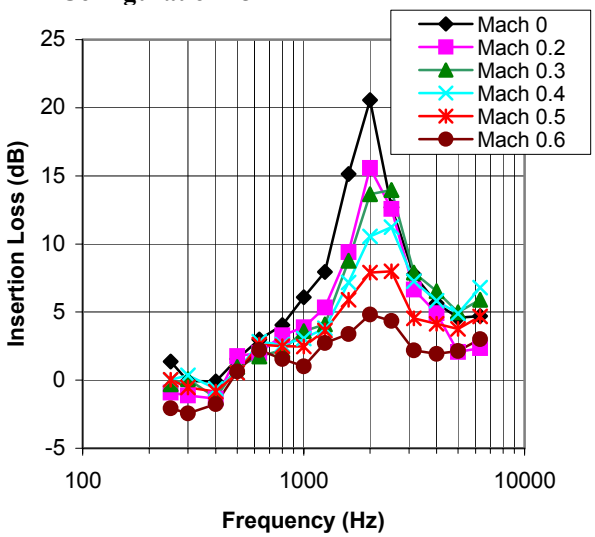

Configuration #38

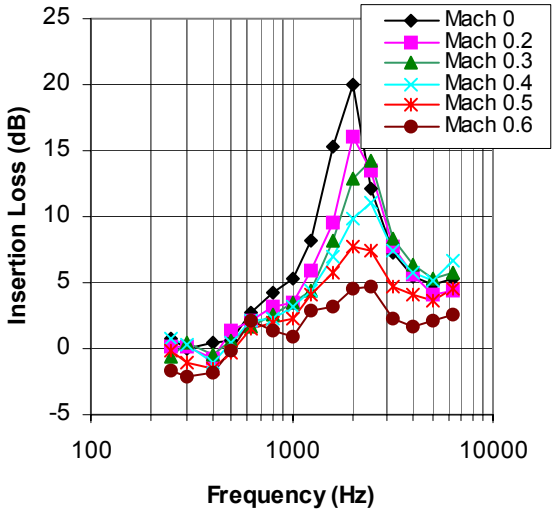

Configuration #39

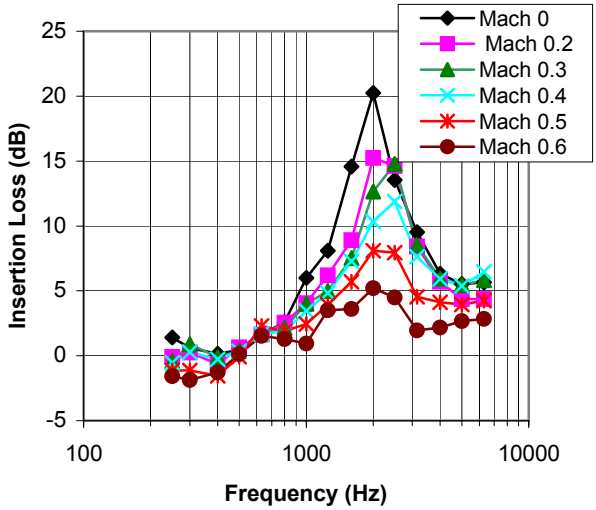

Configuration #40

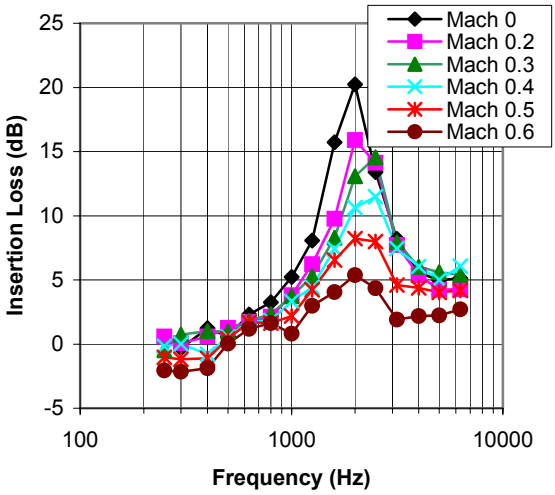

Configuration #41

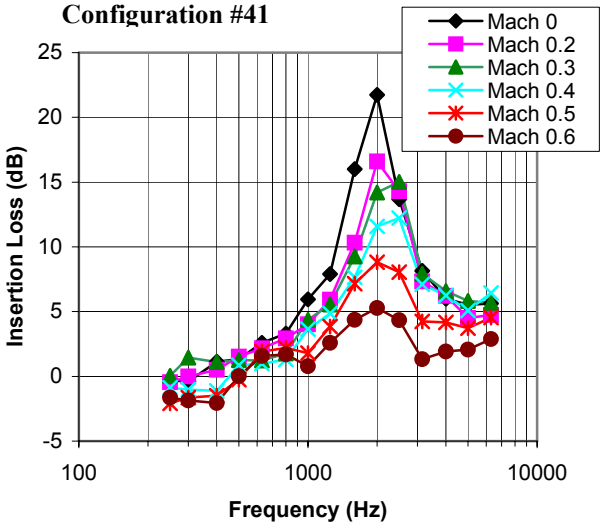

Configuration #42

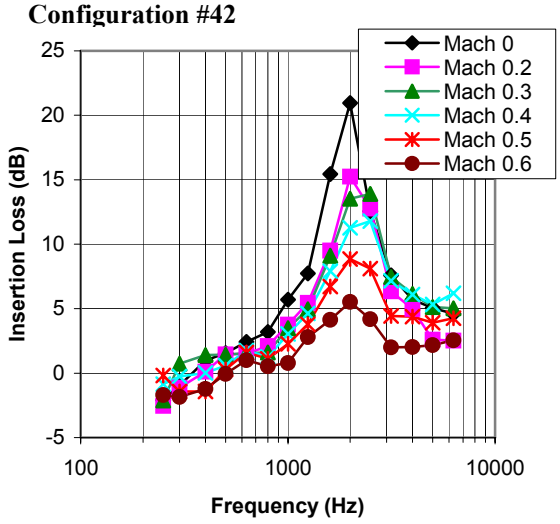

Vita

Jeonghoon Kim was born on September 5, 1971 in Seoul, Korea. In 1990, he entered Chung-Ang University in Seoul. After finishing military service, he transferred to Pennsylvania State University in the United States. He received a degree of B.S. in mechanical engineering in 1999.

He then began graduate studies in the Mechanical Engineering Department of Virginia Polytechnic Institute where completed his master's degree in September, 2001.